2022

INNOVATIONS

VIII INTERNATIONAL SCIENTIFIC CONGRESS

INNOVATIONS 2022

20-23.06.2022 VARNA

PROCEEDINGS

SCIENTIFIC-TECHNICAL UNION OF MECHANICAL ENGINEERING - INDUSTRY 4.0
BULGARIA

VII INTERNATIONAL SCIENTIFIC CONGRESS

INNOVATIONS

PROCEEDINGS

"INNOVATION POLICY AND INNOVATION MANAGEMENT"
"INNOVATIVE SOLUTIONS"

20 – 23 JUNE, 2022,
VARNA, BULGARIA

INTERNATIONAL EDITORIAL BOARD

C O N T E N T S

Development of predictive maintenance based on artificial intelligence methods

Ivan Kuric*, Daria Fedorová, Vladimír Stenchlák, Martin Bohušík, Michal Bartoš, Milan Sága Jr.

University of Žilina, Faculty of Mechanical Engineering,

Department of Automation and Production Systems, Slovakia

ivan.kuric@fstroj.uniza.sk

Abstract: Artificial intelligence become more widespread in all manufacturing subjects. In manufacturing artificial intelligence deals with such tasks as quality control, robot navigation, computer vision, processes controlling, etc. The area of maintenance in machining is a great prospect for implementing artificial intelligence tools for analysis, prediction of monitored parameters, optimization, and improvement of the quality of the maintenance process. In particular, the article refers to predictive maintenance as a modern trend in mechanical engineering. In this article, a quick review of using methods of artificial intelligence and predictive analytics in maintenance and one practical implementation case of NAR network for time-series prediction was provided.

Keywords: ARTIFICIAL INTELLIGENCE, PREDICTIVE MAINTENANCE, MATLAB, NAR NETWORK

1. Introduction

The industry is the part of the economy that produces materials and goods with a high degree of mechanization or automation to ensure the requirements for the quality of products and the productivity of the production process. Fundamental changes in technologies and methods of production, which were characterized by the introduction of new technologies at the whole stage of the development of industrialization, are now called industrial revolutions.

Nowadays, smart technologies, together with the massive introduction of information technology in the industry, large-scale automation of business processes, and the spread of artificial intelligence, create the basis for the future new industrial revolution called Industry 4.0.

When starting a new production process, a lot of attention is given to such points as the economic calculation of production efficiency, the choice of equipment, suppliers, and materials. The goal of any modern production is the productive, economical, and safe production of goods in the right volume while maintaining the desired level of quality.

At the same time, the progress of technology is causing the implementation of new highly productive machining methods, which also place higher demands on production machines and tools, their reliability, and the reliability of the production process itself.

Reliability is the ability of the equipment to perform required functions in the specified technical conditions over the operation. One of its most important features is faultlessness, which is defined as the ability of a machine to complete all specified conditions and parameters by the manufacturer's technical documentation and recommendations within the specified manufacturer's time.

And a reduction in the machine's ability to operate in a fault-free or operational mode leads to errors and defects in machine operation, production failures and can ultimately lead to faulty failures and emergencies.

2. Maintenance in the industry

The great importance of maintenance for the industry is difficult to underestimate, as its neglect is a major cause of failure and the associated costs and losses in the production process, as preventing failure is always cheaper in the end than eliminating its consequences.

The term "maintenance" according to the standard STN EN 13 306 means a summary of all activities (management, technical and administrative), the aim of which is to maintain, maintain the equipment in working order, or restore such conditions.

We often talk about maintenance strategies, which are divided into post-failure maintenance (reactive maintenance) and pre-failure maintenance. The main division of maintenance strategies is shown in Fig. 1.
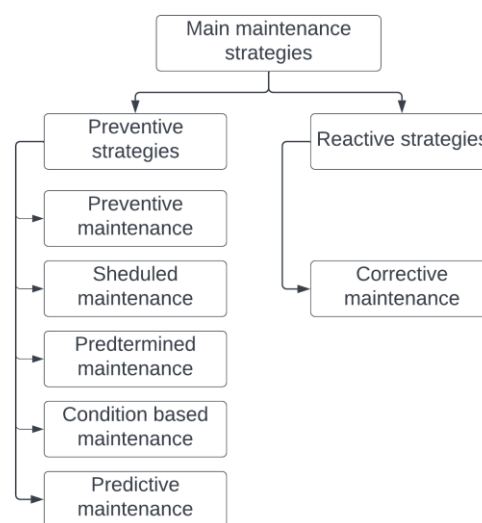
Fig. 1 *The division of maintenance strategies*

The main goal of maintenance is to maintain the operability of the machines, which means ensuring the smoothest possible operation of the production process, minimizing the time of production interruption, and eliminating the negative consequences of machine downtime. Maintenance goals also include achieving and extending the planned technical life of production machines, minimizing threats to environmental damage, and preventing occupational accidents and health [2].

3. Predictive maintenance as a modern trend

The obvious advantages of preventive maintenance over reactive maintenance are, for example, a lower risk of failures that will cause a long-term shutdown of the equipment, a reduction in the risk to the health and life of workers working with the equipment. The possibility of maintenance planning in connection with planned outages causes a significant reduction in maintenance costs. However, the maintenance interval specified by the manufacturer is not always optimal and appropriate for a particular operation, and the separate determination of such an interval may be associated with downtime risks and unforeseen costs.

Predictive Maintenance (PdM) deals with the problem of determining the correct length of maintenance cycles. The goal is to schedule maintenance at the most convenient and cost-effective time to optimize equipment life before the equipment will be

damaged. Unlike preventive maintenance, the maintenance of each device is assessed and planned based on the current state of the device. The basis of predictive maintenance is perfect "condition monitoring" - using a summary of certain measured physical parameters (such as system pressure, temperature, vibration, etc.), the current state is determined continuously. Furthermore, based on these data, we use statistical and artificial intelligence methods to try to estimate the failure time. With this procedure, we enable a sharp reaction to a change in the condition of the equipment, and subsequently, depending on the real situation, it is possible to extend or shorten the maintenance cycle for a specific machine.

Predictive maintenance is a current trend in the industry, as predictive maintenance is in principle more effective than preventive maintenance because it is based not only on the actual current state of the equipment but also on the historical load and considers other factors. It also reduces the number of unplanned downtimes, increases productivity, reduces the cost of maintaining operability, and increases the safety of the production process

4. Artificial intelligence and machine learning in PdM

Unlike traditional maintenance procedures that rely on the life cycle of machine components, a predictive approach based on the principle of machine learning prevents the loss of resources and insufficiently optimized use of resources for maintenance tasks.

Artificial intelligence in predictive maintenance can adapt routine maintenance activities to the needs of each device. The implemented artificial intelligence system can be taught to visually identify errors and patterns in the device, can follow the instructions of a computer-aided design without further programming of the system, and even use the currently obtained data for subsequent training and real-time model improvement. Automatic anomaly detection reduces unplanned downtime and costs by quickly providing an estimate of when a device will fail. Successfully implementation of artificial intelligence for predictive analytics tasks is shown in [3-5].

In terms of predictive maintenance of machines and equipment, continuous monitoring has great importance. By using the sensor on the investigated machine, it is possible to create a mass of data on the state of the device continuously in time. These, in turn, together with the historical data after establishing the dependencies between the normal and faulty states of the system and the corresponding parameters, already allow the top of the prediction model.

The maintenance interval prediction task is essentially a time series prediction task. The time series is arranged according to the time of occurrence of the series of quantities of some investigated parameter. The values of the examined parameter are usually recorded in equally long-time intervals. The time series is used to monitor time changes and monitor trends in the development of the examined parameter. Furthermore, changes to any parameters are chaotic because they change randomly in the real world.

The most used in research and practice models for time series prediction are linear autoregressive models (AR and ARX). moving average model (MA), autoregressive moving average (ARMA), LSTM neural networks model, and nonlinear autoregressive (NAR and NARX) neural network models.

AR and ARX models were successfully implemented for example in [6,9] for regulation of the climate parameters in buildings and greenhouses. Among the main benefits of the ARX model is the simple structure of the model - a small number of model parameters, simplicity of interpretation of model parameters, and simplicity of possible integration of the model into the control system. However, ARX models are not able to estimate nonlinear dependencies.

The ARMA (autoregressive moving average) model class can be used to solve problems in engineering, economics, and the natural sciences, which have a large amount of data where the observed quantities are interdependent. The models can be used for both deterministic and stochastic modeling using historical data and prediction errors to generate forecasts, dynamic analyses, and other statistical information with a minimum number of parameters used to represent system dynamics.

Algorithms that use ARMA models for prediction show good results for short-term prediction and this can be seen in studies [8,10], but the accuracy of the model decreases significantly as the time for which parameter values need to be predicted increases. The response tends to over-reproduce the average of values observed in the past. In addition, these methods work with homogeneous time series, where input and prediction are within the same set of values.

All the above models can be used to construct the recurrent neural network (RNN) for time-series prediction. However, they have a problem storing and spreading errors in time. It happens because the backpropagated error either disappears quickly or increases sharply, as the magnitude of the error signal propagated back in time depends exponentially on the size of the scales.

This problem can be solved by using long-short time memory (LSTM) networks. The structure of the LSTM neural network consists of cells (Fig. 2), which are formed by an entrance gate, an exit gate, a forgetting gate, and a memory cell.
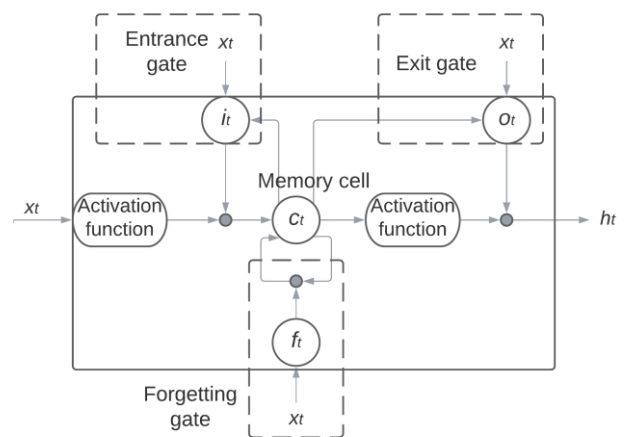
Fig. 2 *The LSTM cell structure*

Using the LSTM network allows tracking the dependencies of new observations with past (even very distant) ones. However, this capability, due to the tendency of the cell state values to increase linearly (especially when observing a continuous data flow), can cause the LSTM module to fall into a normal error backpropagation network. This means that the main ability - to keep the error in time will be eliminated. In general, LSTM models are complex and are rarely used to predict a single time series because they require a large amount of data to be estimated. However, they are commonly used when predictions are needed for many time series [1].

One of the modern and most widely used time prediction methods is prediction using NAR (Nonlinear AutoregRession) and NARX (Nonlinear AutoregRession with exogenous inputs) neural networks.

A NAR neural network is a type of dynamic neural network based on time series. The relationship between the input and output variables of the model is not just a static mapping, but the output of each moment is synthesized based on the dynamic results of the system before the current moment, so it has a feedback and memory function.

In the case of a neural network NAR, the delayed time series values are used as inputs to the neural network. The output from the neural network is a predicted value, corresponding to the value of the parameter that needs to be predicted at a certain point in time[5].

5. An example of time-series prediction using NAR network

To visually illustrate the predictive ability of a nonlinear autoregressive neural network to make predictions, a simple model was developed in the MATLAB software package to predict the magnitude of the output signal for acceleration data.

To generate a gyroscopic dataset an M5-StickC microcontroller (see Fig. 3) was used.

Fig. 3 The M5-StickC microcontroller

The M5-StickC microcontroller can read acceleration along the X, Y, and Z axes as well as gyroscopic data in the same axes at a frequency of 18 measurements per second. The created data set was then saved in .csv format.

Before entering the neural network, data must be pre-processed to eliminate error values and possible completion of missing points. The result is shown in Fig. 4.
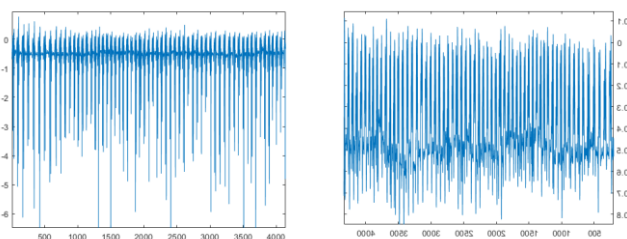
Fig. 4 Data before pre-processing (left) and after pre-processing (right)

The Designed NAR network consists of the input layer, 3 hidden layers with tangent sigmoid function as an activation function, and the output layer with linear function as an activation function. The structure of the neural network is shown in Fig. 5.

For time series prediction tasks, the NAR neural network architecture, unlike conventional recurrent networks, is designed as a time-delay neural network (TDNN). It means that the output of each moment is synthesized based on the dynamic results of the system before the current moment, so it has a feedback and memory function.
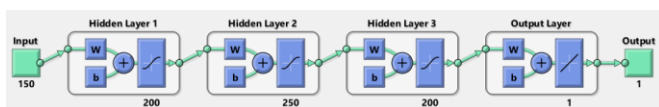
Fig. 5 The structure of the designed NAR network

After creating the training dataset, the neural network was trained, and a one-step-ahead prediction plot was built. In Fig. 6 prediction values (orange plot) and real-time values (blue plot) are shown for one-step prediction.
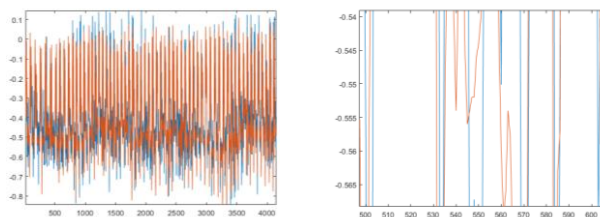
Fig. 6 Predicted and real-time values

6. Results and discussion

The proposed neural network model showed a high preliminary result for predicting the values of the time series. When predicting one step, the prediction accuracy reached 90%. This is illustrated by the regression plot (Fig. 7).
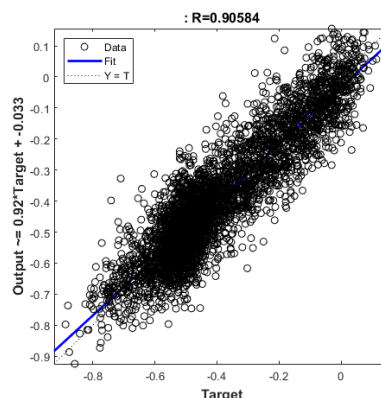
Fig. 7 Regression plot for one step ahead prediction

However, in the case of predicting more steps, the accuracy of the proposed model dropped significantly (see Tab. 1).

Tab. 1 Accuracy of proposed neural network

Number of ahead prediction steps	Correlation coefficient value
5	0,76
10	0,57
20	0,28

As can be seen from Tab. 1, the predictive accuracy for predicting 20 steps is approximately 28%, which means that the accuracy for using the proposed neural network in practice for predictive maintenance tasks is not suitable.

The decrease in accuracy can be due to the insufficient quality of the data taken - the data acquisition technique did not assume a cyclic change in the parameters, and because of this, the parameters were chaotic. It is possible to partially eliminate this disadvantage with the help of better data pre-processing. However, the methodology for obtaining data needs to be developed more carefully.

Another possible reason for poor prediction may be the architecture of the neural network itself. It is probably worth trying to use a different number of hidden layer neurons and the number of layers itself, as well as other activation functions.

7. Conclusion

In this paper, a brief analysis of artificial intelligence models used for predictive analytics in predictive maintenance tasks was made. A model was proposed, and an example was given of using a neural network with non-linear autoregression to predict the behaviour of acceleration data along with one of the axes.

Experimental data showed insufficient reliability of the proposed model for real practical problems. The presumably negative results were contributed by the chaotic nature of the data (the stable dependence of the microcontroller readings on the moment in time in the future) and the too simple structure of the neural network. In the future, it is planned to develop another neural network model with non-linear autoregression for a more accurate forecast and the possibility of using such a model in practice.

8. *References*

1. Burba, D. (2019). An overview of time series forecasting models. Towards Data Science. https://towardsdatascience.com/an-overview-of-time-series-forecasting-models-a2fa7a358fcb

2. Červeňan, A. (2015). Systém údržby. 70. https://www.sjf.stuba.sk/buxus/docs/docs/edicne/Udrzba_farebna_final.pdf

3. Chan, R. W. K., Yuen, J. K. K., Lee, E. W. M., & Arashpour, M. (2015). Application of Nonlinear-Autoregressive-Exogenous model to predict the hysteretic behavior of passive control systems. Engineering Structures, 85, 1–10. https://doi.org/10.1016/J.ENGSTRUCT.2014.12.007

4. Liu, Q., Chen, W., Hu, H., Zhu, Q., & Xie, Z. (2020). An Optimal NARX Neural Network Identification Model for a Magnetorheological Damper With Force-Distortion Behavior. Frontiers in Materials, 7, 10. https://doi.org/10.3389/FMATS.2020.00010/BIBTEX

5. Ma, Y., Yuan, D., Yan, J., & Qu, Y. (2018). Predictive Guidance Scheme with NAR Neural Network for Autonomous Aerial Refueling. IEEE CSAA Guidance, Navigation and Control Conference, CGNCC. https://doi.org/10.1109/GNCC42960.2018.9018859

6. Mustafaraj, G., Lowry, G., & Chen, J. (2011). Prediction of room temperature and relative humidity by autoregressive linear and nonlinear neural network models for an open office. Energy and Buildings, 43(6), 1452–1460. https://doi.org/10.1016/J.ENBUILD.2011.02.007

7. Pang, X., Huang, R., Wen, J., Shi, Y., Jia, J., & Zeng, J. (2019). A lithium-ion battery rul prediction method considering the capacity regeneration phenomenon. Energies, 12(11). https://doi.org/10.3390/EN12122247

8. Rajagopalan, S., & Santoso, S. (2009). Wind power forecasting and error analysis using the autoregressive moving average modeling. 2009 IEEE Power and Energy Society General Meeting, PES '09. https://doi.org/10.1109/PES.2009.5276019

9. Ríos-Moreno, G. J., Trejo-Perea, M., Castañeda-Miranda, R., Hernández-Guzmán, V. M., & Herrera-Ruiz, G. (2007). Modelling temperature in intelligent buildings by means of autoregressive models. Automation in Construction, 16(5), 713–722. https://doi.org/10.1016/J.AUTCON.2006.11.003

10. Valipour, M., Ebrahim Banihabib, M., Mahmood, S., & Behbahani, R. (2012). Parameters Estimate of Autoregressive Moving Average and Autoregressive Integrated Moving Average Models and Compare Their Ability for Inflow Forecasting. Journal of Mathematics and Statistics, 8(3), 330–338.

Some aspects of remote exams

Milena Racheva
Technical University of Gabrovo, Bulgaria[1]
milena@tugab.bg

Abstract: *The paper is devoted to distance exams, as in that the focus is on mathematical disciplines. Some advantages are standing out, as well as significant disadvantages have been discussed. Current modern tools are considered, which are applied both in the preparation of students and in distance exams.*

Keywords*: REMOTE EXAM, TEST, PLATFORM, MATHEMATICAL SOFTWARE, ONLINE TOOLS*

1. Introduction

Over the last 25 years, as part of the general technological development of the modern world, universities have increasingly embraced a variety of forms of both hybrid and full distance education in all kinds of undergraduate and graduate programs. This process has been forced in the previous two years due to the epidemic of COVID-19 and the need for social isolation. Thus distance learning at all stages of training has become a necessary and inevitable standard in education.

The organization and implementation of partially or fully distance of distance learning have specific characteristics different from those of standard, face-to-face training. This specificity requires that the fulfillment of certain necessary conditions, the satisfaction of which is not always possible, for example:

- availability of appropriate technical equipment - computers, cameras, microphones, tablets, electronic media for transmission and storage etc.;
- availability and choice of an appropriate educational platform;
- sufficient level of computer competencies of both teachers and students;
- refined and synchronized regulatory and legal framework to rules and parameters are regulating this type of training.

The above are just some of the conditions that need to be met, specified, and refined in training that is in at least some distance learning. At the same time, they are related and interconnected.

For example, when a training platform is chosen by a university or a lecturer, the guiding criteria are: that the platform is more the platform is free of charge; has minimal software, hardware, and network requirements; to launch basic functionalities fast enough; to provide sufficiently good visualization capabilities as well as data transfer and storage. The choice of the platform therefore requires the availability of appropriate technical equipment; it also sets a challenge at a proper level to computer skills, knowledge and work habits, not so much of the students as of their teachers.

With the emergence, development, and use of methods, tools, and environments for of distance learning logically arise and increasingly begin to methods, algorithms, and corresponding tools for remote delivery of examinations [1]. This is the subject of the following sections.

2. Remote Exams Implementation

The constraints associated with the global epidemic of COVID-19 have forced universities en masse to begin conducting, and students to take remote exams. Preparations for their implementation and all the accompanying questions are being modified, refined, and improved in a way that is different from traditional written examinations. It is worth noting here that distance testing in a large is not only dependent on the digital skills of the examiner and the student, but also on the functionality and capabilities of the available software and hardware. In a number of cases, for a student to participate in an examination There are a number of mandatory requirements, for example, the use of a desktop or laptop computer rather than a mobile phone; the use of specific web browser with the latest updates; use of a camera, that is switched on during the exam. Alongside this, the following are also given recommended conditions, such as using an operating an operating system that does not predate Windows 7; or a newer version; using wired internet connection, etc.

Remote testing may take different forms:

- written assignments sent by e-mail;
- posting assignments on the web;
- completing online tests.

The most popular and widely used tests are. Even in mathematical sciences, not only in distance learning but also in face-to-face exams, the common practice is to use tests preferred over traditional exam topics requiring detailed problem-solving and analytical proof of propositions. A number of authors have argued that with appropriate structure and content tests, the examination process is not formal but substantive and is to actually check and correctly establish the level of students' knowledge.

Questions are used in mathematical tests (see, e.g. [2]):

- multiple choice (one or more correct answers);
- requiring a short answer (word, phrase, number);
- a choice of true and false statements;
- for calculation;
- requiring a description.

3. On Some Advantages and Disadvantages of Remote Exams

Remote testing relies primarily on closed-ended questions on the grounds that they cannot be applied by copying passages from electronic textbooks or online available resources. Also, for closed-ended questions, the results are automatically scored, which is a convenience for the examiner. You should be noted, however, that in this practice, even with a correct examination paper is correctly completed without the use of additional resources, people, and circumstances, an accurate diagnosis of the depth of the student's knowledge. And this is fully valid mainly for mathematical sciences.

There are a number of electronic platforms for creating online tests – Moodle, Google Forms, Microsoft Forms, DisPeL, SmarTest, etc. [3,4]. Most of them have a similar working principle. Examination and assessment through remote testing – both online and offline conducted – have some obvious advantages:

- Reduces the time required by the teacher to process the results, especially in tests with closed-ended questions. At the same time, however, exam preparation requires many more resources compared to a traditionally administered exam.
- The training organization saves money on logistics, and maintenance of study rooms. Each student uses their own device for the exam.
- There is flexibility in terms of time and venue. Facilitates access to the exam for a large number of students at a time convenient for them regardless of their geographical location.
- Students save the time and money needed to travel to university.

On the other hand, however, the following disadvantages should be noted:

- On the teacher's side, the preparation and creation of tests require high qualification, time, and effort [A4]. For this reason, it is most sensible to create so-called dynamic tests (e.g. in Moodle, DisPeL, etc. [3,4]). Initially, a question base is created, which is quite labor-intensive. The database is structured into categories and subcategories. The test questions are set of an optional type and each time the test, a combination of questions from the different categories and subcategories. This is many times beyond the capabilities of a teacher to manually create combinations of questions and test options.
- For the student, the examination process is highly dependent on the availability of computer equipment and a stable internet connection during the exam. Note that when starting a test, the execution time is most often fixed.
- The results that students demonstrate are highly dependent on their prior experience and computer proficiency [5].
- During the exam, there is a strong dependency on network stability and security. In the event of a system failure, the exam results may be irretrievably deleted.
- Maintaining correctness in the execution of the exam topic and preventing opportunities and attempts at manipulation are under strong in a remotely administered examination.

The last of the disadvantages listed above is of utmost importance, as it compromises and frustrates the entire examination process. However, the purpose of any examination is to establish the scope and depth of a student's knowledge of the relevant subject, resulting in which an adequate grade will be given [6].

Recognizing this, many professors have suggested in their scholarly articles and apply in practice the following not very fruitful approaches:

- ➢ making the tests visible to the students immediately before the start of the exam, with the password for access then announced to the test;
- ➢ setting a time limit for the test, which is sufficient only to solve the problems, but not to search for ancillary resources;
- ➢ adding a timer to each question automatic swapping of the task sequence;
- ➢ automatic swapping of multiple-choice questions;
- ➢ displaying questions one by one, without the possibility of going back;
- ➢ use of dynamic tests with the option of the uniqueness of each set questions and tasks.

These efforts are undoubted to be admired, but without exception have for aim to prevent students in a course from copying each other, or a student all alone trying and searching for somewhere to transcribe.

However, other scenarios are possible, especially in mathematics exams, which we will list at the end of this section.

In remote examinations, it is difficult to check the identity of examinees. It is theoretically possible to conduct video surveillance by the camera through the conferencing program, as and to use software to monitor and/or record the screen actions on the computer [1]. However, this is unlikely to become a regular practice (especially when testing large numbers of students at the same time) and faces massive disapproval worldwide due to apprehension, concerning the invasion of privacy and misuse of personal data.

For now, many universities in this country and around the world are content with using the assignment of the test subject's IP address, access key, and exam time slot. The identity of the examinee is assumed to be the profile that the user has in the system.

Due to these realities, remote exams are extremely inefficient and their results are far from real. Completely some of the following scenarios are possible:

A. A student takes an exam remotely using the help of one or more experienced assistants;

B. A student has enlisted another to take the exam for him or her, by providing a device and internet connection;

C. A student takes an exam remotely using the assistance of an online available software tools for solving mathematical problems (see next section).

In all of these scenarios, it is possible to use more than one device for exam purposes.

4. Some Online Computational Software Tools

This section is devoted to some of the most used and convenient mathematical tools available online – the so-called math(ematical) solvers. Generally speaking, math solvers are mathematical modeling and problem-solving software systems.

These tools are successfully applied by the teachers in remote learning for immediate demonstration and illustration of theoretical facts, dependencies, and statements, as well as by the students during practical exercises and for preparing for an exam.

Usually, math solvers provide a wide range of resources for working with numerical, symbolic, and graphic data: derivatives; functions and sequences properties; integrals; integral transforms, matrix manipulations; equations and systems solving; vector calculations; data fit; statistics; some plots as well as some strong mathematical definitions. Most of them have got the capability to provide step-by-step solutions.

Math solvers are very useful for students in their self-study. With their help, one can check the correctness of an answer to a problem solved by a student, and the same manner is used when solving closed-type questions in examination tests. The option of obtaining a step-by-step solution is extremely useful in self-study because it provides a solution to the corresponding mathematical problem in sequential detail. At the same time, it is actively used for deriving a solution and applying it in the examination work in remote examinations. Note that the time required to get independently a solution of a problem or an answer to a question from an exam topic, regardless of open or closed type, is comparable to the time for performing these activities using a math solver! The crucial point here is the level of computer skills on the part of the user.

Wolfram|Alpha, for example, can be successfully used during remote examination and for questions of a theoretical nature as such, that require a word/word sequence as an answer, as well as those with a multiple choice answer. The main obstacle here is the level of preparation in English of Bulgarian (and not only) students.

4.1. **Wolfram|Alpha** is an online computational knowledge engine or answer engine that answers factual queries directly by computing the answer from externally sourced curated data, rather than providing a list of documents or web pages that might contain the answer, as a search engine might. Additional data is provided from both academic and commercial websites and some of the data is kept updated in real time [7,8,9].

Wolfram|Alpha is developed by WolframAlpha LLC, a subsidiary of Wolfram Research with purpose to provide integrated storage, interface, computation, knowledge, linguistics and deployment capabilities. In Wolfram|Alpha is built-in free form input, which is most often preferred by the students and young scientists. At the same time, use of the syntax of Wolfram Language is also possible. Wolfram|Alpha has a clean and simple user interface.

This engine can be on-line used successfully and completely free of charge, without any registration. For purpose to use Wolfram notebook, where to keep his own information, one should make a registration. Wolfram|Alpha is free for personal noncommercial use, but access to enhanced features, like step-by step solution, and ad-free site use is available through a subscription to Wolfram|Alpha Pro. The fee starts at £4.50 per month.

4.2. Symbolab is one of the most popular and useful free mathematical solver. It is an advanced math education tool, which allows users to learn, practice and discover math topics using mathematical symbols and scientific notations as well as text [10].

Here, digital notebooks could be used for purpose to keep notes and a track of mathematical problems, which are already solved. However, registration is required to use this tool.
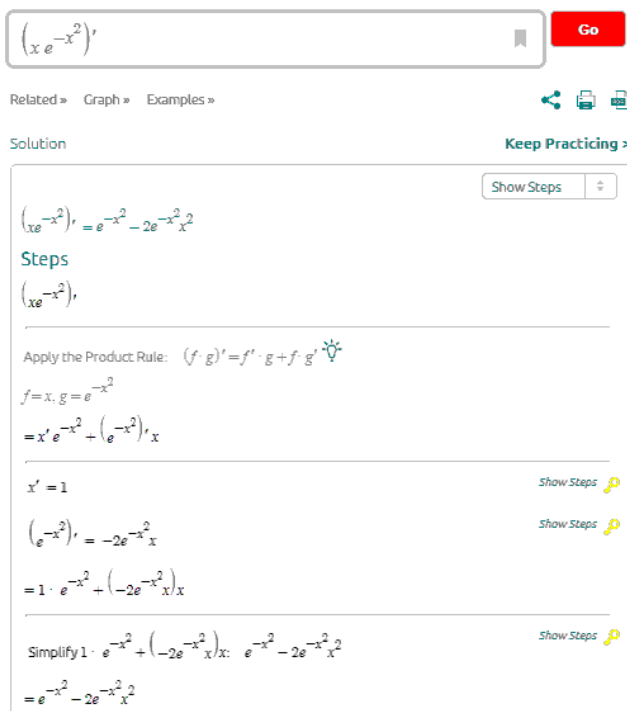
Fig. 1 Obtaining the derivative of the function $f(x)=xe^{-x^2}$ by means of Symbolab

Symbolab offers a wealth of smart calculators including: equations, simultaneous equations, inequalities, integrals,

derivatives, limits, tangent line, trigonometric equations, functions and more. The stated goal of the site is to make scientific content universally accessible by expanding the searchable data space onto scientific notations, expressions, equations and formulas. This is done by applying proprietary machine learning algorithms in order to understand the meaning and context of the queries.

Symbolab solves any problem for free. Automated step-by-step solutions are provided to algebraic, trigonometric and calculus topics covering from middle school through university. Getting a sketch of a step-by-step solution, which is quite enough for any purpose, is free (see Fig. 1). In order to view step-by-step solutions in the smallest details, one can subscribe weekly ($1.99), monthly ($4.99), or yearly ($29.99).

4.3. Cymath is a mathematical solver, powered by a combination of artificial intelligence and heuristics, so that it solves mathematical problems step-by-step like a teacher would [11]. Let us note that cymath.com frequently ranks #1 on Google for searches on math solvers, and the Cymath app is one of the most popular education apps in the iOS App Store and on Google Play.
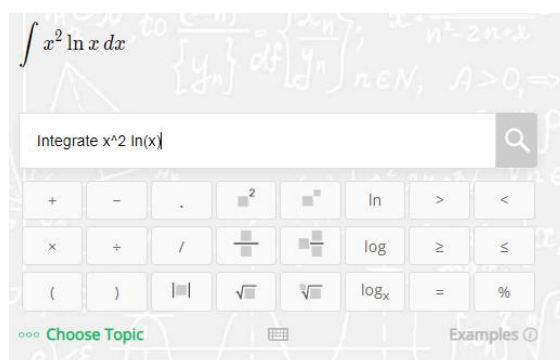
Fig. 2 Step-by step calculating of indefinite integral $\int x^2 \ln x\, dx$ using Cymath

Here, input of a concrete problem which has to be solved is not very convenient and sometimes strange, but in general the integrface is not bad (Fig 2).

Cymath can be used completely free of charge (Fig. 2). For additional help, you can join Cymath Plus for $4.99 USD per month. Such being the case, one can see how a step is done and why a step is taken on most problems and on a variety of topics.

4.4. Open Omnia

It is worth mentioning the mathematical solver Open Omnia [12]. It provides very detailed and well-described step-by-step solutions for a huge variety of problems concerning various fields of mathematics.

For instance, in Fig.3 and Fig. 4 correlation analysis of samples $x=\{5,4,7,10,11,8,9,11,8,9\}$ and $y=\{30,27,38,48,59,54,42,63,52,47\}$ is shown.
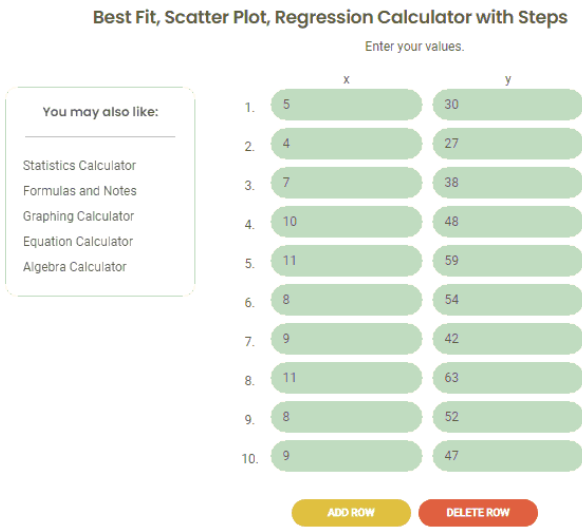
Fig. 3 *Input of the data that are subject of correlation analysis*

In Fig. 4 sample correlation coefficient can be seen as well as the regression model (linear).
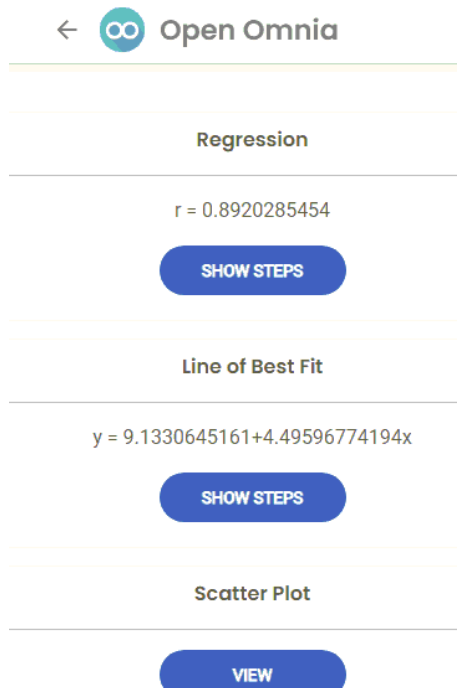
Fig. 4 *Correlation results given by Open Omnia for the samples x and y under consideration*

By clicking the corresponding button (Fig. 4), one can see in details obtaining of the sample correlation coefficient, the linear dependence giving best linear fit and its graphics.

There is still much to be desired from the provided graphics. The use of Open Omnia is completely free.

5. *References*

1. Sindre, G., Vegendla, A. (2015). *E-exams versus paper exams: A comparative analysis of cheating-related security threats and countermeasures.* In Norwegian Information Security Conference (NISK) (Vol. 8, No. 1, pp. 34-45).

2. Malinova, A., Kyurkchiev, V., and Spasov, G. (2018, January). *Parameterized examination in econometrics.* In AIP Conference Proceedings (Vol. 1926, No. 1, p. 020-028). AIP Publishing LLC.

3. Terzieva, T., Rahneva, O., Arnaudova, V. and Karabov, A., 2017, November. *Application of DisPeL for adaptivity and individualization in the training.* In: Proceedings of the Scientific Conference Innovative Software Tools and Technologies with Applications in Research in Mathematics, Informatics and Pedagogy of Education (pp. 23-24).

4. https://docs.moodle.org/400/en/Main_page

5. Boekaerts M., *Personality and the psychology of learning*, European Journal of Personality, 10, p. 377-404, 1996.

6. Boevé, A. J., Meijer, R. R., Albers, C. J., Beetsma, Y., and Bosker, R. J. (2015). *Introducing computer-based testing in high-stakes exams in higher education: Results of a field experiment.* PloS one, 10(12), e0143616.

7. www.wolframalpha.com

8. Dimiceli, V. E., Lang, A. S., and Locke, L. (2010). Teaching calculus with Wolfram| Alpha. *International Journal of Mathematical Education in Science and Technology, 41*(8), 1061-1071.

9 Rachev, S., Racheva, M., Andreev, A., and Ganchev, D. *Mathematical software tools applicable to remote learning and scientific research in case of isolation*. Mathematical Modeling 5, no. 1 (2021): 8-12.

10. www.symbolab.com/

11. www.cymath.com/

12. https://openomnia.com/

Development of menstrual panties within the framework of sustainability and creation of a start-up

Roman Knizek, Denisa Knizkova, Ludmila Fridrichova
Technical University of Liberec, Czech Republic
roman.knizek@tul.cz

Abstract: *Direct At the Technical University of Liberec, Faculty of Textiles, there was a cooperation between this state university and a small private company. The cooperation was created for the development of sustainable aids for menstrual periods. All development took place at the university, including the search for local production partners, and the private company financed the development. The output is a utility model owned by the university and the private company, and in addition the private company pays the license fee. The article describes in more detail this cooperation, as well as the development and the developed product, up to its actual commercialization.*
Keywords: *SUSTAINABILITY, START-UP, layer,*

1. Introduction

Menstrual panties are another alternative for women during their periods which aims at increasing the women's feeling of comfort. Another advantage is their sustainability, as it is an aid that can be used repeatedly, unlike the still widespread tampons and pads. Their advantage is the possibility of being washed and reused. In his article, Parent focuses on hygiene aids, including menstrual panties, and the public awareness about them in France. The reason for this study was that no work had been done on this topic so far. In conclusion, the author points out that there is a growing interest in these products among the French public [1]. Medina-Perucha deals with menstrual aids in her work, both disposable and multi-use ones. Respondents were more in favour of the re-usable products. Her work also points out common problems with menstrual cups [2]. The author de Belleville points out common problems with menstrual aids in India and compares India with France. In France, a woman has several types of protection to choose from, whereas in India, only 12% of women have access to protective equipment during their menstruation. Other women use rags and other textile waste [3]. The Stockburger MD describes menstruation and the possibilities of its suppression, but also describes the aids available for menstruation, including menstrual panties. He mentions that all devices have their advantages and disadvantages [4]. Marcelis has dealt with various menstrual aids, including menstrual panties, and a system for evaluating the effects of excreted substances on the skin of the body [5].

The research shows that there are already several manufacturers that manufacture and sell menstrual panties and those are perceived as a positive protection alternative during a woman's period. At the same time, thanks to the possibility of repeated use they seem to be very important for developing countries, where classic disposable aids are just not available.

The development of menstrual panties took place from the very beginning with the emerging start-up, which did not yet have any legal form of business. All development took place at the Technical University of Liberec and the start-up (natural persons) paid for the individual stages of the development. After the successful completion of the first prototype, SaYu s.r.o. (legal entity) was created. The SaYu company, in cooperation with the Technical University of Liberec, arranged production by Czech manufacturers and suppliers. After the completion of this stage a common utility model was created, which is owned by SaYu and the Technical University of Liberec. It is this connection between a university and a company and the creation of a successful product which represents a typical example of a successful transfer.

2. Materials Development of menstrual panties

At the time when the development of menstrual panties began at the Technical University of Liberec, these products already existed, but unfortunately, they had great limitations, especially in terms of their thermo-physiological comfort properties. These were mainly hydrostatic resistance (water column height), vapor permeability and low absorbency. Therefore, the development was focused mainly on finding suitable layers for menstrual panties. Menstrual panties consist of four basic layers. Figure 1 shows a diagram of menstrual panties and their functional layers. Menstrual panties as developed at the Technical University of Liberec have the task to perfectly remove any moisture from the skin, to transfer excess moisture into the absorbent layer and at the same time there is another layer - a nanofiber membrane. The task of the nanofiber membrane is not to let through excess moisture, but at the same time the membrane must be very vapour-permeable.

Fig. 1 Functional layers of menstrual panties

1st layer – transport layer (transports fluids as fast as possible into the next layer)

2nd layer – absorbent layer (highly absorbent and also spreading moisture along the absorbent core)

3rd layer – protective layer (membrane – provides high hydrostatic resistance and at the same time excellent vapour permeability)

4th layer – visible aesthetic layer (the same material as is used for the other parts of the complete final product)

Fabric liquid moisture transport properties in multi-dimensions, called moisture management properties influence the human perception of moisture sensations significantly. Some standards and test methods can be employed to evaluate the fabric's simple absorbency and wicking properties, and the liquid strike-through time of nonwovens also can be tested according to ISO 9073-8. However, the existing standards cannot measure the behavior of fluid transfer of the clothing materials dynamically [6].

The MMT measures textiles' dynamic liquid transport properties, such as knitting and woven fabrics. A series of indexes are defined and calculated to characterize the liquid moisture management performance of the test specimen [7].

3. Results and discussion

Transport layer

In this layer, rapid transport of fluid from the wearer's skin to the absorbent core is particularly desirable. Functional knits based on shaped fibres such as PES, POP or WO are particularly suitable for this purpose. In the case of the development of menstrual panties, a knit of 100% merino wool with areal weight of 105 g / m2 was chosen. The moisture transport rate is best expressed by measuring the absorbency value of the sample [% .s^{-1}] on an MMT instrument (Moisture Management Tester). The devise MMT measure according to the standard AATTC 195 - Moisture Management Tester

At the same time, however, this material is not suitable for the second absorbent layer, precisely because of the low moisture distribution in the area. Table 1 shows the measurement results for the transport layer and Figure 2 shows the spread of moisture over time.

Table 1: The measurement results for the transport layer.

WASHED SAMPLES		Sample No. 3
		Double-face
Wetting time [s]	Top side	7.7
	Bottom side	45.4
Absorbency [%/s]	Top side	210.7
	Bottom side	10.8
Maximum wetting radius [mm]	Top side	5
	Bottom side	8.3
Solution-spread rate through the fabric [mm/s]	Top side	0.67
	Bottom side	0.65
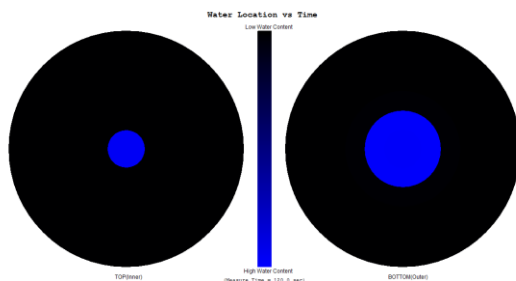
Fig. 2 Moisture spreading in time for the transport layer.

Absorbent layer

For the first layer - the tactile one - the rapid transport of fluid from the wearer's skin towards the absorbent core is most desirable. However, for the second layer – the absorbent one - the level of moisture distribution is very important. 100% cotton was selected for this layer, which has these desired properties. Because it is only the second layer, which is not in contact with the wearer's skin, it can be just knitted fabrics like cotton with a real weight of 165 g / m^2. Table 2 and Figure 3 show the specific results.

WASHED SAMPLES		Sample No. 4
		Double-face
Wetting time [s]	Top side	4.5
	Bottom side	5.3
Absorbency [%/s]	Top side	45.6
	Bottom side	51.4
Maximum wetting radius [mm]	Top side	20
	Bottom side	20
Solution-spread rate through the fabric [mm/s]	Top side	3.69
	Bottom side	2.93

Table 2: The measurement results for the transport layer.
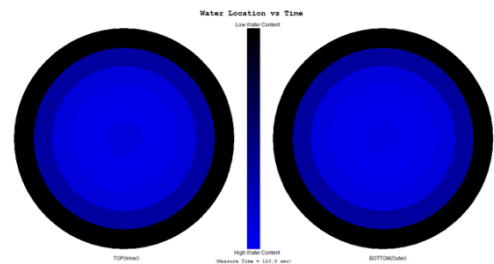
Fig. 3 Moisture spreading in time for the transport layer.

Protective layer

A nanofiber membrane was used as the protective layer. Laboratory production of nanofiber membranes was performed on the Nanospider machine. A polymer solution was added to a basin with a rotating roller. This solution was exposed to an electro field of U = 76.1 kV voltage. A collector was placed above the basin at the distance of 175 mm for the first sample and at the distance of 130 mm for the second sample. The speed at which the base material was moving was set at v = 0.1 m/min. The relative humidity in the spinning chamber was regulated at 21%. The humidity sensor was not placed directly in the spinning chamber, but in the tube bringing the air to the chamber to ensure proper sealing. The turning of the roller (driven by a rotor) in the basin created a thin polymer solution layer on its surface from which in turn nanofibers were formed due to the high voltage and collected on the support-material. The mass per unit area of the created nanofiber layer was 5 g/m^2.

Subsequently, a two-layer laminate was created because a simple nanofiber layer would be easily damaged. For the 2 -layer laminate a warp knitted fabric was used (warp knit with a real weight of 29 g / m2, to affect the thermo-physiological comfort of the nanofiber membrane as little as possible) with lamination points and a nanofiber layer, which was still on the base material. When laminating the top material and the nanofiber layer, the size of both materials was 50x50 cm. A nanofiber layer was put on the top material from the side with the lamination points. The resulting structure was placed on the lower part of the body of the Kannegiesser gluing machine and the required pressure of 3 bar was applied on the upper part of the body for 15 seconds at a temperature of 120 ° C. Thanks to these parameters, the polymer dots on the top fabric melted and a solid 2-layer laminate was formed, which can be seen in Fig. 4 taken by a scanning microscope. The base material is later pulled off.

Table 3: *The measurement results for the transport layer.*

WASHED SAMPLES	Sample No. 5
	2-layer laminate
Steam permeability Ret[Pa.m^2.W^{-1}]	2.4
Air permeability [l/m^2/s]	1.865
Hydrostatic resistance [mm]	10 340
Number of washing cycles before delamination	95
Joint strength [N]	36.7
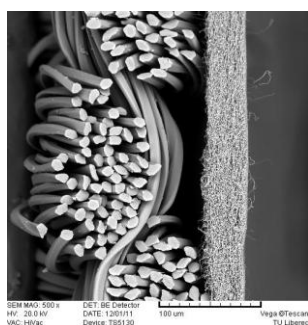
Fig. 4 *Two-layer laminate cross-section.*

The results show that the nanofiber membrane resp. laminate with a nanofiber membrane achieves very good values of thermo-physiological comfort.

3. Conclusion

The results show that the task was to develop menstrual panties with maximum emphasis on their thermo-physiological comfort during periods, meaning that all layers should be as vapour-permeable as possible to make women feel as comfortable as possible while wearing them. At the same time, the development took into account that women should not feel anything during menstruation which means that the first layer has the task of removing moisture from the woman's body as quickly as possible, the second layer has the task of absorbing the excess moisture, so a knitted cotton fabric was chosen. The next layer is a two-layer laminate so that there is no unwanted leakage. However, unlike other commercial panties, a nanofiber membrane was used. Other manufacturers most often use simple coating which has very poor vapour-permeability and lower hydrostatic resistance, properties essential for enabling active movement during a period. Thanks to the development of this product, unique cooperation between the Technical University of Liberec and the SaYu company was created, which at its beginning was a typical start-up, but a successful one. Thanks to this cooperation, joint intellectual property was created in the form of a utility model, where SaYu pays regular license fees for each piece sold. The Technical University of Liberec does not cooperate with anyone else in this field, and SaYu thus has exclusivity in the further development of menstrual panties. This created a model example of cooperation between a state university and a private company. This article wants to show that it is possible not only to start, but above all maintain a long-term cooperation between a state university and a private company.

4. References

1. C. Parent, C. Tetu, C. Barbe, S. Bonneau, R. Gabriel, O. Graesslin, E. Raimond, *Menstrual hygiene products: A practice evaluation,* Journal of Gynecology Obstetrics and Human Reproduction, **51** (2022)
2. L. Medina-Perucha, at all, *Use and perceptions on reusable and non-reusable menstrual products in Spain: A mixed-methods study,* PLOS, (2022)
3. de Belleville, A. Veyrat, The business of menstruation in India, IIMB Publications, (2019)
4. S. Stockburger, H.A. Omar, P. J. A. Hillard, K. Kantartzi, G. Sucato, *Menstrual Health*, PPaAG, 29 (2013)
5. Q. Marcelis, A. Gatzios, E. Deconinck, V. Rogiers, T. Vanhaecke, B. Desmedt, *Development and application of a novel method to assess exposurelevels of sensitizing and irritating substances leaching from menstrualhygiene products*, Emerging Contaminants, **7** (2021)
6. Y. Bao-guo, L. Yi, H. Jun-yan, K. Yi-lin, Y. Kwok-wing, *An improved test method for characterizing the dynamic liquid moisture transfer in porous polymeric materials,* Polymer Testing, 25 (2006)
7. SDL Atlas, *Moisture management tester*, Instruction manual, 62 pp.

Structuring key partnerships in the field of critical infrastructure security systems

Valeri Panevski[1*], Lyudmil Nedelchev[2]

Institute of Metal Science Equipment and Technologies with Hydro- and Aerodynamics Centre "Acad. A Balevski" at the Bulgarian Academy of Sciences, 67 Shipchenski Prohod Street, 1574 Sofia, Bulgaria[1]

panevski@ims.bas.bg

Kozloduy NPP EAD, 3321, Kozloduy[2]

lnnedelchev@npp.bg

Abstract: Joint scientific and applied research occupies its place as a major innovation process in the activities of scientific, educational and business organizations. The purpose of this approach is to gain access to external sources of technology (or other assets) and their integration into products and services to build security of critical infrastructure and strategic sites of national importance.

Partnerships in the development of security systems can bring added value to partner organizations, allowing them to use a wider network of promising assets and markets and helping them gain trust and prestige in society.

The presentation of a variant of structuring key partnerships in the development of security systems is the content of this paper.

Key words: KEY PARTNERSHIPS, COMPETENCE CENTRE

1. Introduction

The purpose of building key partnerships, within the scope of Competence Centers (CCs), is to establish relationships through which to gain access to external sources of high technology (or other assets) and their integration into products and services in the field of security systems for critical infrastructures and objects of national importance. The implementation of research and innovation (R&I) in the development of security systems and the related business model (BM) makes a significant contribution in this area.

R&I refer to that part of BM that represents the ability to acquire knowledge, design, develop and improve products, services, technologies or processes. For high-tech CC partners, R&I is number one on the list of opportunities that are critical to long-term success while at the same time being the key to improving business skills, expanding the portfolio of products and services and maintaining cutting-edge applied research in the interest of the country's security.

CCs are defined as "structured, long-term research and innovation (R&I) collaboration in strategically important areas between academia and industry with frequent interactions with the public sector. A CoC focuses on strategic research agendas, support strong interactions between science and industry and provides truly collaborative research with a medium to long-term perspective" [1]. They are usually located in research organizations and focus on national strategic sectors in applied research projects in collaboration with leading business organizations.

The establishment and operation of CC in our country, such as the Project BG05M2OP001-1.002-0006 Competence Center "Quantum Communication, Intelligent Security and Risk Management Systems (Quasar)", plays a leading role in planning, structuring and negotiating these relationships between research organizations, universities and high-tech companies.

2. Building key partnerships through competence centers

The CC's main operational objective is to strengthen partnerships between research organizations, universities and industry, thus accelerating the innovation process and leading to economic growth.

This is achieved through:

➢ the presence of the private sector in the management and leadership structures;

➢ provision of services to the private sector;

➢ directing the work of the academic circles to modern applied research;

➢ facilitating interregional relations through the participation of international companies.

Competence centers can apply good practices, separate from the work of the research and development program, with a focus on:

➢ use of research results through intellectual property rights and individual products;

➢ training of doctoral students;

➢ dissemination of research results through publications, conferences, etc.;

➢ stimulating networking and knowledge transfer;

➢ acquisition of funding from third countries (including EU sources);

➢ provision of research infrastructure;

➢ providing market information (TAFTIE, 2016) [1]

These good practices should offer key insights for CC management, namely:

➢ to be flexible in finding support and developing research projects with different funding mechanisms, for products and systems with different technology readiness levels (TRL);

➢ a market-oriented integrated CC must offer different types of services to promote cooperation between science and industry;

➢ international cooperation development through bilateral contractual applied research and development should be a strategic goal.

3. More on key partnerships

Organizations form partnerships for many reasons, and partnerships are becoming a cornerstone of many business models. Established partnerships help to optimize business models, reduce risk and acquire resources.

3.1 Motives for key partnerships

Optimization and economy of scale

The most basic form of partnership is designed to optimize the allocation of resources and activities. It is illogical for an organization (in this case a CCP) to have all the resources or to carry out every activity alone. Optimization and economies of scale partnerships are usually set up to reduce costs and often involve outsourcing or sharing infrastructure.

Reduce risk and uncertainty

Partnerships can help reduce risk in a competitive environment characterized by uncertainty. It is not logical and common for competitors to form a strategic alliance in one area while competing in another.

Acquisition of certain resources and activities

Few organizations have all the resources or carry out all the activities described by their business models. Rather, they expand their own capabilities by relying on other organizations to provide certain resources or perform certain activities. Such partnerships may be motivated by the need to acquire knowledge, licenses or access to clients.

3.2 Partnerships, the power of information sharing.

Despite the overall change in attitudes, key CC partners still have reservations about sharing information. The following main areas of concern can be identified:

➢ Partner organizations are concerned about the legal and regulatory implications of disclosing development information;

➢ Organizations are concerned about the public relations aspect;

➢ Organizations are concerned about the confidentiality of the data they work with.

Information security has become a risk management issue due to its potential effects. Leakage of information revealing potential results of scientific research can have legal consequences: the organization may be required to report related issues in order to comply with financial and confidentiality regulations [2]. If security issues become public, they can also harm the way the partner organization is perceived by customers and the business community, potentially affecting the profitability of the CC. For example, information sharing may reveal constructive and technological data that could potentially compromise the privacy of the affected partner organization.

The need to share security information is driven by rapidly changing businesses, technologies and threats. Increasingly, CC consists of a wide variety of key partners. We share business information and often use the same technology or sell or share technology with each other. As we do this, we also share the risks. Understanding the risks our partners face and how they manage those risks can help us protect our own organizations.

Looking more broadly into the technological landscape, all systems and devices are to some extent connected, whether owned by businesses, individuals or service providers. Almost every aspect of society depends on a global, fast-growing, extremely complex network of devices and services. This provides the central nervous system that supports innovation, economic development and social interaction worldwide. But because we are all inherently interconnected, we share common risks. The landscape of threats is dynamic, global and increasingly complex. Threats can arise in any country and then spread rapidly across national and corporate borders, causing significant damage to organizations and individuals around the world. Because threats are spreading so fast and the landscape of threats is so complex, it is difficult for any

individual organization to get a clear picture of all potential vulnerabilities, threats and attacks.

External partnerships can be useful, because they provide additional intelligence that can be used to improve the security position. By sharing information with other organizations, it can be achievedr a better understanding of what is happening outside of our own environment. We learn about new threats before they affect us directly. In this way information is obtained about how other organizations are dealing with these threats and we can touch to the best practices for managing security activities. By using the information we gather from external relationships, we can increase the partner organization's ability to feel, interpret, and act on risk.

Purpose of forming partnerships

There are a number of reasons why developing a key partnership in a CCP can be beneficial. Generally speaking, partnerships can focus on a specific problem, such as developing security systems, to maintain a consistent approach to problems [3].

Some more specific reasons for forming a partnership may be:

➢ Achieve more efficient and effective implementation of development programs and eliminate any unnecessary duplication of effort. Gathering organizations involved in solving a problem can lead to more cohesive and comprehensive intervention. Instead of duplicating efforts, partners can share or coordinate responsibilities in ways that give more participants access to the programs and allow for a wider range of services.

➢ Pooling resources. Many organizations together may have the resources to accomplish a task that none of them could accomplish on their own. In general, organizations form partnerships to achieve together what they cannot do alone.

➢ To increase communication between groups and break stereotypes. Bringing together organizations from many sectors of the community can create alliances where there has been little contact before. Working together to achieve common goals can help organizations break down barriers and perceptions and allow them to trust each other.

➢ To build networks and friendships. Partnerships lead to social benefits for staff and customers, as people can build networks and friendships by participating in the organization.

➢ To revive the withering energy of key partners who are trying to do too much on their own. Partnerships can help step up efforts around a problem. For organizations that have worked too long in a vacuum, adding other hands to the task can be a huge source of new energy and hope.

➢ Planning and launching community-wide initiatives on various issues. In addition to addressing pressing security issues or promoting or providing services, partnerships can serve to pool long-term campaigns.

➢ To develop and use influence to obtain services or other benefits of the CC. The partnership can be more effectively advocated by different organizations working independently. In addition, a broad partnership can put pressure from all sectors of industry and have a large amount of power.

➢ To create long-term, permanent change. Real change usually takes place over a period of time through the process of gaining trust, sharing ideas and overcoming existing challenges in order to understand the real problems underlying the needs of industry and security. The partnership, with its structure of cooperation between different organizations and focus on solving security problems, can facilitate and accelerate the process of change, according to the dynamics of the security situation.

➤ To receive or provide services. A long-term partnership is needed to design, obtain funding within the scope of the CC's specialization.

4. Key partnerships in the QUASAR project

The partnership under the project for the Center of Competence "Quantum Communication, Intelligent Security Systems and Risk Management" (Quasar) comprises the following 8 organisations:

➤ Institute of Robotics "St. Ap. and Gospeller Matthew" at the BAS (Lead partner);

➤ Institute of Metal Science, Equipment and Technologies with Center for Hydro- and Aerodynamics "Acad. Angel Balevski" at the BAS;

➤ "Nikola Vaptsarov" Naval Academy – Varna;

➤ "Vasil Levski" National Military University – Veliko Tarnovo;

➤ Technical University of Gabrovo;

➤ Institute for Nuclear Researches and Nuclear Energy at the BAS

➤ Faculty of Geology and Geography of the Sofia University "St. Kliment Ohridski";

➤ Association "Advanced Flight Technologies", Sofia.

The concept for the construction of the Quasar competence center is aimed at creating a network of resources, forming a modern large-scale research infrastructure in the field of information and communication technologies, which will help achieve the goals of Bulgaria and the EU in the field of research and technological development.

The center is a set of facilities, resources and related services needed by the scientific community composed of CC researchers, but also other scientists, companies, organizations, including associate partners from our country and abroad, who will use the built infrastructure for conducting research in the relevant fields.

The research areas in which the QUASAR team specializes and work are information and communication technologies, sensorics and energy conversion, transmission of information through non-traditional channels and creation of models for events, phenomena and processes that pose a risk to the anthropogenic environment. Overcoming the interruption of radio waves and radio communications in major earthquakes, nuclear or nuclear accidents, volcanic eruptions or disasters can be overcome through the quantum communication of intertwined photons in the space-time continuum. Intelligent security systems will be able to predict accidents, disasters and prevent a terrorist threat.

Data collection will be done through micro- and nano-sensor systems based on the multisensor principle, operating in a wide temperature range. Increasing the conversion efficiency will be achieved both by lowering the operating temperature and by new modifications of the conversion elements. In general, QUASAR covers a wide market niche in communication and sensor technologies and systems

Within QUASAR, activities systematized in 4 work packages (WP) are in the process of implementation, namely:

➤ WP 1. Quantum communication (Leading partner: Institute for Nuclear Research and Nuclear Energy);

➤ WP 2. Intelligent security systems (Leading partner: Institute of Metal Science, Equipment and Technologies with Center for Hydro- and Aerodynamics "Acad. Angel Balevski";

➤ WP 3. Risk management (Leading partners: the Varna Naval Academy;

➤ WP 4. Innovative sensor technologies with multi-purpose application (Leading partner: Institute of Robotics "St. Ap. and Gospeller Matthew".

Structured in this way, the Competence Centre QUASAR has no analogue at national and European level. This is a clear niche, through which the capacity built through a key partnership will become a leading area of multidisciplinary importance. The expertise of scientists and specialists involved in the CC is such that they successfully format the innovative space of the object area of specialization with new ideas, patents for inventions and prototypes of original products and systems.

The leadership role of the team is clear as an asset and as a future potential that combines avant-garde topics: quantum communication, sensory and risk management through intelligent systems. This scope is of multidisciplinary importance and is a generator of new ideas that can be protected by patents for inventions. This is one of the few cases where a fundamental result / fundamental results of theory can lead to specific engineering solutions with a clear commercial effect. The leadership role of the thus formed scientific team is definitely proven as a potential and opportunity.

Significant contribution, as a key partner in the development of security elements and systems, including ESC, has Institute of Metal Science Equipment and Technologies with Hydro- and Aerodynamics Centre "Acad. A. Balevski". Through its innovative developments, known and delivered to national and international partner organizations, the Institute contributes to the implementation of QUASAR activities.[3-10]

5. Conclusions

The key partnerships established through the centers of competence create relationships for the integration of the activity for the development of the products and services in the field of the security systems of critical infrastructures and sites of national importance.

Market-oriented and integrated structures, such as the QUASAR Central Committee, offer various forms of promoting structured cooperation between science, education and industry. With its organization of cooperation between different organizations and focus on solving security problems, QUASAR can accelerate the process of research and innovation, depending on the dynamics of the security environment, while helping to reduce risk in a competitive environment, characterized by uncertainty.

References:

[1] Michael Dinges, Michael Ploder, Marita Paasi, Future Competence Centre Programmes Report of the TAFTIE Task Force on Competence Centre Programmes CompAct, May 2016, DOI:10.13140/RG.2.2.24376.96009;

[2] https://link.springer.com/chapter/10.1007/978-1-4842-1455-8_4;

[3]   Busch, Nathan E., and Austen D. Givens. "Public-Private Partnerships in Homeland Security: Opportunities and Challenges." *Homeland Security Affairs* 8, Article 18 (October 2012). https://www.hsaj.org/articles/233;

[4]   Dimitar D., „Preventive and protective measures against insider threats in nuclear facilities", International Scientific Journal Security & Future, Vol. 5 (2021), Issue 3, International Scientific Journals of Scientific Technical Union of Mechanical Engineering „Industry 4.04, 2021, ISSN:Print ISSN 2535 - 0668, Online ISSN 2535- 082X, pp. 88-91;

[5]   Dimitrov D., „Developing the opportunities for building nuclear security", Technics. Technologies. Education. Safety. 2021. , Military sciences and national security., Proceedings 3, 3(13), Scientific Technical Union of Mechanical Engineering "Industry - 4.0", 2021, ISSN:ISSN 2535-0315 (Print), 2535-0323 (Online), pp. 208-211;

[6]   Dimitrov D., „Examples of nuclear security measures for nuclear facilities", Technics. Technologies. Education. Safety. 2021, Military sciences and national securityy, Proceedings 3, 3(13), Scientific Technical Union of Mechanical Engineering "Industry - 4.0", 2021, ISSN:ISSN 2535-0315 (Print), 2535-0323 (Online), pp. 212-215;

[7]   Dimitrov D., „Basic regulations and associated administrative measures providing nuclear security", Proceedings of the Annual University Scientific Conference, 5, Publishing House of Vasil Levski National University, 2021, ISSN:ISSN 2367-7481, pp. 73-80;

[8]   Georgiev N., Boychev Y., Kosev V., "Investigation of seismic fluctuations caused by a type of heavy chain equipment", Sb. reports of the XVIII International Scientific Congress "Machines. Technologies. Materials ", 1, NTS in Mechanical Engineering, 2021, ISSN: 2535-0315, pp. 23-26;

[9]   Boychev, Y., Assenov S., "Sensors and systems for detection of improvised explosive devices", Proceedings of the Annual University Scientific Conference. 5, V. Levski National University, 2021, ISSN: 2367-7481, pp. 53-63;

[10]   Tumbarska A., "Trends in the development of non-lethal technologies and protection systems" IMSETHC-BAS, 2020, ISBN: 978-619-7466-07-2, pages 402.

Segmentation of railway transport images using fuzzy logic

Balovsyak S.V.[1], Derevyanchuk O.V.[1], Derevianchuk Ya.V.[2], Tomash V.V.[1], Yarema S.V.[1]

[1]Physical, Technical and Computer Sciences Institute – Yuriy Fedkovych Chernivtsi National University, Chernivtsi, Ukraine
[2]Department "Wagon Engineering and Product Quality" – Ukrainian State University of Railway Transport, Kharkov, Ukraine

Abstract: *A prototype of a system for segmenting images of trains and wagons has been developed. Video cameras and specialized websites are used as the source of the original images. Median filtering of images and increase of their local contrast is carried out. The contours of the objects were calculated using the Sobel and Canny methods. Image segmentation is performed by the method of contour lines. As a result of the processing on the images of trains and wagons, meaningful areas (segments) were identified, for example, windows, headlights, etc. Detection of content areas of the object is performed using fuzzy membership functions. The hardware and software implementation of the computer system is made in Python using scipy and scikit-fuzzy libraries, the Google Colab cloud platform and Raspberry Pi 3B+ microcomputer.*

KEYWORDS: DIGITAL VIDEO CAMERA, PYTHON, IMAGE SEGMENTATION, LOCAL CONTRAST, FUZZY LOGIC.

1. Introduction

The relevance of the study is due to the fact that currently there is a need to develop automatic tools for analyzing the state of rolling stock in railway transport, namely the state of trains and wagons [1, 2]. In many cases, information about trains and wagons is obtained using video cameras in the form of digital images. To simplify image processing, content areas (segments) are highlighted on them. For example, windows, headlights, homogeneous sections of walls, license plates, wheels, etc. are distinguished as segments of locomotives. Image segmentation [3, 4] greatly simplifies their further computer processing, in particular, determining the rotation, size and area of objects, object recognition. The scope of segmentation of images of trains and wagons is quite wide. Such image processing is currently used, for example, for technical diagnostics of objects, control of their position and speed of movement. The system of analysis of the condition of vehicles on the railway has much in common with other similar transport systems, in particular, for road transport. Such systems are the basis for the development of modern intelligent transport systems, in which information about vehicles is obtained from many sensors of different types.

However, the experimental images of trains and wagons contain a certain level of noise, the images have a heterogeneous background and contrast. This leads to the fact that a significant part of the segments is uninformative. Therefore, it is proposed to perform pre-processing of images before their segmentation by filtering noise and increasing local contrast. Experimental images do not always show unambiguous correspondence of segments to certain objects. For example, the image of a locomotive window can be divided into several segments. Therefore, the paper proposes to perform object detection on images based on their segments using fuzzy functions of segment belonging to a specific object (for example, to a window).

2. Algorithm for image processing and analysis

Based on the analysis of existing methods of reducing the noise level in images, increasing local contrast, contouring and segmentation [3, 4] developed an algorithm for processing and analyzing images in the form of an activity diagram [5] (Fig. 1). Reading of initial images is carried out both from video cameras, and from graphic files. The initial color image is read as a three-dimensional array $f_{RGB}(i, k, c)$, where $i = 0, ..., M-1$; $k = 0, ..., N-1$; M is image height in pixels, N is image width in pixels, $c = 0, ..., 2$ –color channel number (Red, Green, Blue). Color f_{RGB} images are converted to grayscale (f_0 images).

Images f_0 are programmatically processed as rectangular matrices $f_0 = (f_0(i, k))$, where $i = 0, ..., M-1$, $k = 0, ..., N-1$.

As a result of the median filtering [3] of the image f_0, the image f with reduced noise level is calculated.
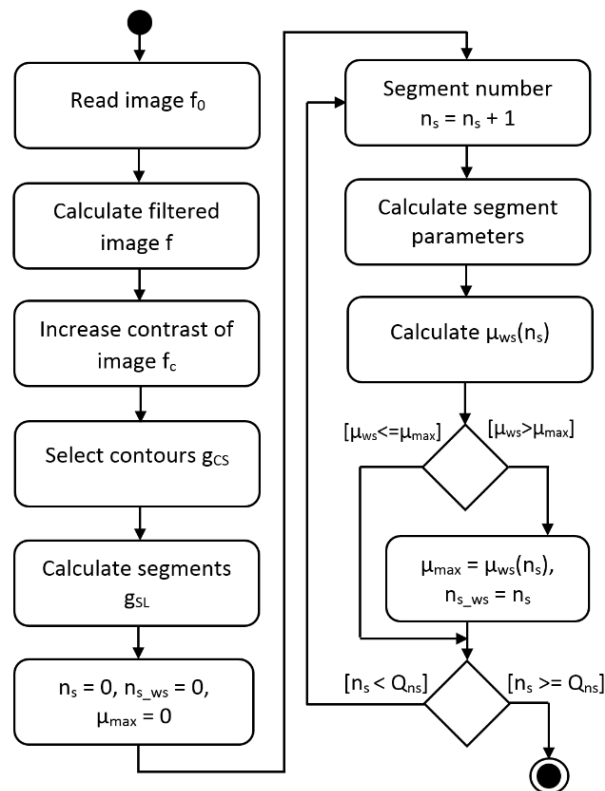
Fig. 1. *Diagram of the activity of the image segmentation system of trains and wagons*

Next, based on the filtered image f, the image f_c with high local contrast is calculated. Increasing the local contrast of images is performed by window processing of the image f using its envelope of brightness [6]. As a result of window image processing, its lower and upper envelope of brightness are first calculated, and then their smoothing is performed. Due to such smoothing distortions of the images which arise at increase in their local contrast decrease. In addition, by subtracting the lower envelope, it is possible to remove the inhomogeneous background of the image.

The sequence of increasing the local contrast is as follows. First, the dimensions of the local windows w of the image are determined, namely their height M_w and width N_w. By default, it is assumed that the windows w are square, i.e. $M_w = N_w$. When processing locally, windows w are formed for each pixel of the image f, while the pixel is placed in the center of the window at a distance of $M_{w2} = [M_w /2]$ from its upper edge and at a distance of $N_{w2} = [N_w / 2]$ from its left edge. To prevent the windows from going beyond the image, the images f are expanded before their window processing, namely the expansion in all directions by half the height M_{w2} and half the width N_{w2} of the window. The result is an expanded image of f_e. A symmetric extension is used in this work, in which stripes of width N_{w2} are added to the left and right

images of f_e, and stripes of width M_{w2} are added at the top and bottom. The brightness of the bands is calculated as the brightness of the pixels of the image f, symmetrical about the boundary. Subsequently, the window processing of the extended image f_e is performed, in which the centers of the windows w are shifted by the value of M_{w2} from the edge of the image in height and by the value of N_{w2} in width. Due to this, the windows w do not go beyond the image and within each window you can correctly calculate its minimum and maximum value.

Within each window w, the minimum and maximum brightness values are calculated. The obtained values of local minima are written in the rectangular matrix of the lower envelope $f_{min} = f_{min}(i, k)$, where $i = 0, ..., M\text{-}1$; $k = 0, ..., N\text{-}1$. The obtained values of local maxima are written in the rectangular matrix of the upper envelope $f_{max} = f_{max}(i, k)$, where $i = 0, ..., M\text{-}1$; $k = 0, ..., N\text{-}1$.

To avoid distortion of brightness when increasing local contrast, the lower (f_{min}) and upper (f_{max}) brightness envelopes are filtered. Envelope filtration is performed by Gaussian filter with a standard deviation σ_{wG} (for example, $\sigma_{wG} = 16$) by convolving the envelopes (f_{min}, f_{max}) with the w_G core of the Gaussian filter (size $M_{wG} \times N_{wG}$ elements) according to the formulas:

$$f_{\min c}(i,k) = \sum_{m=1}^{M_{wG}} \sum_{n=1}^{N_{wG}} f_{\min}(i-m-m_c, k-n-n_c) \cdot w_G(m,n), \quad (1)$$

$$f_{\max c}(i,k) = \sum_{m=1}^{M_{wG}} \sum_{n=1}^{N_{wG}} f_{\max}(i-m-m_c, k-n-n_c) \cdot w_G(m,n), \quad (2)$$

where $f_{minc} = f_{minc}(i, k)$ is filtered lower envelope; $f_{maxc} = f_{maxc}(i, k)$ is filtered upper envelope; $i = 0, ..., M\text{-}1$; $k = 0, ..., N\text{-}1$; $m_c = (M_{wG2} + 1)$ is center of the filter core w_G in height; $n_c = (N_{wG2} + 1)$ is center of the filter core w_G in width; M_{wG2}, N_{wG2} are whole parts of half the size of the core of the Gaussian filter w_G.

On the basis of envelopes (f_{minc}, f_{maxc}) and the filtered image f the image-result f_c with the increased local contrast and the removed inhomogeneous background according to the formula is calculated

$$f_c(i,k) = \frac{f(i,k) - f_{\min c}(i,k)}{f_{\max c}(i,k) - f_{\min c}(i,k)}, \quad (3)$$

where $i = 0, ..., M\text{-}1$; $k = 0, ..., N\text{-}1$.

Formula (3) can also be written as

$$f_c(i,k) = \big(f(i,k) - f_{\min c}(i,k)\big) \cdot k_c(i,k), \quad (4)$$

where $k_c(i, k) = 1/(f_{maxc}(i,k) - f_{minc}(i,k))$ are local contrast coefficients.

In order to prevent the appearance of artifacts (for example, parasitic contours) on the restored images fc for the maximum values of the local contrast coefficients k_c set the limit k_{CMax} (for example, $k_{CMax} = 5$).

When processing color images, the pixel values of the high-contrast g_{RGB} color image are calculated by the formula

$$g_{RGB}(i,k,c) = \frac{f_c(i,k) \cdot f_{RGB}(i,k,c)}{f(i,k)}, \quad (5)$$

where $i = 0, ..., M\text{-}1$; $k = 0, ..., N\text{-}1$; $c = 0, ..., 2$ are color channel number; f_{RGB} is the initial color image.

In high-contrast f_c images, g_{CS} contours are calculated by Sobel and Canny methods [3]. Sobel's method provides higher speed, and Kenny's method - higher accuracy.

According to the activity diagram (Fig. 1), after reading images from the video camera, noise filtering, contrast enhancement and contour selection, segmented g_{SL} images are calculated by method of contour lines [3, 4].

The obtained segment parameters are used to assess the condition of the studied objects (trains and wagons) and to detect objects (e.g. windows) using fuzzy membership functions [7]. In the cycle by segment number n_s all segments with numbers from 1 to Q_{ns} are traversed. Segments are selected by size. Segments with a height greater than s_{iw_min} (minimum segment height) and a width greater than s_{kw_min} (minimum segment width) are selected.

Selection of objects in the image (windshield, headlights, license plates, etc.) based on their segments is performed using fuzzy sets [7]. Based on the parameters of the segments (height,

width, center coordinates), the values of the fuzzy membership function μ_{ws} of the segment ns belonging to a certain object (for example, to a window) are calculated. The loop calculates the segment with the number n_{s_ws} and the maximum value of the membership function μ_{max}, because such a segment best fits the desired object in the image (for example, a window). For all segments, their normalized height s_{iwN} is calculated and the corresponding values of the function of belonging of the segment $\mu_{wsh}(s_{iwN})$ to a certain object, taking into account its height. The values of membership functions are also calculated taking into account the normalized widths of the s_{kwN} segments and the coordinates of their centers (s_{icN}, s_{kcN}) in height and width. The value of the resulting membership function μ_{ws} of the segment with the number ns to the object, taking into account all the parameters of the segment (height, width, center coordinates in height and width) is defined as the product of the values of the corresponding membership functions:

$$\mu_{ws}(n_s) = \mu_{wsh}(s_{iwN}) \cdot \mu_{wsw}(s_{kwN}) \cdot \mu_{wsic}(s_{icN}) \cdot \mu_{wskc}(s_{kcN}). \quad (6)$$

By the maximum of the membership function $\mu_{ws}(n_s)$ calculates the segment number n_{s_ws}, which most fully belongs to the specified object. Other objects in the image are detected similarly.

3. Hardware and software implementation of image segmentation system

2.1. Hardware implementation of image segmentation system

The hardware (physical) model of the train and wagons image segmentation system is constructed using the UML deployment diagram (Fig. 2).
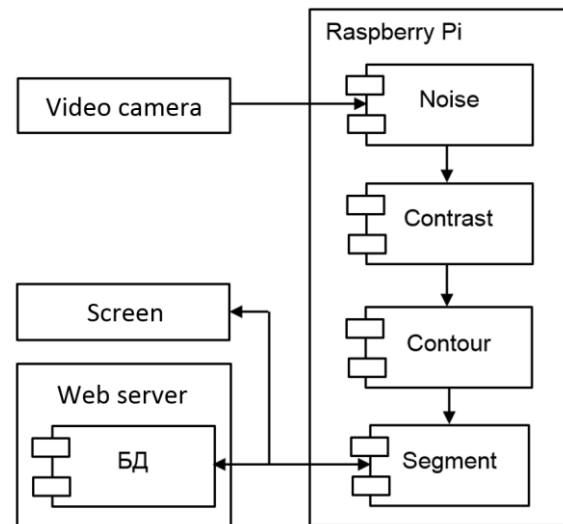
Fig. 2. *Physical model of the system of segmentation of images of trains and wagons*

The deployment diagram shows the location of system components at system nodes. According to the physical model, the initial images are read from a video camera (connected to a Raspberry Pi 3B +) and processed using a Raspberry Pi 3B + microcomputer [8]. The «Noise» software module reduces noise by filtering, the «Contrast» module increases the local contrast of the image, and the «Contour» module calculates image contours (which are then used as segment boundaries). The «Segment» module segmented images and calculated segment parameters. The «Detection» module detects objects using fuzzy membership functions. The received data is also transmitted to a remote web server for further analysis and displayed on the screen.

The hardware part of the prototype of the trains and wagons images segmentation system consists of a Raspberry Pi3B +

microcomputer [8], a digital CSI video camera or a USB video camera (Fig. 3).

Fig. 3. *Photo of the Raspberry Pi 3 Model B + microcomputer*

2.2. Software implementation of image segmentation system

The software part of the trains and wagons images segmentation system was developed in Python first by Google Colab cloud service (in the Jupyter Notebook) [9], and then transferred to the hardware platform of the Raspberry Pi3B + microcomputer (with Raspbian operating system installed) in the development environment Thonny Python IDE [10]. The program uses libraries such as scipy, numpy, matplotlib, opencv, scikit-fuzzy.

The initial (input) data for the developed program are digital images read from a video camera or from graphic files (images of trains, locomotives, wagons). The program supports reading images of basic graphic formats (.bmp, .jpg, .tiff).

The source data (results) of the program are image segments and coordinates of rectangles that correspond to the content areas of objects (for example, windows, license plates).

4. Test results of image segmentation system

Let's consider an example of segmentation of the image of a locomotive by means of the developed system. First, the initial color image is read from the graphic file (Fig. 4a) and the original image in shades of gray is calculated (Fig. 4b).

a)
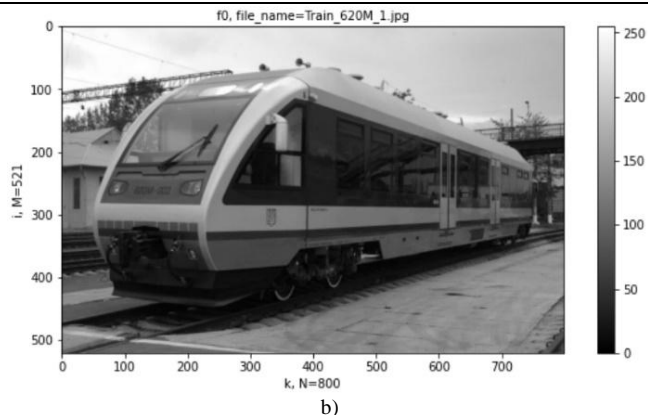
b)

Fig. 4. *Initial color image f_{RGB} (a) and image f_0 in shades of gray (b) [2]*

As a result of the median filtering of the image f_0 in shades of gray (Fig. 4b), the image f is obtained with a reduced noise level. Based on the image f, the image f_c (3) with increased local contrast is calculated (Fig. 5).

Fig. 5. *Image f_c with high local contrast, obtained on the basis of the image f*

The g_{CS} contours were calculated by the Sobel method (Fig. 6).
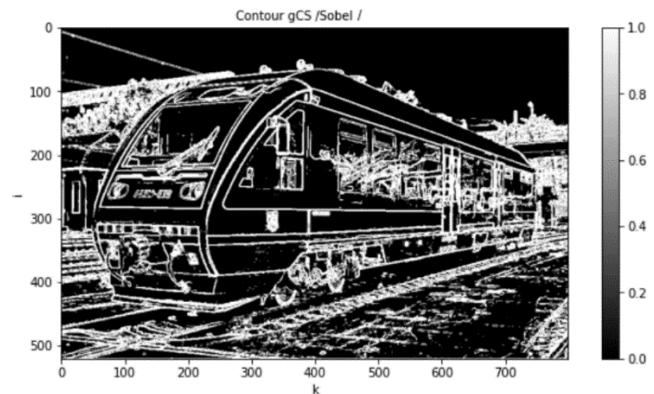
Fig. 6. *Contours of g_{CS} images obtained on the basis of f_c images by Sobel method*

Image segmentation is performed based on their g_{CS} contours, which highlight the boundaries of the segments. The numbers of the received segments are written in the g_{sL} array. Segments with a height greater than s_{iw_min} (minimum segment height, $s_{iw\_min} = 30$) and a width greater than s_{kw_min} (minimum segment width, $s_{kw\_min} = 30$) were selected. As a result, the most significant segments in the form of g_{sL2} images were selected (Fig. 7).
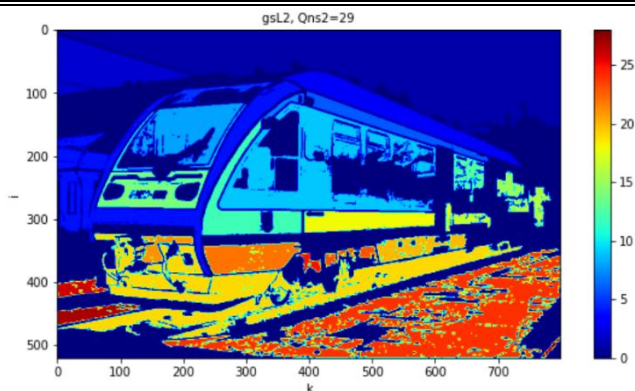
Fig. 7. *Segmented g_{sL2} image after segment selection; Q_{ns2} is number of segments*
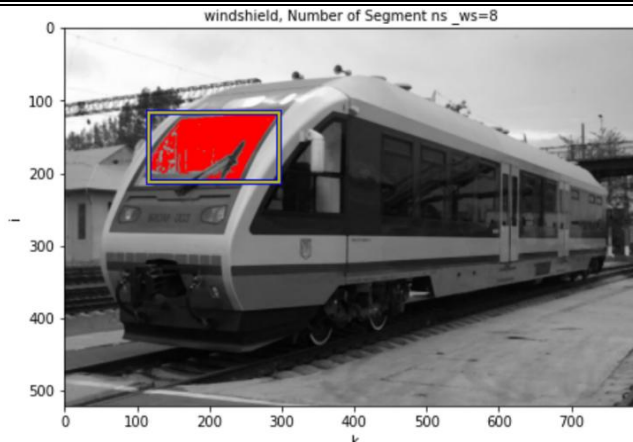
Fig. 9. *The result of windshield detection*

The windshield was detected using fuzzy sets. Based on the analysis of the parameters of the segments corresponding to the windshield, the parameters of fuzzy triangular membership functions were determined (Fig. 8). For each segment with the number ns its normalized height s_{iwN} (for the image height of 1000 pixels) was determined and the corresponding value of the function of belonging of the segment μ_{wsh} (s_{iwN}) to the windshield was found taking into account its height (Fig. 8).
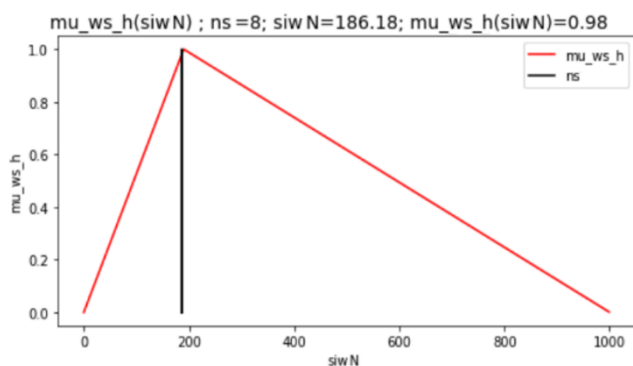
Fig. 8. *Membership functions of fuzzy sets, which describe the belonging of the segment with the number n_s to the windshield depending on the normalized height of the segment s_{iwN}*

Similarly, the values of membership functions are determined taking into account the normalized width of the segment s_{kwN} and the coordinates of its center (s_{icN}, s_{kcN}) in height and width. The value of the resulting function of belonging of the segment with the number n_s to the windshield, taking into account all the parameters of the segment is determined by formula (6). The maximum of the membership function μ_{ws} (n_s) calculates the segment number n_{s_ws}, which most fully belongs to the windshield (Fig. 9). The result is correct.

The results of windshield detection for other images of locomotives are also correct.

Headlights and license plates are similarly detected in the images.

5. *Conclusions*

1. The prototype of the system of images segmentation of trains and wagons is developed. The activity diagram and physical model of the system are developed.
2. Created a program in Python for noise filtering, increasing local contrast, contouring and image segmentation.
3. Fuzzy logic is used to detect train components in images.
4. Hardware and software implementation of the system in Python using Google Colab cloud platform and Raspberry Pi 3B + microcomputer is performed.
5. Processing of test images showed high accuracy of detection of components of trains on their images.

6. *References*

1. Roads Service. URL: https://www.roadsni.gov.uk.
2. Ukrzaliznytsia. URL: https://www.uz.gov.ua/press_center/photogallery/gallery-265193/.
3. Russ J.C. The Image Processing. Handbook. Abingdon-on-Thames, Taylor & Francis Group, 2011, 885 p.
4. Image Segmentation. URL: https://scikit-image.org/docs/dev/user_guide/tutorial_segmentation.html.
5. The Unified Modeling Language. URL: http://www.uml-diagrams.org.
6. Balovsyak S.V., Kravchenko H.O., Derevyanchuk O.V., Kroitor O.P., Tomash V.V. Computer system for increasing the local contrast of railway transport images. – Proc. SPIE, Fifteenth International Conference on Correlation Optics, V. 12126, 2021, P. 121261E1-7.
7. Hooda D., Raich V. Fuzzy Logic Models and Fuzzy Control. An Introduction. Alpha Science International Ltd., Oxford, U.K., 2017. 408 p.
8. Raspberry Pi Compute Module 3+. URL: https://datasheets.raspberrypi.com/cm/cm3-plus-datasheet.pdf.
9. Google Colab. URL: https://colab.research.google.com.
10. Thonny. Python IDE. URL: https://thonny.org.

Opportunities to improve product quality with the support of industrial robots

Erika Hrušková[1,*], Miriam Matúšová[2]
Slovak University of Technology, Slovakia[1]
Slovak University of Technology, Slovakia[2]
erika.hruskova@stuba.sk, miriam.matusova@stuba.sk

Abstract: *In the industry, the concept of "production quality" means a very important and inseparable role, which has a large share in the final quality of the product. Various factors affect product quality. Above all, state-of-the-art technologies are used in every industry, which helps to adapt quickly and efficiently to changes in market conditions, which has a significant impact on the competitiveness of manufacturers to become market leaders. The manufacturers 'efforts are made to produce a flawless product that will excessively meet customers' requirements for the perfect product. An integral part of the production process is the quality control of products at certain stages of production. Measurement requirements are defined by satisfactory accuracy, variability, total cost and speed. An important factor in product inspection is currently the creation of a three-dimensional virtual model of a real product, where you can easily compare the created 3D model with the original CAD model and display dimensional deviations.*
Keywords: *QUALITY OF THE PRODUCT, PRODUCTION PROCESS, VIRTUAL MODEL, 3D MODEL, DIMENSIONAL DEVIATIONS.*

1. Introduction

The role of materials management is to extend technologies so that they can respond flexibly to new economic conditions, the determining factor of which is no longer the supply side but the demand side. If the company does not ensure efficient and effective control of the material flow of input materials, the production process will not be able to produce products at the required price, at a time when these products are required for distribution to customers. In a production environment, a lack of the right materials and low-quality semi-finished products at the time they are needed can lead to a slowdown or even cessation of production, which can then lead to depletion of stocks (finished products). For these reasons, due attention must be paid to material flow management in the manufacturing plant. The goal of material movement management is to solve material problems from a company-wide point of view, by coordinating the performance of various material functions, providing a communication network and managing material flow.

Four basic activities in the field of material flow management:

- anticipation of material requirements,
- identifying the resources and obtaining materials,
- transport and introduction of material into the working space of the machine,
- material condition monitoring. [1]
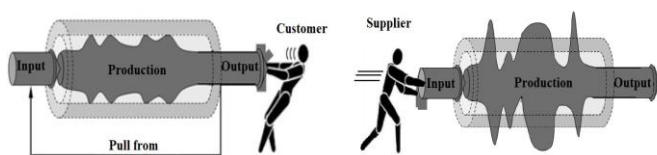
Fig. 1 *Pull system a Push system of controlling in the manufacturing process* [2]

With a focus on the goals of Industry 4.0, it is possible to create an automatic and flexible adaptation of the production process designed to track the position of materials and products. The output is to simplify and streamline communication between the material, the machines and the product itself.

2. Description of product and its assembly workplace

Bearings as mechanical components are among the most extensive products in the automotive and industrial sectors.
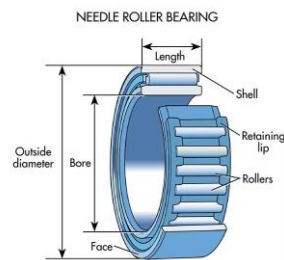
Fig. 2 *Bearing as a product of analyse [3]*

They are found in common industrial production facilities. The assembly process is fully automated and human personnel are needed at the exit of line Fig.3, when checking the inner diameter of bearings (HK) on the measuring mandrel, when packing the finished bearings into a box and then placing the full boxes on a pallet.
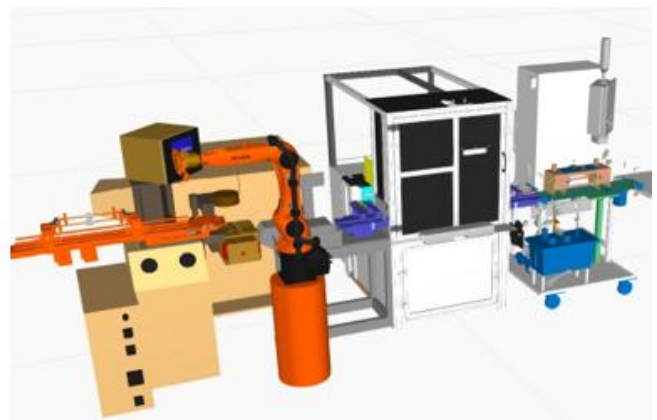
Fig.3 *Workplace of assembly line*

3. Product assembly with usage of industrial robot

Automatic control of the inner diameter of bearings can be performed manually or using a robotic workplace. A robotic workplace using a conventional robot or a collaborative robot must take into account:

- placing the robot in a confined space of an existing workplace,
- reach of the industrial robot to all parts of the workplace,
- robot load more than 0.5 kg.

The KUKA LBR isyy collaborative robot was used to design the robotic workplace to compare the measurement of the inner diameter of bearings, human vs. collaborative robot. Fig.4

Collaborative robot	KUKA LBR isyy
Number of controlled axies	6
Reliability of robot positioning	±0,015mm
Weight controlling	18,8kg
Max. carrying capacity	3kg
Max. distance from rotary axies	600mm
Max. operation speed	1000mm/s
Max. operation noisy	Not up 67dB
Safety level	IP40
Operation range of temperature	+5°C - +45°C
Assembly	Floor
Controlling	KR robot cotroller
Process of programming and simulation	KUKA Sim Pro 3.1
Manual controlling panel	KUKA SmartPAD
Manual programming	Manual directing

Fig. 4 Parameters of robota [4]

Industrial robot programming is possible in several ways. In the classic way in offline mode, with manual KUKA smartPAd control or manual programming, so-called learning. When programming manually, the robot is manually guided to the desired position, which is saved. Quick and easy programming of the collaborative robot allows quick changes in the program and reduces the time needed to change the program and its implementation in the workplace.

All movements of the KUKA LBR isyy collaborative robot should be sensed by speed sensors as well as torque sensors directly in the joints of the collaborative robot. The aim is to measure the required values in real time and the possibility of using these values in the automated process of measuring the inner diameter HK on the roller bearing NK.

Sensor representation of the environment is an important part of an intelligent robotic perception system. The display here covers the metric model and its semantic interpretation, which allows to represent the environment. Machine learning is used at various levels in process. Choosing a method of work of robots often comes down to getting the latest prepared information from an online repository and fine-tuning it to the current problem. Usage collaborative robots has greatly improved performance in a variety of tasks such as follows: object detection, recognition, semantic segmentation, etc. development is possible this direction for availability of experiments on publicly available data sets, as well as their comparison with other methods using standard criteria. Perception is a very important part of a complex, embodied, active, and goal-driven intelligent robotic system. fig.5
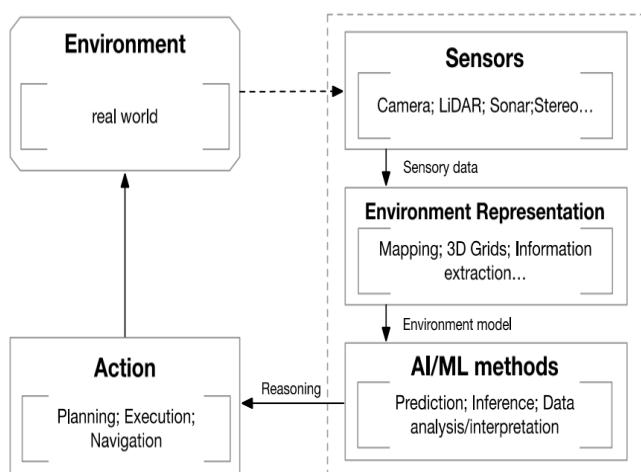
Fig. 5 Parameters of robot [5]

3. Methods of measuring the inner diameter of the bearing

The possibilities of measuring the inner diameter of the bearing must be analyzed based on the choice of method and the possibility of using the end effector. When choosing the method of measuring the average, the following methods were analyzed these possibilities:

a) The inner diameter is measured from the image obtained using the 2D optical projection method.

b) Hole diameters are measured by bending the optical axes of two sensor heads 90° using a prism.

c) During insertion, the pressure force of the roller bearing on the measuring mandrel is automatically measured. After reaching the pressing force of 50N, the control system of the collaboration robot reads the position of the roller bearing on the measuring mandrel according to the coordinate system of the collaboration robot. [6]
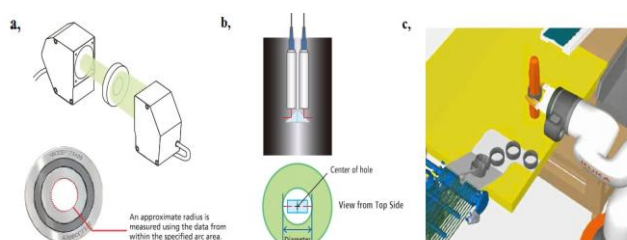
Fig.5 Diameter measurement options [6]

When designing the automation of the inner diameter control, it is necessary to determine the trajectory of the robot's work cycles. Compared to the activity of measuring the inner diameter of a bearing by a human, the trajectory of the robot is given by the algorithm fig.6, but the trajectory of human labor is irregular. Different trajectories and man-made times arise due to imperfections in determining the pressing force of the roller bearing on the gauging mandrel.
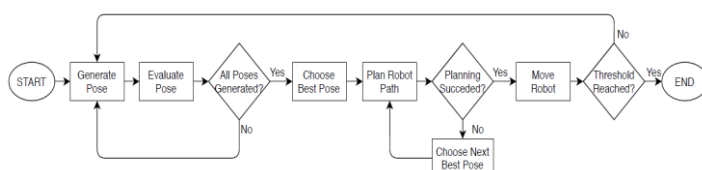
Fig.6 The manipulator's movement to the pose [7]

If the operator exceeds the specified value of the pressing force, the bearing will jam on the mandrel and it is necessary to use more force to pull the bearing out of the measuring mandrel. When using the robot to measure the inner diameter of the bearing, the speed and force of sliding the bearing onto the measuring mandrel must be clearly defined. When planning the trajectory of the robot, it is necessary to ensure the boundaries of safety zones. According to the ISO / TS 15066 specification, it is necessary to define three zones in which specific safety conditions apply. Fig.6

Fig. 6 Safety zones of robot [4]

The simulation model can be used to verify the availability of a collaborative robot and a possible collision with other objects. Subsequently, it is possible to compare the measurement time of the inner diameter HK at the NK bearing by a human factor, i.e. this operation is performed manually, with the time of the same measurement and in an automated simulated process. Fig.7
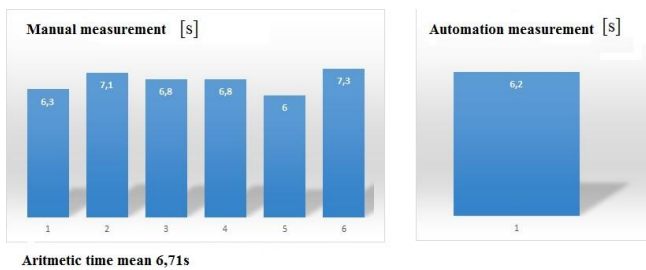
Fig. 7 Comparison of times of manual and automatic measurement of the inner diameter of the bearing

The time difference of manual measurement compared to automated measurement is 0,51s. The time difference of the measurement was compared on the number of 4500 pieces of measured roller bearings in one working day and the time saving in ideal conditions is 17 minutes.

When looking at time savings, only a small time difference can be seen. Therefore, there is a need to compare manual and automated measurements based on several criteria such as:

- Accuracy of the pressing force of the roller bearing on the measuring mandrel.

- Quality of evaluation of good and bad inner diameter HK.

- The real time measured during the working day.

- Human factor error.

The accuracy of the pressing force on the measuring mandrel is very important for the correct reading of the value of the inner diameter HK on the roller bearing NK, which must be within the tolerance range of the value of the inner diameter HK. The change in the pressing force therefore has a direct effect on the learning quality of the good or bad inner average of the HK, especially at the tolerance limits. The comparison was based on measurement operation time and did not take into account, for example, the rotation of operator changes, the time taken for operator breaks and many other aspects that enter into the manual measurement process. A more extensive analysis with regard to all aspects entering the measurement process would be needed to determine the exact times of the manual measurement.

With the automated measurement process, there are no common aspects enter into that to extend the measurement time. Fig.8

Fig. 8 Robot workplace and simulation of measuring process

Unforeseen aspects that enter into the automated process, such as slowing down or stopping the collaborative robot when the workspace is disturbed, or the failure, cannot be taken into account when comparing time in the manual and automated measurement process. In this process, the human factor is removed, thus eliminating the error rate during the measurement process. In conclusion we can state that mismatched roller bearing pieces do not continue into the package, but end up in a box for mismatched roller bearings.

3. Conclusion

The constant effort to streamline and improve the production system leads to efforts to reduce time, eliminate downtime, unnecessary costs for maintenance, operation and the technological, handling, transport and other functions. For all these areas, the solution is automation itself, which, if set correctly on the basis of detailed professional analyzes, provides a full-fledged substitute for the human factor.

As a substitute for the human factor, the use of a collaborative robot, which with its properties comes closest to the characteristics and movements of man.

The aim of the research was to simulate the automatic measurement of the pitch circle (HK) on roller bearings using a collaborative technique in comparison with manual measurement. A description of the method of measuring the inner diameter of roller bearings on the measuring mandrel on both sides, which is performed in cooperation with the human factor on the basis of the ISO 1132-2 standard, was characterized. The analysis took into account the following criteria: increased measurement quality, reduced line service, overall safety, increased degree of automation, complexity of equipment used and use of the latest technologies.

4. Acknowledgement

5. *References*

1.   R. Bolebruch, Streamlining of material flow in coach building shop of C-SUV Volkswagen Slovakia, Diploma thesis, (2021)

2.   P. Malega, Modern tools to improvement of logistics flows https://www.sjf.tuke.sk/umpadi/taipvpp/2015/index.files/05_Malega _Moder ne_Nastroje.pdf, [cit.2021-04-21]

3.   https://www.machinedesign.com/learning-resources/whats-the-difference-between/article/21831901/whats-the-difference-between-bearings, [cit.2021-04-21]

4.   M. Polák, Design of the concept of automatic measurement of the pitch circle (HK) on roller bearings, Diploma thesis, (2020)

5.   R. Galin, R. Meshcheryakov, Collaborative Robots: Development of Robotic Perception System, Safety Issues, and Integration of AI to Imitate Human Behavior. In: Ronzhin A., Shishlakov V. (eds). Proceedings of 15th International Conference on Electromechanics

6.   https://www.keyence.eu/ss/products/measure/measurement_lib rary/measuring/in_diameter/, [cit.2021-04-21]

7.   J. Santos, M. Oliveira, R. Arrais, G. Veiga, Autonomous scene exploration for robotics: A conditional random view-sampling and evaluation using a voxel-sorting mechanism for efficient ray casting. Sensors, 20(15), (2020)

Disturbance rejection in a one-half vehicle suspension using a fuzzy controller

Katerina Hyniova

Faculty of Information Technology– Czech Technical University in Prague, Czech Republic

hyniova@fit.cvut.cz

Abstract: *Generally, passenger ride comfort can be interpreted as an attenuation of sprung mass acceleration or as peak minimization of sprung mass vertical displacement, while good handling can be characterized as an attenuation of unsprung mass acceleration. This effort devoted to passive suspension design is ineffective because improvements to ride comfort are achieved at the expense of handling and vice versa. Instead, the best result can be achieved by active suspension, i.e. when an additional force can act on the system and simultaneously improve both of these conflicting requirements. Another important goal of the control design is to maintain robustness of the closed loop system. In the paper, fuzzy logic is used to simulate active suspension control of a one-half-car model. Velocity and acceleration of the front and rear wheels and undercarriage velocity above the wheels are taken as input data of the fuzzy logic controller. Active forces improving vehicle driving, ride comfort, and handling properties are considered to be the controlled actuator outputs. The controller design is proposed to minimize chassis and wheels deflection when uneven road surfaces, pavement points, etc. are acting on tires of running cars. As a result, a comparison of an active suspension fuzzy control and a spring/damper passive suspension is shown using MATLAB simulations.*

Keywords: ACTIVE SUSPENSION, FUZZY LOGIC, CONTROL, ONE-HALF-CAR MODEL, SIMULATION

1. Introduction

At the Czech Technical University in Prague various alternative strategies and innovations to classical passive suspension systems improving ride comfort of the passengers, providing steering stability, maximizing safety, and improving handling properties of vehicles has been researched. In order to improve handling and comfort performance instead of a conventional static spring and damper passive system, an alternative active suspension system has been developed. Certainly, there are numerous variations and different configurations of vibration suspension. In known experimental active systems the force input is usually provided by hydraulic or pneumatic actuators. As an alternative approach to active suspension system design, electromechanical actuators have been studied by the research group. Such actuators provide a direct interface between electronic control and the suspension system. Connection of a passive spring-damper suspension to an active system has a potential of improving safety and comfort under nominal conditions. Perhaps more important is that such a combination allows continuous adaptation to different road surface quality and driving situations.

A number of studies on structural vibration control have been done recently and practical applications have been realized [1]. It is used both, passive solutions for vibration isolation, and active systems, usually based on PID controllers. In addition, semi-active vibration isolation methods are often proposed and used. Liu *et al.* [3] designed a slightly more intricate fuzzy controller for a magneto-rheological damper and were able to reduce vibrations of single-degree of freedom bridge model subjected to random inputs. Simulation of active vibration isolation of a one-quarter-car model with fuzzy logic device has been designed by Nastac [4].

2. Problem Formulation

For the design of active suspension, we know how to create a suspension model and how to define objectives of control in order to reach a compromise between contradictory requirements like ride comfort and road holding by changing the force between a wheel and chassis masses. In the past, it has been reported on this problem successively, about the base of optimization techniques, adaptive control and even, H-infinity robust methods [6]. In this paper, fuzzy logic is used to control the active suspension of a one-half-car model that uses linear electrical motor as an actuator. There are taken velocity and acceleration of the front and rear wheels and undercarriage velocity and vertical acceleration above these wheels as input data of the fuzzy logic controller, and active forces f_1 and f_2 as its output data. The objective of fuzzy control is to minimize chassis deflections to reach passenger comfort and wheels (not to damage the road surface, respectively) when road disturbances are acting upon the running car.

Passenger comfort can be interpreted as an attenuation of sprung mass acceleration or as peak minimization of sprung mass vertical displacement, while good handling can be characterized as an attenuation of unsprung mass acceleration. This effort devoted to passive suspension design is ineffective because improvements to ride comfort are achieved at the expense of handling and vice versa. Instead, the best result can be achieved by active suspension, i.e. when an additional force acts on the system and simultaneously improves both of these conflicting requirements. Another important goal of the control design is to maintain robustness of the closed loop system.

3. Active Suspension System

All suspension systems are designed to meet various specific requirements. In suspension systems, mainly two most important points are supposed to be improved – vibrations absorbing (videlicet passenger comfort) and attenuation of the disturbance transfer to the road (videlicet car handling). The first requirement could be understood as an attenuation of the sprung mass acceleration or as a peak minimization of the sprung mass vertical displacement. The second one is characterized as an attenuation of the force acting on the road or – in simple car models – as an attenuation of the unsprung mass acceleration. The goal is to satisfy both these contradictory requirements.

Satisfactory results can be achieved when an active suspension system generating variable mechanical force acting between the sprung and unsprung masses is used.

Such an actuator can be a linear electric motor [2]. In comparison with traditional actuators that use revolving electromotors and a lead screw or toothed belt, the direct drive linear motor enables contactless transfer of electrical power according to the laws of magnetic induction. The gained electromagnetic force is applied directly without the intervention of mechanical transmission. Linear electric motors are easily controllable and for features like low friction, high accuracy, high acceleration and velocity, high values of generated forces, high reliability and long lifetime. Their usage as shock absorbers seems to be ideal.

Fig.1 shows the basic principle and structure of the linear electric motor used as an actuator in the designed unique active suspension system. The appreciable feature of linear motors is that they directly translate electrical energy into usable mechanical force and motion and back. They are linear shaped.

Linear motor translator movements reach high velocities (up to approximately 4 m/s), accelerations (up to g multiples) and forces (up to 10 kN). The electromagnetic force can be applied directly to the payload without an intervention of mechanical transmission.
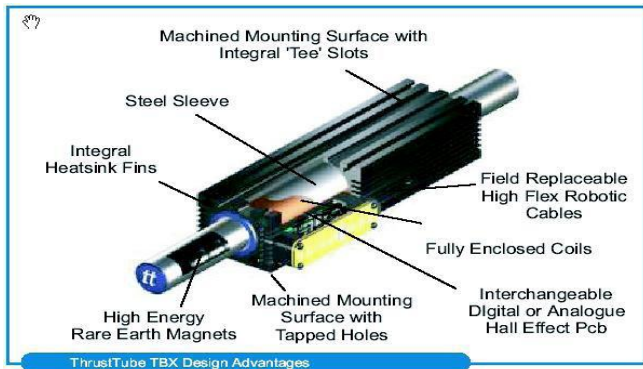
Fig. 1 *Linear motor basic design (manufacturer spread sheet).*

4.Linear Motor Model

In order to verify control algorithms we created a linear motor model including a power amplifier in Matlab/Simulink[TM]. The model enables to demonstrate the conversion of electrical energy to mechanical energy.

In the model, it is assumed that the magnetic field of the secondary part with permanent magnets is sinusoidal, the phases of the primary part coils are star-connected, and a vector control method is used to control the phase current [6]. Here, PWM voltage signal is substituted by its mean value to shorten (about 10 times) the simulation period (inaccuracies caused by such a substitution can be neglected).

The principal inner representation of the model is shown in Fig.2. The model input vector is given by the instantaneous position [m] necessary to compute the commutation current of the coils, instantaneous velocity [m/s] (the induced voltage of the coils depends on the position and velocity) and desired force [N].

The designed model function we verified comparing dynamics of the model in Fig.3 and the real motor. The simulation parameters correspond to catalogue parameters of TBX3810 linear motor fy Thrust-tube.

For example, time responses caused by changes of the desired force have been compared.
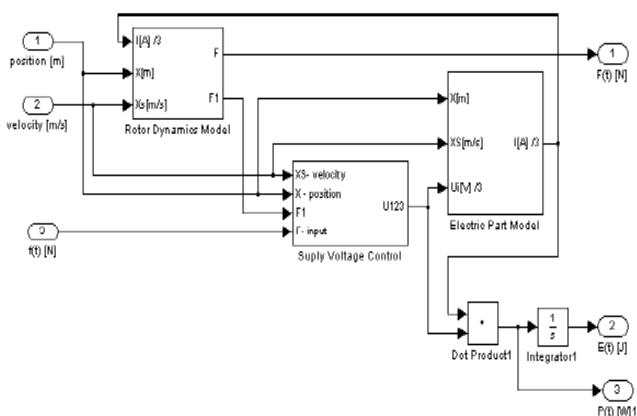
Fig.2. *Principal inner model representation.*

The linear motor input-output model is shown in Fig. 3.

Fig.4 and Fig.5 represent simulated and real time responses, respectively (rightangular force signal: 0→200 [N], power supply of 150 [V], velocity: 0 [m/s]).
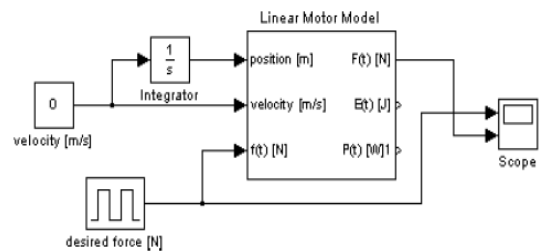
Fig. 3 *Linear motor input/output model for dynamics verification.*
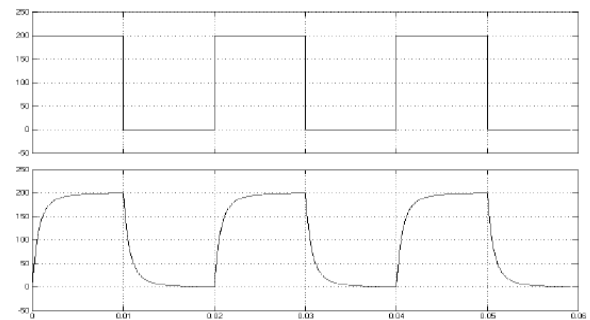
Fig.4 *Simulated time response.*
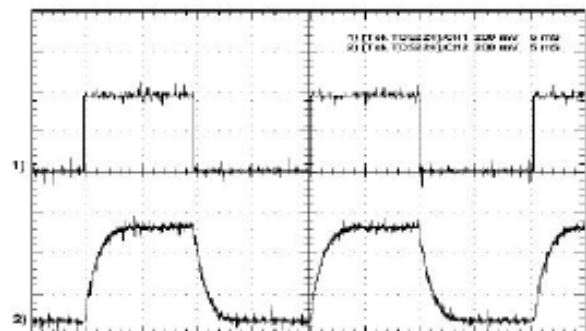
Fig.5 *Real time response.*

Comparing the time responses in Fig.4 and Fig.5 it can be seen very good matching of the model and the real motor behavior.

On the base of the experiments that were taken on the model, we gained values of electric power necessary to be supplied or consumed when velocity and force of the motor are constant.

In Fig. 6 an input/output model of the linear motor (with concrete simulation values) is represented.

It results from many experiments we made [6] with TBX3810 linear motor that the designed model describes the real linear motor equipped with necessary auxiliary circuits very authentically and enables to verify control algorithms developed to control the linear motor as an actuator of the active suspension system.
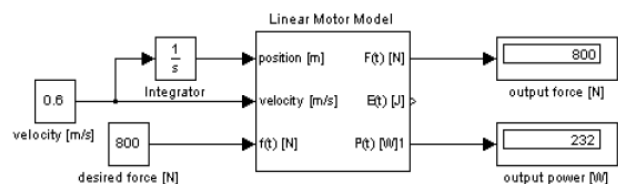
Fig.6 *Linear motor input-output model.*

5.One-half-car Suspension Model

In this paper, a one-half-car model in Fig.7 which includes two one-quarter-car models connected to a homogenous undercarriage [2] is considered.
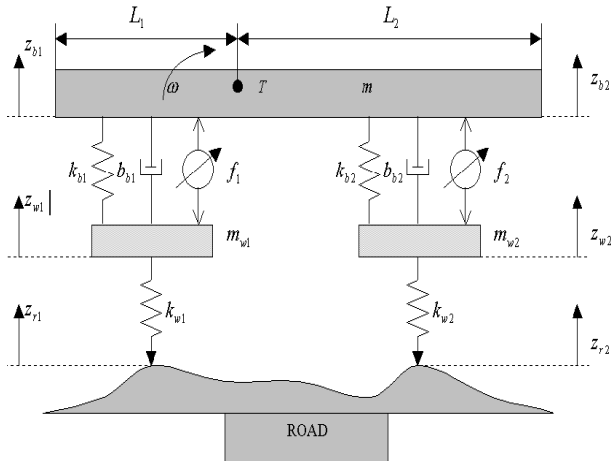
Fig. 7 *One-half-car model.*

The undercarriage is determined by its mass - m [kg] (taken as one half of the total body mass - 500 kg), length L [m] (L = L_1 + L_2 = 1,5m + 2,5m = 4m) , center of gravity position T [m] (given by L_1 and L_2) and moment of inertia J_P=2700 kgm^2.

The motion equations of the car body and the wheels are as follows:

$$m_{w1}\ddot{z}_{w1} = -f_1 + k_{b1}(z_{b1} - z_{w1}) - k_{w1}(z_{w1} - z_{r1}) + b_{b1}(\dot{z}_{b1} - \dot{z}_{w1}) \quad (1)$$

$$m_{w2}\ddot{z}_{w2} = -f_2 + k_{b2}(z_{b2} - z_{w2}) - k_{w2}(z_{w2} - z_{r2}) + b_{b2}(\dot{z}_{b2} - \dot{z}_{w2}) \quad (2)$$

$$m_{b1}\ddot{z}_{b1} = f_1 - k_{b1}(z_{b1} - z_{w1}) - b_{b1}(\dot{z}_{b1} - \dot{z}_{w1}) = F_1 \quad (3)$$

$$m_{b2}\ddot{z}_{b2} = f_2 - k_{b2}(z_{b2} - z_{w2}) - b_{b2}(\dot{z}_{b2} - \dot{z}_{w2}) = F_2 \quad (4)$$

where the position variables are taken with respect the static equilibrium position, m_{w1}, m_{w2} - wheel masses (35 kg each), k_{b1}, k_{b2} - passive suspension spring stiffnesses (16 kN/m each), k_{w1}, k_{w2} - tire stiffness (160 000 N/m each), b_{b1}, b_{b2} - passive suspension damping coefficients (980 Ns/m each), f_1,f_2 - active forces between the front/rear sprung and unsprung masses[N], z_{r1}, z_{r2} - road displacements [m], z_{b1}, z_{b2} - body (chassis) displacements [m], z_{w1}, z_{w2} - wheel displacements [m].

To model the road input, we assume that the vehicle is moving at a constant forward speed. Then the vertical velocity is a white noise process which is approximately true for most of real roadways.

The pitching equation is given as :

$$F_1 L_1 - F_2 L_2 + J_p \dot{\omega} = 0 \quad (5)$$

and motion of the gravity center as:

$$F_1 + F_2 - m_p \dot{v}_T = 0 \quad (6)$$

Note, that:

$$v_{b1} = v_T + \omega L_1 \quad (7)$$

and

$$v_{b2} = v_T - \omega L_2 \quad (8)$$

where the meaning of constants and variables is as follows: v_T [ms^{-1}] - velocity of the center of gravity, ω [rad s^{-1}] - angular velocity, v_{b1} [ms^{-1}] - undercarriage velocity above the front wheel, and v_{b2} [ms^{-1}] - undercarriage velocity above the rear wheel.

6. State-space Model

To transform the motion equations of the one-half-car model to a state space model, the following state variables vector x (9), input variables vector u (14), and the vector of disturbances v (15), are considered:

$$x = [x_1, x_2, x_3, x_4, x_5, x_6, x_7, x_8]^T \quad (9)$$

where:

$$x_1 = z_{b1} - z_{w1} \quad (10)$$
$$x_2 = z_{w1} - z_{r1} \quad (11)$$
$$x_3 = \dot{z}_{w1} \quad (12)$$
$$x_4 = z_{b2} - z_{w2} \quad (13)$$
$$x_5 = z_{w2} - z_{r2} \quad (10)$$
$$x_6 = \dot{z}_{w2} \quad (11)$$
$$x_7 = v_T \quad (12)$$
$$x_8 = \omega \quad (13)$$
$$u = [f_1, f_2]^T \quad (14)$$
$$v = [\dot{z}_{r1}, \dot{z}_{r2}]^T \quad (15)$$

Then the motion equation of the one-half-car model for the active suspension can be written in the state space form as follows:

$$\dot{x} = Ax + Bu + Fv \quad (16)$$

where for the given data A, B and F are derived in [4][6].

Thanks to the negative real parts of all eigen values of matrix A, the model is stable.

7. Fuzzy Logic Controller

The fuzzy control system consists of three stages: fuzzification, fuzzy inference and defuzzification (Fig.8).
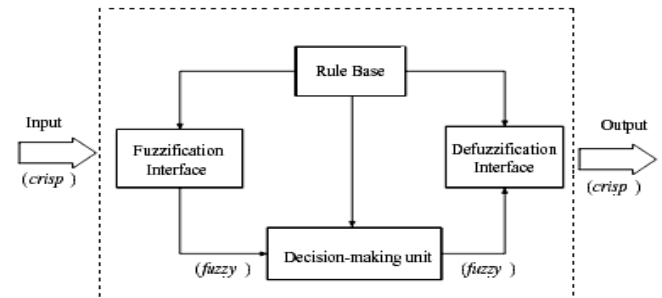
Fig.8 *Fuzzy controller structure*

The fuzzification stage converts real-number (crisp) input values into fuzzy values whereas the fuzzy inference machine processes the input data and computes the controller outputs in cope with the rule base and data base. These outputs, which are fuzzy values, are converted into real-numbers by the defuzzification stage.

The fuzzy logic controller used for the active suspension has nine inputs:

$$[v_{b1}, \dot{v}_{b1}, v_{b2}, \dot{v}_{b2}, v_{w1}, v_{w2}, v_T, \dot{v}_T, \omega]^T \quad (17)$$

and two outputs: f_1 and f_2. All membership functions are of triangular form. Variables ranges are stated experimentally [2] and are given in Tab.1a and Tab.1b bellow.

Table 1a: *Variables ranges*

z_r [cm]	$|f_1|_{max}$ [N]	$|f_2|_{max}$ [N]	$|v_T|_{max}$ [m.s^{-1}]	$|\dot{v}_T|_{max}$ [m.s^{-2}]	ω [rad.s^{-1}]
5	2876,4	2949,4	0,3	6,6	0,1
10	5752,8	6062,5	0,5	13.5	0,2

Table 1b: *Variables ranges*

$|v_{b1}|_{max}$ [m.s^{-1}]	$|\dot{v}_{b1}|_{max}$ [m.s^{-2}]	$|v_{w1}|_{max}$ [m.s^{-1}]	$|v_{b2}|_{max}$ [m.s^{-1}]	$|\dot{v}_{b2}|_{max}$ [m.s^{-2}]	$|v_{w2}|_{max}$ [m.s^{-1}]
0,3	6,8	2,4	0,3	6,8	2,2
0,5	13,5	4,8	0,5	13,5	4,9

The rule base used in the active suspension system for one-half-car model is represented by 160 rules [4], [6] with fuzzy terms derived by modeling the designer's knowledge and experience.

There are two types of rules for the one-half-car model. The rules for unsprung masses are corresponding to the rules of the one-quarter-car model [4], [6] and considering:

$$[v_{b1}, \dot{v}_{b1}, v_{b2}, \dot{v}_{b2}, v_{w1}, v_{w2}]$$

as fuzzy controller inputs, and f_1 and f_2 as controller outputs.

The abbreviations used in Table 2 and Table 3 correspond to:
- NV ..... Negative Very Big
- NB..... Negative Big
- NM.....Negative Medium
- NS..... Negative Small

- ZR..... Zero
- PS..... Positive Small
- PM.....Positive Medium
- PB..... Positive Big
- PV.....Positive very Big

The output of the fuzzy controller is a fuzzy set of control forces. As processes usually require non-fuzzy values of control, a method of defuzzification called "center of gravity method" is used here [2], [4], [6].

Table 2: *Rules for Unsprung mass*

If [v_{w1} =PM]AND[v_{b1} =NM]AND [$\dot{v}_{b1}$ =P]THEN[f_1 =PV]
If [v_{w1} =PS]AND[v_{b1} =NS]AND [$\dot{v}_{b1}$ =P]THEN[f_1 =PB]
If [v_{w1} =PM]AND[v_{b1} =NM]AND [$\dot{v}_{b1}$ =ZE]THEN[f_1 =PM]
If [v_{w1} =PS]AND[v_{b1} =NS]AND [$\dot{v}_{b1}$ =ZE]THEN[f_1 =PS]
If [v_{w1} =NM]AND[v_{b1} =PM]AND [$\dot{v}_{b1}$ =P]THEN[f_1 =NV]
If [v_{w2} =PM]AND[v_{b2} =NM]AND [$\dot{v}_{b2}$ =P]THEN[f_2 =PV]
If [v_{w2} =PS]AND[v_{b2} =NS]AND [$\dot{v}_{b2}$ =P]THEN[f_2 =PB]
If [v_{w2} =PM]AND[v_{b2} =NM]AND [$\dot{v}_{b2}$ =ZE]THEN[f_2 =PM]
If [v_{w2} =PS]AND[v_{b2} =NS]AND [$\dot{v}_{b2}$ =ZE]THEN[f_2 =PS]
If [v_{w2} =NM]AND[v_{b2} =PM]AND [$\dot{v}_{b2}$ =P]THEN[f_2 =NV]

Table 3: *Rules for Sprung mass*

If [v_T =PS]AND[ω =PM] AND [$\dot{v}_T$ =P]THEN[f_1 =NV]AND[f_2 =PM]
If [v_T =NS]AND[ω =PM] AND [$\dot{v}_T$ =P]THEN[f_1 =NM]AND[f_2 =PV]
If [v_T =NM]AND[ω =PM] AND [$\dot{v}_T$ =P]THEN[f_1 =ZE]AND[f_2 =PV]
If [v_T =PS]AND[ω =PS] AND [$\dot{v}_T$ =P]THEN[f_1 =NB]AND[f_2 =PS]
If [v_T =ZE]AND[ω =PS] AND [$\dot{v}_T$ =P]THEN[f_1 =NB]AND[f_2 =PB]
If [v_T =NS]AND[ω =PS] AND [$\dot{v}_T$ =P]THEN[f_1 =NS]AND[f_2 =PB]
If [v_T =PS]AND[ω =NS] AND [$\dot{v}_T$ =P]THEN[f_1 =NV]AND[f_2 =PV]
If [v_T =NS]AND[ω =NS] AND [$\dot{v}_T$ =P]THEN[f_1 =PS]AND[f_2 =NB]
If [v_T =PS]AND[ω =NM] AND [$\dot{v}_T$ =P]THEN[f_1 =PM]AND[f_2 =NV]
If [v_T =NS]AND[ω =NM] AND [$\dot{v}_T$ =P]THEN[f_1 =PV]AND[f_2 =NM]

8. Simulation Results

In this section, the controller was tested in order to compare the results of the designed fuzzy logic control with a traditional passive suspension system. As an example, step responses of the unsprung and front/rear sprung masses are shown in Fig.8- Fig.11.
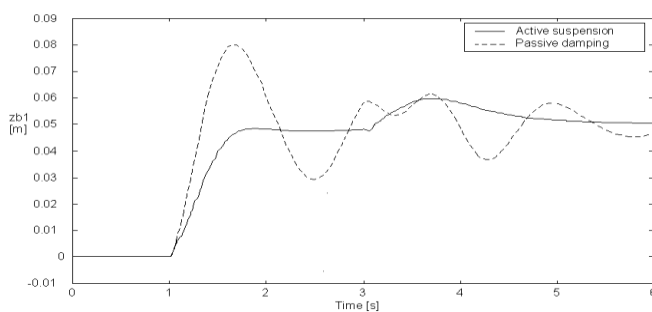
Fig.8 *Sprung mass deflection above front wheel.*
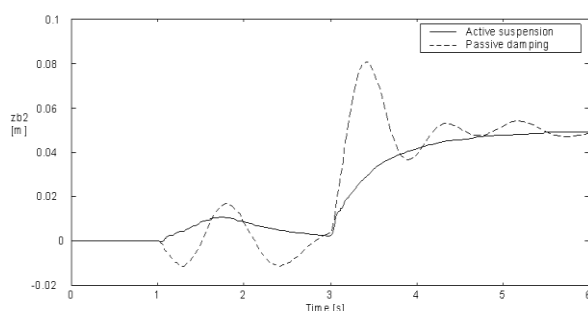
Fig.9 *Sprung mass deflection above rear wheel.*
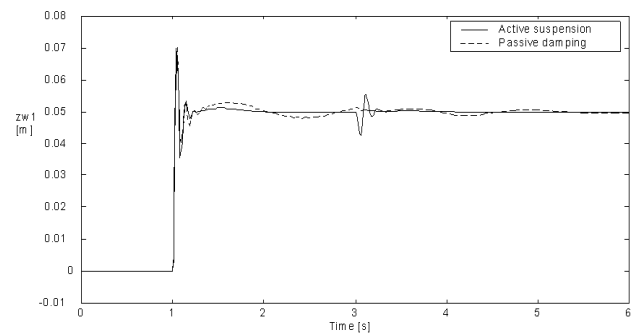
Fig10 *Front unsprung mass (front wheel) deflection.*
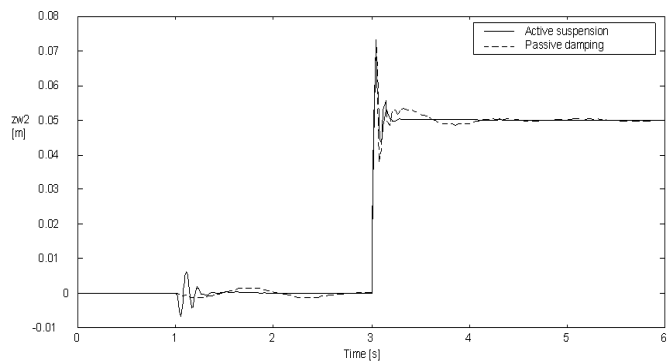
Fig.11 *Rear unsprung mass (rear wheel) deflection*
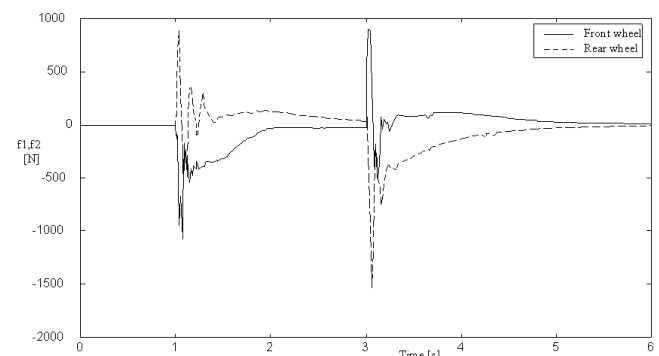
Fig.12 *Active forces acting on front/rear wheel.*

From Fig.9 and Fig.10, it is evident that fuzzy controlled active suspension efficiently suppresses sprung mass oscillations that occur when only passive suspension is used.

Diagram in Fig. 13 represents active forces acting on front and rear wheels in order to optimize ride comfort and good handling of the vehicle.

9. Conclusion

In the paper, we briefly described a basic way of fuzzy controlled active suspension system designed for a vehicle one- half-car model.

The entire analysis was developed in Matlab - Simulink, with Fuzzy Logic Toolbox. The fuzzy inference machine is also on custody of a special module of Simulink. Practically, the entire process of fuzzification - inference – defuzzification is automaton made by the Fuzzy Logic Controller of Simulink. The inference machine operation is based on the set of rules which link the input variables by the outputs. The set of input variables, output variables and inference rules base derived by modeling the designer´s knowledge and experience on vibroisolation devices.

The simulation results have been successfully verified on an experimental test stand. The same configuration like in Fig.7 has been used for test stand design and real experiments. Mechanical configuration of the test stand is obvious from Fig.13. Under the tire there is placed another linear electric motor that uses an input

experimental signal described in [6] to generate road displacement (road deviations) under the running wheel.

Fig.13 *Experimental test stand*

As is mentioned in [2],[4] the controller is developed via Matlab implemented into dSpace a connected to the test stand system.

References

[1] Cuclu, R.: Fuzzy Logic Control of Vibration of Analytical Multi-Degree-of- Freedom Structural Systems, Turkish J. Eng. Env. Sci., p157-167, 2003

[2] Hyniova, K. - Stribrsky, A. - Honcu, J.: Fuzzy Control of Mechanical Vibrating Systems, Proceedings of the International Carpatian Control Conference ICCC 2001, pp. 393-398, Krytica, Poland, 2001

[3] Liu, Y.: Energy minimization-based vibration control of a bridge using magneto-rheological fluid dampers, Proceedings of SPIE, 2000

[4] Nastac, S.: Simulation of active Vibration Isolation with Fuzzy Logic Device, In: Proceedings of the 10th international Conference on mathematical and computational methods in Science and Engineering (MACMESE ´08), pp. 346-351) Brasov,2008.

[5] Stribrsky, A. - Hyniova, K. - Honcu, J.: Using Fuzzy Logic to Control Active Suspension of Vehicles, Intelligent Systems in Practice, pp.41-49, Luhacovice, 2000

[6] Stribrsky, A. - Hyniova, K. - Honcu, J.: Reduction of Vibrations in Mechanical Systems, Proceedings of Workshop 2001, Part A, pp.174-175, CTU Prague, 2001
.

Using a 3D printer to innovate textile products

Ludmila Fridrichová

Technical University of Liberec

ludmila.fridrichova@tul.cz

Abstract: Today, 3D printing is available not only for industrial, semi-professional use, but also for hobbies and schools. Therefore, students TUL make full use of 3D printing within the subject Project Management. One of the topics they address is use of 3D printing for a textile product. They are looking for an answer to the question: How to 3d printing technology use for made a textile product?

Keywords: 3D PRINTING, TEXTILE PRODUCT, DIGITAL TEXTILES

1. Introduction

The 3D printing belongs to the rapidly emerging technologies which have the chance to revolutionize the way textile products are created. This is why it is necessary to acquaint students of textile specialization with news in this area also in the subject of project management too.

Teaching takes place in several steps:

- Students are looking for everything that has already been discovered or solved in the field of 3D textile printing.

- Students learn to create their own designs in the AutoCad program.

- Students are acquainted with the technology and possibilities of 3D printing.

Students create their own project of 3D printing.

- They design their own product

- They print the designed product

- They defend their work

There are several types of 3D printing, but the 3D printing of principle fused deposition modelling (FDM) is the most popular. It is conceptually simple and most of all the printing apparatus is cheap and of small size. We use the device Prusa i3 MK3S+ for teaching, as is shown in Figure 1.
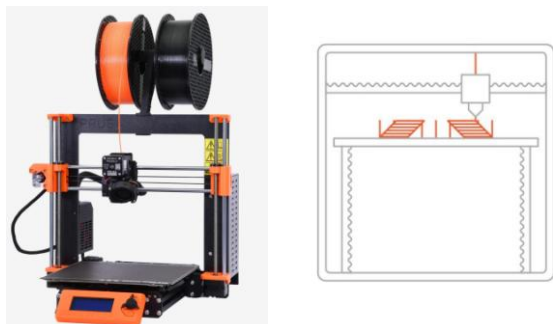
Fig. 1 3D printing Prusa i3 MK3S+and principle of FDM [1]

3D printing is a form of additive manufacturing, i.e. creating objects by sequential layering, for pre-production or production. After creating a 3D model with a CAD program, a printable file is used to create a layer design which is printed afterwards. [2]

As can be seen from Figure 1, the thermoplastic fiber is continuously fed into a small heated chamber (extruder) where it melts and becomes a highly viscous liquid. The melt is then extruded through a die and then deposited in layers on a heated table according to a pattern calculated by the printer control software that will reproduce the desired geometry of the object. [1]

We use for printing different types of fibers (PLA, ABS, PET, PETG, TPU, Nylon, ASA, PC, HIPS, Carbon Fiber and many more.)

2. Areas of application of 3D printing for textile products

Several ways of using 3D printing technology in textile production are known. The purpose of this article is to summarize the possibilities that 3D printing provides for textile production. The aim is to present here various approaches to the use of 3D printing for the creation of a textile product.

For clarity, we identify four areas of use of 3D printing that can be applied in the textile industry:

A. 3D printing of knitted or fabric

B. Fashion of the Future to be 3D Printed

C. 3D printing on textiles or as clothing accessory

D. 3D printing of clamping device for ITC

3D printing of knitted or fabric

When 3D printing was created, it seemed that it would soon replace fabrics. Thousands of years of developing textile technology cannot be replaced that easily that is why every new project is a small step to figure out solutions to make the 3D printed textiles a reality one day.

Many issues need to be addressed in order for 3D printing to become a reality. The digital cloth should resemble the traditional textiles as much as possible, which means it should be thin, soft, airy, flexible. [3]

The 3D printing of textile of flexible structures of knitted is still in its infancy. Researchers approached the creation of 3D fabric in various ways. However, all of them to combine the main aspects of real textiles - to develop of 3D printing textile product which are of flexibility and strength. [4]

In order to print 3D structures, a 3D CAD drawing is required. Authors often use the software Autodesk to generate a 3D model of the weft knitted structure [5] as is shown in the Figure 2.
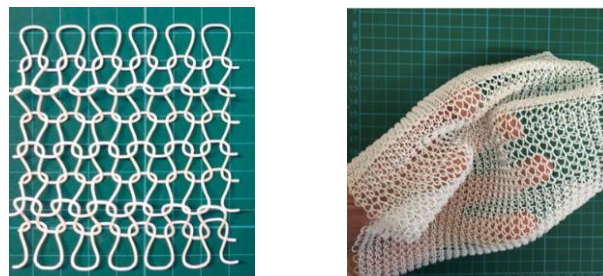
Fig. 2 Weft knitted structures printed form CAD [5]

In order to 3D print knit-based structures a 3D CAD drawing is required. This CAD drawing needs to consider the pipe wall thickness and distance between objects, par   ticularly when creating inter-looping structures such as knitting. [6]

Fabrics are also created using 3D printing. The open source program Google SketchUp is used for this project to design fabrics

with canvas weave. Warp and weft yarns are created as separate components that are grouped into a single model that can be exported to a * .stl file. [7]
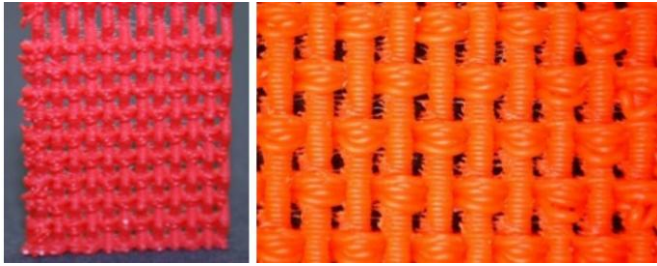
Fig. 3 *The weave fabric samples 3D print*

Fashion of the Future to be 3D Printed

The work [8] presented is part of a project to create garments using fused deposition modelling as 3D printing technology. Structures with various geometries are designed and tested with different materials starting from rigid to flexible. As a result, a fully 3D printed dress is created. Selecting this dress as a model, consumer acceptance for 3D printed garments is evaluated realizing an online survey containing 100 respondents. The data gathered show that respondents have knowledge of 3D printing, its advantages and the majority of them would accept wearing a 3D printed dress.

Recently, there have been many fashion designs printed on a 3D printer. Here are some photos of the products.

Fig. 4 *The clothes from 3D printing [1]*

3D printing on textiles or as clothing accessory

It is clear from the article authors [9], [10] work that the production of clothing accessories can also be an interesting area.

Fig. 5 *The clothing accessories from 3D printing [9], [10]*

3D printing of clamping device for ITC

The author [11] introduced the DefeXtiles technique, a fast and low-cost technique (FDM) that will make it possible to produce the tulle fabric used for made on the ironing pocket. The DefeXtiles thermal bonding ability allows users to extend existing clothing with a pocket. The pleated structure PLA pocket holds multiple items and is automatically retracted when these items are removed.

Fig. 6 *The pleated DefeXtile pocket [11]*

3. Conclusion

The topic of 3D printing is relevant for us in the Czech Republic also because the 3D printers we use in teaching are of Czech origin. The Company PRUSA, is celebrating its 10th anniversary this year. The establishment of a company can be compared to the American Dream. Let me mention part of the text from their website:

That was back in 2009 when Prusa built first 3D printer to make parts for my music controllers. He and his brother had a small workshop and they used to ship homemade 3D printer parts to enthusiasts all over the world, everything packed inside generic pizza boxes. Then, in May 2012, the Prusa Mendel i3 3D printer design came into existence. Prusa was flying around the world, giving talks at conferences about 3D printing but back home, in Prague, pretty much no one knew what 3D printing was.

4. References

[1] BREJCHOVÁ, Jana. Využití moderních technologií v oděvu. B.m., 2019. Technical University of Liberci. Fakulty of Textiles. Supervisor: Svatoslav Krotký.

[2] MAZZANTI, V, L. MALAGUTTI a F. MOLLICA. FDM 3D Printing of Polymers Containing Natural Fillers: A Review of their Mechanical Properties. Polymers [online]. 2019, 11(7), 1094. ISSN 2073-4360. Dostupné z: doi:10.3390/polym11071094

[3] KUNZOVÁ, N.. 3D Printed Fabric.. Masaryk University Faculty of Informatics 2020.

[4] MELNIKOVA, R, A EHRMANN a K FINSTERBUSCH. 3D printing of textile-based structures by Fused Deposition Modelling (FDM) with different polymer materials. IOP Conference Series: Materials Science and Engineering [online]. 2014, 62, 012018. ISSN 1757-8981, 1757-899X. Dostupné z: doi:10.1088/1757-899X/62/1/012018

[5] BEECROFT, M. 3D printing of weft knitted textile based structures by selective laser sintering of nylon powder. IOP Conference Series: Materials Science and Engineering [online]. 2016, 137, 012017. ISSN 1757-8981, 1757-899X. Dostupné z: doi:10.1088/1757-899X/137/1/012017

[6] BEECROFT, M.. Digital interlooping: 3D printing of weft-knitted textile-based tubular structures using selective laser sintering of nylon powder. International Journal of Fashion Design, Technology and Education [online]. 2019, 12(2), 218–224. ISSN 1754-3266, 1754-3274. Dostupné z: doi:10.1080/17543266.2019.1573269

[7] PARTSCH, L N, S VASSILIADIS a P PAPAGEORGAS. 3d Printed Textile Fabrics Structures. Inspire to Innovate. 2015, 8.

[8] SPAHIU, T, E. CANAJ a E. SHEHI. 3D printing for clothing production. Journal of Engineered Fibers and Fabrics [online]. 2020, 15, 155892502094821. ISSN 1558-9250, 1558-9250. Dostupné z: doi:10.1177/1558925020948216

[9]   SABANTINA, L, F KINZEL, A EHRMANN a K FINSTERBUSCH. Combining 3D printed forms with textile structures - mechanical and geometrical properties of multi-material systems. IOP Conference Series: Materials Science and Engineering [online]. 2015, 87, 012005. ISSN 1757-899X. Dostupné z: doi:10.1088/1757-899X/87/1/012005

[10]   VALTAS, A. a D. SUN. 3D Printing for Garments Production: An Exploratory Study. Journal of Fashion Technology & Textile Engineering [online]. 2016, 04(03) [vid. 2022-06-13]. ISSN 23299568. Dostupné z: doi:10.4172/2329-9568.1000139

[11]   FORMAN, J. a M. Doga DOGAN, Hamilton FORSYTHE a Hiroshi ISHII. DefeXtiles: 3D Printing Quasi-Woven Fabric via Under-Extrusion. In: UIST '20: The 33rd Annual ACM Symposium on User Interface Software and Technology: Proceedings of the 33rd Annual ACM Symposium on User Interface Software and Technology [online]. Virtual Event USA: ACM, 2020, s. 1222–1233 [vid. 2022-06-13]. ISBN 978-1-4503-7514-6. Dostupné z: doi:10.1145/3379337.3415876

A Fuzzy-AHP-VIKOR Approach to Evaluating Innovation Projects

Zeki Ayağ

Faculty of Ind. Eng. Kadir Has University, Istanbul, Turkey

zekia@khas.edu.tr

Abstract: *In this study, an intelligent approach is presented for the evaluation and selection of innovation projects. Selecting the best innovation project is a complicated multiple criteria decision making (MCDM) problem with several potentially competing quantitative and qualitative criteria. In this paper, two fuzzy MCDM methods; fuzzy Analytic Hierarchy Process (F-AHP) and fuzzy VIsekriterijumska optimizacija i KOmpromisno Resenje (F-VIKOR) are integrated to evaluate and rank innovation projects. In the fuzzy AHP-VIKOR, F-AHP is used to find fuzzy evaluation criteria weights and F-VIKOR is implemented to rank innovation project alternatives. A numerical example is given where five innovation projects are evaluated based on twelve criteria by three decision makers.*

Hybrid reinforced concrete with controlled volume deformations for hydrotechnical facilities

Valeriy Naidenov[1,], Ivan Rostovsky[2], Mirona Mironova[1]
Institute of Mechanics, Bulgarian Academy of Sciences, Sofia, Bulgaria[1]
University of Architecture, Civil Engineering and Geodesy, Sofia, Bulgaria[2]
Valna53@mail.bg

Abstract: The development of hydration processes in cement concrete is associated with the release of significant amounts of heat, which leads to a significant exothermic temperature increasing in the concrete body, especially valid for massive structures. This creates a temperature gradient from the inside of the array to the surface. The latter may be related to the development of unacceptable internal stresses, often leading to cracking, defects and reducing the durability of the facility. The report presents the individual stages of the search for an optimal technical solution for the construction of a specific hydro-technical facility - a massive hybrid reinforced trapezoidal wall of a water catchment gorge, in the area of Stara Zagora town. In the context of specified geometric dimensions of the facility, the specific features of the exothermic increase of the temperature in the concrete body as a function of the hydration processes are discussed. A reasonable choice of a specific type of cement is proposed in order to limit the amount of heat released - slag cement CEM III-A 42.5 N with a specific heat of hydration up to 280 J/g. A specific concrete mix design has been proposed, providing a balanced increase in temperature within acceptable limits, preventing cracking, in two possible scenarios - winter and summer outdoor temperature conditions. An additional advantage of the mix is the inclusion in the recipe of fiber-reinforcement and high-tech chemical admixtures - deep internal crystallization and shrinkage-compensating one. Specific calculation data for the kinetics of temperature increasing are presented, and the obtained values are critically evaluated in terms of guaranteed cracks eliminating in the structure.

Keywords: PORTLAND CEMENT CONCRETE, SLAG CEMENT HYDRATION PROCESSES, KINETICS OF EXOTHERMIC TEMPERATURE, CRACKING PREVENTION, CALCULATION TEMPERATURE INCREASING

1. Introduction

The development of hydration processes in cement concrete is associated with the release of significant amounts of heat, which leads to an increase in temperature in the concrete body, especially valid for massive structures. This creates a temperature gradient from the inside of the array to the surface. The latter may be related to the development of unacceptable internal stresses, often leading to cracking, defects and reducing the durability and long-life of the facility.

According to **ACI 116R-00**, the term "massive concrete" means "any volume of concrete of sufficient size that requires measures to be taken with regard to the heat of hydration of the cement and the volume changes of the concrete, in order to prevent the cracks formation" [1]. It is known that the physical-chemical interaction (hydration) between Portland cement and water takes place with the release of a certain amount of heat, which depends on the mineral composition of Portland cement clinker, the fineness of cement grinding, the presence of mineral additive, etc.

The hydration heat release Q (J/g) of the main clinker minerals of cement is shown in Table 1:

Table 1 *Heat of hydration of the main clinker minerals of cement*

Reaction	Heat release at full hydration Q, J/g			
	Pure components		Clinker (measured)	Cement (calculated)
	measured	calculated		
$C_3S \rightarrow$ C-S-H + CH	380	520	570	490
$C_2S \rightarrow$ C-S-H + CH	170	260	260	225
$C_3A \rightarrow C_4AH_{13} + C_3AH_8$	1160	-	-	-
$\rightarrow C_3AH_6$	900	880	840	-
$\rightarrow$ Etringite	1670	1670	-	-
$\rightarrow$ Monosulfo-aluminate	1150	1140	-	1170
$\rightarrow C_4AF \rightarrow C_3(A,F)H_6$	420	420	335	-
Monosulfoaluminate	-	-	-	380
Etringite	730	-	-	-

It is seen that the presence in the composition of the cement of an increased amount of alite (3CaO.SiO2) and, in particular, of tricalcium aluminate (3CaO.Al$_2$O$_3$), leads to increased heat releasing, and in the initial periods of hardening. Such behavior is typical for rapid hardening cements - **Type III** according to **ASTM C 150-11** [2], cement or type "R" and to **BDS EN 197-1: 2011** [3].

Cements with increased content of belite (β-2CaO.SiO$_2$) and celite (4CaO.Al$_2$O$_3$.Fe$_2$O$_3$) emit less heat during hydration. The latter is typical for low thermal cements - Type IV according to ASTM C 150-11 or ordinary low thermal cements according to BDS EN 197-1: 2011.

In Bulgaria, the production of low-thermal cement CEM II/B-P 32.5 N LH from the plant "Vulkan", Dimitrovgrad, is currently suspended for the moment.

Cement exothermic is of great practical importance. At low outdoor temperatures, the heat released favors the hydration processes and vice versa, with massive facilities, especially in summer, can lead to a problematic increase in temperature in the concrete section to and above 50^0C. In the event of a subsequent decrease in the ambient temperature, there is a risk of a significant difference between the temperature of the concrete inside the structure and that on its surface. The occurrence of a temperature gradient generates tensile stresses, especially in the surface layer of solid concrete. At the same time, the concrete inside the array tends to expand and is under the action of compressive stresses. Under certain conditions, this leads to cracking in the surface layer of concrete, reducing the load-bearing capacity, increasing the permeability and reducing the durability of the structure at all.
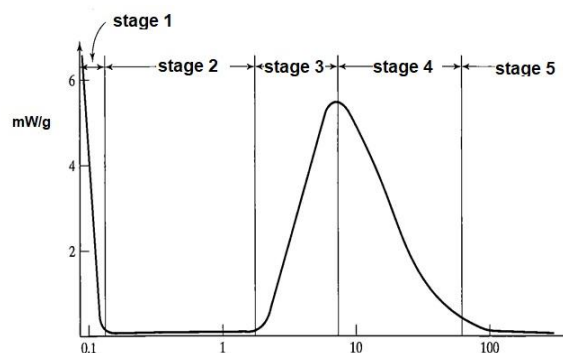
Fig.1 Time depending differential curve of heat release of concrete

It is known that the heat release of Portland cement is a staged process [4]. The first stage covers a time of 30-40 minutes after mixing the water with the cement and is characterized by intense heat release (especially in the initial 5-8 minutes), followed by a period of relative "calm". The second stage, also called induction,

covers the time of 1-3 hours from the contact of the cement with the mixing water. Its duration depends mainly on the mineral composition of the cement, the fineness of grinding and the amount of gypsum (bonding regulator). The third stage, which is mainly due to the hydration of the alite, takes a time interval of 3-8 h from the homogenization of cement and water (initial setting of cement) and is characterized by increasing heat release within 5-10 h. Usually the maximum heat coincides with the end of setting time of cement. Then the intensity of the processes decreases (stage 4) and reaches a stable state (stage 5) - Figures 1 and 2.
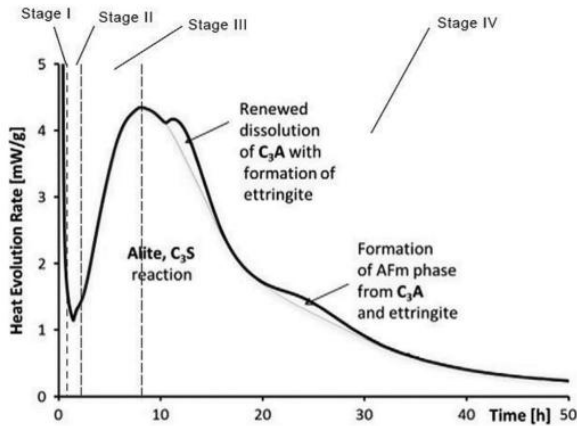
Fig. 2 Typical calorimetry plot of ordinary Portland cement showing different stages in hydration process [4]

It is well known that mineral admixtures, in proportion to the amount, used in the composition of cement, help to reduce the heat of hydration. As for chemical admixtures for concrete and mortars, they generally do not change the amount of heat released, but can significantly affect the intensity of heat release and its change in the initial setting time. A clear peak of heat release, respectively retarders cause the opposite effect - a smoother change in exotherm, delayed in time.

2. Concrete heat release stresses and deformations

In no standard document related to the concrete and reinforced concrete structures static calculation, even in the latest editions of **ACI 318-11** [5], **fib Bulletin 55 and 56** [6] and **EN 1992 Eurocode 2** [7], does not address the issue of thermal impact derived from the heat of hydration of cement.

An approximate empirical methodology for calculating the increase in temperature in concrete ground slabs due to the heat release of cement is included in **ACI 207.4R-93** [8].

With such a focus are many scientific studies related to prediction of the thermal stress of massive concrete structures, as a result of which specific methods for on-site monitoring have already been developed [9,10]. The obtained experimental results for the development of the temperature in the concrete section, compared with those of the existing empirical dependences, allow to increase the reliability of the predictions. And this works in the direction of increasing the security, serviceability and durability of the facilities.

3. Concrete facility data

Two main cases of authoritative fragments of the facility are considered (Fig. 3), technologically performed separately from each other on different concreting strokes:
- reinforced concrete step with approximate dimensions length 10 m; width 3,0 m; height 1,0 m;
- trapezoidal reinforced concrete body approximately 9,5 m long; width 2,0 to 0,50 m; height 4,0 m.

4. Prescribed concrete mix design

From a design point of view, the design compressive strength class of concrete can vary from relatively low levels.

Relevant in this case are the achievement of the requirements to it, caused by the operating environment (environmental impact factors within the meaning of the requirements of **BDS EN 206: 2013 +2016 [10]**, and **BDS EN 206: 2017 / NA National Annex** [11] - see **NA 5.3 and NA.F.1a** Limit values for concrete composition and properties.
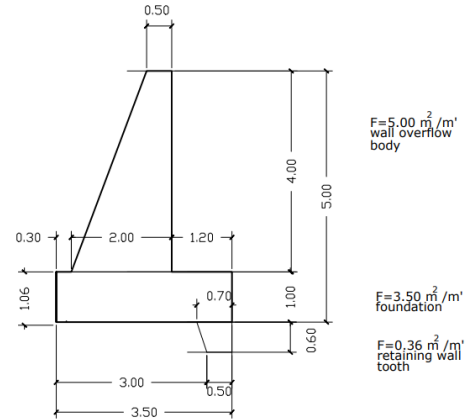
Fig. 3 Facility cross section - geometric dimensions

In this case, the limiting requirement is the resistance of the concrete to cyclic freeze-thaw without the presence of anti-icing agent (XF 3) and cyclic wetting and drying (XC 4) – in accordance of **Table 1 Impact classes** [11].

Simultaneous satisfaction of the above requirements imposes the following limits on the composition of concrete:
- minimum compressive strength class C30/37;
- cement content - min 320 kg/m³;
- maximum water-cement ratio 0,50.

In order to limit the amount of heat released, slag cement CEM III-A 42.5 N (heat of hydration 280 J/g) was chosen for the production of concrete, which is produced in our country by the cement plants in Devnya. The other types of cements available on our market have a heat of hydration of about 400 and 440 J/g, which makes them unacceptable in this case.

Table 2 Prescribed concrete mix design

Components	Quantity, kg/m³
Cement CEM III- A 42,5 N, LH	360
River sand, fraction 0-4 mm	840
Crashed stone – dolomitized limestone or similar, two fractions - 4/11,2 mm and 11,2/22,4 mm	990
Internal crystallization admixture with permanent action **KRYSTALINE Add1**	1,00
Shrinkage compensating admixture **KEPTONITE**	15,00
High range water reducing admixture (HRWRA) – Polycarboxylate Ether (PCE)	2,0
Mixing water	≈170

In this case, it is appropriate to apply an innovative approach to the composition of concrete with the inclusion of highly effective deep-crystallizing and shrinkage-compensating chemical admixtures of the latest generation. The latter provide a number of technical advantages - complete permanent impermeability of the concrete section, high physical and mechanical properties, increased frost resistance in cyclic freeze-thaw conditions, elimination of drying shrinkage of concrete and complete crack resistance.

Trying to ensure the best quality performance of the concrete mix design an innovation approach is proposed by additionally inclusion of a deep-crystallizing internal chemical admixture KRYSTALINE Add1 HD with permanent action in time, capable of compacting additionally formed concrete structure, ensuring the impermeability of the built protective section and shrinkage compensating admixture KEPTONITE [12, 13, 14].

It preliminary is assumed that the two parts of the wall will be casted separately, and the period between concreting will be more than one week, so as not to coincide with the peaks of heat release.

5. Calculation temperature increase in concrete

ACI 207.4R-05 presents a simplified method for calculating the maximum temperature rising of concrete in ground-based slabs. In this case, the software "Concrete works" V.2, developed by the University of Austin, Texas, USA, is used.

For the foundation slab respective initial conditions are specified:
- Air temperatures - during the day 22-25^{0}C; at night 14-16^{0}C;
- Temperature of the fresh concrete during casting - about 20^{0}C;
- Start of application - about 10 hours before noon.

Respective calculating results are presented in Figures 3-7.

It is visible that the maximal temperature difference within the foundation + 16^{0}C and maximal temperature of concrete + 36^{0}C.
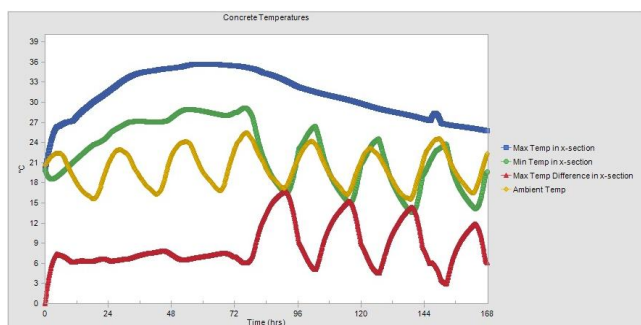
Fig. 3 Change in ambient temperature, minimum element temperature, maximum temperature and temperature difference
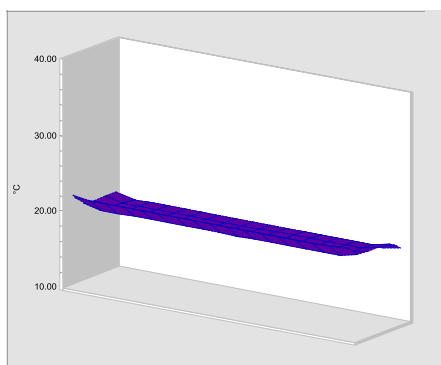
Fig. 4 Temperature in the concrete massive at casting stage
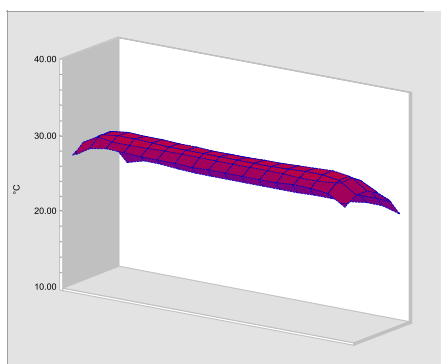
Fig. 5 Temperature in the concrete massive at 24 hours after casting
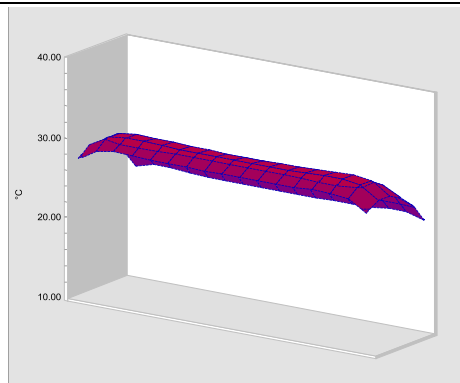
Fig. 6 Temperature in the concrete massive at 48 hours after casting
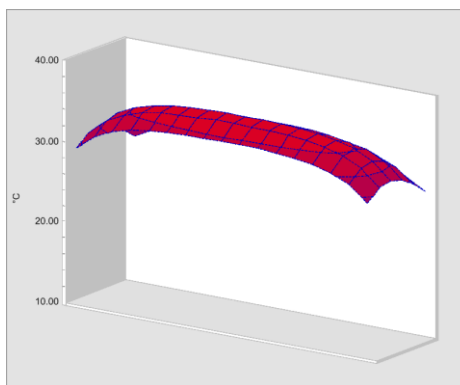
Fig. 7 Temperature in the concrete massive at 72 hours after casting

Concerning the wall body of the facility the same respective initial conditions are specified:

- Air temperatures - during the day 22-25^{0}C; at night 14-16^{0}C;
- Temperature of the fresh concrete during casting - about 20^{0}C;
- Start of application - about 10 hours before noon.

Respective calculating results are presented in Figures 8-12.
It is visible that the maximal temperature difference within the foundation + 19^{0}C and maximal temperature of concrete + 39^{0}C.
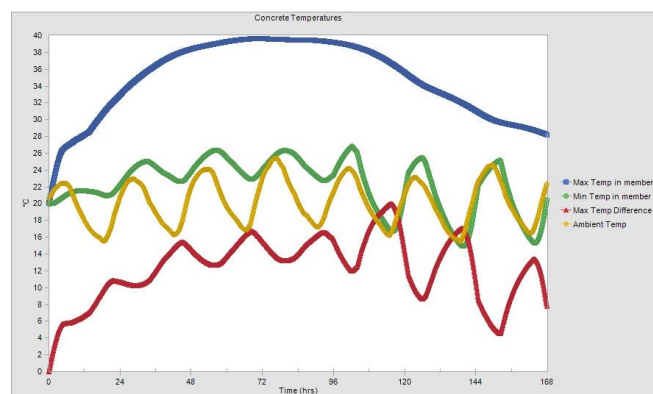
Fig. 8 Change in ambient temperature, minimum element temperature, maximum temperature and temperature difference

Acknowledgments
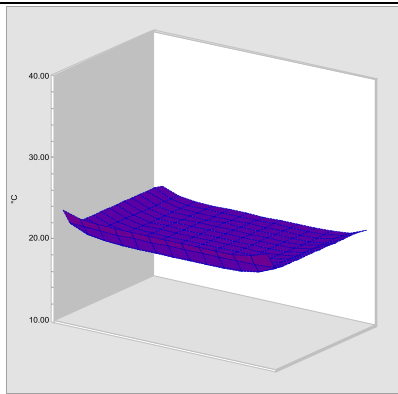
Fig. 9 Temperature in the concrete massive at casting stage
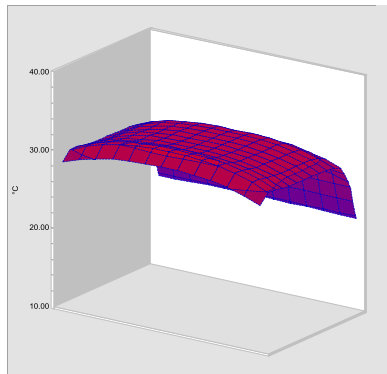
Fig. 10 Temperature in the concrete massive at 24 hours after casting
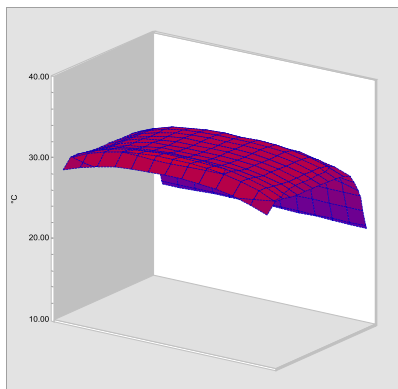
Fig. 11 Temperature in the concrete massive at 48 hours casting
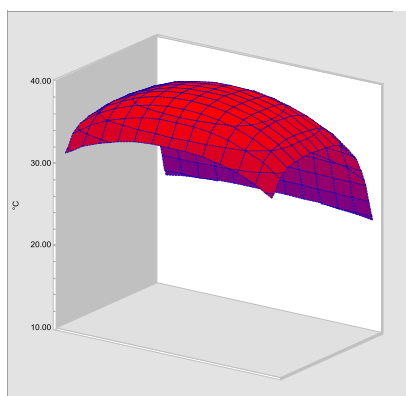
Fig. 12 Temperature in the concrete massive at 72 hours after casting

6. Conclusion

The analysis of the problem related to rising temperatures in the cross section of massive concrete and reinforced concrete structures due to active hydration processes in the cement shows opportunities for the development of additional stresses, often leading to unregulated cracking with potential to compromise durability of the facility under construction.

As a result of the proposed prescribed concrete mix design for the specific facility, the temperature difference in the concrete body is expected to be within acceptable limits - up to 20-25^{0}C, which does not pose a risk of compromising the facility during operation.

References

1. American Concrete Institute Report ACI 116R-00 Cement and Concrete Terminology
2. ASTM C 150-11 Standard Specification for Portland Cement
3. BDS EN 197-1: 2011 Cement. Part 1: Composition, requirements and conformity criteria for ordinary cements.
4. Scrivener, K. L.; Juilland, P. and Monteiro, P. J. M., "Advances in Understanding Hydration of Portland Cement," Cement and Concrete Research, V. 78, Part A, 2015, pp. 38-56.
5. ACI 318-11 Building Code Requirements for Structural Concrete and Commentary.
6. fib Bulletin 55 and 56: Model Code 2010, First complete draft - Volume 1 and 2.
7. EN 1992 Eurocode 2: Design of concrete and reinforced concrete structures. Part 1-1 General rules and rules for buildings.
8. ACI 207.4R-93 Cooling and Insulating Systems for Mass Concrete.
9. Sagam Y., M. Faytaouni, K. Riding, K. Wang, Ch. Jahrem, J. Shen, Predicting thermal performance of a mass concrete foundation – a field monitoring case study, Case Studies in Construction Materials, Vol. 11, Dec. 2019, https://doi.org/10.1016/j.cscm.2019.e.00289
10. BDS EN 206: 2013 +2016 Concrete. Specification, properties, production and compliance.
11. BDS EN 206: 2017 / NA National Annex.
12. Naidenov V., M. Mironova, Ivan A. Rostovsky, Investigation on the efficiency of internal crystallization chemical admixtures for cement concrete - mechanical characteristics, Materials, Methods & Technologies ISSN 1314-7269, Volume 14, 2020 (25-31)
13. Naidenov V., M. Mironova, Investigation on the efficiency of internal crystallization chemical admixtures for cement concrete – structural characteristics, International Scientific Journal **"Machines. Technologies. Materials"**, Issue 3/2020, Year XIV, ISSN PRINT 1313-30226, ISSN WEB 1314-507X (114-128).
14. Naidenov V., M. Mironova, Opportunities for drying shrinkage minimizing in fiber-reinforced concrete overlays for repairing of corroded industrial structures, Materials, Methods & Technologies ISSN 1314-7269, Volume 14, 2020 (32-40).

Innovative method for repair of reinforced concrete water facilities by "wet" shotcreting

Valeriy Naidenov[1], Mirona Mironova[1]

Institute of Mechanics, Bulgarian Academy of Sciences, Sofia, Bulgaria[1]

Valna53@mail.bg

Abstract: The report presents the different stages of development and implementation of two similar innovative technical solutions for repair and restoration of defected reinforced-concrete constructions of existing swimming pool and artificial lake using the methods of "wet" shotcreting. In the first case, the object of renovation is a seriously defected outdoor mineral pool of a prestigious hotel in the town of Hissarya. Given the significant leaks of water from the pool in the surrounding area over the years, a specialized technical inspection was initially conducted to determine the causes of defects in the main load-bearing monolithic steel-reinforced concrete construction - walls and bottom slab. An innovative technical solution has been proposed to restore the operational suitability of the pool, based on the possibility of using the existing load-bearing structure as external formwork for a new built-in load-bearing structure of the facility. The proposed solution envisages jointless thickening of the existing walls through additional reinforcement and concrete laying of new high-tech sprayed concrete. The bottom of the pool is being renovated by additional new layer of a hybrid fiber-reinforced jointless concrete slab and machine power-floated of the finishing surface. A composition of high-tech concrete with the participation of an internal crystallization chemical admixture and shrinkage-compensating one is proposed. A similar solution has been applied for the repair and restoration of the walls and bottom of an artificial lake in West Park, Sofia. Implementation of the project creates a unique art vision of the lake, the rock garden and the surrounding park space. This pilot implementation creates objective preconditions for expanding the range of innovative concrete structural systems, which, in addition to specific functions, are also applicable as opportunities for aestheticizing the urban and park environment.

Keywords: WATER FACILITIES, HYBRID FIBER-REINFORCED CONCRETE, INTERNAL CRYSTALLIZATION CHEMICAL ADMIXTURE AND SHRINKAGE-COMPENSATING ADMIXTURE, CONCRETE JOINT-FREE SLAB, SHOTCRETING

1. Introduction

It is well-known that shotcreting is a special building technology patented in 1911 by Dr. Carl Akeley, curator at the Field Columbian Museum in Chicago. The system enables one to deposit a cement-sand mix or concrete on various surfaces via high pressure and without shuttering (forming) using a special equipment- a shotcreting machine and air compressor. In fact, this is a method of conveying concrete or mortar through a hose and pneumatically projecting it at high velocity onto a surface without additional compaction. This predetermines a number of essential advantages - high density and strength, low permeability (high water impermeability), high corrosion resistance, minimized shrinkage etc.

Two basic methods of shotcreting exist – "dry" and "wet" method.

A mix with cement and added sand, fraction (0-4 mm), prepared "dry" and deposited on a surface is known as "dry" shotcrete while that with aggregate fraction up to 20 mm - as "dry" sprayed concrete. Water is separately supplied through another hose.

The system for "wet" shotcreting employs special machines and supposes deposition of a specific concrete "wet" mix design. Its preparation is centralized at concrete batching plant and its consistency is précised (the usual water/cement ratio is below 0,45). Wet" shotcreting is based on work with certified concrete mixes, being "intentionally" designed and industrially prepared. Their optimization is flexible to meet the specific technical requirements and conditions of exploitation. A potential of multi-factor optimization of the mix composition also exists. It consists in the variability of selection of cement, aggregates, special chemical admixture with high-range water reduction effect, special in-depth crystallizers and polymer modifiers, fiber-reinforcement consisting of various types of fibers etc. The basic advantages of the method are its increased productivity, possibilities of a single-stage deposition of a thick layer, minimal operational subjectivity and increased ecology-friendliness of mix homogenization and deposition. A disadvantage of the method is the impossibility of its application if there is no certified concrete plant nearby.

Summarizing all advantages and possible specific building applications of "wet" shotcreting it could be concluded that new innovative methods for repair of damaged reinforced concrete water facilities (as swimming and spa-pools, artificial lakes etc.) by "wet" shotcreting is very attractive one [1].

It should be preliminary added that most of these types of reinforced-concrete structures are with special geometrical shapes - oval, elliptical, variable sizes in plan and height. That's the reason to estimate all conventional formworks available as unappropriated for using ones. Logically observe, in such specific cases, damage repairing by shotcreting is should be estimated as most preferable one.

In this connection below are discussed two specific innovative technical solutions for repairing works in such facilities - spa outdoor swimming pool in a prestigious hotel in Hissarya, and an artificial lake in West Park in Sofia.

2. Spa-outdoor swimming pool

2.1. Pool characteristics

The pool complex was designed and built in 2003 and contain 3 closely connected areas located in different design levels – main pool, children pool and water bar. Total area of the pool is around 1500 m^2 - (Photos 1 and 2). Main load-bearing structure is monolithic reinforced concrete - walls and bottom slab with plumbing channels located in it. From the provided reinforcement plans it is seen that the steel reinforcement for the bottom slab and walls of the pool should be double (Ø12 every 15 cm in both directions). The designed concrete is intended to have a compressive strength class C12/15 (water tightness 0,4). The thickness of the walls and bottom of the pool is 20 cm.

During the nearly 20 years of operation in the construction of the pool, many defects were observed (mainly visible structural cracks and damage to the ceramic cladding on the walls and bottom slab), which led to abundant water leakage and flooding of the surrounding area.

In order to establish the causes of such defects, a detailed constructive inspection was initially carried out.

In the scope of the constructive survey performed are included:

- Study of the available technical documentation;
- Technical inspection on site, verification of the geometry according to the provided geodesy survey, establishment of dimensions of characteristic sections of the structural elements, establishment of local defects;
- Cracks width measuring – Photos 3 and 4;
- Determining the compressive strength of concrete by testing test specimens (cores) cut from the structure of the site and checking their compliance with standard requirements – Photos 5, 6 and 8;
- Determining the degree of carbonization of existing concrete – **Photo 7**;
- Establishing the type and technical parameters of existing steel reinforcement by direct scanning – Photos 9 and 10.

All tests are performed in accordance of actual national BG and EN standards.

Photo 1 Pool general view

Photo 2 Pool general view from above

Photo 3 Crack width measuring

Photo 4 Crack width measuring

Photo 5 Core cutting

Photo 6 Bottom slab core №3 with length 25 cm (lower steel reinforcement Ø8 cm, located at 17 cm from the upper edge of the bottom, only)

Photo 7 Zero concrete carbonation established by colorization method

Photo 8 Concrete compressive test

Photo 9 Direct scanning existing steel reinforcement

Photo 10 Direct scanning existing steel reinforcement - visualization

The most of obtained objective results from the implementation of the planned specialized measures within the framework of the constructive inspection for the condition of the bearing steel-reinforced concrete construction of the facility can be summarized as follows:

- The experimentally determined compressive strength class of the executed concrete for the walls and bottom slab is C30/37, exceeding the design one (C12/15);
- It was found zero carbonization in the cross section, which means that the steel reinforcement is reliably protected against corrosion;
- The design details for the implementation of the bottom slab are not performed correctly, both in terms of design thickness and in terms of the method of reinforcement - the waterproofing of the "lower edge" elevation provided in the project is missing, design thickness of 20 cm has not been observed (there are thicknesses between 7 and 27 cm), only the lower steel reinforcement of Ø8 in 20 cm is made, instead of the designed double one of Ø12 in 15 cm;
- The design details for the construction of the walls of the pool have not been fulfilled, too - Instead of two rows steel reinforcement with Ø12 in every 15 cm, two rows Ø8 in every 20 cm are made, the project lacks a connection detail (with watertightness provided) between the individual stage of the walls casting.

Summarizing all mention above, these are the main reasons for the defects and damages found during the operation of the facility.

2.2. Technical solution for repairing

Taking into account all structural and technological consideration, plus the results and conclusions from the structural investigation performed, innovative technical solution for repairing works is proposed - Fig. 1 and 2:

Fig. 1 Principal cross-section

Fig. 2 Cross-section steel-reinforcement

- **NEW WALLS - thickness 10 cm, reinforced with N8/10 mesh made of B500 steel (doweled in the existing walls), executed by on the existing walls without removing the existing finish. One-stage execution without any joints.**

Concrete requirements: High-tech fine-grained (D_{max} 8 mm) fiber-reinforced waterproof sprayed concrete with compressive strength class C35/45, micro-polypropylene fiber-branched 12/18 mm (dosage rate 1,00 kg/m^3), 4G-internal crystallization chemical admixture KRYSTALINE Add1 (dosage rate 1,0 kg/m^3), shrinkage compensating admixture KEPTONITE (dosage rate 15,00 kg/m^3), high-range water reducing agent, with additionally resistance to aggressive environmental factors XC3, XF3, XD2 and consistency class S2 with water-cement ratio below 0,45.

- **NEW BOTTOM SLAB - thickness 22 cm, reinforced with N8/10 lower mesh made of B500 steel, executed on the existing bottom slab without removing the existing finish. One-stage execution by power floating machines without any joints.**

Concrete requirements: High-tech ordinary-grained (D_{max} 22,4 mm) fiber-reinforced waterproof pumpable concrete with compressive strength class C35/45, micro-polypropylene fiber-branched 12/18 mm (dosage rate 1,00 kg/m^3), steel firbres HE 0,75x35 mm (dosage rate 25,00 kg/m^3), 4G-internal crystallization chemical admixture KRYSTALINE Add1 (dosage rate 1,0 kg/ m^3), shrinkage compensating admixture KEPTONITE (dosage rate 15,00 kg/m^3), high-range water reducing agent, additionally with resistance to aggressive environmental factors XC3, XF3, XD2 and consistency class S3 with water-cement ratio below 0,45.

The main principle of the proposed technical solution is the requirement that the repair work on the walls and bottom slab to be carried out in one technological cycle (stage), without any joints. In this way the best adhesion connection between the walls and the bottom is achieved and the watertightness of the facility is ensured. In such a direction is the need to install in detail and water-swellable tape in the contact zone between the bottom and the bottom. The security of the proposed jointless solution is based on the specific action of the included special chemical admixtures [2,3] and the method of hybrid reinforcement - a combination of conventional steel reinforcement and disperse reinforcement, including different types of fibers.

2.3. Execution of the solution

All designed structural repairing works are executed in one-stage in the of February, 2022. Fresh concrete is produced in the new equipped respective batching plant ECOMIX in accordance of specially prepared concrete mix design.

Photo 11 ECOMIX concrete batching plant

Photo 12 Walls and bottom slab steel mesh fixing

The concrete casting sequences fully complied to the planned one – at first all walls shotcreting works are finished and after them the bottom slab casting was started.

Shotcreting is performed by using 2 specialized machines and compressors, working in parallel - Photos 11-14. After that bottom slab concreting was started by using additional stationary concrete pump. The finishing works were based on special power floating machines.

Photo 13 Concrete pumps used

Photo 14 Piping for concrete horizontal transport

Photo 15 Walls shotcreting

Photo 16 Walls shotcreting

Photo 17 Botom slab concrete casting

Photo 18 View of finished concrete works

Approximately 250 m^3 innovative sprayed and conventional concrete were casted, as the entire structural repairing works are completed and finished in range of 18 hours. After respective concrete curing measures additional polymer-finishing works will be in progress. Dead line of all repairing works is the end of April, 2022.

3. Artificial lake

In pursuance of the investment program of the SOFIA CITY MUNICIPALITY, in the period 2019-2021 a complete renovation of "West Park", the second largest park in Sofia, was in progress, including emblematic for the city parts of it - the artificial lake and rock garden.

We proposed an innovative technical solution for the execution of concrete works on walls and bottom slab by using high-tech hybrid fiber-reinforced sprayed concrete according to a specially developed recipe of a multifunctional capillary crystallization system for permanent autogenous waterproofing of concrete, based on the use of a deep crystallizing chemical additive KRYSTALINE Add 1 (dosage rate 1,0 kg/m^3 concrete) - Fig. 3.

One stage of concrete slab and walls spraying in participation of KRYSTALINE Add 1 and special admixture KEPTONITE (dosage rate 15,00 kg/m^3) for full range shrinkage controlling, leads to form completely joint-free water-tight structural system. This innovation makes it possible to eliminate the need for all additional waterproofing works.

The implementation was carried out in the autumn of 2020 by TORCREET EXPERT Ltd. in a continuous production process for 20 hours with parallel use 3 teams with three sets of mechanization - modern shotcrete machines and technological kits to them, pipelines and spray nozzles.

After two weeks of curing the sprayed concrete, in accordance with the developed architectural and landscape project, the

installation of the lining of part of the lake walls with natural stone (granite), laid and adhered to the executed sprayed concrete using high quality polymer-modified silicate binder material.

After nearly a year of trouble-free operation, the overall implementation of the project creates a unique art vision of the lake, rock garden and the surrounding park area.

Cladding of decorative stones
Jointless flooring from hybrid disperse-reinforced innovative sprayed concrete with compressive strength class C35/45, with internal crystallization additive KRYSTALINE Add1 (1kg/m3) and a shrinkage compensating agent KEPTONITE (15kg/m3)
Electro welded reinforcing mesh N10 with apertures 20/20 cm
Soil nails for anchoring the reinforcing mesh to an existing compacted ground base
Compacted ground base of the lake Eo>=30MPa

min.20см

10-12

Exemplary water level

10-12

20   Existing concrete slab

Existing ground base of the lake

Fig. 3 Cross-section detail

This pilot implementation creates objective preconditions for expanding the range of innovative structural systems, which, in addition to specific structural functions, are also applicable as opportunities for aestheticizing the urban and park environment.

Photo 19 Deployment of two concrete pumps for simultaneous operation

Photo 20 Wall spraying

Photo 21 Wall spraying

Photo 22 Finished area – walls and bottom slab

Photo 23 Final art vision with natural rocks lining

Photo 24 Final art vision with natural rocks lining

4. Conclusions

In summary of the above, it can be argued that the use of high-tech hybrid reinforced sprayed "wet" concrete for the construction and repair of water facilities is an innovative approach with certain advantages. The inclusion in the concrete mix design high-performance special chemical internal-crystallization chemical admixtures improve the watertightness of the cross-section with additional benefits for self-heling of cracking. Additionally proposed shrinkage compensating admixture allows to design and execute some join-free surface concrete structures (walls and bottom slabs), without organization of different types of joints – daily, cold and saw cut etc.

The proposed and successfully implemented innovative technical solutions for specific water facilities are a good prerequisite for successful expansion of the scope of this approach, which increases the efficiency of the performed repair works and shortens the construction period.

Acknowledgments

References

1.   Morgan D., Shotcrete – Materials, Performance and use. Modern concrete technology 22, CRC Press, Taylor & Francis Group LLC, 2022.
2.   Bernard J., Shotcrete supply: Dry or Wet? Shotcrete Magazine, Spring 2006.
3.   Naidenov V., M. Mironova, I. Rostovsky, Investigation on the efficiency of internal crystallization chemical admixtures for cement concrete - mechanical characteristics, Materials, Methods & Technologies ISSN 1314-7269, Volume 14, 2020 (25-31)
4.   Naidenov V., M. Mironova, Investigation on the efficiency of internal crystallization chemical admixtures for cement concrete – structural characteristics, International Scientific Journal "MACHINES. TECHNOLOGIES MATERIALS", Issue 3/2020, Year XIV, ISSN PRINT 1313-30226, ISSN WEB 1314-507X (114-128).

Effect of Overlay Paper Properties on the Surface Quality of Laminate Flooring

Mehmet Erdal Kara[1], Nadir Ayrilmis[2], Arman Uncu[1]

[1]Kastamonu Entegre Ağaç Sanayi ve Ticaret A.Ş., Kastamonu Organize Sanayi Bölgesi 7. Cad. No:2/8 37200 Halife Köyü/Kastamonu/Türkiye

[2]Department of Wood Mechanics and Technology, Forestry Faculty, Istanbul University-Cerrahpasa, Bahcekoy, Sariyer, 34473, Istanbul, Turkey

erdal.kara@keas.com.tr

Abstract: *In this study, the effect of overlay paper properties on the surface quality of laminate flooring was investigated. For this aim, only the upper surface of 22 gr/m² raw overlay papers impregnated with 53% melamine formaldehyde resin in the glue pool was sprinkled by corundum (Al_2O_3) in two different ratios (23 and 28 gr/m²) from different companies at 140-160 °C. In the drying ovens, the impregnated overlay papers with a final weight of 135 and 140 gr/m² and a humidity of 7.5% were produced. The panels obtained at the end of these processes were tested according to TS-EN 14323 and related standards, which are surface quality features such as surface abrasion, surface scratch and ash test. According to the test results, it has been observed that under the same pressing conditions, different corundum type and amount as well as laminate floorings covered with overlay papers with different final weights have an effect on the surface quality properties. It was observed that although the increase in the amount of corundum did not have a significant effect on surface scratching, it had a significant effect on surface wear values. According to the results of the ash test, it was observed that the amount of corundum increased and its distribution on the overlay paper surface was homogeneous.*
KEYWORDS: OVERLAY, SURFACE QUALİTY, LAMINATE FLOORING, FIBERBOARD, CORUNDUM

1. Introduction

The laminate flooring is an engineered wood composite consisting of three layers. The base layer is an impermeable layer, which improves the structural stability. The thick and core layer is a composite wood base [1,2[. The highest layer is the wear surface (overlay layer) and the decorative layer (Fig. 1).
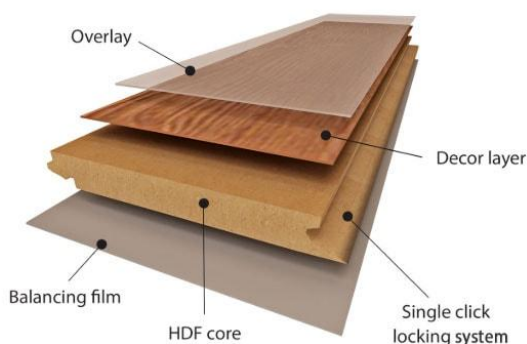
Figure 1. Layers of laminate flooring.

Decor paper is a special high-quality paper that is bonded to suitable substrates such as wood based panels using special synthetic resins. Papers impregnated with a resin have gained wide acceptance as facing materials for industrial gradeparticleboard. The base papers for the decorative films are alpha-cellulose papers, which are used exclusively. Forimpregnating, papers must have a high moisture resistance and the right porosity to accept the proper amount of resin. The surface print quality of the decor paper is essential for creating decorative designs by use of gravure printing process. Moreover, the paper shall be suitable for impregnation with applicable synthetic resins such as urea formaldehyde, melamineformaldehyde, acrylic and phenolic resins. The type of resin used for impregnation of decor paper influences the quality ofsubstrate after the lamination. It is laminated under high pressure and heat with particleboard or other substrates. Quality ofcauls, cleanliness, and temperature are key factors that influence coating or laminating quality [3].

In this study, the effect of overlay paper properties on the surface quality of laminate flooring was investigated. For this purpose, overlay papers were produced by using corundum types from different companies in different weights (25-30 gr/m²) in the corundum pouring system only on the upper surface after the overlay papers were glued. It is aimed to obtain products that comply with AC3-AC4-AC5 criteria according to the surface quality class by comparing the test results made on laminate flooring test boards obtained by pressing decor paper under the same pressing conditions.

2. Materials and methods
2.1. Materials

In the production of HDFs, 50% pine (*Pinus nigra*) and 50% eastern beech (*Fagus orientalis*) woods used as raw materials in the production of high density fiberboards (HDFs). The HDF panels were produced from wood fibers dried to 5% and 9 wt% melamine urea formaldehyde (MUF, solids content 60 wt%) resin.

The HDF panels with dimensions of 8 mm x 2060 mm x 2650 mm and a density of 870 kg/m³ were produced at a press temperature of 200±20 °C, and a pressure of 3.5-4 N/mm². After conditioning for about 4-7 days depending on the season in the semi-finished warehouse, it was sanded to a net thickness of 7.3 mm ±0.1 raw thickness.

Two different ratios (80-85 gr/m²) of 100% melamine formaldehyde resin were impregnated on the lower and upper surfaces of these papers. Then, impregnated overlay papers with a final weight of 135 and 140 gr/m² in drying ovens at 100-160 °C by sprinkling corundum material Al_2O_3 in two different ratios (23-28 gr/m²) only on the upper surface, which improves the upper surface properties of laminate flooring. Produced.

Corundum (Al_2O_3): There are two types of alumina: α-type and γ-type. Naturally occurring α-alumina crystals are called corundum and are often found in different colors (usually blue or yellow to gray).

2.2. Methods

The test methods used in the investigation of surface properties of the overlay paper are givne in Table 1.

Table 1. Test methods used in the experiments.

Tests	Specimen size (mm)	Standard no	Specimen number
Surface abrasion	100x100	TS EN 13329	8
Scratch resistance	100x100	TS EN 14323	8
Ash quantatity	100x100		6

The equipments used in the determination of the surface properties are presented in Figure 2.

A.   B.

Figure 2. A. Surface abrasion test. B. Surface scratch test.

3. *Results and discussion*

The average values of the test results, in which the effect of overlay paper properties on the abrasion resistance of the surface quality properties of laminate flooring are given in Figure 1. The highest abrasion resistance values were seen in overlay papers produced with 28 gr/m² brand B corundum and 140 gr/m² final weight at 5000 rpm. The lowest abrasion resistance values were found in the overlay papers produced with 23 gr/m² brand A corundum and 140 g/m² weight at 4000 rpm. (Fig. 3).
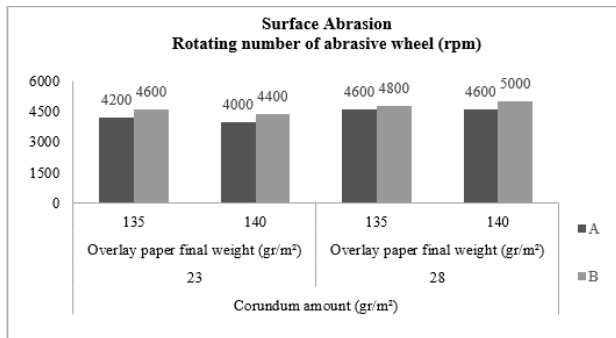
Figure 3. Abrasion resistance of the overlay paper

The highest scratch resistance values were seen in overlay papers produced with brand B corundum with a final weight of 140 gr/m² with 4 N. was determined that the test panels produced with brand B corundum at similar rates had higher scratch values than the test samples produced with brand A corundum.
From the test results, it was understood that the color of the decor paper was different, the amount of glue, the final weight of the finished paper and the increase of the corundum ratio did not have an obvious effect on the surface scratch values.

According to these results, it is recommended that lower rates of corundum material can be used for the surface scratch values of overlay papers to be produced for AC3 and AC4 classes. The average values of the test results, in which the effect of overlay paper properties on the ash-burning test. As a result of the combustion test of overlay paper samples produced at the same corundum ratios, it was seen that brand B corundum was higher in % compared to brand A corundum, according to the remaining solid matter/ash amount.

In general, the wear resistance of overlays produced with brand B corundum was found to be better at the same corundum usage rates, while the opposite was the case with brand A corundum. According to these results, it was determined that in the overlay papers to be produced for AC3 and AC4 classes, it was possible to produce more economical overlay paper, especially with brand B corundum at lower rates (20gr/m²).

The average values of the test results in which the effect of overlay paper properties on surface scratching from the surface quality properties of laminate flooring are determined are displayed in Figure 4. This situation can be explained as the structure, shape, size, powder ratio and the rate of containing other elements of brand B corundum according to brand A corundum, having the desired properties and values. In this way, it has been understood that the bonding and distribution with the surface is more homogeneous during the sprinkling of brand B corundum on the overlay paper surface.
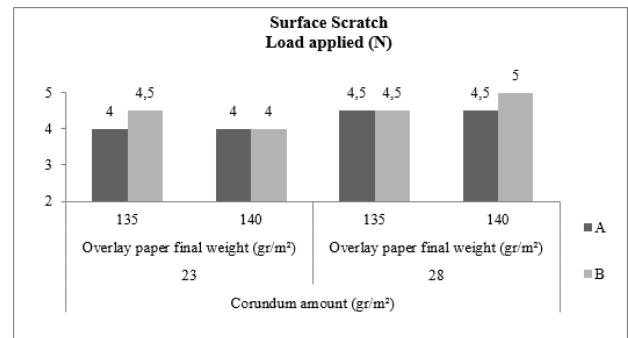
Figure 4. Scratch resistance of the overlay

In general, as the usage rate-amount increased in both corundum species, an irregular increase was observed in the amount of corundum material remaining after the ash test (burning test), albeit irregularly. It has been observed that this situation reflects the working set values of the corundum pouring system to the overlay paper surface (Fig. 5).
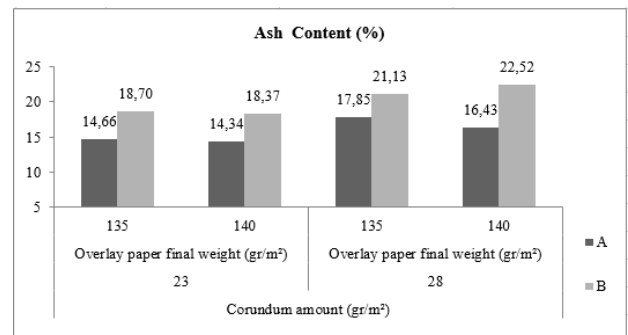
Figure 5. Ash content of the overlay paper.

The test result showed the highest amount of ash with 22.52%, 28 gr/m² brand B corundum and overlay papers produced with 140 gr/m² final weight. The lowest ash percentage was found with 14,34% in the overlay papers produced with 23 gr/m² brand A corundum and 140 gr/m² final weight.

4. Conclusions

Depending on the different pressing conditions, it has been determined from the test results of the produced coated boards that the surface wear and scratch values increase as the amount of the corundum and therefore the final weight of the overlay paper increases in the same pressing time.

In addition, from the ash test results, it was observed that the amount of ash as a result of combustion increased as the amount of B brand corundum increased. This can be explained by the more homogeneous and strong bonding of the corundum on the overlay surface. The surface quality of laminate flooring is a feature that can vary depending on the type, amount and weight of corundum as well as the surface quality of the board. For this. According to the surface wear, surface scratch and ash test results of the surface quality properties of the laminate flooring; It was determined that the best values were obtained as a result of using brand B corundum. In addition to its effect on overlay paper quality, it should be known that brand B corundum is 13.33% cheaper than brand A corundum in terms of cost.

As a result of the results of this study carried out for the laminate flooring surface quality, it was observed that all the values determined were within the desired standards. In order to be sure of this work, it should work at these values for a certain time and according to the test results to be done, it should be started to work at optimum values. It is possible to determine more economical productions by following the panel and overlay paper production conditions very well.

5. References

[1] Kara, M.E,. Özçifci, A,. Nemli, G., Çelik, U., Effect of Lamination Conditions on Technological Properties of HDF Laminate Parquet.'' IFC 2016 International Furniture Congress 13-15 October 2016.
[2] Kara, M.E., İstek, A., Esgin, E., Effect of Coating Conditions on Surface Properties in Particle Boards, III. Uluslararası Odun Dışı Orman Ürünleri Sempozyumu 8-10 May 2014, Kahramanmaraş.
[3] Istek, A., Aydemir, D., and Aksu, S. The effect of decor paper and resin type on the physical, mechanical, and surface quality properties of particleboards coated with impregnated decor papers, BioRes. 2010;5(2):1074-1083.

Морфология и грапавост на сплав Ti6Al4V, произведена чрез фрезоване и селективно лазерно стопяване

Surface morphology and roughness of Ti6Al4V alloy manufactured by milling and selective laser melting

Tsanka Dikova, Dzhendo Dzhendov, Yavor Gagov

Faculty of Dental Medicine, Medical University of Varna, 84 Tsar Osvoboditel Blvd, 9000 Varna, Bulgaria

E-mail: tsanka_dikova@abv.bg

Abstract: The aim of the present paper is to examine the morphology and surface roughness of Ti6Al4V alloy produced by CAD/CAM milling and selective laser melting (SLM) in as-produced state and after sandblasting. Surface morphology is investigated by optical microscopy and BAC and ADC curves of its profile. The Ra, Rq and Rz parameters are used for evaluation of the surface roughness. It is established that the surface morphology of the samples is very different and is typical for each production process. The surface of the milled plates is characterized by a periodical profile with almost uniform distribution of peaks and valleys and a larger radius of the peaks. The individual molten layers and a large number of partially melted particles are observed on the surface of the SLM details, predetermining the topography consisting mainly of peaks with a larger radius of curvature. The roughness of the SLM samples (Ra = 6.7 μm and Rz = 36.36 μm) is several times higher than the milled ones (Ra = 0.86 μm and Rz = 4.61 μm). Sandblasting reduces the roughness of SLM parts by about 10%, but almost doubles the roughness of milled parts. After sandblasting, the peaks on the surface of both groups of samples become with sharper edges, the surface profile of the milled plates is characterized by uniform amounts of peaks and valleys, and that of SLM samples changes and consists mainly of valleys.

Keywords: Ti6Al4V, CAD/CAM MILLING, SELECTIVE LASER MELTING, SURFACE MORPHOLOGY, ROUGHNESS

1. Увод

В последните години чистият титан и неговите сплави намират широко приложение в медицината предимно като имплантологични материали поради тяхната висока корозионна устойчивост, биосъвместимост, добри механични свойства и модул на еластичност, който е най-близък до този на костната тъкан [1,2]. Напоследък, поради ниската относителна маса, Ti и сплавите му започват да се използват и в протетичната дентална медицина за изработване на неснемаеми и надимплантатни протезни конструкции от металокерамика [2-5]. Високите температура на топене и реактивоспособност на титана затрудняват производството на дентални конструкции чрез леене. CAD/CAM фрезоването и селективното стопяване с лазер (СЛС) се явяват успешни алтернативи на конвенционалния технологичен процес [4-6]. Те принадлежат към две основни групи технологии, които се различават по начина на получаване на детайла.

CAD/CAM фрезоването спада към групата на технологиите за изработване чрез отнемане на материал, а СЛС – към групата на адитивните технологии, или производство чрез добавяне на материал [2,4-6]. При първия процес детайлът се изработва от плътна заготовка с гарантирани механични свойства чрез фрезоване. Следователно, не се очаква механичните свойства на конструкцията да се променят. Повърхностните характеристики в този случай зависят от вида, формата и габаритите на използвания режещ инструмент, от параметрите на процеса на рязане – скорост, подаване, дълбочина и стратегия на обхождане, както и от разположението на детайла спрямо заготовката и координатната система на машината [2,4,6].

Селективното лазерно стопяване е съвременна технология на 3D печат, при която обектите се изграждат слой по слой чрез стопяване на метален прах с помощта на лазер и наваряването му върху предходния обем [6-8]. При тази технология свойствата и повърхностните характеристики на детайла зависят от три групи фактори. Първата е свързана с изходния материал – вид на сплавта, едрина и форма на праха, начин на получаване. Втората се отнася до параметрите на процеса - вид и мощност на лазера, диаметър на петното на лазерния лъч, скорост и стъпка на сканиране, дебелина на стопения слой, стратегия на сканиране [9-10]. Третата включва конструкцията

на детайла и разположението му спрямо посоката на изграждане.

Установено е, че грапавостта на повърхността на титанови сплави, произведени чрез СЛС, е неколкократно по-висока от тази на фрезованите, като стойностите на параметрите варират в широки граници при различните автори. Според Cevik ZA et al. [11] средното аритметично отклонение на профила Ra на СЛС произведена сплав Ti6Al4V достига 6.98-9.69 μm в сравнение със CNC фрезована – 0.235-0.919 μm. Antanasova M. et al. [4] установяват, че Ra на лазерно изградената сплав Ti6Al4V е почти два пъти по-голяма от тази на фрезованата – 2.17 μm и 1.33 μm съответно. Подобни резултати са получени от същия колектив и при изследване на повърхностните параметри на текстурата на Ti6Al4V чрез атомно-силов микроскоп – Sa на фрезованата сплав е 0.59 μm, а на СЛС произведената – 2.31 μm [5]. След пясъкоструене грапавостта на фрезованата сплав се повишава до Sa=1.9 μm, а на лазерно изградената се понижава до Sa=1.11 μm.

На пазара навлизат масово машини за селективно лазерно стопяване на дентални сплави от различни производители, които имат различен тип лазерен източник и работят с различни параметри. За да може да се гарантира качеството на денталните конструкции, произведени с тях, е необходимо да се провеждат постоянно изследвания на техните геометрични и повърхностни характеристики и механични свойства. Целта на настоящата статия е да се изследват морфологията и грапавостта на повърхността на сплав Ti6Al4V, изработена чрез СЛС и CAD/CAM фрезоване, и да се направи сравнителен анализ на данните от образци преди и след пясъкоструене.

2. Материали и методи

2.1. Материали и технологии за изработване на образците

Образците, използвани в изследването, са с формата на пластина с дължина 25+/-1 mm, ширина 3+/-0,1 mm и дебелина 0,5+/-0,05 mm съгласно стандарт БДС EN ISO 9693:2019 „Стоматология. Изпитване за съвместимост на металокерамични смеси и смеси от различни керамични компоненти". Произведени са общо 56 броя пробни тела, разделени на две групи в зависимост от технологията на

производство - CAD/CAM фрезоване (28 бр.) и селективно лазерно стопяване (28 бр.).

Пластините от първата група са фрезовани на машина CORITEC 650i Loader (Imes-Icore GmbH, Eiterfeld, Германия) от диск от титанова сплав Starbond Ti5 Disc (Ti6Al4V за фрезоване Grade 5 "ELI") за дентални реставрации тип 4 по ISO 22674.

Образците от втората група са изработени от фирма 3Д МЕДИКЪЛ ПРИНТ (Плевен, България) на машина SYSMA MySint 100 (SYSMA S.p.A., Vicenza, Италия). Използвана е сплав във вид на прах CT PowderRange Ti64 F (Ti6Al4V) от Carpenter Additive (Liverpool, UK). Машината за СЛС е снабдена с фибров лазер и за титанова сплав работи с мощност на лазера 100 W, скорост на сканиране 600 mm/s, диаметър на петното на лазерния лъч 55 μm, дебелина на слоя 20 μm, стъпка при сканиране - 0,020 mm и защитна среда от аргон. При производството, ширината 3 mm на пластината е успоредна на направлението Z, т.е. на изграждане на обекта, а повърхнината 25 mm x 0.5 mm е успоредна на равнина X-Y на машината и по нея са разположени технологични опори. След изработването им, детайлите са подложени на изотермично отгряване за снемане на вътрешните напрежения. Повече подробности за производството на образците са дадени в [2].

Пробните тела от двете групи са пясъкоструени по едната повърхност, почистени с пароструйка и изсушени на въздух. Пясъкоструенето е извършено с Al$_2$O$_3$ (размер на частиците 110 μm) под налягане 2 bar за време 10 s.

2.2 Изследване на образците

Морфологията на повърхността на образците след фрезоване, СЛС и пясъкоструене е изследвана на оптични микроскопи Olympus SZ51 и JL-17A, снабдени с дигитална

камера №ТР6080000В.

Параметрите на грапавостта са изследвани с помощта на апарат Surftest SJ-210 (Mitutoyo Corporation, Takatsu-ku, Japan). На всеки образец е измерена грапавостта по двете повърхнини 25 mm x 3 mm след изработване и по едната след пясъкоструене. Направени са по 3 измервания по дължина на всяка повърхнина от един и същи изследовател. Общата дължина на измерване е 4 mm, състояща се от 5 секции по 0.8 mm.

Изследвани са стойностите на Ra – средно аритметично отклонение на профила, Rq – средно квадратично отклонение на профила и Rz - максимална височина на профила. Показани са графиките на BAC и ADC кривите на профила на повърхността на образците преди и след пясъкоструене. BAC кривата показва съотношението материал-профил в оценяваната дължина, като стойностите на материала (mr) са по абсцисата, а интервалите от профила – по ординатата [12]. ADC (amplitude distribution curve) е крива на разпределение на амплитудата. Плътността на амплитудата е съотношението (изразено в %) на сумата от хоризонталните дължини на секциите от оценявания профил, които попадат между двете нива, и оценяваната дължина. ADC кривата се построява като се използва първото ниво като ордината и плътността на амплитудата за всеки отрязък като абсциса.

3. Резултати

3.1. Морфология на повърхността

Морфологията на повърхността на образци от титанова сплав, изработени чрез фрезоване и СЛС, е показана на фиг. 1. Ясно се вижда, че тя е коренно различна и е характерна за всеки един производствен процес. По повърхността на фрезованите пластини се забелязват следите, оставени от фрезовия инструмент (Фиг. 1а, б). Вижда се, че пробните тела
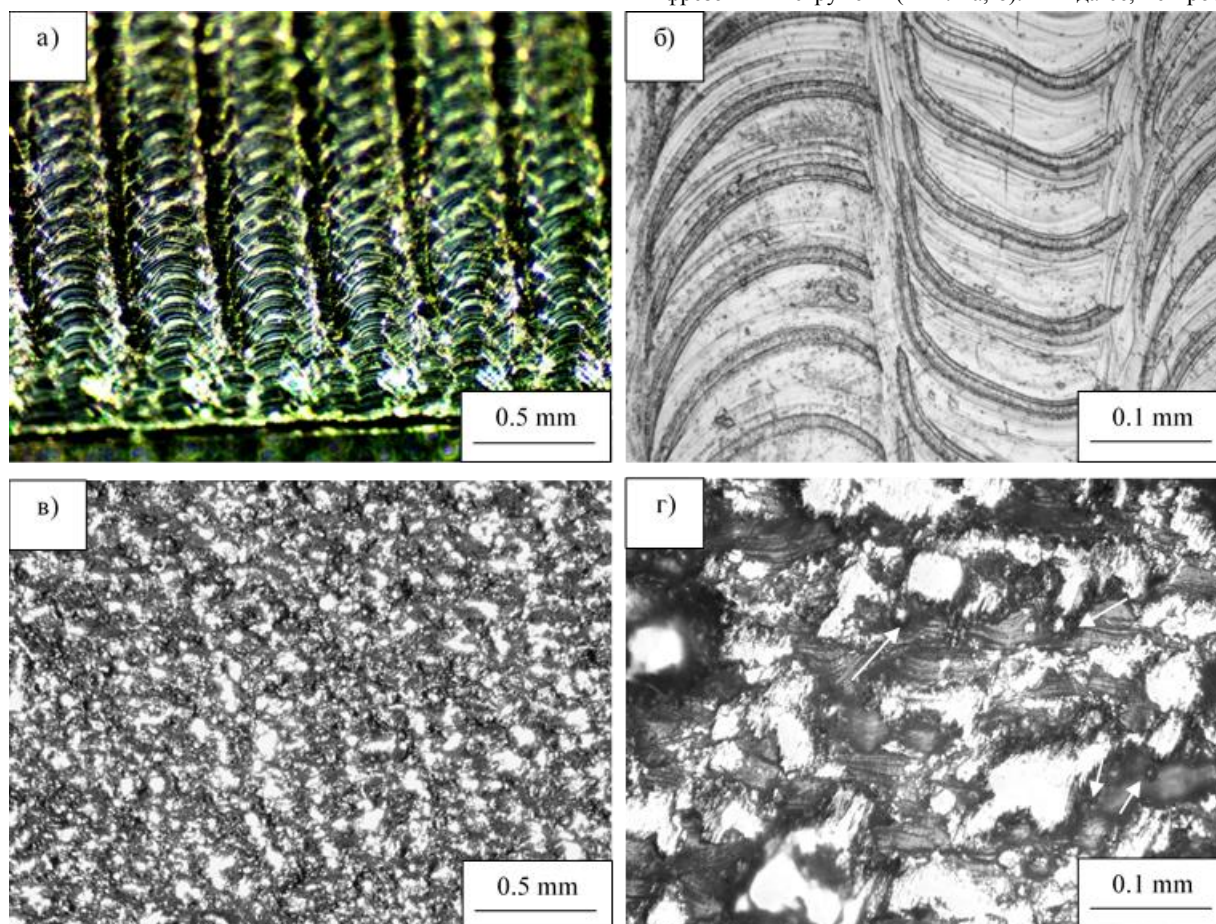
Фиг. 1 Морфология на повърхността на образци от титанова сплав, изработени чрез фрезоване – а), б) и СЛС - в) и г).
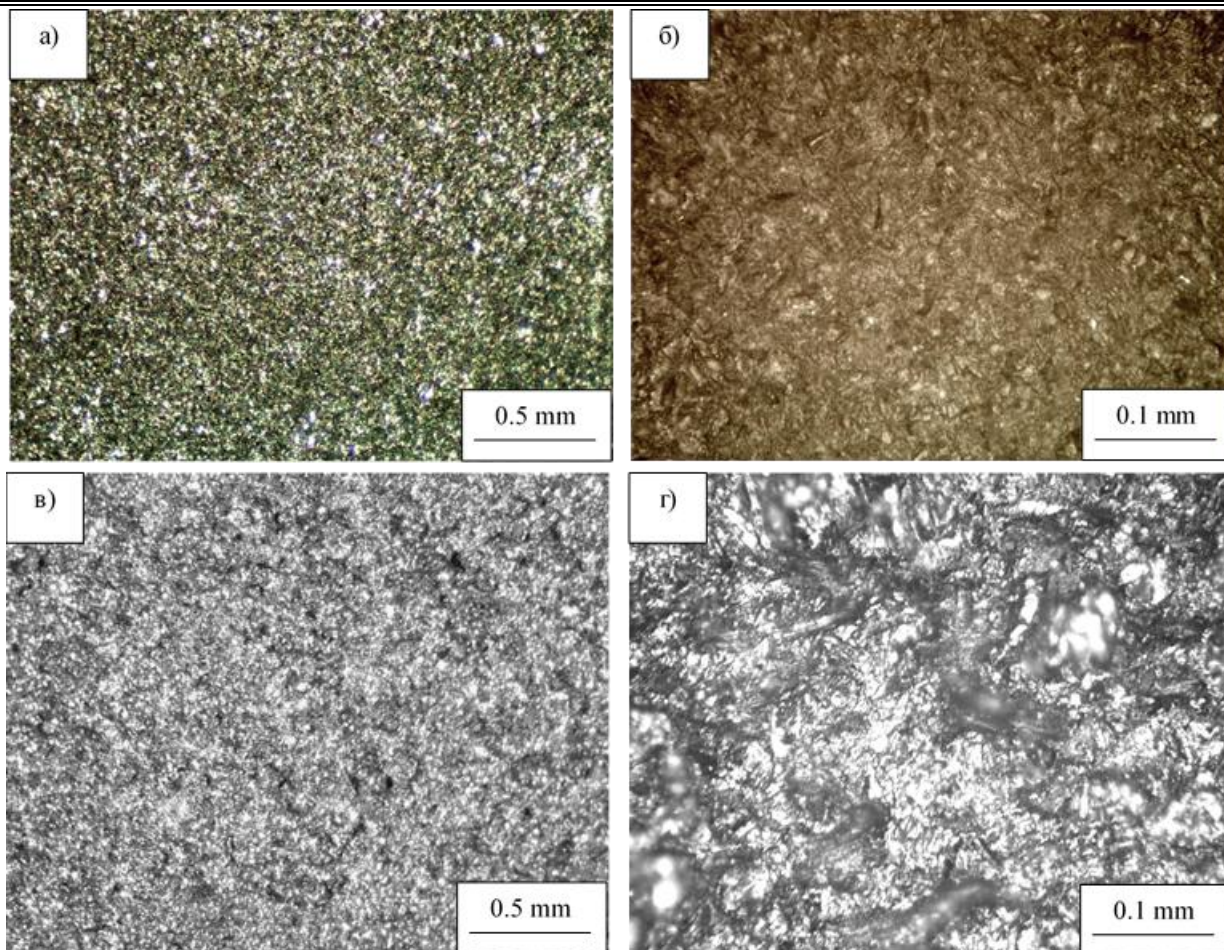
Фиг. 2 Морфология на пясъкоструена повърхност на образци от титанова сплав, изработени чрез фрезоване – а), б) и СЛС - в) и г).

са изработени по метода на обхождане, като фрезерът е извършвал постъпателни движения в права и обратна посока напречно на тяхната дължина. Образецът, изработен чрез СЛС, е изграден чрез последователно стопяване на слой прах с определена дебелина, който се наварява върху предходния слой от обема. В резултат, на повърхността на детайла се забелязват отделните слоеве, както и частично разтопени прашинки (Фиг. 1в, г).

След пясъкостеуене морфологията на повърхността на двете групи образци много се доближава по външен вид. Изчезват следите от фрезовия инструмент при първата група (Фиг. 2а, б) и стопените слоеве при втората (Фиг. 2в, г). При по-големи увеличения се забелязва наличие на падини и изпъкналости по повърхността на фрезованите образци (Фиг. 2б), а по повърхността на СЛС образците – намаляване количеството на неразтопените прашинки и повишаване площта на плоските участъци (Фиг. 2г).

Тези резултати са потвърдени при изследване профила на повърхността чрез грапавомер. Периодичността на профила (в обхвата -3μm/+3μm) на фрезованата повърхност и силното понижаване, почти до изчезване на тази периодичност (но в по-широк обхват на грапавостта -6μm/+6μm), след пясъкоструене на образците са показани на фиг. 3. Съотношението материал-профил и разпределението на амплитудите при BAC и ADC кривите, съответно, го потвърждават (Фиг. 4). При ADC кривата на фрезования образец амплитудите са предимно в рамките до 2%, но има голямо и почти равномерно разсейване в целия обхват (Фиг. 4б). След пясъкоструене, разпределението на амплитудата е симетрично, концентрирано между 25-75% от обхвата, а амплитудата се повишава до 3% (Фиг. 4г).

Морфологията и профила на повърхността на лазерно стопен образец са показани на Фиг. 5. За разлика от фрезованата пластина, тук не се наблюдава периодичност на профила, което се определя от технологичния процес на производството му. Максималната височина на профила е в значително по-голям обхват -20μm/+25μm, като повечето от върховете са закръглени (Фиг. 5б). След пясъкоструене максималната височина на профила леко се понижава (в обхват -20μm/+20μm), а линиите на профила не са толкова гладки (Фиг. 5в). Тази слаба промяна в профила на повърхността на СЛС образеца почти не е отразена при съотношението материал-профил на BAC кривите на Фиг. 6. Но при разпределението на амплитудите на ADC кривите има разлика. Амплитудите преди и след пясъкоструене са в рамките на 3%, като са разпределени асиметрично в обхвата 25-90%. При СЛС пробата по-голямата част от амплитудите с високи стойности са разположени под средната линия 50% от обхвата (Фиг. 6б). След пясъкоструене асиметричността се променя – амплитудите с високи стойности са разположени над средната линия от 50% (Фиг. 6г).

3.2. Грапавост

Измерените стойности на грапавостта показват значително по-ниска грапавост на повърхността на фрезованите образци (Ra=0.86 μm и Rz=4.61 μm) в сравнение с изработените чрез СЛС (Ra=6.7 μm и Rz=36.36 μm) (Фиг. 7). Пясъкоструенето оказва различно влияние при двете групи образци. Грапавостта на фрезованите образци се повишава почти два пъти и достига Ra=1.38 μm и Rz=9.73 μm, а тази на лазерно стопените се понижава с около 9-10% (Ra=6.12 μm и Rz=32.54).

4. Анализ на резултатите

Морфологията и грапавостта на детайлите се определят от технологията на тяхното производство, от параметрите на

технологичния процес и от разположението на детайла върху масата на машината [7-10,13]. В настоящото изследване са използвани два коренно различни технологични процеса – фрезоване и селективно лазерно стопяване. Първият е представител на групата субтрактивни технологии, или процеси за изработване с отнемане на материал, а вторият – на групата адитивни технологии, т.е. с добавяне на материал. За производството на образците по двата технологични процеса е използван един и същи виртуален модел. Освен това,

машините, на които са изработени детайлите, са предназначени специално за дентални конструкции и режимите на работа са установени от фирмите производителки. Следователно, за фрезоване и СЛС на образците са използвани строго фиксирани параметри за съответните титанови сплави. В такъв случай, основни фактори, които оказват влияние върху морфологията и грапавостта на повърхността, са видът технологичен процес и разположението на детайла.
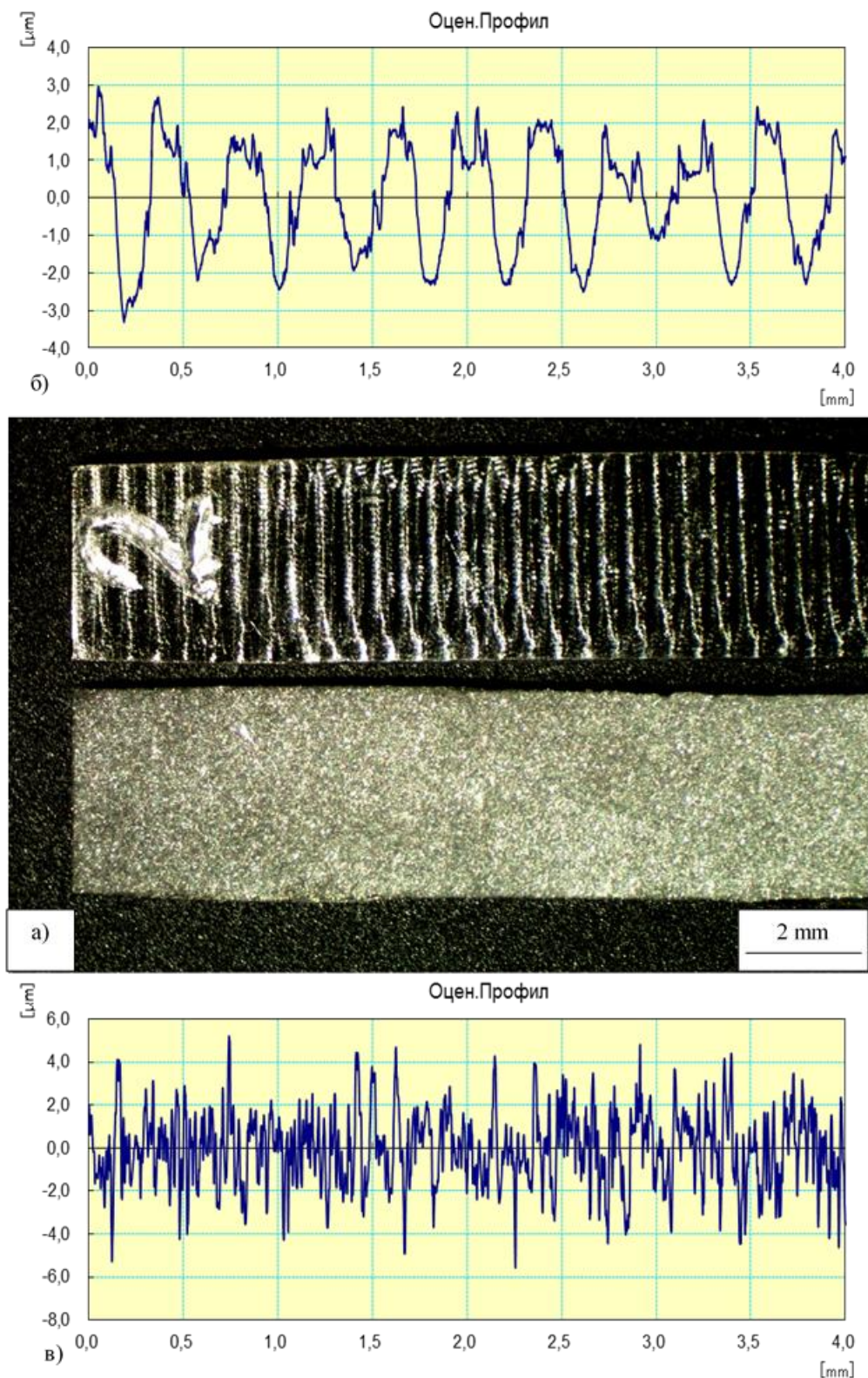
Фиг. 3 Морфология на повърхността на образци от титанова сплав – а), изработени чрез фрезоване (2) и фрезоване и пясъкоструене (долу). Профили на повърхността на фрезован – б) и на фрезован и пясъкоструен - в) образци.

Грапавостта на фрезованата повърхност е Ra=0.86 μm и Rz=4.61 μm, което потвърждава резултатите от изследванията на други учени [3,5,11]. Съгласно изискването при фрезоване, опорите са разположени по дебелината на детайла (0.5 mm) и по този начин двете работни повърхнини 25 mm х 3 mm (успоредни на равнината X-Y на машината) са получени чрез обхождане и отнемане на материал от дисковата заготовка. Пътят на фрезера е успореден на късата страна и той извършва възвратно постъпателни движения. Това доведе до формиране на морфология на повърхността (Фиг. 1а, б) с периодично повтарящ се профил (Фиг. 3а, б), което освен избраната стратегия на отнемане на материала вероятно се дължи и на препокриване траекторията на инструмента.

Разпределението на амплитудите, изразено чрез ADC кривите, има връзка с други два параметъра Rku (Kurtosis) и Rsk (Skeweness) на грапавостта на повърхността [12]. Rku (Kurtosis) и Rsk (Skeweness) са статистически параметри на повърхностната текстура, които се определят чрез хистограма на височините на всички измерени точки и тяхната симетрия, представена чрез отклонение от идеалното нормално разпределение [13]. Rku (Kurtosis) представлява степента на концентрация около средната линия на кривата на разпределение на амплитудата. Rsk (Skeweness) е степента на асиметрия и дава отклонението на кривата на разпределение на амплитудата от идеалното нормално разпределение [12]. ADC кривата на фрезования образец (Фиг. 4б) има по-скоро форма на квадрат, което предполага Rku около 1 [12]. Тъй като

Kurtosis е критерий за определяне на остротата на повърхността, то в този случай пиковете на грапавините са с по-голям радиус на върха [13], което се доказва и от профила на повърхността на фрезования образец (Фиг. 3б).

Стойностите на изследваните параметри на грапавостта при СЛС образците (Ra=6.7 μm и Rz=36.36 μm) са неколкократно по-високи от тези на фрезованите. Това се дължи от една страна на особеностите на процеса на селективно лазерно стопяване, а от друга на разположението на детайла спрямо посоката на изграждане. И тук основното изискване е опорите да са разположени по дебелината (0.5 mm), а ширината 3 mm да е успоредна на направлението на изграждане, т.е. двете работни повърхнини 25 mm х 3 mm да са успоредни на равнината X-Z на машината [2]. Това вертикално разположение на работните повърхнини доведе до високата грапавост, дължаща се най-вече на наличието на множество частично разтопени прашинки [10,13]. Основни фактори за големия брой частично разтопени прашинки са краткото време на взаимодействие на лазерния лъч с прахообразния материал по страничните повърхности и високата плътност на енергията E_d=416 J/mm^3 на използвания режим на СЛС [9,10]. Високата плътност на енергията и наличието на частици с по-малки размери в обема на фракцията метален прах може да причини отворени пори и т.н. "balling effect", които допълнително да повишат грапавостта по повърхността.

Анализът на ADC кривата на СЛС образец (Фиг. 6б) показва, че тя също има по-скоро формата на квадрат, т.е. с Rku
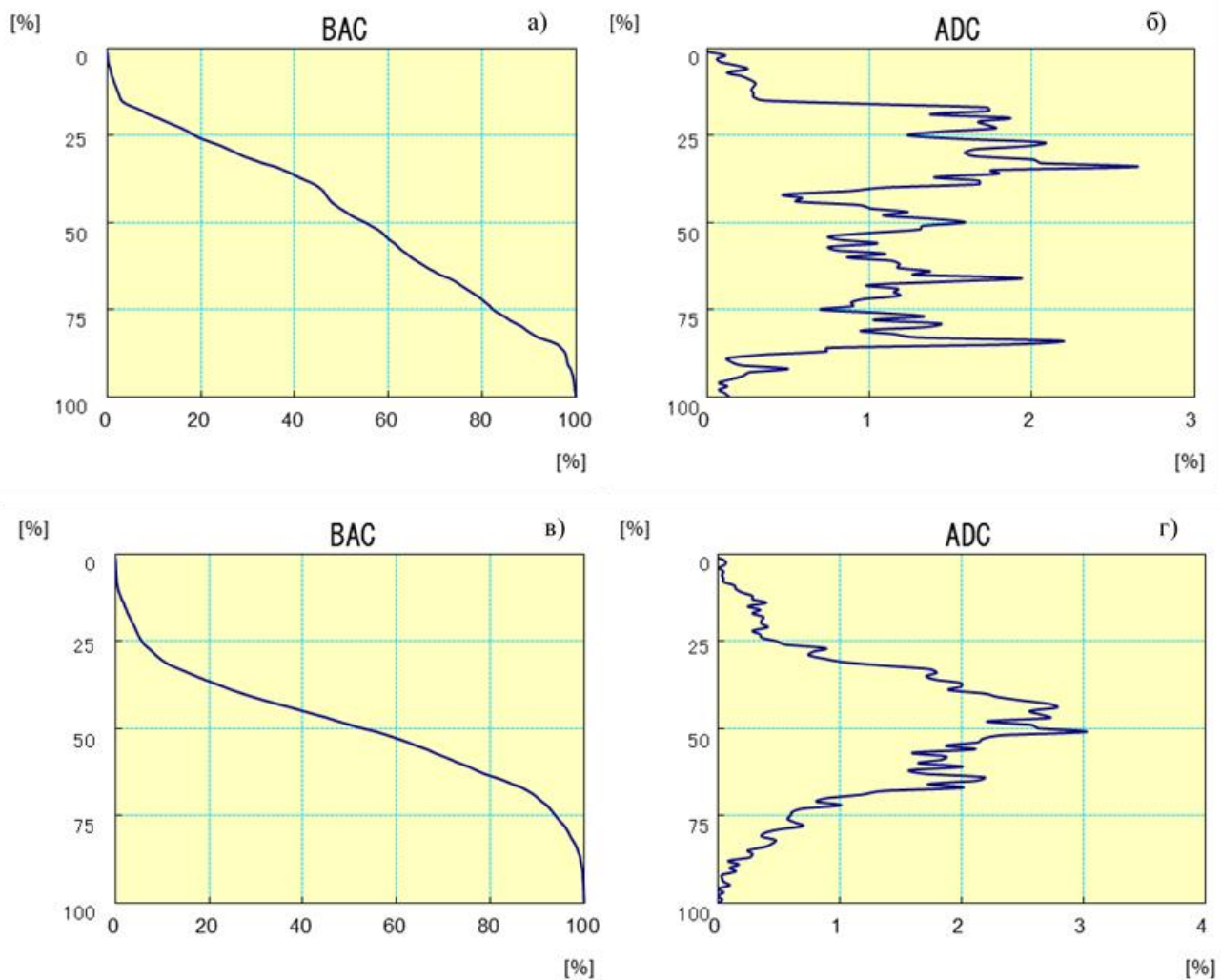
Фиг. 4 ВАС и ADC криви на профила на фрезован – а), б) и фрезован и пясъкоструен - в) и г) образци от титанова сплав.

около 1 [12]. Следователно, и тук пиковете на грапавините са с по-голям радиус. Но относно симетрията на върховете и падините спрямо средната линия – има отклонение под нея, което значи, че Rsk>0 [12]. В такъв случай, повърхността се характеризира предимно с пикове [10,13], което се вижда от микроскопските снимки на Фиг. 1в и Фиг. 1г и от графиката на нейния профил на Фиг. 5б.

Пясъкоструенето оказва различен ефект върху грапавостта и топографията на образците от двете групи. То повишава почти два пъти грапавостта на фрезованите планки, но понижава с около 10% грапавостта на детайлите, изработени чрез СЛС. Променя се профилът на ADC кривите – и при двете групи те имат характер, близък до синусоида, което означава,

че Rku се повишава до около 1.5 [12], т.е. пиковете по повърхността са с по-остри ръбове (Фиг. 3в и Фиг. 5в). Но симетрията е различна - при фрезованите образци има симетричност при разпределение на амплитудата (Фиг.4г) (Rsk е близко до нула) [12], т.е. профилът на повърхността се състои от равни количества върхове и падини (Фиг. 3в). Докато пясъкоструенето променя симетричността на кривата на разпределение на амплитудата при СЛС образците (Фиг.6г) – отклонението е над средната линия (Rsk<0) [12]. Следователно, пясъкоструената повърхност на СЛС пробата се характеризира предимно с падини, което е потвърдено от микроскопското изследване на Фиг. 2г и от графиката на нейния профил (Фиг. 5в).
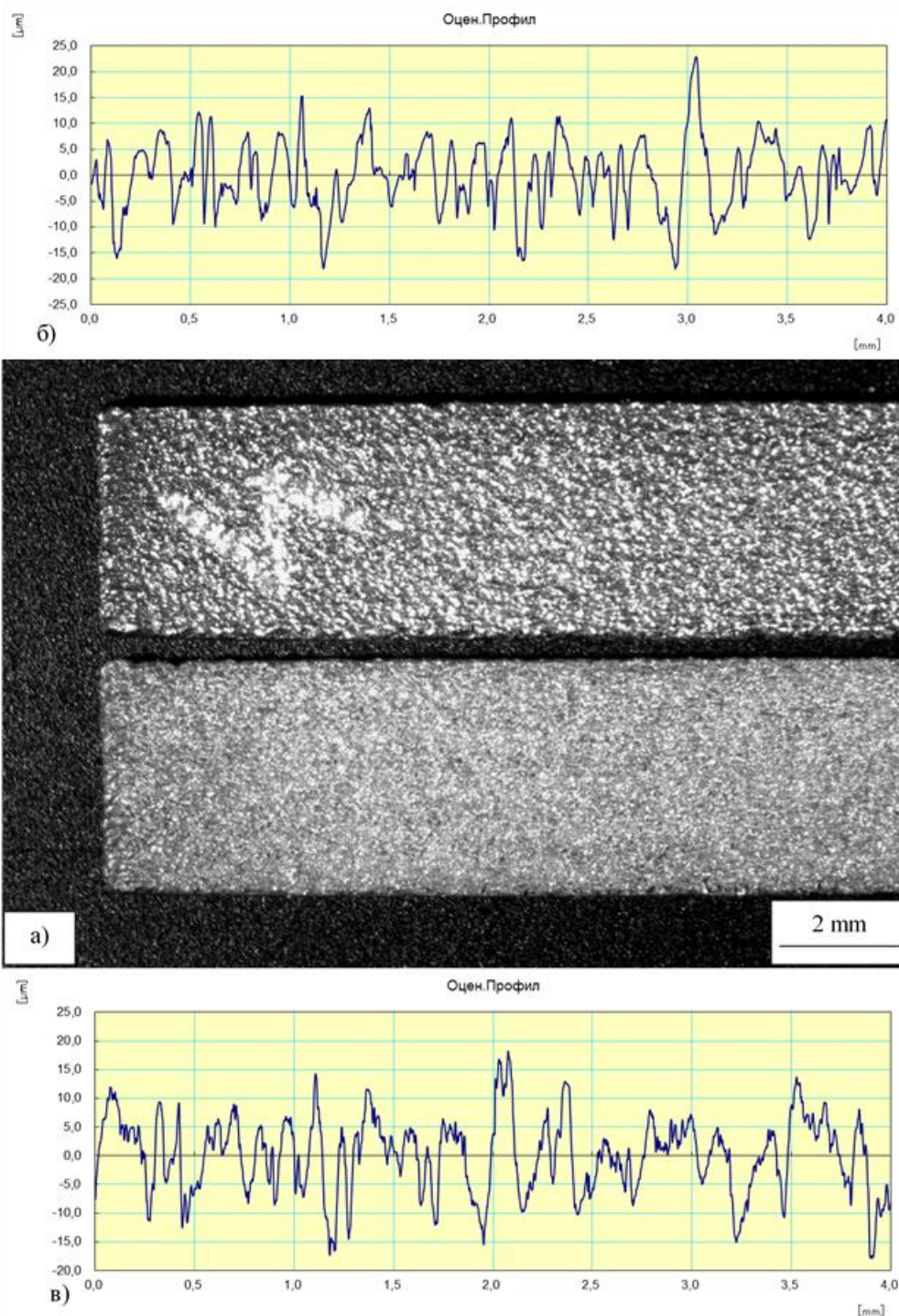
Фиг. 5 Морфология на повърхността на образци от титанова сплав– а), произведени чрез СЛС (4) и СЛС и пясъкоструене (долу). Профили на повърхността на СЛС – б) и на СЛС и пясъкоструен - в) образци.
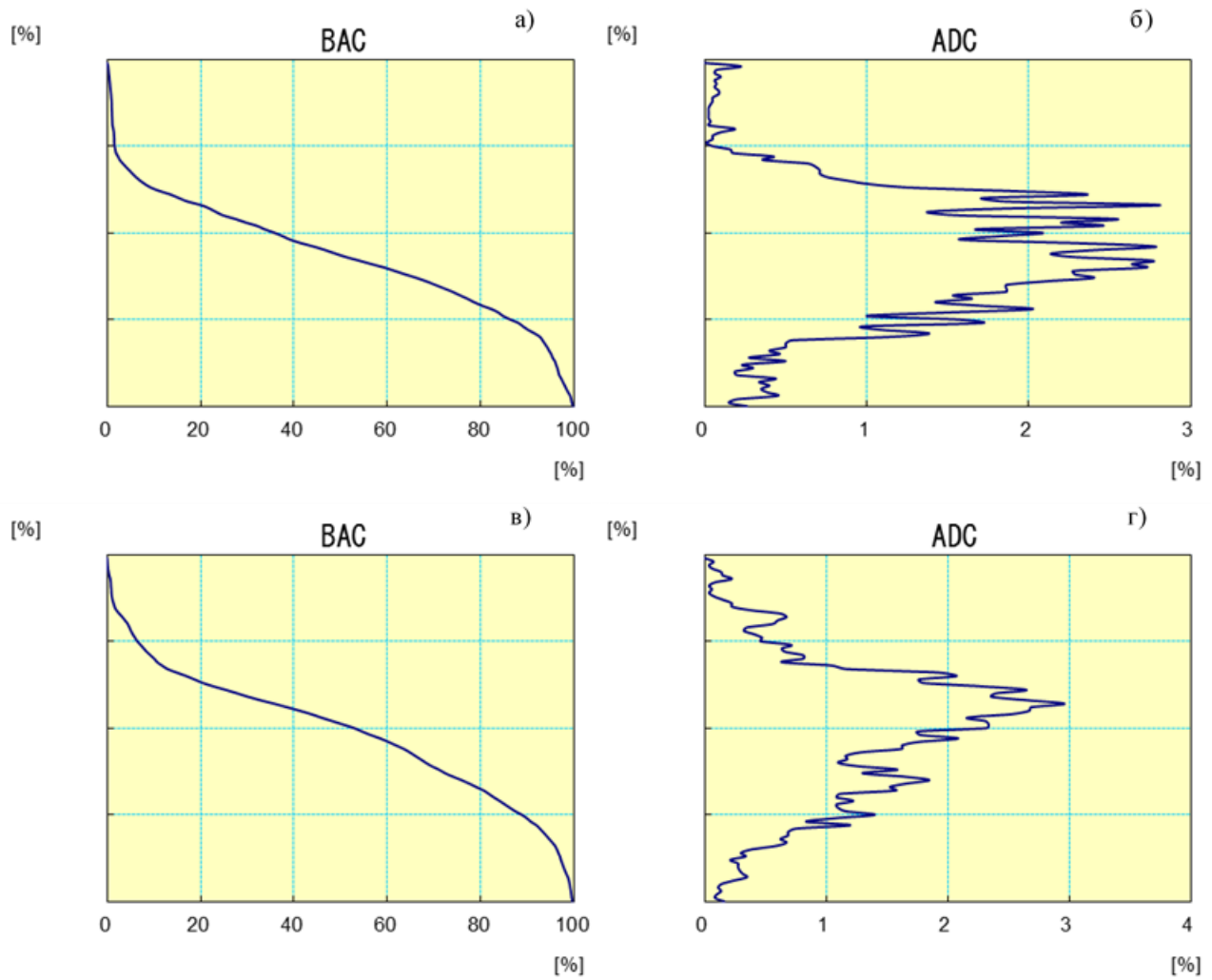
Фиг. 6 ВАС и ADC криви на профила на образец от титанова сплав, изработен чрез СЛС – а), б) и СЛС и пясъкоструене – в) и г).
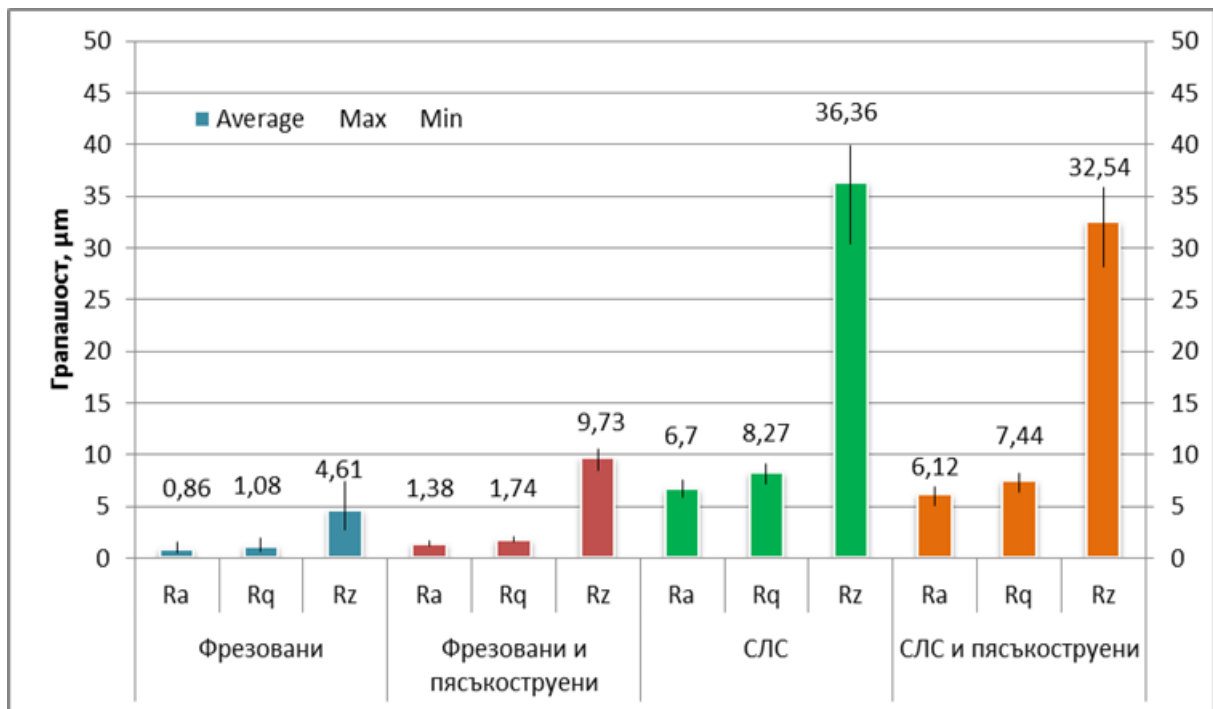
Фиг. 7 Грапавост на образци от титанова сплав, произведени чрез фрезоване и СЛС и последващо пясъкоструене.

4. Заключение

В настоящата статия са изследвани морфологията и грапавостта на повърхността на образци от титанова сплав Ti6Al4V, произведена чрез CAD/CAM фрезоване и селективно лазерно стопяване. Основните фактори, които определят повърхностната топография в това изследване, са видът технологичен процес и разположението на детайла.

Установено е, че морфологията на повърхността на образците от двете групи е коренно различна и е типична за всеки един производствен процес. Повърхността на фрезованите пластини се характеризира с периодично повтарящ се профил с почти равномерно разпределение на върхове и падини и с по-голям радиус на пиковете. По повърхността на лазерно изградените детайли се забелязват отделните стопени слоеве и голям брой частично разтопени прашинки, което предопределя топографията да се характеризира предимно с пикове с по-голям радиус на закръгление. Грапавостта на образците, произведени чрез СЛС (Ra=6.7 µm и Rz=36.36 µm), е няколкократно по-висока от фрезованите (Ra=0.86 µm и Rz=4.61 µm).

Пясъкоструенето оказва различен ефект върху грапавостта и топографията на образците от двете групи. То понижава с около 10% грапавостта на лазерно изградените детайли, но повишава почти два пъти грапавостта на фрезованите. След пясъкоструене пиковете по повърхността и на двете групи образци стават с по-остри ръбове, профилът на повърхността на фрезованите пластини се характеризира с равномерни количества върхове и падини, а този на СЛС пробите се променя и се състои предимно от падини.

Благодарност

Литература

1. Dikova T. Nano-engineered coatings on titanium implants. Scripta Scientifica Medica. 2012 Dec 20;44(2):23-5.
2. Gagov Y, Dzhendov D, Parushev I, Dikova T. Geometrical characteristics and density of Ti6Al4V alloy fabricated by milling and selective laser melting. Proceedings, XXVII International Scientific and Technical Conference "Foundry 2022", 06-08 April 2022, Pleven, Bulgaria, STUME "Industry 4.0". 2022;1(4):40-45.
3. Mohsen CA. Effect of surface roughness and thermal cycling on bond strength of CP titanium and Ti–6Al–4V alloy to ceramic. Journal of Prosthodontic Research. 2012;56(3):204-9.
4. Antanasova M, Kocjan A, Kovač J, Žužek B, Jevnikar P. Influence of thermo-mechanical cycling on porcelain bonding to cobalt–chromium and titanium dental alloys fabricated by casting, milling, and selective laser melting. Journal of prosthodontic research. 2018;62(2):184-94.
5. Antanasova M, Kocjan A, Hočevar M, Jevnikar P. Influence of surface airborne-particle abrasion and bonding agent application on porcelain bonding to titanium dental alloys fabricated by milling and by selective laser melting. The Journal of prosthetic dentistry. 2020 Mar 1;123(3):491-9.
6. Dikova T, Dzhendov D, Simov M, Katreva-Bozukova I, Angelova S, Pavlova D, Abadzhiev M, Tonchev T. Modern trends in the development of the technologies for production of dental constructions. Journal of IMAB–Annual Proceeding Scientific Papers. 2015 Dec 30;21(4):974-81.
7. Kazantseva N. Main factors affecting the structure and properties of titanium and cobalt alloys manufactured by the 3D printing. 2018 J. Phys.: Conf. Ser. 1115 042008;
8. Kazantseva N, Krachmalev P, Yadroitsev I, Ezhov I, Merkushev A, Davidov D. COMPARATIVE ANALYSIS OF THE STRUCTURE AND PROPERTIES OF TITANIUM AND COBALT MEDICAL ALLOYS MANUFACTURING BY 3D PRINTING. RAPDASA 2019 Conference Proceedings, p. 331-342, ISBN 978-0-6398390-0-4;
9. Wang D, Dou W, Yang Y. Research on selective laser melting of Ti6Al4V: Surface morphologies, optimized processing zone, and ductility improvement mechanism. Metals. 2018 Jul;8(7):471.
10. Pal S, Lojen G, Hudak R, Rajtukova V, Brajlih T, Kokol V, Drstvenšek I. As-fabricated surface morphologies of Ti-6Al-4V samples fabricated by different laser processing parameters in selective laser melting. Additive Manufacturing. 2020 May 1;33:101147.
11. ÇEVİK ZA, ÖZSOY K, ERÇETİN A. THE EFFECT OF MACHINING PROCESSES ON THE PHYSICAL AND SURFACE MORPHOLOGY OF Ti6Al4V SPECIMENS PRODUCED THROUGH POWDER BED FUSION ADDITIVE MANUFACTURING. International Journal of 3D Printing Technologies and Digital Industry. 2021;5(2):187-94.
12. Surface Roughness Measuring Tester SJ-210, No. 99MBB122A2, Series No.178, User's Manual, Mitutoyo Corporation, Kawasaki, Japan, 2016.
13. Sidambe AT. Three dimensional surface topography characterization of the electron beam melted Ti6Al4V. Metal powder report. 2017 May 1;72(3):200-5.

Studing the temperature microclimate in beehives made out of defferent materials

Todorka Lepkova, Lyuben Lakov, Mihaela Aleksandrova

Bulgarian Academy of Sciences, Institute of Metal Science, Equipment and Technologies with Hydro- and Aerodynamics Centre "Acad. A. Balevski", Shipchenski Prohod Blvd. 67, 1574 Sofia, Bulgaria, e-mail:d_ora@abv.bg

***Abstract**: The use of clay as a structural material has been known for centuries. The authors set the task of studying the applicability of clay as a constructive material in the production of beehives. The study aims to make a comparative analysis of temperature conditions in different types and identical in construction beehives by comparing the indicator for ceramic and wooden hives. For the purpose were used three 10-frame hives type "Dadan-Blat" - two ceramic (one made entirely of marl clay, and the other - with increased kaolin content, both ceramic tiles are with high cavity) and one wooden (pine). Measurements of the air temperature and the temperature inside the hives were made for one month. From the obtained results it is established that for the studied beehives, the ceramic hive with high kaolin content has the best thermal insulation properties.*

KEYWORDS: CERAMIC BEEHIVE, TEMPERATURE

1. Introduction

The last decade has been marked by numerous alarming facts about the extinction of honey bees, without which life on earth would be unthinkable. The reasons for this scary phenomenon are multi-layered and complex. Evidence shows that certainly there is a reason to believe that the living conditions that bees have inside the hives that they are inhabiting are essential for their well-being. Given the advantages of ceramics as a constructive material, it is assumed that it has a high potential to provide favorable and sustainable living conditions for the bee colonies [1]. One of the key factors of the microclimate in the hive is the temperature. The optimal temperature in the breed is around 35-36°C [2]. Higher temperatures can cause the death of the family. Lower temperatures especially temperatures below 0°C will lead to protective diapause behaviour or will have a lethal effect. The extreme temperatures affect the bee products as well. Overheating causes wax melting and too-quick dehydration of the honey while the low temperatures slow down the dehydration of the nectar which causes problems in the production of the honey.[3] The bees have own regulation mechanisms to maintain the healthy temperature of the hive. Whenever the weather is too hot, they start fanning the hot air out or use evaporative cooling mechanisms. If the temperature gets too low they start generating metabolic heat by contracting their flight muscles[4-6]. Both these mechanisms consume high energy of the bees and increase their need for food.

Therefore, it is extremely important to maintain the optimal temperature in the hive. To achieve a better insulating effect, we produce ceramic plates for beehives with standard dimensions for Dadan-Blatt hive with high cavity. The role of well-formed internal cavities is to reduce the coefficient of thermal conductivity inside the hive and to reduce heat loss from the inside to the outside at lower air temperatures. [5-7]

Aim

The aim of the present work is to study and compare the temperature conditions in uninhabited ceramic hives and in a traditional wooden hive, when placed in natural conditions.

2. Methodology

For the purposes of the study, two Dadan-Blatt ceramic hives were made from two different mixtures. The first mixture is made of marl clay from the deposit of the town of Debelets. The other mixture is with high content of kaolin. High-hollow slabs were made from the two mixtures, from which the two ceramic beehives were made (Fig. 1 - from marl clay and Fig. 2 - with increased kaolin content). A standard wooden (coniferous wood) 10-frames Dadan-Blat was purchased for the experiment (Fig. 3). The hives were placed in a natural environment - Fig. 4

***Fig. 1** - from marl clay and **Fig. 2** - with increased kaolin content*

***Fig.3** 10-frames Dadan-Blat was purchased for the experiment **Fig. 4** The hives were placed in a natural environment.*

3. Results and discussion

The field measurement was conducted in natural environment in the Industrial Zone of the town of Debelets, Veliko Tarnovo region. (Fig. 4) On each of the hives were placed digital thermometers model AURIOL, board IAN: 373028_2104, with sensors for monitoring the temperature in the hive and monitoring the outside temperature. The data is displayed. Technical characteristics of the digital thermometer: Table 1 Technical characteristics of the digital thermometer.

Internal temperature measurement range	from -10 ℃ to +50℃
Outdoor temperature measurement range	From -50℃ to + 70℃
Tolerance	from -50℃ to 0℃+/-2℃ from 0℃ to +30℃+/- 1℃ from +30℃ to + 70℃+/- 2℃
External sensor	IP44 protection against liquid

The measurement was carried out within the period of one month, from 28.04.2022. to 28.05.2022

For the purposes of the study, temperatures are measured at different parts of the day to determine the temperature differences between the air temperature and the temperature inside the hives. The measurements are grouped and analyzed in three categories, according to the information about the optimal temperature in beekeeping. Accordingly, measurements are conducted in cold conditions (at air temperature around 0^oC) are differentiated; optimal temperature (between 5°C and 30°C); and high temperature (air temperature above 30^oC). The graphs present the average values for the daily measurements made at 00:00, 10:30 and 14:15, respectively.

	1	2	3	4
T°C air	-1	-0,5	-0,1	-0,5
T°C Beehive 1	0,2	0,5	0,8	0
T°C Beehive 2	0,2	0,2	0,9	0
T°C Beehive 3	-0,3	-0,3	0,3	-0,3

Fig.5 Measurement in cold conditions

When comparing the obtained results, it was found that at low temperatures, in the ceramic hives (hive 1 and hive 2), temperature differences are between 0.8°C and 1°C higher than the outside temperature. In the wooden hive, the temperature is 0.2°C higher than outside.

	1	2	3	4	5	6	7	8	9	10	11
T°C air	10,3	16,3	23	25,2	27,5	28,4	28,8	29,2	29,5	30,2	30,3
T°C Beehive 1	11,4	11,6	18	18,7	22,4	26,4	26,4	26,6	26,9	28,1	28,9
T°C Beehive 2	11,3	11,5	17	17,1	26,4	26,2	26,2	26,3	26,5	27,8	28,8
T°C Beehive 3	11,5	12	18,7	23,8	27,7	28,3	30,4	30,5	30,7	31,3	31,4

Fig. 6 Measurements during optimal temperature conditions

At optimum temperature, the wooden hive heats up faster than the ceramic ones, as when reaching daily temperatures above 28°C, the difference in temperatures outside and inside the wooden hive is on average 0.2°C, while the difference for ceramic hive 1 is 2.0°C and for ceramic hive 2 is 2.8°C.

	1	2	3	4
T°C air	31,9	38,2	38,6	39,5
T°C Beehive 1	29,6	33,5	33,7	36,9
T°C Beehive 2	29	33,2	33,2	36,5
T°C Beehive 3	31,8	38	38,3	38,6

Fig. 7. Measurements during heat

During heat, the temperature difference between outside and inside the hive is respectively for Beehive 1 - 2,3℃; for Beehive 2 - 2,6℃; for Beehive 3 - -0,3 ℃.

4. Conclusion:

In conclusion, based on the results obtained within the present study, we can say that in cases of sudden temperature changes hive 2 has the highest insulating properties, respectively stable microclimate, followed by hive 1 and hive 3. At the next stage, identical measurement and analysis should be performed with inhabited beehives.

References:

1.Heldmaier, G. (1987). Temperature Control in Honey Bee Colonies. *BioScience*,*37*, 395–399. https://doi.org/10.2307/1310562

2. Lakov, L., Ivanova, Y., Partalin, T., Aleksandrova, M., Lepkova, T., & Mutafchieva, G. (2021). Study of the thermal and sound insulation properties of ceramic plates with cavities designed for beehives. *Mathematical Modeling*, *5*(2), 59–61.

3. Lakov, L., Stoimenov, N., & Aleksandrova, M. (2021). Investigation of hollow ceramic structures by contactless computer-tomographic nondestructive method. *Industry 4.0*, *6*(1), 21–24.

4. Lakov, L., Stoimenov, N., Aleksandrova, M., Lepkova, T., & Mutafchieva, G. (2021). Study of temperature changes in ceramic cavity walls of beehives. *Innovations*, *9*(2), 78–82.

5. Lepkova,T., Martinova,I., Martinova,G., Marinova,I., & Pincheva,B. (2019). *Ceramic Beehive—A Conceptual Paper*. *IV*(2), 52–54.

6. Tautz, Jürgen. 2008. *The Buzz about Bees: Biology of a Superorganism*. Berlin Heidelberg: Springer-Verlag.

7. Winston, Mark L. 1991. *The Biology of the Honey Bee*. Harvard University Press.

Possibilities of reducing the degradation of molds for high-pressure of Al alloys

Ján Hašuľ[1, *], Janette Brezinová[1]

Department of Technology, Materials and Computer Supported Production, Technical University of Košice, Slovakia[1]

jan.hasul@tuke.sk, janette.brezinova@tuke.sk

***Abstract:** The paper focuses on the degradation of molds that are used for the technology of high-pressure casting of Al and its alloys. The method of high-pressure casting of aluminum products is one of the widely used production methods, which at the same time meets the requirements for precision and productivity in the production of cars and various mechanical parts. In the high-pressure casting process, the molds are exposed to various thermal and mechanical loads, where the molds and their shaped parts are degraded. The paper presents the results of research focused on the use of duplex PVD coatings to increase the life of shaped parts of molds for high-pressure casting of Al and its alloys.*

Keywords: ALUMINUM, DIE CASTING, DEGRADATION, COATINGS, ADHESION, CRACKS

1. Introduction

The high-pressure die casting process is used to produce parts mostly from aluminum, magnesium, zinc, and cooper alloys by injection of the molten metal in the mold cavity. The mold cavity that are used to produce those parts are constantly exposed to highly severe conditions, such as high pressure, rapid temperature fluctuations and erosion from fast moving molten metal. The usual molten metal input speed is comprised between 20 and 60 m/s and the temperature, depending on aluminum alloy type is around 700 °C. The maintenance of replace of these molds require a huge cost which implies that producers need to find the best solution to increase their lifespan. The industrial environmental and working conditions increase the capacity to induce some failure mechanisms on hot work tool steel, such as erosion, corrosion, wear, and thermal fatigue. Parts produced by this method conform accurately to the die size, have favorable mechanical features and are low in cost [1,2].

The die casting method of aluminum products is one of the widely used manufacturing methods as it is a technology that can simultaneously satisfy precision and productivity requirements during the production of automobile and various mechanical parts. However, during the rapid solidification process, defects like porosity and shrinkage might remain and significantly reduced the ultimate mechanical properties, e.g., tensile strength, wear resistance and fatigue strength [3]. During die casting process operations, the tools steel used to this process are exposed to a several thermal and mechanical loads, which can lead to damage the molds for high-pressure die casting. The improvement of these structures' lifetime was strongly required due to several economic and environmental reasons. Corrosion, soldering, erosive wear, and thermal fatigue are the primary failure mechanisms that limit die life in aluminum high-pressure die casting. Corrosion and soldering are caused by the physical impingement of the incoming liquid aluminum. Thermal fatigue results from the change in stress caused by alternate heating and cooling of the die surface during the casting process. Under the combined effects of these failure mechanisms, the die will crack; fragments are broken off the die, necessitating die removal and a consequent increase in process costs. One of the major damage mechanisms occurring in die casting process, under cyclic thermal loads is the formation of a network of interconnected cracks [4-6].

The stress cracking, which presents another variant of thermal fatigue cracks, was clearly marked in areas exposed to local stress concentrations and can lead to crack initiation in a die casting mold. Then, these cracks can grow and became, more pronounced driven by several factor including thermal fatigue, erosion, oxidation, soldering of the molten metal to the die surface, deformation of die contact surface and dangerous fracture. The formation of thermal fatigue cracks may lead to a loss of surface material as small fragments splinter off from the surface. To endure these severe conditions the tools are made of hot-work tool steel, designed to have and adequate combination of hot strength, toughness, and ductility, as well as thermal conductivity and thermal expansion. Die and its shaped parts maintenance may be done by grinding or welding if the surface quality or dimensions of the castings are no longer sufficient [4-6]. However, the tool and service costs constitute a remarkable part of the production costs in die casting and there are numerous approaches to optimize the lifetime of the dies. In general die life may be enhanced by geometric factors in die design (governing stresses and thermal gradients), die material considerations e.g., machinability, heat treatment, toughness, resistance to wear and heat checking, processing conditions (preheating, heating and cooling cycles, machine closing force, lubricants, service intervals) and die surface considerations [5,6]. The Fig. 1 shows the degradation mechanism of the mold part - the mold insert used for high-pressure aluminum die casting due to the repetitive cycles of the casting process.

***Fig.1** Degradation of the mold part*

Surface treatments, such as nitriding, hard PVD coatings and others are often applied for casting dies to reduce failure mechanisms (abrasive wear) and improved thermal fatigue resistance. In recent years, hard PVD coatings on nitride-based to the surface of the mold and its shaped parts have been applied to increase the overall life of the molds and their parts used in high-pressure die casting of aluminum and its alloys. In Fig. 1 is a comparison of the life of a mold for high-pressure aluminum die casting without the use of PVD coatings and using PVD coating based on nitrides CrN, Ti (C, N). Hard coatings based on nitrides and carbides of transitions metals (TiN, CrN, CrAlN, CrC) and duplex treatments that combine surface modification of the die with a hard coating have also been developed. The use of PVD coatings has been shown to increase the service life several times (4 to 17 times). The die coating system to be far superior to that of the uncoated die with respect to cost performance criteria. The die coating system must be [7-9]:

➢ Non-wetting with liquid aluminum

➢ Wear and oxidation resistance

➢ Able to accommodate the thermal residual stresses induced by shot cycling (temperature and pressure) during pressure die casting process

➤ Adherent to the die material – and engineered interface

➤ Able to delay the onset of thermal fatigue cracking (heat checking)

The Fig. 2 represents a diagram of an optimized coating architecture for die coatings used in aluminum high pressure die casting [7]:
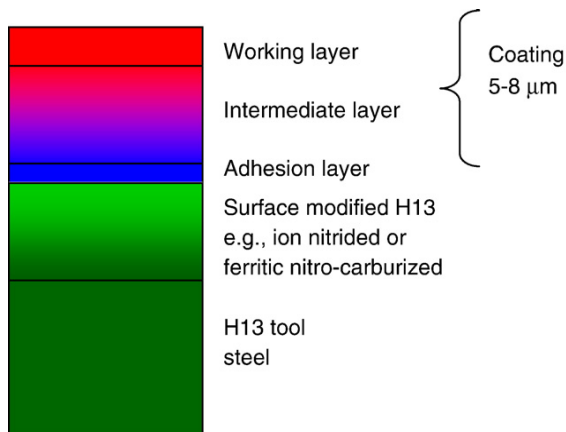
Fig.2 *A diagram of an optimized coating architecture for die coatings used in aluminum high pressure die-casting.*

2. Materials and Methods

Uddeholm Dievar was used as the base material for experiment, which is used in the production of die casting molds for aluminum and their shaped parts. The chemical composition of the base material is in Tab.1.:

Table 1: Chemical composition of Uddeholm Dievar

Element	C	Si	Mn	Cr	Mo	V
Wt. %	0.38	0.2	0.5	5	2.3	0.6

The mold parts were manufactured according to the drawing documentation and were tempered to a hardness of 48 HRC and subsequently fitted into the mold body for high-pressure casting of aluminum alloy base on Al-Si-Cu realized on machines with a cold filling chamber. The mechanical properties of the base material are shown in Tab.2:

Table 2: Mechanical properties of Uddeholm Dievar

Mechanical properties of Uddeholm Dievar				
Hardness [HRC]	Tensile strength Rm [MPa]	Yield strength Rp$_{0,2}$ [MPa]	Ductility [%]	Relative narrowing [%]
52	1900	1560	12.5	52

AlXN^3 and nACRo^3 coatings were used to perform PVD coating. For the nano-multilayer coating, ALXN3 (X=Cr) is the basic adhesive coating of CrN, followed by Al/CrN nano-coating and the top coating is AlCrN. It is a tough coating with high resistance to abrasion at high temperatures up to 900 °C.

The nACRo^3 is a nanocomposite coating consists of AlCrN nanocrystalline grains that are embedded in an amorphous Si$_3$N$_4$ matrix. The coating are three layers: the first adhesive coating consists of CrN, the second coating is AlCrN, and the three final top coating is formed by a nc-AlCrN/a-Si$_3$N$_4$ nanocomposite coating. This nanocomposite coating is very tough, resistant to abrasion to high temperature up to 900 °C – 1100 °C. The light microscopy technique was used for crack site analysis. The quality control of the mold surface before coatings process consisted of a visual control, which was carried out in accordance with ISO 13018. The visual control was followed by a capillary control according to ISO

23277. Scanning electron microscopy was used for chemical elemental analysis at the crack site. The Mercedes test (Tab.3) was used to measure the adhesion of the coatings, which was performed on a universal hardness tester UH 250 with a Rockwell indenter at a load of 1500 N according to ISO 18265. The evaluation is performed by assigning it to the appropriate category with the adhesion number HF1 – HF6, which characterizes the degree of cracking and peeling layer.

Table 3: Coating adhesion by the Rockwell indentation test

Evaluation of coating adhesion by the Rockwell C indentation test		
	HF 1- good adhesion a small amount of cracks	HF 4 - reduced adhesion peeling around the edge of the indent
	HF 2 - satisfactory adhesion small peeling between cracks	HF 5- insufficient adhesion peeling even at greater distances from imprint
	HF 3- reduces adhesion peeling over more than two cracks	HF 6- unsatisfactory adhesion complete peeling around the indentation

A Jeol JSM 7000F scanning electron microscope with an EDX analytical unit was used to determine the chemical elemental analysis of the defect environment according to ISO 15362. Microhardness measurements were performed on a Leco LM 700 microhardness tester with a Vickers indenter HV 0.025 according to ISO 6507-1. Scratch test was used to evaluate adhesion of coatings and was performed on an AMI CSEM -Revertest device (feed 10 N/mm, load up to 80 N, track length approx. 8 mm). All samples for analysis were prepared by metallographic procedure. The samples were prepared in conductive dentacryl Polyfaste, then were ground on sandpaper of various grits (240, 400, 600 and 800), moistened with water, polished with 1/0 diamond paste, washed, and rinsed with benzine alcohol. Prior to observation, all samples were purified in methanol in an ultrasonic device. Samples were taken from the molded parts of the mold half according to Fig. 3:

Fig.3 *Sampling procedure from the mold part*

3. Results and discussion

In Fig.4 is worn solid half of the mold part - mold insert and appearance of cracks of the mould after capillary test.
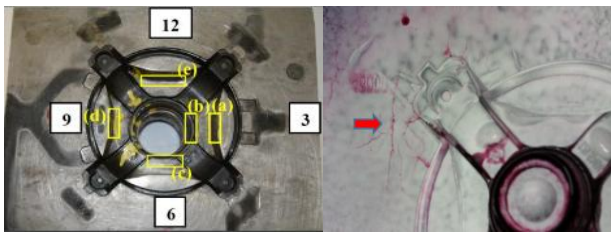
Fig.4 Worn solid half of the mold insert (left); appearance of cracks by capillary method (right)

Wedge-shaped branched crack were observed in the analyzed places of the mold part due to cyclic stressinf of the mold parts in the area of elastic deformations. The cracks that formed in the areas of sharp transitions in the corners of the mold parts were filled with oxides and a release agent during the repetitive casting process. It is precisely due to the repetitive elastic deformations during the repetitive cycle of the casting process that the oxide filler and the release agent acted as a wedge, which was pressed into the mold material and caused wedge branched cracks. The analyzed cracks observed by light and electron microscopy are shown in Fig.5:
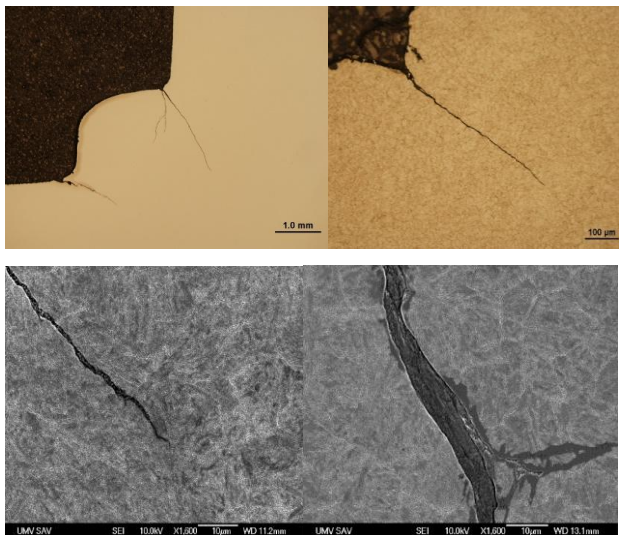
Fig.5 Cracks in the zones of sharp transitions of the surfaces of shaped parts of the mold (light and electron microscopy)

The presence of other chemical elements, namely the presence of oxygen, calcium and silicon, was observed in the filling of wedge shaped cracks formed by oxide and a separating agent. Outside the crac-containing zones, the microstructure was formed by heterogeneous sorbitol together with fine globulite carbides on Fe-Cr-Mo-V.

The presence of other chemical elements, namely the presence of oxygen, molybdenum, chromium and silicon, was observed in the filling of wedge shaped cracks (Fig.6) formed by oxide and a separating agent. Outside the crac-containing zones, the microstructure was formed by heterogeneous sorbitol together with fine globulite carbides on Fe-Cr-Mo-V. EDX analysis was also performed at the crack location according to the Fig.6 on the mold part shown in the Tab. 4:
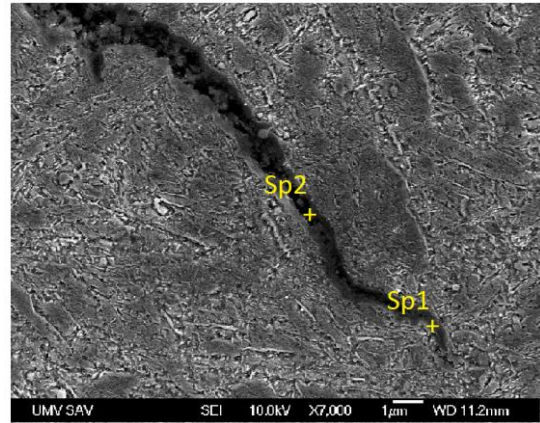
Fig.6 Zone of sharp transitions of the surfaces of the shaped parts of the mold

Table 4: EDX analysis (Sp1, Sp2) at a crack site

	Element	Wt. %	At. %
Sp1	O	24.85	52.57
	Si	3.13	3.78
	Fe	7.2	43.65
	Totals	**100**	
Sp2	O	23.58	51.02
	Si	3.91	4.82
	Fe	65.83	40.8
	Cr	3.13	2.8
	Mo	3.54	1.28
	Totals	**100**	

3.1 Adhesion of PVD coatings

Good adhesion of PVD layers to the substrate was confirmed, determined by the ratio cohesive and the degree of HF = 1, which was characteristic for the occurrence of only isolated cracks and minimal disruption of the integrity of PVD coatings around the indentations. Fig.7 shows the morphology the indentations into the coating surfaces, with only isolated radial cracks in both cases reaching of max. 200 µm. It was measured a degree of adhesion HF = 1-2 according to the Tab.3, which means good adhesion of a coating.
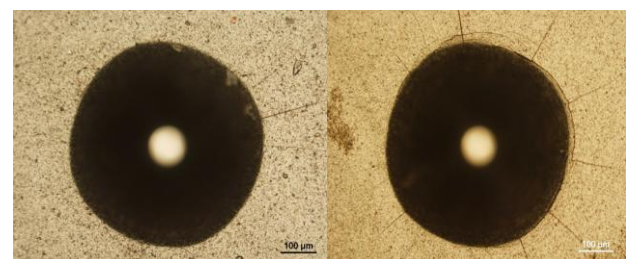
Fig.7 Indentation impression after Mercedes test; AlXN[3](left), nACRo[3] (right)

3.2 Tribological properties of PVD coatings

The device records the course of the increasing normal Fn and the tangential force Ft acting on the indenter, the values of the coefficient of friction and the acoustic emission signal AE. The output is a graphical record of the AE emission signal and the COF depending on the size of the load. The value of the critical load Fz

at which the substrate. In practice, the value of the critical load Fz = 40 N is referred to as satisfactory adhesion. Satisfactory adhesion was recorded on the subject tested samples with applied coatings, because the failure or detection of the substrate occurred at values of about 50 N (Fig.8).
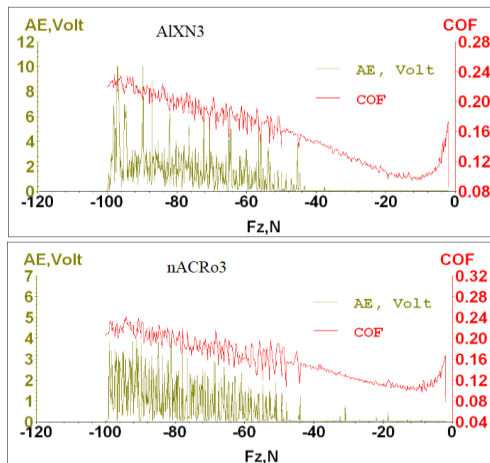
Fig.8 Dependence of acoustic emissions (AE) on the coefficient of friction (COF) of coatings

3.3 Microhardness of PVD coatings

By evaluating the microhardness of the Vickers indenter HV 0.025 of PVD coatings, an increase of about 18% - 25 % compared to the base material of mold was recorded. The microhardness measurement was performed in 16 places, and a graph of microhardness values was subsequently constructed from the measured values. Both minimum and maximum values were measured:

- In the case of the ALXN[3] coating, the minimum microhardness value was 600 HV and the maximum microhardness value was 720 HV

- In the case of the nACRo[3] coating, the minimum microhardness value was 610 HV and the maximum microhardness value was 810 HV

Fig.9 presents hardness profile of coatings and shows an arrow from the area of the coatings to the base material:
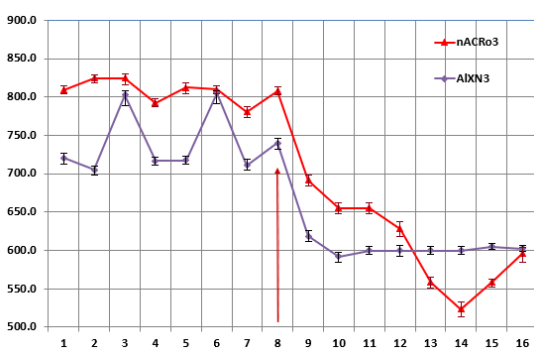
Fig.9 Graph of measured microhardness values

4. Conclusions

The paper is the results of research aimed at finding out the degradation mechanisms of molds for high-pressure aluminum die casting and the possibility of modifying the quality of functional surfaces of molds using PVD nanostructured coatings of a new generation. In the first phase, the degradation mechanisms in the corners of shaped parts (inserts) of the mold in the form of branched cracks due to elastic deformation due to repeated of the casting process were analyzed. In the second phase, a conventional ALXN3

coating and a new generation nanostructured nACRo3 coating were applied to the mold parts. The PVD coatings were of high quality, which was confirmed by tests performed to assess the adhesion, hardness, and COF of coatings. The coatings were compact, intact, and formed a barrier between the base material and the molten metal Al after the high-temperature corrosion test (680 ±20 °C).

6. References

1.   D. Abid, A. Ktari, D. Mellouli, N. Gafsi, N. Haddar: Failure analysis of shot-sleeves used in brass high pressure die-casting process, In: Engineering Failure Analysis, 2019, Volume 104, pp. 177-188

2.   V. Nunes, F.J. Silva, M.F. Andrade, R. Alexandre, A.P.M. Baptista: Increasing the lifespan of high-pressure die cast molds subjected to severe wear, In: Surface & Coatings Technology, 2017, Volume 332, pp. 319-331

3.   S. H. Kang, J.J. Han, W.T. Hwang, S.M. Lee, H.K. Kim: Failure analysis of die casting pins for an aluminum engine block, In: Engineering Failure Analysis, 2019, Volume 104, pp. 690-703

4.   D. Mellouli, N. Haddar, A. Koster, H.F. Ayedi: Thermal fatigue failure of brass die – casting dies, In: Engineering Failure Analysis, 2012, Volume 20, pp. 137-146

5.   J. Wang et.al.: On the failure mechanism for high pressure die casting A390 hypereutectic alloy in low cycle and high cycle fatigue, In: Materials Science & Engineering A, 2018, Volume 723, pp. 48-55

6.   R. Ding et.al.: Failure analysis of H13 steel die for high pressure die casting Al alloy, In. Engineering Failure Analysis, 2021, Volume 124, pp. 105330

7.   J. Lin et.al.: Design methodology for optimized die coatings: The case for aluminum pressure die-casting, In: Surface & Coating Technology, 2006, Volume 201, pp. 2930-2941, Elsevier

8.   K. Bobzin, et. al: Analysis of CrN/AlN/Al$_2$O$_3$ and two industrially used coatings deposited on die castings cores after application in an aluminum die casting machine, In: Surface & Coating Technology, 2016, Volume 308, pp. 374-382, Elsevier

9.   B. Wang, et.al.: Method to evaluate the adhesion behaviour of aluminum-based alloys on various materials and coatings for lube-free die casting, In: Journal of Materials Processing Technology 2016, Volume 237, pp. 386-393, Elsevier

Foam ceramic blocks with low thermal conductivity suitable for the construction of roads and urban square pavements and non-load-bearing partition walls

Gergana Mutafchieva, LyubenLakov, Mihaela Aleksandrova, Rositza Dimitrova, Gabriel Peev

Bulgarian Academy of Sciences, Institute of Metal Science, Equipment, and Technologies with Center for Hydro- and Aerodynamics "Acad. A. Balevski ", Shipchenski Prohod Blvd. 67, 1574 Sofia, Bulgaria, cl.creativeline@gmail.com

Abstract: *Lightweight porous ceramic has a number of advantages over the tightly sintered one depending on the field of application. As a building material with low thermal conductivity and good sound insulation properties, foam ceramic is a suitable material for the production of thermal and sound insulation panels, partition walls, as well as for layers laid under asphalt to protect road and urban square pavements from freezing. As a filling, foamed ceramic materials are also added during the production of lightweight concrete used in construction and architecture and in the manufacture of decorative and non-structural insulation elements. In the present study we consider the characteristics of marl clay, found around the village of Lovets near the town of Shumen, with coal as a foaming additive, and the technological regulation for the manufacture of foam ceramic blocks.*

Keywords: *FOAM CERAMIC, LIGHTWEIGHT CERAMIC MATERIALS, POROUS COMPOSITE MATERIALS, LIGHTWEIGHT EXPANDED CLAY.*

1. Introduction

Foam ceramic materials included in various composites [1] are becoming increasingly popular in the manufacture of construction and technical elements (bricks, filters, etc.). The present study considers the possibility of using marl clay in the production of foam ceramic insulation material by foaming the latter with added coal powder [2]. For the purposes of the study, samples were developed with different weight percentages of foaming agent. The temperature dependences of the properties of the ceramic mass on the content of coal powder were studied. The chemical analysis and the phases obtained after high-temperature liquid-phase synthesis are presented and a tomographic analysis of a sample of foam ceramic material is performed.

2. Experimental part

The composition of the sample was developed on the basis of sedimentary marl rock from a deposit around the village of Lovets near the town of Shumen. The material is suitable for making ceramic products with densely sintered ceramics, as well as ones with high porosity such as insulation blocks, e.g. bricks. Since the compaction after synthesis depends on the modification of the raw material and on the temperature regime, in order to obtain foamed ceramics, to the multicomponent mass is added coal powder which releases CO_2 during combustion and acts as a foaming agent [3-4].

3.1.Research

The following studies were performed: differential thermal analysis of the modified composition (Fig. 1); chemical analysis of the clay, presented in Table. 1; X-ray phase analysis, shown in Figure 2; temperature regime in synthesis, presented in Table. 2 [5]; tomographic analysis, presented in Figures 3, 4 and 5. The ratio between closed and open pores, as well as the total porosity are shown in Table. 3, and the amount of pores with sizes from 1 to 3 mm – in Table. 4 [6].

Table 1. *Chemical analysis*

Chemical composition	Percentage
Na_2O	0,7
MgO	2,24
Al2O$_3$	11,36

SiO_2	35,19
P2O$_5$	0,1
K_2O	2
CaO	19,58
TiO_2	0,47
MnO	0,11
Fe_2O_3	4,85

Based on the experiments conducted on the marl sedimentary rock, the fireclay obtained from it, as well as on kaolin and coal powder, an optimal composition for the production of ceramic thermal insulation blocks was developed. The added foaming agent constituted up to 10% of the total weight, and the high-temperature synthesis was carried out at a temperature in the range of 1,115-1,120° C. Obtained as a result was a lightweight foam ceramic material, with a low coefficient of heat conduction in the range of 0.095 to 0.12 W/m2K, compressive strength of 120 to 130 MPa, and wear resistance of 0.75 g/cm2.
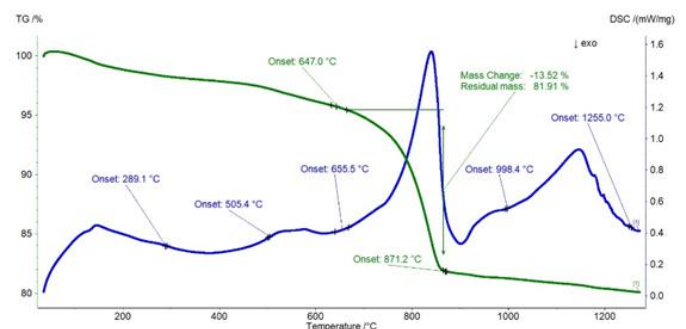
Fig. 1. *Differential thermal analysisof a modifiedcompositionbasedonmarlsedimentaryrockwiththeadditionof 10% coaldust.*

A loss of mass of 13.52% is observed following the ignition of the composition's mass modified with the foaming agent (Fig. 1). Mass losses are due to the processes of dehydration, de-carbonization and oxidation of the carbon from the coal dust. There is a change in the thermogram at different temperatures, with the above mentioned processes starting as early as at 290° C. An endothermic effect is observed in the temperature range from 800 to 900°C, associated with the decomposition of the carbonates. Liquid-

phase transition at a temperature of 1,150° C is observed, and complete melting at a temperature of 1,255° C, which means that the sintering must take place before the maximum temperature is reached. X-ray phase analysis of the obtained foam-ceramic material has also been performed showing the presence of the petrurgical phases diopside and anortite.
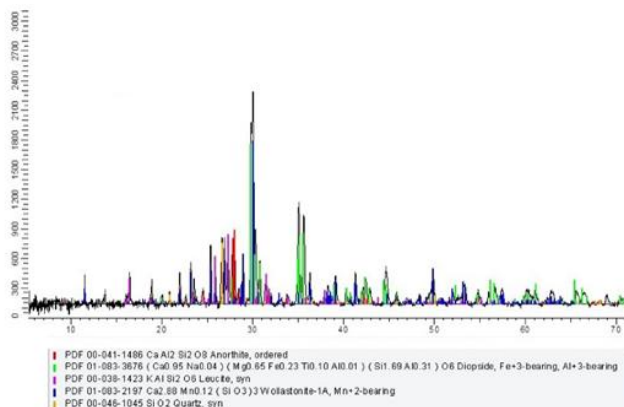
Fig. 2. *XRD of the modified marl clay.*

The temperature regime of the synthesized sample is presented in Table 2. Heating is done gradually, raising the temperature by 2°C / min. The retention of the temperature is in several intervals - the first one allows to separate the freely bound water, the second one helps to dehydrate the structural water, the third one allows to complete the decarbonization processes, and finally the liquid-phase transition takes place.

Table 2. *Temperature regime in the synthesis of the studied materials.*

Temperature,°C	Retention, min
150	60
650	60
950	180
1120	180

The computer tomography method was used to obtain information about the volume of the material, as well as to calculate the porosity. After irradiation using 3D X-ray micro-tomographerSkyScan 1272, a reconstruction of the sample was performed using NRecon software, where the obtained X-ray projections were "assembled" to produce a digital model of the sample. Using CTVox software, 3D images of the sample and images of its different sections can be obtained. The software for calculating various geometric parameters is CTAn, which in our case yielded data on the closed and the open pores, on the total porosity, on pore diameters and on the pore percentage distribution in the sample volume. Figure 4 shows visualizations of the sample, which is irregularly shaped, has dimensions of approximately 35 x 20 x 5 mm, and is rotated around a vertical axis. Clearly visible are the open pores formed in the synthesized sample. Airspaces of different sizes and shapes are observed, passing through the whole volume of the sample.
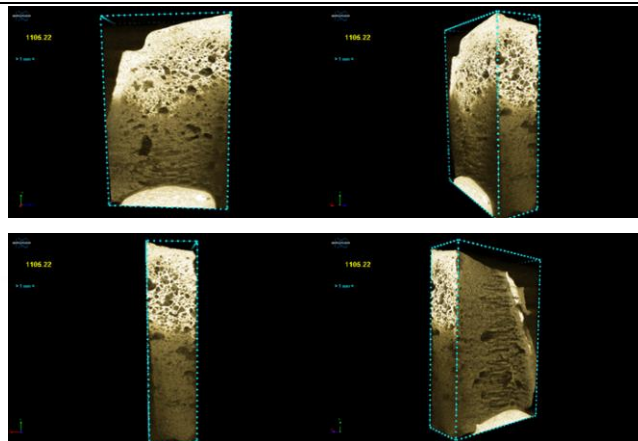
Fig. 3. *Visualizationofthesamplerotated around a verticalaxis.*

Fig. 3 shows a longitudinal section of the scanned sample in 1 mm steps. Deeper inside can be observed the formation of new air spaces in the individual layers.
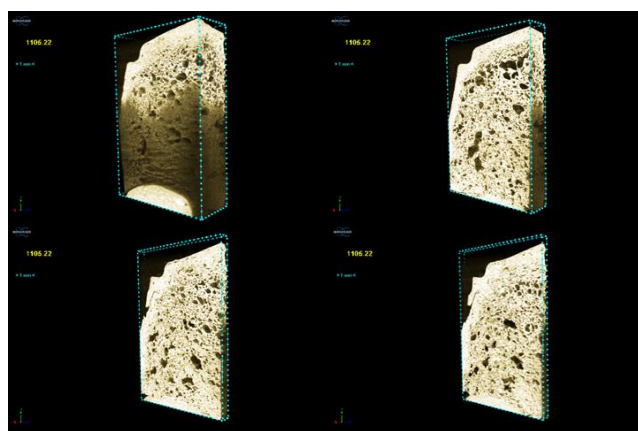
Fig. 4. *Visualization of the longitudinal section of the sample in steps of 1 mm.*

Fig. 4 shows a cross section in steps of 1 mm. The formation of larger open pores below the surface layer is observed, which indicates that the surface layer is significantly denser. This might facilitate the process of forming products with a relatively smooth and dense surface and a porous structure.
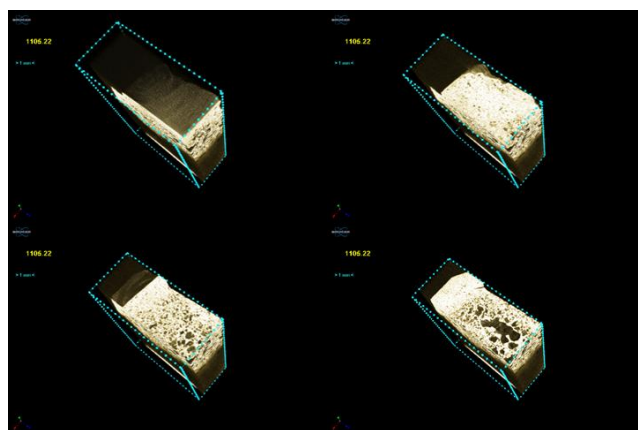
Fig. 5. *Visualization of the cross-section of the sample in steps of 1 mm.*

A total of 1374 layers of the scanned sample were examined at an image resolution of 1224 x 980 pxl, with a pixel size of 21.57 µm, at a rotation step of 0.6° and full rotation of the sample (360°). The filter used was 0.11mm Cu at source voltage and current respectively 100 kV and 100 µA. The percentage of closed and open pores, as well as the total porosity, are presented in Table 3. In

Table 4 is shown the percentage of pores with dimensions from 1 to 3 mm relative to the total amount.

Table3.*Ratio between closed and open pores, as well as total porosity of the studied sample.*

Pores type	Percentage
Closed pores	2.47
Open pores	26.41
Total porosity	28.88

Table4.*Percentage of pores with sizes from 1 to 3 mm.*

Pore size	%
under 1 mm	83.65
from 1 to 2 mm	14.50
from 2 to 3 mm	1.85

3. Conclusion

A foam-ceramic thermal insulation material has been created that can be used for the making of products with improved physical-mechanical and tribological indicators, with a low coefficientofheatconduction, and suitable for application in the road and civil construction industry.

4. References

1. Roces, E.,Muniz-Menendez, M.,Gonzalez-Galindo, J.,Estaire, J. Lightweightexpandedclayaggregatepropertiesbasedonlaboratorytesting. Construction and Building Materials. 313. 2021.

2. Марковска И., Богданов Б., Христов Я., Георгиев Д., Русев Д.: Олекотени керамични материали с пълнител от боотпадъци. Научни трудове на Русенския Университет, том 49, серия 9.1, 2009, страници: 70-74.

3. Berkowicz-Płatek, G., Leski, K., Zukowski, W., Wrona, J. Processingoflow-densitywasteinfluidizedbedmadeoutoflightweightexpandedclayaggregate. JournalofCleanerProduction. 349. 2022.

4. Steiner, A. Foam glass production from vitrified municipal waste fly ashes. Eindhoven. 2006. ISBN 90-386-2748-3. p.p. 139-169.

5. B. T. Jivov, Y. B. Dimitriev, E. P. Kashchieva, C. T. Petkov,„Glasses and Glass Ceramics in the System P_2O_5-B_2O_3-Ag_2O", Physics and Chemistry of Glasses, 41 (6), 2000,pp. 352-354.

6. Petkov, V.; Dimitrova, R.; Lakov, L. Structure and composition of innovative porous composite material. Machines, Technologies, Materials. Issue 8. 2020. p.p. 362-365.

Development of innovative commercial dishwasher using gas-heated water for energy efficiency

Zafer Kahraman[1], Murat Hacı[1], Soner Gürcü[1], Hakan Serhad Soyhan[2,3]

[1]Öztiryakiler Madeni Eşya San. Ve Tic. A.Ş, R&D Technology Center
34500 Büyükçekmece, İstanbul, Turkey
[2]Sakarya University, Fire and Combustion Research Centre, Esentepe Campus, Sakarya, Turkey
[3]Team-San Ltd. Sti., Esentepe Campus, Sakarya University, 54050, Sakarya, Turkey
zkahraman@oztiryakiler.com.tr

Abstract: *Commercial dishwashers are among the most important products for commercial kitchen personnel as they clean dirty products (plates, glasses, cutlery, etc.) in a short time (between 1 and 4 minutes according to the program). In recent years, customers' demands for energy-saving products have been increasing. Therefore, instead of using the electrical energy to be obtained after the combustion of natural gas in power plants, the use of direct natural gas in a commercial dishwasher contributes to reducing the carbon footprint. In this study, the original design studies of the combustion system of the innovative commercial dishwasher prototype using water heated with gas were carried out. For the first time in our country, the system that enables the heating of water with gas was designed as a module other than the existing commercial dishwasher. An independent combustion system has been developed to provide easy use to other commercial dishwashers on the market. Simulation studies have been used effectively in the design verification phase in order to provide the most efficient combustion conditions for different gases (natural gas and LPG) in the original designed combustion system. Combustion analyses were carried out by parametric study for different operating conditions. In the innovative commercial dishwasher prototype that uses water heated with gas, optimum temperature values have been obtained for effective washing at the water inlet and water outlet points of the uniquely designed combustion system. As a result of the tests and evaluations, the most effective working range of the innovative prototype was determined.*

Keywords*: COMMERCIAL DISHWASHER, COMBUSTION TECHNOLOGY, WATER HEATED SYSTEM DESIGN*

1. Introduction

Various models of commercial dishwashers (undercounter, hood type, conveyor, etc.) have wide areas of use depending on the size of the commercial kitchens. Our company produces all models of these commercial dishwashers for commercial kitchens. In our country and in Europe, commercial dishwashers are used with electrical energy. However, gas-heated water commercial dishwashers have usage shares in the North American market. There are various studies to improve energy efficiency on dishwashers.

Studies carried out in the research of scientific publications related to energy efficiency in the field of dishwashers have been determined to be related to household dishwashers [1-7]. Various studies in this field are summarized below;

Santori and his team investigated the operating performance of an adsorption household dishwasher using different desiccants such as 13X zeolite, microporous silica gel and SAPO-34 zeolite. Thermodynamic comparison of the indicated adsorbents was carried out on the basis of experimental measurement of the main thermophysical parameters such as specific heat, adsorption equilibrium curves and sorption enthalpy. They stated that they achieved 0.636 kWh of consumed electrical energy savings, 41% lower than the standard cycle performed by a standard household dishwasher with a class A energy label [1].

Mohedano and his research team evaluated household dishwashers with camera data processing (PEPT - Positron Emission Particle Tracking) system and simulation analysis (CFD - Computational Fluid Dynamics) under different operating conditions (with/without detergent, at various pump and wash arm speeds). Empty/full basket etc. during the washing process analyzed the water movements according to the variables. They stated that the detergent effect can be neglected in water movements and the effects of design data (washing arm, distribution of dishes, etc.) according to different dish areas [2].

Hauer and Fischer reported that energy consumption was reduced by up to 24% by reducing the energy consumption values from 1.05 kWh to 0.8 kWh in household dishwashers with zeolite mineral added drying system compared to the standard product. In addition, they reported that an environmentally friendly product was obtained by contributing to the reduction of CO_2 emission rates with the mineral additive drying system [3].

In 2021, 32.7% of our electricity production in Turkey was obtained from natural gas. [8].

The distribution of natural gas use in electricity generation in our country by years (2000-2019) is shown in Fig. 1 [9].
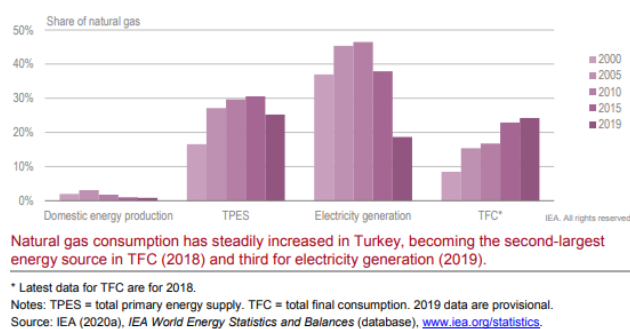
Fig. 1 *Share of natural gas in the Turkish energy system, 2000-2019 [9].*

The gross electricity generation distribution by primary source in the first ten months of 2021 in Turkey is shown in Fig. 2 [10].
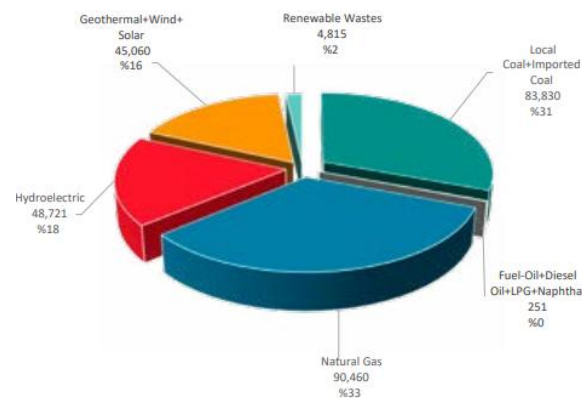
Fig. 2 *Gross Electricity Generation by Primary Source During the First Ten Months of 2021 (GWh). [10].*

In the coming years, in terms of energy efficiency, the use of natural gas in various applications instead of electrical energy will provide significant advantages in terms of the environment.

2. Methodology

With the data obtained from the concept development studies, the design activities of the commercial dishwasher prototype that heats gas and water were carried out. At the last stage of the design activities, the original designs were obtained before the prototype production by utilizing the simulation studies.

Within the scope of this study, the hood (guillotine) type commercial dishwasher was preferred among the existing commercial dishwashers in terms of the application of the original designed combustion system.

The main body of the hood type commercial dishwasher and separate combustion system is made of stainless steel (AISI 304) material.

The draft drawing of the commercial dishwasher prototype using gas and water is shown in Fig. 3.
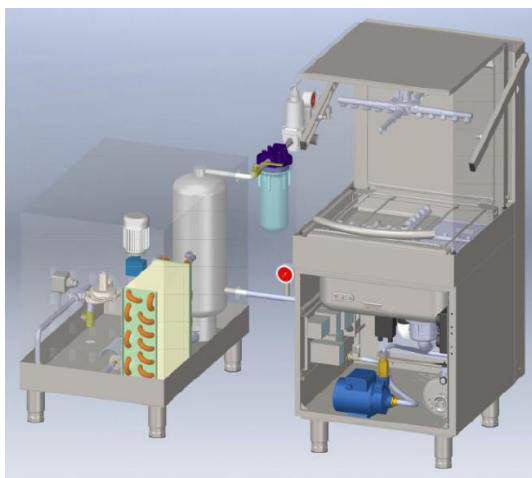
Fig. 3 *The draft drawing of the commercial dishwasher prototype using gas-heated water.*

With the combustion provided in the burner of the combustion system with simulation studies, temperatures close to the adiabatic flame temperature have been reached.

The uniquely designed combustion system consists of three separate parts. The first part consists of the burner where the combustion takes place, the second part consists of the heat exchanger water flow area and the third part consists of the copper heat exchanger.

In the heat exchanger area, after this temperature is transferred to the water, it has been observed that the temperature towards the chimney section decreases, but there is still a usable heat energy in the flue gas.

In the original designed combustion system of the innovative commercial dishwasher prototype, which uses water heated with gas, a boundary layer is placed on the wall areas. Studies were carried out by applying a sweep mesh to a certain region of the flow.

For this reason, it has been seen that a lower capacity heat load can be sufficient by using this energy. Examples of simulation studies on temperature, combustion products, heat exchanger zone heat exchange in a uniquely designed combustion system are shown in Figure 4-7.

Originally designed combustion system of the innovative commercial dishwasher prototype is shown in Fig. 4.
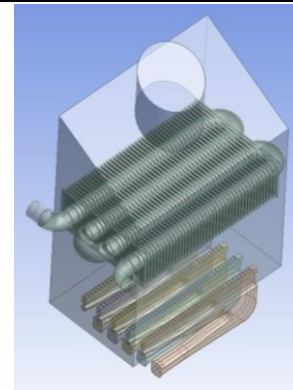
Fig. 4 *Originally designed combustion system of the innovative commercial dishwasher prototype.*

The view of the mesh distribution in the original design combustion (water heating) system design is shown in Fig. 5.
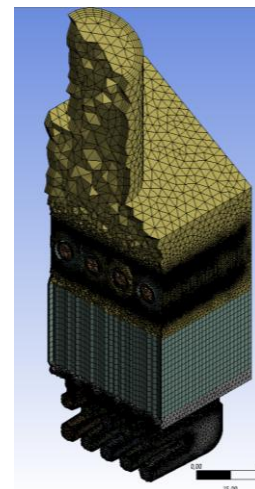
Fig. 5 *The view of the mesh distribution in the original design combustion system design.*

The simulation study of temperature change in the working process of the original designed combustion system of the innovative commercial dishwasher prototype is shown in Fig. 6.
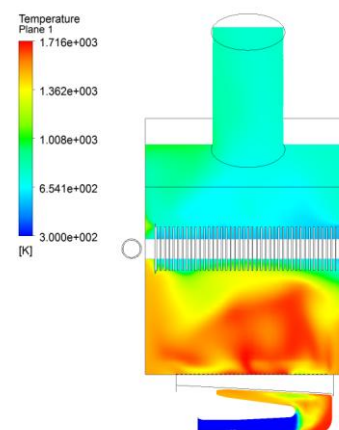
Fig. 6 *Simulation of temperature change in the working process of the original designed combustion system of the innovative commercial dishwasher prototype.*

Simulation analysis of combustion products in a uniquely designed combustion system.
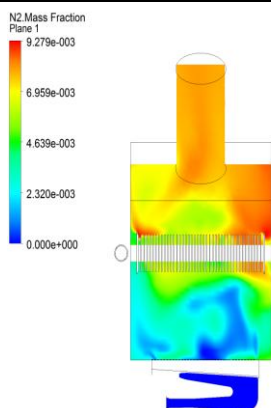
Fig. 7 *Simulation analysis of combustion products in a uniquely designed combustion system.*

The fact that almost all of the oxygen is consumed during the combustion process and the N_2 formation reaches its highest levels in the exhausted gas is an indication that the combustion is complete, and the simulation data shows that the project will be successful.

3. Experimental procedure

The photograph of the innovative commercial dishwashing machine prototype using gas-heated water used in the testing and evaluation phase is shown in Fig. 8.

Fig. 8 *Front view of the innovative commercial dishwasher prototype.*

A photograph of the original designed module providing gas-heated water is shown in Fig. 9.

Fig. 9 *A photograph of the original designed module providing gas-heated water.*

Tests and evaluations of the innovative commercial dishwashing machine prototype using water heated with gas were made according to different gases (natural gas and LPG) and various operating conditions (gas pressures, gas application time, etc.).

4. Conclusions

The most important innovative aspect was the efficient use of gas-heated water for the first time in our country, in the studies carried out with R&D systematics in the original designed commercial dishwashing machine prototype. The gains obtained through various R&D activities are shown below;

By comparing the data in the combustion simulation studies with the data obtained during the test phase, the efficient operation of the innovative prototype using different gases (natural gas and LPG) was ensured.

Different injector diameters (Ø0.90 mm for natural gas and Ø0.65 mm for LPG) and different gas pressures (20 mbar for natural gas and 30 mbar for LPG) have yielded positive results in terms of efficient combustion, depending on the gas usage in the uniquely designed water heating system.

A temperature increase of approximately 65°C was observed between the water inlet temperature and the outlet temperature of the uniquely designed water heating system. It has been determined that a lower capacity heat load may also be sufficient.

As a result of the test and evaluation studies, the prototype of the commercial dishwasher using gas-heated water was successfully obtained. Thus, for the first time in our country, the innovative commercial dishwasher prototype that uses direct gas (natural gas and LPG) instead of electrical energy has been achieved with scientific data.

Acknowledgment

5. References

1. Santori G., Frazzica A., Freni A., Galieni M., Bonaccorsi L., Polonara, F., Restuccia G., Energy, **50**, 170-176, (2013)
2. Pérez-Mohedano R., Letzelter N., Amador, C., VanderRoest C.T., Bakalis S., Chemical Engineering Journal, **259**, 724-736, (2015)
3. Hauer A., Fischer F., Chem. Ing. Tech, **83**, 61-66, (2011)
4. Erdogan M., Baub U., Bardowa A., Applied Thermal Engineering, **160**, 113942, (2019)
5. Bengtsson P., Berghel J., Int Journal of Refrigerator, **67**, 1-9, (2016)
6. Bengtsson P., Eikevik T., Applied Thermal Engineering, **99**, 1295-1302, (2016)
7. Persson T, Applied Thermal Engineering **27**, 120–128, (2017)
8. https://enerji.gov.tr/bilgi-merkezi-enerji-elektrik (01.06.2022)
9. Turkey 2021 Energy Policy Review, The International Energy Agency (IEA), 138, March 2021
10. Energy Outlook 2021, Türkiye Sınai Kalkınma Bankası A.Ş. (TSKB), 12, (2021)

Optimization of technological parameters of blasting process on metal surface roughness

Dagmar Draganovská[1,*], Gabriela Ižaríková[2,*], Róbert Moro[3,*]

Technical University of Košice, Slovak Republic[1,2,3]

dagmar.draganovska@tuke.sk[1], gabriela.izarikova@tuke.sk[2], robert.moro@tuke.sk[3]

Abstract: *The main goal of this contribution is study the microgeometry of blasted surfaces. The aim is to design suitable microgeometric characteristics for the description of pretreated surfaces, experimentally verify the influence of blasting agents of various shapes and sizes on the microgeometry of metal surfaces. The following types of evaluation are used to meet this goal: 2D roughness determination and profilograms, 3D surface visualization and surface volume determination. The results of the experimental part will contribute to the optimization of technological parameters of the tearing process.*

Keywords: *abrasive blasting, surface, microgeometry, blasting means, parameters of roughness*

1. Introduction

Blasting is a mechanical type of surface treatment of the base material. Upon impact with the surface of the blasted material, the blasting agent (tool) causes qualitative changes in its surface layers, thus creating the typical surface morphology that characterizes this method of material processing. The character of the blasted surface is given mainly by the shape of the applied grain of the blasting means. The microgeometry of the surface after blasting is also influenced by the hardness of the grain, the particle size distribution of the fraction, the type of material and the weight of the grain of the blasting means. The quantitative effect of blasting is characterized by the blasting regime. Its main parameters are grain flight speed, angle of incidence and substrate quality. [1-2]

The aim of pretreatment of surfaces on which coatings will be subsequently applied is, in addition to achieving the required surface morphology, also its perfect cleaning of scale, corrosion products and other impurities. The type of blasting means and also the different properties of the dirt to be removed have a predominant effect on blast cleaning. When applying the round blasting agent, the dirt is partially pushed into the surface layers, while when blasting with a sharp-edged blasting mean, secondary contamination occurs through the graining of the grains into the surface of the substrate. The impact of the round blast grain on the base material causes a surface trace, the edges of which are pushed above the surface level. As a result of the tensile and compressive stresses which are induced in the scale layer, the integrity of the scale is disrupted at the point of impact, which largely contributes to their separation from the base material. [3-5]

A characteristic feature of the incident sharp-edged grains of the blasting means are the jams in the base material, where there is also the possibility of pushing the scale. Despite the fact that large grains have a larger thickness, it is possible to obtain a better quality blasted surface by the action of small grains, with better coverage of the surface with traces of falling grains. The paper deals with the optimization of technological parameters of the blasting process for the roughness of the metal surface, especially in terms of the choice of type and size of blasting agent.

2. Materials and methods

1. Planar surface characteristics – the evaluation in 2D

The experiment was performed on test specimens marked S235JR + AR. It is a hot-rolled structural steel with dimensions of 100x50x10 mm. The chemical composition of the material is given in Table 1.

Table 1: Chemical composition of materials S235JR+AR, wt. %

Fe	C	Si	Mn	P	S
99.04	0.154	0.179	0.416	0.006	< 0.002
Cu	**Al**	**Cr**	**Mo**	**Ni**	**V**
0.048	0.019	0.056	0.012	0.048	< 0.002

For the purpose of the experiment, the individual surfaces of the nine test specimens were blasted with three different types of blasting means. - metal blasting means of regular spherical shape - steel granulate steel shot - SS - is made of specially modified super-ectoid steel. Its characteristic feature is a fine homogeneous structure, which is ensured by tempered martensite. This structure shows ideal resilience and good fatigue resistance of the material. - metal blasting means of irregular sharp-edged shape - steel grit steel grit - SG - is produced by crushing specially heat-treated grains of steel granulate.

This blasting means has a generally sharp-edged grain shape and is used for surface treatment and cleaning. - non-metallic blasting agent of irregular sharp-edged shape - brown corundum - brown corundum - BC - It is a synthetic material based on alumina (Table 2). It is used where a high quality blasted surface is required. Each of these blasting means was used at three different grain sizes. Table 2 shows the individual sample sizes and designations.

Table 2: Overview of types and designations of used blasting means

Blasting means	Medium grain size [mm]	Identification of the sample
Steel shot S280	0.85	**SS1**
Steel shot S330	1	**SS2**
Steel shot S390	1.18	**SS3**
Steel grit GH40/8	0.5 – 0.6	**SG1**
Steel grit GH25	0.85 - 1	**SG2**
Steel grit GH18/13	1.18 – 1.4	**SG3**
Brown corundum F30	0.5 – 0.71	**BC1**
Brown corundum F24	0.6 – 0.85	**BC2**
Brown corundum F20	0.85 – 1.18	**BC3**

The steel sheet samples required for the experiments were blasted using an Airblast ABSC 1440 pneumatic blasting machine. The blasted samples were then measured for roughness parameters using a Mitutoyo Surftest SJ-201 contact roughness tester. The surface classification in terms of roughness was performed in accordance with STN EN ISO 4287. The basic source of information is the surface profile, which is created by cutting the actual surface with a defined area. The parameters Ra - the middle arithmetic deflection of elaborated profile on the basic length, Rz - the largest height of the profile on the basic length, RPc - the average number of peaks per the average were evaluated.

The display of blasted surfaces of test specimens in 3D, realized by software, was performed for the purpose of a more detailed analysis of the character of blasted surfaces and in order to obtain their visualization. The scanning tip of the Surftest SJ-201 profilometer produces mutually parallel profile curves with a defined scanning spacing (0.1 mm perpendicular to the measuring

length), on the basis of which the resulting 3D interpretation of the surface is created.

3. Results

The values of the roughness parameters for surfaces blasted with different types of blasting means with different grain sizes are shown in Fig. 1.
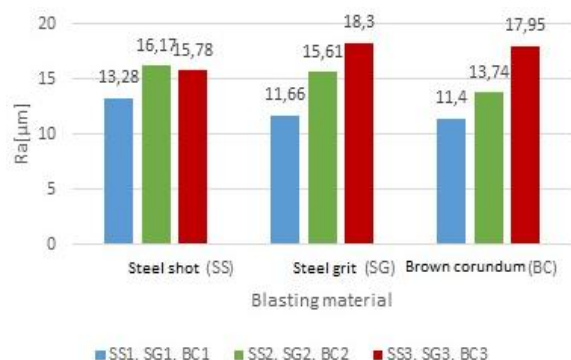
Fig. 1: Ra parameter values

From Fig. 1, it can be stated that the largest increase in the parameter Ra was found in samples blasted with steel grit and brown corundum. The increases were minimal in the samples blasted with steel granulate (SS1 - SS3). This fact can be explained by the type of blasting agent used in terms of shape, as well as by the gradation of the diameters of the individual blasting grains.
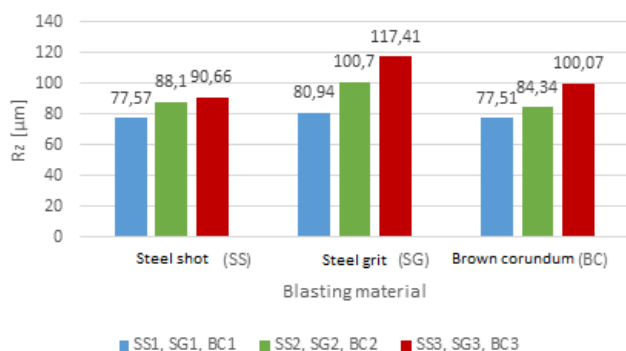
Fig. 2: Rz parameter values

The parameter Rz, according to Fig. 2, shows the largest increases in samples blasted with steel grit (SG). The course of samples blasted with steel granulate is similar to the parameter Ra.
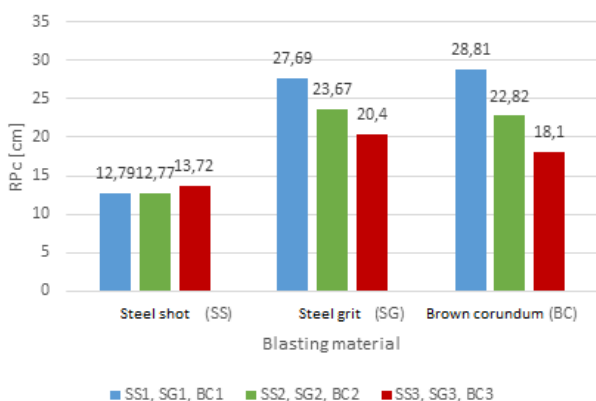
Fig. 3: RPc parameter values

In Fig. 3, the surface area was evaluated by the RPc parameter. Here it can be stated that the samples blasted with steel granulate do not show a significant change in surface fragmentation, which is caused by the use of a round type of grain. Samples blasted with steel grit and brown corundum showed more pronounced differences in segmentation using different grain sizes, with the most significant change occurring with brown corundum blasting.

The performed measurements on different types of blasted surfaces proved the unambiguous influence of the use of the type, size and shape of the blasting mean on the final character of the blasted surfaces in terms of roughness and articulation. Based on the measurements and their results, it can be stated that in addition to the characteristic Ra, which is the most commonly used quantity in the evaluation of surface roughness, it is necessary to qualify the evaluation of microgeometry with other characteristics, allowing more detailed definition such as Rz and RPc, or other suitable parameters (e.g. RSm). Visualization of surfaces using their 3D is shown in Fig. 4 - 9.

The views were created based on the processing of the measured data matrix using the MATLAB software. Imaging the surfaces of the test specimens by means of 3D and topographic images obtained on the basis of the measured values helps to improve the idea of the condition of the surfaces after blasting with different blasting means with different grain sizes. The effect of the shape and grain size of the blasting agent on the final character of the surface after blasting was also demonstrated by means of these images.

The sample surfaces blasted with steel granulate (spherical blasting agent) shown in Figs. 4-6, show typical, intersecting spherical canopies, the size of which depends on the grain size. Fig. 7-9 represent surfaces blasted with steel grit - a sharp-edged blasting agent, where greater articulation is visible.

This is due to deep jams in the base material, which is the result of sharp, uneven grains of crushed steel and brown corundum. The size of the clogs was determined by the grain size of the blasting means.
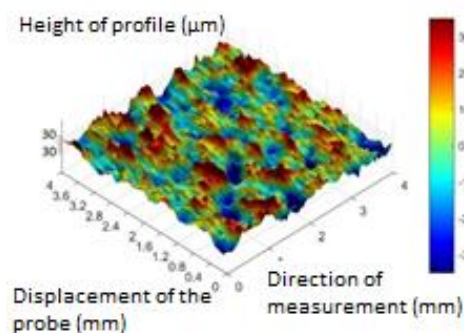
Fig. 4: 3D surface after blasting with steel shot - SS1
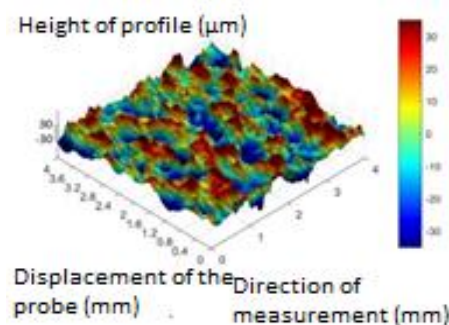
Fig. 5: 3D surface after blasting with steel shot - SS2
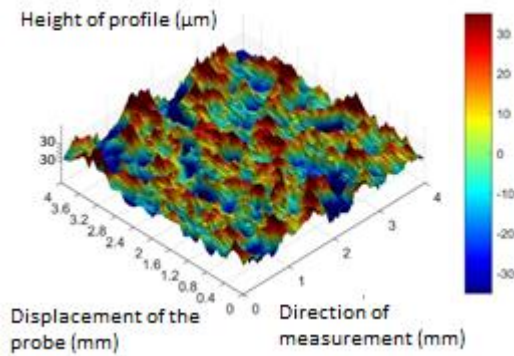
Fig.6: 3D surface after blasting with steel shot - SS3
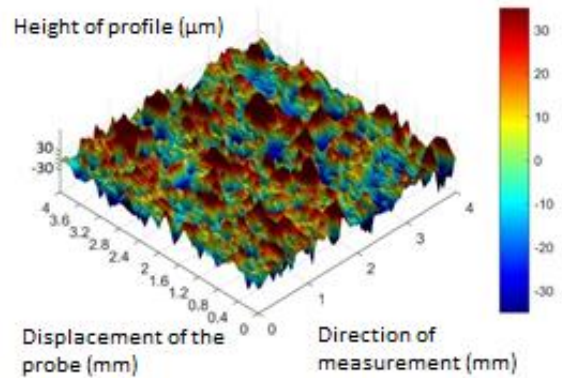
Fig. 9: 3D surface after blasting with steel grit - SG3
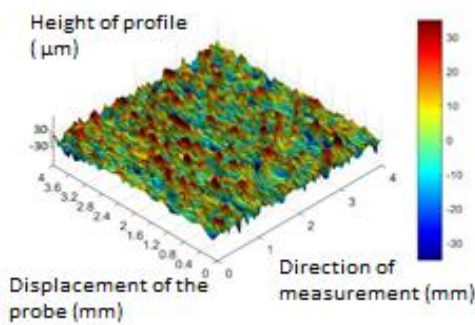
Fig. 7: 3D surface after blasting with steel grit - SG1
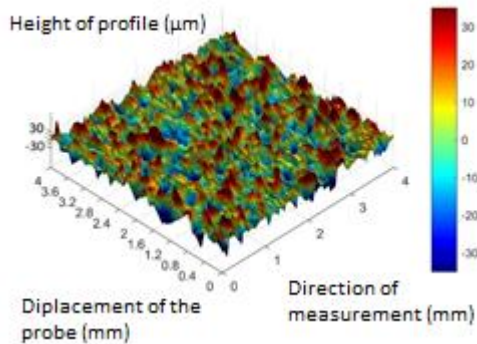
Fig. 8: 3D surface after blasting with steel grit - SG2

Conclusion

The essence of surface blasting, as a form of their mechanical pretreatment, lies in the creation of a new surface with new properties, which form a prerequisite for the ideal anchoring of subsequently applied coatings.

The quality of the blasted surface is determined primarily by the selected type of blasting means - (material, grain size and shape) and the blasting mode. The mentioned parameters form the basis for the blasting process and are chosen with regard to the subsequent use.

The surface after blasting shows characteristic features in terms of roughness and articulation, which are different when blasting with a sharp-edged and round type of blasting material. The surface blasted with sharp-edged grains (eg steel grit, brown corundum) does not show as uniformity as the surface blasted with round-shaped granules. For this reason, the more rugged surface after blasting is sharp-edged blasting means.

Such a surface is suitable as a surface under coatings, ensuring optimal surface cleanliness and adhesion of coatings.

Acknowledgement

References

1. J. Brezinová, A. Guzanová, D. Draganovská. *Abrasive Blast Cleaning and Its Application.* Pfaffikon: Trans Tech Publications, (2015)

2. D. Draganovská, G. Ižaríková, A. Guzanová, J. Brezinová, Metals **8**, 11, (2018)

3. X. Tang et al., Scientific reports **7**, 568 (2017).

4. Yu Xiangyong et al., Journal of Engineering Science and Technology Review **3**, 13 (2020)

5. K. Rokosz, Metals **9**, 11 (2019)

The change of microgeometry of metal surface after application of chemical pretreatments

Róbert Moro[1,*], Dagmar Draganovská[2]
Technical University of Košice, Slovak Republic[1,2]
robert.moro@tuke.sk[1], dagmar.draganovska@tuke.sk[2]

Abstract: *Currently, one of the most important and monitored surface properties is the ability to achieve the highest possible level of adhesion after applying a layer of paint or glue. To guarantee this property, it is extremely important to choose the right surface pretreatment. The paper is focused on chemical surface pretreatment and subsequent evaluation of morphological surface changes after application of various selected types of chemical pretreatment based on roughness parameters.*

Keywords: *chemical pretreatment, surface, microgeometry, roughness*

1. Introduction

The condition of the surface is determined by the resulting properties of the metal components. Surface imperfections are constantly affected by the properties of the material. In practice, the actual metal surface is characterized by conditions and therefore it is necessary to study the properties and subsequent changes of the material already on the surface layer. The resulting surfaces of the components reflect the applied production processes, which significantly affect the achieved surface roughness and therefore it is necessary to continuously monitor these surface changes in terms of roughness. Among other essential surface properties, we also specify the ability of the material to achieve the highest possible degree of adhesion.

Subsequently, the adhesion of the applied coating or the best possible bond between the substrate and the adhesive in the technology of gluing materials is observed. The technology of joining materials is known in practice and is constantly one of the widely used technologies due to its advantages, which it provides in comparison with other technologies using an additional adhesive element. Therefore, it is necessary to consider the application of the correct surface pretreatment, which will significantly contribute to achieving high adhesion of bonded surfaces. Pretreatment can be performed by chemical surface pretreatment, so-called conversion coatings.

The formation of conversion coatings consists in the reaction of the metal surface with the surrounding environment in which the metal is present during surface pretreatment. Conversion coatings are characterized by their high electrical resistance, which affects the corrosion protection of metal surfaces. Conversion coatings have a high level of adhesion to the base material and insolubility in water and solvents. [1-3]

Coatings or adhesives, which are then applied to conversion coatings, show excellent anchorage to the pre-treated surface. The paper is focused on the evaluation of surface changes after the application of different types of chemical pretreatments with the subsequent comparison roughness parameters. [5,7]

2. Materials and methods of surface evaluation

2.1 Used basic materials and their properties

The basic materials used in this research were DC04 and HX340LAD + Z steel sheets with a thickness of 0.8 mm and dimensions of 100 x 25 mm. An overview of the materials used and their chemical and mechanical properties are visible in Table 1 and Table 2.

DC04 (W.Nr.1.0338) - it is a surface-treated steel, which is primarily intended for deep drawing of demanding external and internal parts of car bodies and other moldings.

HX340LAD + Z (W. Nr. 1,0933) - it is a hot-dip galvanized microalloyed steel, which is characterized by a fine structure and at the same time increased cold formability. Used with ana dynamically stressed car parts.

Table 1: HX340LAD + Z material properties

Material	Re Min (MPa)	Re Max (MPa)	Rm Min (MPa)	Rm Max (MPa)	A80 Max (%)
HX340LAD+Z	340	420	410	510	21

Table 2: DC04 material properties

Material	Re Max (MPa)	Rm Min (MPa)	Rm Max (MPa)	A80 Max (%)
DC04	210	270	350	38

2.2 Examined chemically pretreated surfaces

a) Without surface treatment - The manufacturer states that the sheet is preserved by electrostatic oiling with an oil weight of 0.5 - 2.5 g.m^{-2}

b) Surface treated with chip-free zirconate passivation - the chromate-free passivation process usually follows the phosphating of steel by all types of phosphating baths. It does not contain chromium ions or other substances harmful to the environment. The product also passivates active surfaces made of unphosphated steel, aluminum and magnesium alloys, zinc coatings after degreasing or otherwise activated metal surfaces. It can also be used as a conversion layer before coating or gluing. The procedure for passivation with chromium-free zirconate was as follows: degreasing, washing, passivation of zirconate (RT, 3 min.), Rinsing, rinsing in demineralized water, drying.

c) Surface with a layer of zinc phosphate - is predestined for phosphating steel, galvanized and hot-dip galvanized objects. The phosphate layer is formed by small crystals that provide protection to the surface against corrosion or as a base layer under the coatings to improve their adhesion. The phosphating process was as follows: degreasing, rinsing, activation at RT - 3 min. - bath stirring, phosphating at 60 ° C - 5 min., Rinsing, rinsing in demineralized water, drying. The activating rinse serves to form phosphate crystal nuclei, resulting in a particularly fine and thin layer of phosphate.[4]

2.3 Methodology of surface microgeometry evaluation and used device

A profilometer with the production designation Surftest - SJ 301, Mitutoyo, Japan was used to measure the individual selected roughness parameters. The profilometer is characterized as a tactile device, the principle of which consists in sensing the examined surface of the sample with a probe with a diamond tip with a radius of curvature 5ym.

The evaluation of the surface roughness measurement was carried out in accordance with the international standard STN EN ISO 4287, by means of which the individual normalized / non-normalized roughness parameters were assessed. [6,7]

The parameters of the device were as follows:

- Measured profile: R,
- Filter: GAUSS,
- A sampling length λc = 0,8 mm,
- A number of sampling lengths N = 5,
- An evaluation length ln = 4 mm.

3. Achieved results and evaluation

3.1 Profilograms and Firest - Abbot curves of assessed chemically pretreated materials

In the attached profilograms of individual surfaces of materials Fig. 1 – Fig. 6 we recorded a change in the surface roughness of both tested materials and on the basis of this fact we can state that the chemical surface pretreatment has an effect on the individual roughness parameters of the monitored samples.

Fig. 1: Profilogram + Firest-Abbot curve for DC sample

Fig. 2: Profilogram + Firest-Abbot curve for DC - BP sample
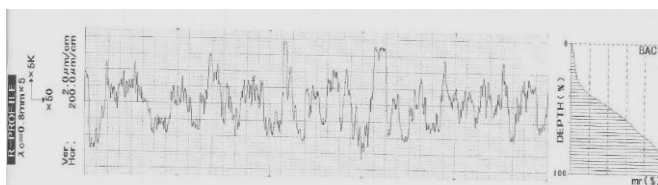
Fig. 3: Profilogram + Firest-Abbot curve for DC - PHZn sampl
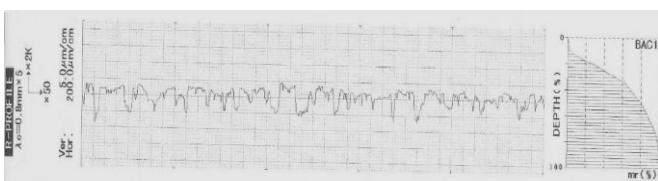
Fig. 4: Profilogram + Firest-Abbot curve for Zn sample
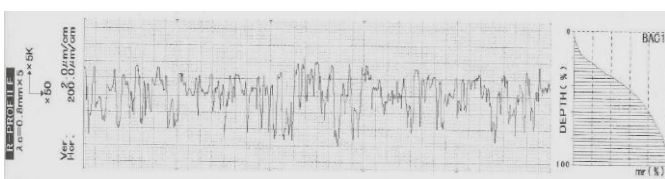
Fig. 5: Profilogram + Firest-Abbot curve for Zn - BP sample
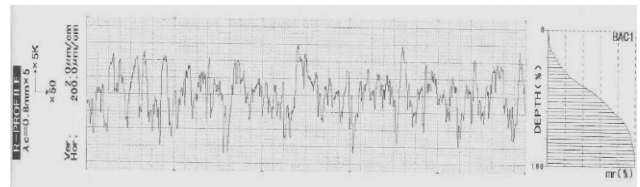
Fig. 6: Profilogram + Firest-Abbot curve for Zn - PHZn sample

3.2 Analysis of the parameter Ra

The assessed statistical characteristics for the parameter Ra are given in Table 3 From the measured values we can state that the highest average value of Ra was recorded in the sample with the designation: DC - PHZn, which showed a value of 1.14 μm.

While the lowest average value of the parameter Ra was recorded for the sample with the designation: Zn - BP with a value of 0.85 μm. The highest measured value of Minima and Maxima was represented by a sample with the designation: DC - BP, which showed values (MAX - 1.44 μm, MIN - 0.9 μm).

While the lowest maximum and minimum values were recorded for the Zn - BP sample with values (MAX - 0.96 μm, MIN - 0.72 μm). Variability characteristics: The Zn - BP sample has the lowest standard deviation value, which was 0.06 μm. The highest standard deviation value was recorded for the sample with the designation: DC - BP, which was defined by a value of 0.15 μm.

Variability characteristics: The Zn - BP sample has the lowest value of the standard deviation, which was 0,06 μm. The highest value of the standard deviation was recorded for the sample with the designation: DC - BP, to which the value of 0,15 μm belongs.

Table 3: Ra parameter values and characteristics

Ra (μm)			
Sample	**Average**	**Min.**	**Max.**
DC	1,05 +- 0,11	0,89	1,30
DC - BP	1,13 +- 0,15	0,90	1,44
DC - PHZn	1,14 +- 0,11	0,89	1,34
Zn	1,07 +- 0,1	0,87	1,28
Zn - BP	0,85 +- 0,06	0,72	0,96
Zn - PHZn	0,87 +- 0,09	0,73	1,01

3.3 Analysis of the parameter Rz

The measured values of the parameter Rz are shown in Table 4. From the following values that were measured, it can be stated that the highest average value of Rz was recorded in the sample with the designation: DC - BP. This sample had a value of 5.96 μm.

The lowest recorded average value of the parameter Rz belonged to the sample with the designation: Zn - BP with a value of 4.96 μm. The maximum and minimum values of the samples were compared. The highest measured value of Maxima was represented by the sample with the designation: Zn, which showed values (MAX - 6.93 μm) and, conversely, the lowest value of the maximum was recorded in the sample Zn - BP, for which we recorded the value (MAX - 5.90 μm).

The highest value of the minimum was shown by the sample marked DC - BP (Min. 4.95 μm), while the lowest measured value of the minimum was represented by the sample Zn - BP (Min. 4.21 μm).

Variability characteristics: Sample Zn - BP has the lowest value of the standard deviation, which was 0,35 μm. The highest value of the standard deviation was recorded for the sample with the designation: Zn, to which the value of 0,51 μm belongs.

Table 4: Rz parameter values and characteristics

Rz (μm)			
Sample	**Average**	**Min.**	**Max.**
DC	5,42 +- 0,5	4,79	6,54
DC - BP	5,96 +- 0,47	4,95	6,91
DC - PHZn	5,72 +- 0,37	4,85	6,5
Zn	5,44 +- 0,51	4,43	6,93
Zn - BP	4,96 +- 0,35	4,21	5,9
Zn - PHZn	5,07 +- 0,47	4,32	6,05

3.4 Analysis of the parameter RSm

All measured values and characteristics for the RSm parameter are given in Table 5. From the values that were measured, it can be stated that the highest average value of RSm was recorded in the sample with the designation: DC, which had a value of 236.03 μm.

While the lowest average value of the RSm parameter was recorded for the sample with the designation: Zn - BP, whose value was 99.37 μm. The highest measured value of Maxima was represented by the sample with the designation: DC, which showed values (MAX - 401 μm), while the lowest value of the maximum was recorded in the sample Zn - BP, at which we recorded the value (MAX - 119 μm). The highest minimum value was recorded for the sample marked DC - BP (Min. 175 μm). The lowest value of the minimum belonged to the sample Zn - PHZn (Min. 80 μm).

Variability characteristics: The Zn - BP sample has the lowest value of the standard deviation, which was 9.87 μm. The highest value of the standard deviation was recorded for the sample with the designation: DC, to which the value of 50.90 μm belongs.

Table 5: RSm parameter values and characteristics

RSm (μm)			
Sample	**Average**	**Min.**	**Max.**
DC	236,03 +- 50,9	158	401
DC - BP	231,53 +- 39,22	175	349
DC - PHZn	171,03 +- 34,35	122	257
Zn	137,8 +- 16,87	107	175
Zn - BP	99,37 +- 9,89	81	119
Zn - PHZn	107,83 +- 17,47	80	173

4. SEM analysis of chemically pretreated surfaces

SEM analysis was performed on all samples with applied surface treatment. The appearance of individual surfaces is visible in the Fig. 7 – 9.

From the SEM analysis of the investigated surfaces, it can be stated that the applied chemical surface pretreatments have an effect on the resulting surface roughness and adhesion of the material itself.
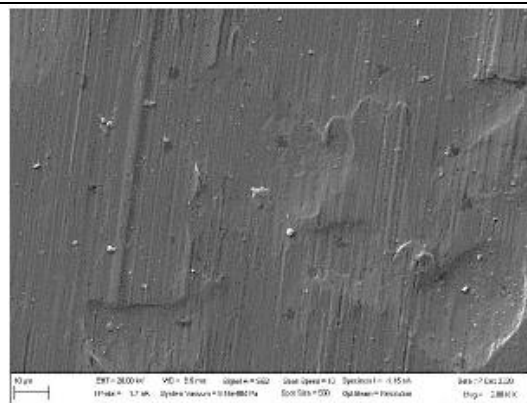
Fig. 7: *DC original surface*
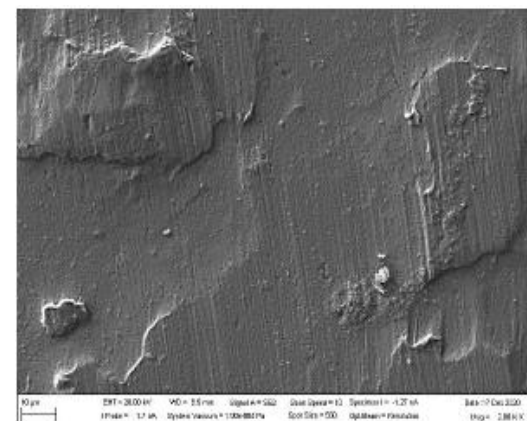
Fig. 8: DC – BP surface
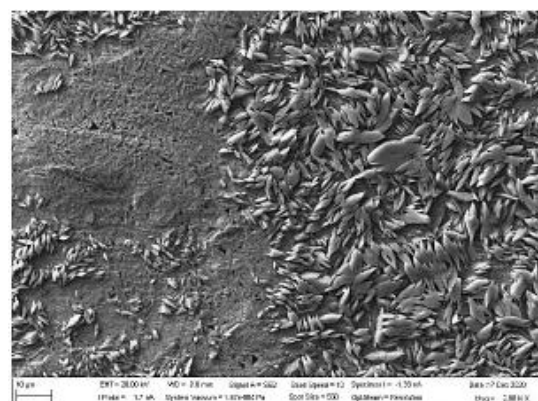
Fig. 9: DC – PHZn surface
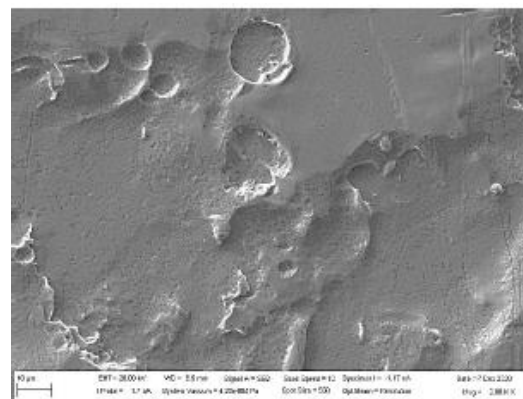
Fig. 10: Zn original surface
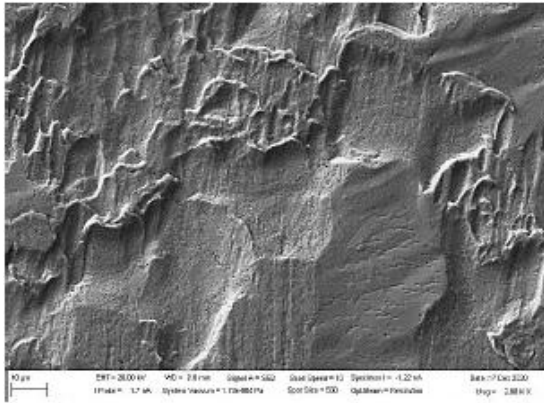
Fig. 11: *Zn + BP surface*

Fig. 12: *Zn + PHZn surface*

Conclusion

Two types of steels were used as sample material, namely uncoated steel DC 04 and hot-dip galvanized steel HX340LAD + Z. 2 types of surface pretreatment were applied to these materials - chromate-free zirconate passivation, application of zinc phosphate.

The samples were subjected to the measurement of the selected surface roughness parameters with a touch profilometer marked Mitutoyo Surftest SJ - 301 in accordance with the standard STN EN ISO 4287 to capture surface differences. The measured results were then subjected to a detailed statistical analysis.

Based on the experimental results, it can be stated that all applied types of chemical pretreatments have an effect on the achieved values of the investigated surface roughness parameters for both investigated materials, which can be demonstrated by measured parameter values and documented Firest-Abbot roughness curves.

References

1. P. Pokorný. Koroze a ochrana materiálu **57**, 4, 115-126 (2013).

2. P. Pokorný. Tribotechnika **6** (2012)

3. M.D . Banea, M. Rosioara, R. J. C. Carbas, L. F. M. da Silva, Composites Part B **151** (2018)

4. M. Tamilselvi, P. Kamaraj, M. Arthanareeswari, S. Devikala S., IJACSA **3**, 1 (2015)

5. J. Brezinová, J. et. al. *Korózia materiálov a špeciálne technológie povrchových úprav.* (Technická univerzita v Košiciach, Elfa Košice, 2020)

6. D. Draganovská, G. Ižaríková, J. Brezinová, A. Guzanová, Mater. Sci. Forum **818** (2015)

7. D. J. Whitehouse, Meas. Sci. Technol. **8** (1997).

Friction stir welding of dissimilar materials based on aluminum alloys

Nikita Veligotskyi[*], Ján Viňáš, Anna Guzanová
Technical University of Košice, Faculty of Mechanical Engineering,
Department of Technology, Materials and Computer Supported Production
nikita.veligotskyi@tuke.sk

Abstract: The paper focuses on the application of friction stir welding (FSW) technology for welding of unequal materials based on aluminum alloys. Joints were made from AW 5083 and AW 6082 materials using FSW technology at different weld speed values. The joints were analyzed metallographically, the hardness of the materials was tested across the cross section of the joint and the strength of the joint was tested by destructive static tensile test. At the lowest weld speed, the materials were not perfectly mixed, there was a macroscopically visible gap at the joint location, which was reflected in the lack of joint strength. At the medium and highest weld speed values, a joint with mechanical properties comparable to those of the base material was formed. Metallographically, the bond between the materials was free of any internal defects.

Keywords: FRICTION STIR WELDING, ALUMINUM ALLOYS, STATIC TENSILE TEST, HARDNESS, MICROSTRUCTURE

1. Introduction

The challenges in metal joining technology are becoming more intense across the industry. Along with the introduction of new materials for use in industry, there is also the task of researching and innovating, or developing new technologies for processing these materials. However, when applying new joining methods, it is always necessary to guarantee the quality and strength of the products.

Trends in car development are leading to an increase in the share of light alloys in cars. The application of aluminum and magnesium alloys in the automotive industry results in more efficient and economical operation of automobiles, while maintaining or improving the required properties. Friction stir welding (FSW) technology in automotive serial assembly-line production was first implemented in 2012 [1]. Satisfactory results of welding aluminum-steel alloys to the load-bearing parts of components show improved driving characteristics as well as shorter car production time.

Welding tools and optimal process parameters are important elements in FSW welding. By choosing the material and the geometric shape of the tool together with the combination of configuring the process parameters, welding of materials according to the valid standards can be ensured. The tool consists of two parts: pin and shoulder. The FSW welding process consists in that, the rotating tool pin is gradually pressed into the components or blanks to be weld, where the entire tool then performs a rectilinear movement along the welding gap between the components. During this movement, the materials are mechanically mixed by the action of the tool without external heating. The increased process temperature is due to internal friction in the materials. The tool can move clockwise or counterclockwise [2-3].

The practical part of the article is focused on the assessment of mechanical properties and microstructure of joints of two aluminum alloys performed by FSW technology. The microstructure of the joints was assessed by metallography and mechanical properties of the joints by hardness measurement and static tensile test [4-5].

2. Materials and methods

FSW welding of unequal materials was performed between AW5083 (AlMg4.5Mn0.7) and AW6082 (AlSi1MgMn) alloys. The welded plates had a constant thickness of 10 mm. The chemical composition of welded alloys is given in Tab.1.

Table 1: Chemical composition of alloys in wt.% , Al - balance

alloy	Si	Fe	Cu	Mn	Cr	Ni	Zn	Ti	Mg
5083	0.075	0.14	0.033	0.60	0.068	0.002	0.33	0.053	4.35
6082	0.85	0.32	0.01	0.62	0.18	-	0.12	0.08	0.75

The mechanical properties of welded alloys are given in Tab.2.

Table 2: Mechanical properties of welded alloys

	$R_{p_{0,2}}$ [MPa]	R_m [MPa]	A_5 [MPa]
AW 5083	237	330	16,3
AW 6082	185	243	11,5

The dimensions of the test plates machined for welding were: 200×250×10 mm.

Aluminum alloy AW 5083 contains magnesium and manganese as main alloying elements. Its advantage is high strength and hardness and therefore it is easy to machine by drilling, turning, milling. It has very good machinability, resistance to corrosion caused by seawater. It can be used in mechanical engineering for welded structures and foaming molds, for shipbuilding, tools and vehicle production.

Aluminum alloy AW 6082 contains silicon, magnesium and manganese as main alloying elements. Due to the higher addition of silicon and manganese, it has good strength and hardness and, again, is therefore easy to machine by drilling, turning and milling. It has good corrosion resistance, outstanding thermal conductivity and good anodizing. It is used in mechanical engineering for welded structures, for transport technology building and shipbuilding.

The welding tool had a simple conical shape. It was made of tool steel X40CrMoV5-1. Shoulder diameter was ø25 mm, pin diameter ø12 mm, pin length 9.7 mm with 10° taper, Fig. 1.
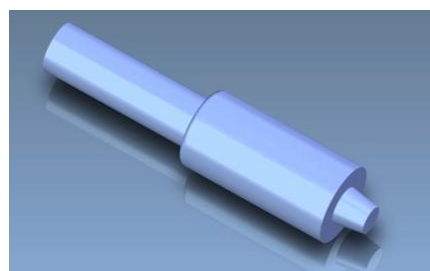
Fig. 1 *Welding tool in 3D view*

Welding parameters are given in Tab.3. When testing the parameters, only the tool feed speed (welding speed) changed from 100 mm/min to 60 mm/min. The tool rotation speed and angle of inclination of the tool were kept constant.

Table 3: Sample welding parameters

Sample number	Tool rotation speed (rpm)	Welding speed (mm/min)	Tool inclination (°)
1	600	100	1.5° to 4.5°
2	600	60	1.5° to 4.5°
3	600	80	1.5° to 4.5°

The following tests were performed on the welds:

1. Metallographic analysis of welds according to ISO 42 0461

2. Microhardness testing of welded joints according to ISO 9015-2. The hardness was measured by the Vickers method at a load of 200 g. Microhardness was evaluated in the base materials (BM), the heat affected zone (HAZ) and in the weld metal (WM). The microhardness of the test specimens was evaluated on electropolished metallographic sections. A Shimadzu HMV 2 hardness tester was used for this test.

3. Transverse tensile test according to ISO 4136. A universal tensile test machine Instron 8806 was used. 3 samples from each welded plate were tested in the experiment.

3. Results

The appearance of the welds is shown in Fig. 2.
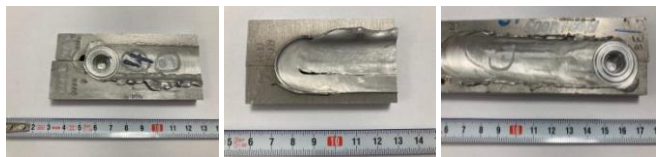
Fig. 2 *Sample No.1 (left), sample No.2 (middle), sample No.3 (right)*

From Fig. 2, it can be seen a gap on sample No. 2 after welding, which indicates unmixed materials.

The hardness of the joints across all weld areas is given in Tab.4.

Table 4: *Microhardness of welds HV 0.2*

Sample	BM	HAZ	WM	HAZ	BM
1-1	83	81	85	80	82
1-2	82	82	83	82	82
1-3	83	81	84	81	83
2-1	-	-	-	-	-
2-2	-	-	-	-	-
2-3	-	-	-	-	-
3-1	82	80	84	81	82
3-2	81	80	85	81	83
3-3	82	82	84	82	83

BM – base material, HAZ – heat affected zone, WM – weld metal

In sample No. 2, the microhardness measurement was not performed due to the presence of cavity in the weld metal. Based on the measured values, it can be stated that the microhardness values of the welded joints varied within the range of 80 to 85 HV0.2. HAZ showed minimum average values of 81 HV0.2. The base materials had an average microhardness value of 82 HV0.2. The maximum value of microhardness was shown by the weld metal, namely 84HV0.2. Differences in joint hardness in different joint areas are negligible. This indicates a minimal temperature influence of the material during welding

From a macroscopic point of view, a small volume of material can be observed on the specimens squeezed out of the weld site above the level of the material. The main causes of these defects may be excessive immersion of the welding tool in the weldment. Such a weld joint may have an unacceptable appearance, requiring additional mechanical machining of the surface, but nevertheless the strength properties may be satisfactory.

The results of the tensile test of the welded joint are given in Tab.5. The results are the average of 3 measurements.

Table 5: *Tensile test results*

Sample	$R_{p0.2}$ [MPa]	Rm [MPa]	A_5 [%]	Location of failure
1	192	282	14	WM
2	66	77	5.6	WM
3	198	285	14	WM

Based on the tensile tests of the welded joint in the transverse direction, it can be stated that the minimum values of tensile strength reached the samples made of plate No. 2. The reason was poor weld quality, the presence of internal defects, insufficient mixing and joining of materials. Samples made from plates No. 1 and 3, where the welding speed was 100 and 800 mm/min respectively, showed the highest average values. Destruction of all samples occurred in the weld metal.

Sample No.1: Figs. 3 - 5 show metallography analysis (macroscopic and microscopic view) of sample No.1.
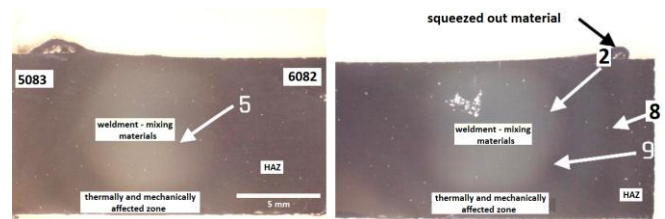
Fig. 3 *Sample No.1 macroscopic view, indication of positions for microscopic observation*
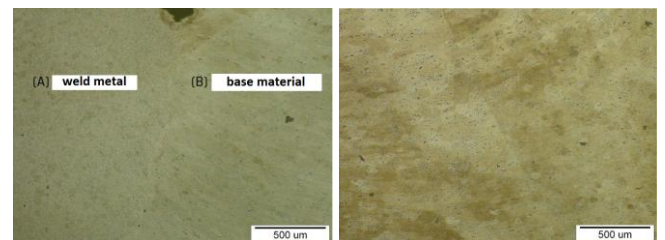
Fig. 4 *Microscopic view, position 2 (left) and position 5 (right)*
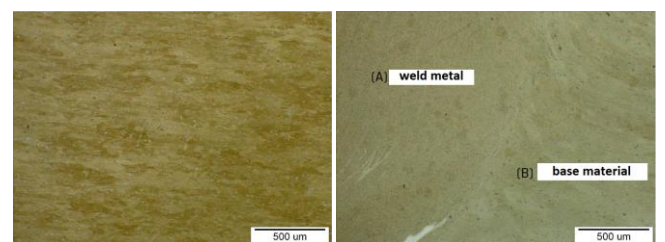
Fig. 5 *Microscopic view, position 8 (left) and position 9 (right)*

From Fig. 3-5 is clear, that both materials were thoroughly mixed during welding. The boundary between the base material and the mixed area cannot be distinguished microscopically.

Sample No.2: Figs. 6 - 8 show metallography analysis (macroscopic and microscopic view) of sample No.2.
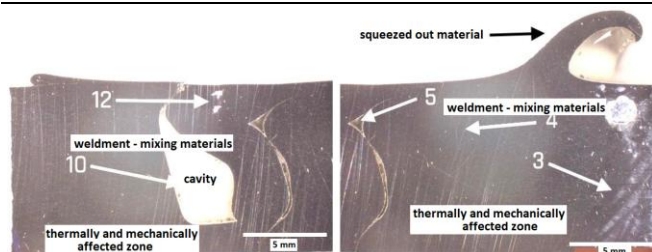
Fig. 6 Sample No.2 macroscopic view, indication of positions for microscopic observation

Fig. 7 Microscopic view, position 4 (left), position 5 (in the middle) and position 12 (right).
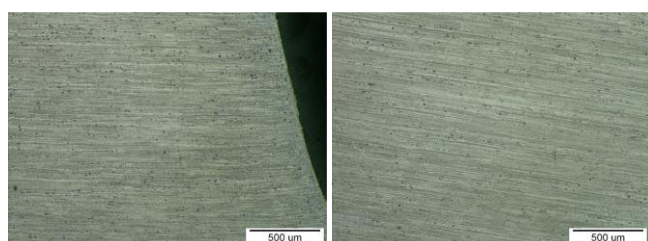
Fig. 8 Microscopic view, position 10 (left) and position 3 (right)

When observed with the naked eye of sample No.2, it is possible to see a surface defect in the weld. The surface gap along the weld line was probably due to the low welding speed. Microscopic view of sample No.2 in Figure 7 (positions 12 and 5) shows unmixed materials in the weld metal.

Sample No.3: Figs. 9 - 11 show metallography analysis (macroscopic and microscopic view) of sample No.3.
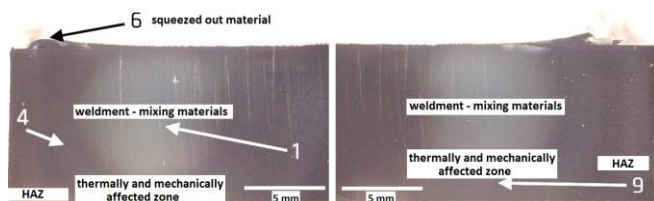
Fig. 9 Sample No.3 macroscopic view, indication of positions for microscopic observation
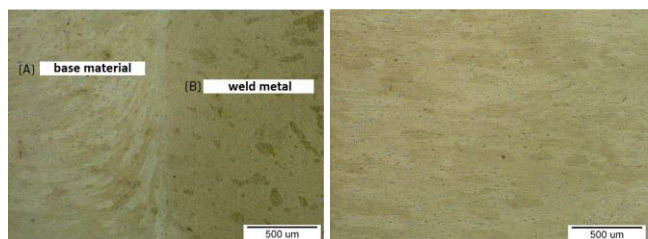
Fig. 10 Microscopic view, position 1 (left) and position 4 (right)
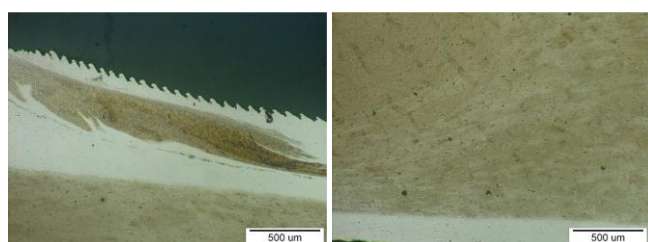
Fig. 11 Microscopic view, position 6 (left) and position 9 (right)

There is no microscopically distinguishable interface between the base materials and the mixing zone, there is a perfect mixing of the welded materials without the presence of defects and cavities, positions 1, 4 and 9, Figs. 10, 11. The surface of the sqeezed material (position 12) has a sawtooth character indicating a gradual uniform plastic deformation of the material surface during welding.

4. Conclusion

Different microhardness and tensile test results could be observed on the test specimens made from aluminum alloys AW5083 and AW6082, which had different process parameters. The increased hardness above the weld zone is directly influenced by grain refinement. In the case of specimen 2, the presence of defects on the weld surface could already be observed after visual inspection. The microstructure of the individual materials was similar for all the samples examined. The maximum average values of the mechanical properties were exhibited by sample 3, where the welding speed was at the middle values of all the examined samples. Recrystallization of the material occurred in the core of the weld for all specimens. The material that was at a greater distance was only thermally affected, without recrystallization. Based on the set of metallographic images, it can be argued that the microstructure in the weld is not homogeneous.

References:

1. M. Miličić; P. Gladović; R. Bojanić; T. Savković; N. Stojić, Metalurgija, Vol. 55 No. 1, 2016, 107-110. https://hrcak.srce.hr/141848

2. R.S. Mishra; Z.Y. Ma, Materials Science and Engineering: R: Reports, Volume 50, Issues 1–2, 2005, 1-78. https://doi.org/10.1016/j.mser.2005.07.001

3. W.M. Thomas; E.D. Nicholas, Materials & Design, Volume 18, Issues 4–6, 1997, 269-273. https://doi.org/10.1016/S0261-3069(97)00062-9

4. W. Deqing; L. Shuhua, C. Zhaoxia, Journal of Materials Science, Volume 39, 2004, 1689-1693. https://doi.org/10.1023/B:JMSC.0000016171.50107.e4

5. B. Meyghani; M.B. Awang; S.S. Emamian; M.K.B. Mohd Nor; S.R. Pedapati, Metals, Volume 7, Issue 10, 2017, 450. https://doi.org/10.3390/met7100450

Optimization of joining parameters of thin-walled materials by flowdrill technology

Anna Guzanová[*], Erik Janoško, Nikita Veligotskyi

Technical University of Košice, Faculty of Mechanical Engineering,
Department of Technology, Materials and Computer Supported Production
anna.guzanova@tuke.sk

Abstract: *This paper deals with the investigation of the effect of speed on the form fit joint of dissimilar materials. Thin-walled materials based on steel and aluminium alloy were joined by thermal drilling. The shape and size of the resulting bushing were evaluated. It turned out that the best material combination for joining by flowdrill technology are joints made of steel and aluminum alloy. Aluminum alloy must always be placed in the bottom position. The best parameters of the formed bushing were achieved with the combination of DC-Al or TL-Al materials, at tool speeds of at least 2400 rpm.*

Keywords: *JOINING, FLOWDRILL, THIN-WALLED METAL SHEETS, STEEL, ALUMINUM*

1. Introduction

Minimizing emissions in transport is a dominant theme today. In order to meet this objective, conventional steels are being replaced by non-conventional high-strength steels, which make it possible to reduce the cross-sections of components and the weight of the whole, as well as to save raw materials. Furthermore, steels are being replaced by other materials with good specific strength, such as aluminum, magnesium alloys or even composites. The individual parts of vehicles are assembled in a customized manner and hence there is a need to address the joining of dissimilar materials that differ from each other by their very nature - the internal arrangement of the constituent units, microstructure, mechanical, physical properties as well as the nature of the response of these materials to different types of loads [1-12]. Joining dissimilar materials by welding encounters problems especially in joints between steel and aluminum, which are associated with insolubility of the elements and formation of brittle intermetallic compounds. Adhesive bonding solves many of these problems, but the joints have a limited temperature of use and slow down the production cycle of the component due to the time required for the adhesive to cure. A promising joining technology is mechanical joining with one of the many variations of clinching or riveting. These technologies are already fairly well studied, but require in many cases a two-sided approach to the parts to be joined.

Schmerler et al. [13] in their publication dealt with the idea of joining materials by thermal drilling technology, although this technology is not primarily intended for this purpose. The idea is based on the premise that if two or three thin-walled materials are layered on top of each other and drilled with a flowdrill tool, coaxial bushings could be formed, mechanically wedged together, which could form a form-fit joint. This possibility was also tested by Guzanova et al. in [14], using thermal drilling technology to form joints between pairs of dissimilar materials based on steel and aluminum alloy. They found that the best joints were formed when one of the materials was an aluminum alloy placed in the bottom position. It also showed the relationship of the bushing formation with the thermal conductivity of the materials. However, the joints were formed at constant parameters. Therefore, there was a need to test other process parameters, in particular rotational speed and its effect on the formation of the joint bushings.

The paper therefore aims to test the effect of rotational speed on the size and shape of the bushings formed during the thermal drilling of a pair of thin overlapped plates, where the intended joint is always to be formed from a pair of dissimilar materials. This should result in the determination of the appropriate rotational speed for the successful formation of joints from dissimilar materials.

2. Materials and methods

The following materials were used for the joints formation:

- Cold rolled uncoated deep drawing steel DC04, used for the production of interior and exterior parts of car bodies and for other stampings, thickness 0.8 mm, next denoted as **DC**.

- Zinc-galvanized fine-grained high-strength low alloyed steel TL 1550-220+Z with increased cold formability, thickness 0.8 mm, next denoted as **TL**.

- Precipitation hardened aluminum alloy EN AW-6082 T6 (AlSi1MgMn), thickness 1.0 mm, next denoted as **Al**.

The chemical composition of materials, their mechanical properties and surface conditions are given in Tables 1-2.

Table 1: *Chemical composition of materials, wt. %.*

DC									
C	Mn	P	S	Fe					
0.04	0.25	0.009	0.008	bal.					
TL									
C	Mn	Si	P	S	Al	Nb	Ti	Cu	Fe
0.10	1.00	0.50	0.08	0.03	0.015	0.10	0.15	0.20	bal.
Al									
Si	Fe	Cu	Mn	Mg	Cr	Zn	Ti	Al	
1.00	0.40	0.06	0.44	0.70	0.02	0.08	0.03	bal.	

Table 2: *Mechanical properties and some specific conditions of materials.*

materials	YS [MPa]	UTS [MPa]	Elongation [%]	Thickness [mm]	condition
DC	197	327	39	0.8	electrostatically oiled
TL	292	373	34	0.8	Zn coated, 100 g·m^{-2}
Al	290	340	14	1.0	solut. treated, artificially aged

The shape and dimensions of the test specimens were designed according to EN ISO 12996 depending on the thickness of the materials to be joined and the diameter of the tool used, Fig. 1. Flowdrill Long ø 5.3 mm thermal drilling tool was selected for joints formation.
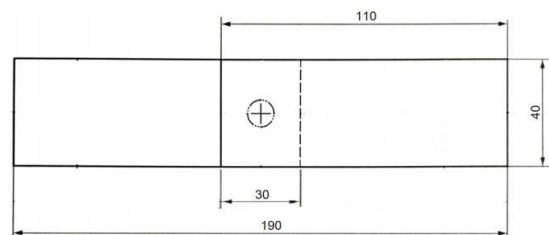
Fig. 1 *Shape and dimensions of joint assembly*

The joints were created in manual mode using radial drilling machine, where the only variable was tool rotational speed. Tool

feed rate towards the material was implemented manually. The rotational speeds used were 1900, 2400 and 3800 rpm.

The formed joints are intended to be tested for shear strength under tensile stress in the next step, but this paper mainly presents a metallographic study of the formed bushings. This is because the material properties and thickness of the bushing formed from the top material in the joint will determine the load carrying capacity of the joint. Since the position of the materials in the joints is important, the material combinations were constructed according to the following scheme, Table 3.

Table 3: Matrix of created joints.

Positioning materials in the joint	Mat. in upper position	Mat. in lower position
	DC	TL
		Al
	TL	DC
		Al
	Al	DC
		TL
		Al

3. Results

The joints formed according to Table 3 were cut in the axis of the hole, embedded in resin and ground for macroscopic observation and measurement of the thickness of the formed bushings. The individual metallographic sections are shown in Table 4. In order to save space, only one side of the joint is always shown in Table 4.

Table 4 shows the following findings:

- Joints where Al is in the top position (Al-Al, Al-DC, Al-TL) are characterized by the fact that the plates are pushed apart by the bushing of the top material, there is no formation of two concentric bushings, thus no joint is formed and this regardless of the rotational speed. Due to its mechanical and physical properties, Al cannot be placed in the top position in the joint. Although its mechanical properties are at the level of TL steel (see Table 2), heating of Al due to frictional heat reduces the mechanical properties rapidly. Al is thus pushed laterally away from the hole location instead of forming a bushing.

Table 4. Metallographic cross-sections through joints – one side view (right).

Rotation speed	Al-Al	DC-Al	TL-Al	DC-TL	TL-DC	Al-DC	Al-TL
1900 rpm						Not successful	Not successful
2400 rpm							Not successful

3800 rpm
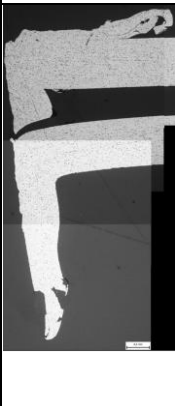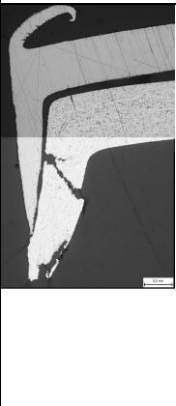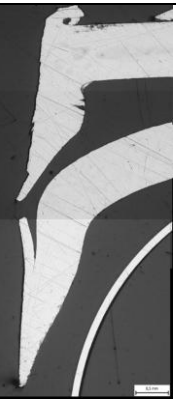
Not successful
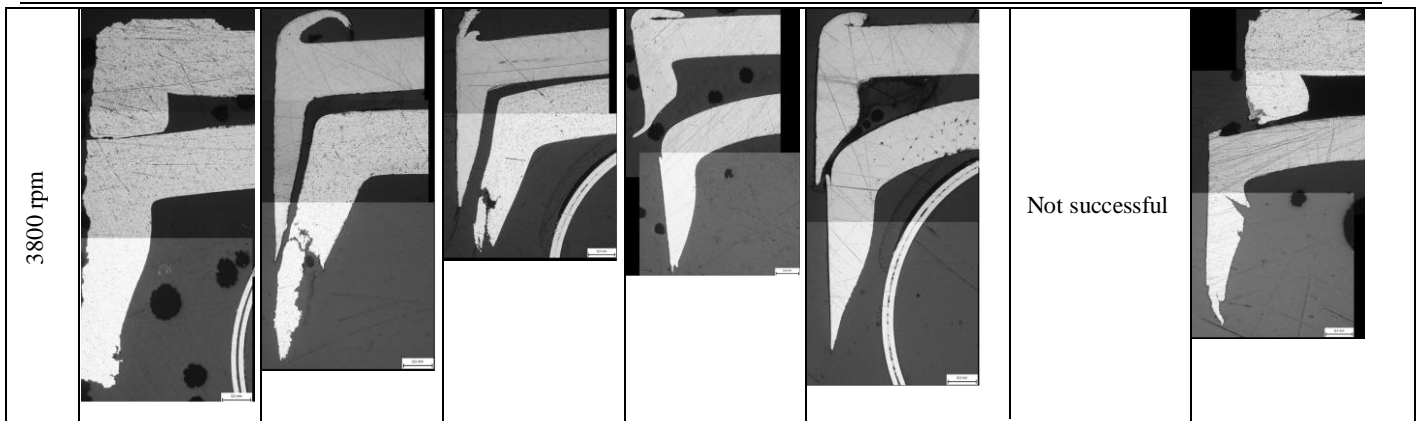
- Joints formed from dissimilar steel materials (DC-TL, TL-DC) also do not exhibit suitable properties. From the metallographic sections it can be seen that the inner bushing formed from the top material thins very intensely towards the bottom material, which seems to cause a low load carrying capacity of the joint. In addition, a strong springback effect is evident, which will cause separation of the materials to be joined after the tool cycle is complete. This also does not contribute to the load carrying capacity of the joint. This phenomenon appears for both steel combinations (DC-TL, TL-DC) and at all three rotational speeds tested.

- The most successful joints have been made between steel and aluminum (DC-Al, TL-Al) when the aluminum alloy is in the bottom position. The inner bushing is formed from the upper steel stronger material and the aluminum alloy, softened by the frictional heat transferred from the steel, is shaped by copying the emerging steel bushing. Contact between the Al and the tool does not appear to occur at all. The springback effect is minimal. The thickness of the steel bushing is between 0.5 - 0.7 mm, which is a good result considering the thickness of the steel plate (0.8 mm). These connections are expected to have the highest load carrying capacity and energy dissipation, which is also an important indicator of the connections, especially for automotive applications.

- The effect of rotational speed was evident only in steel-aluminum joints (DC-Al, TL-Al). For DC-Al joints, the height of the steel bushing increases with increasing rotational speed. The bushing in the DC-Al joint formed at 1900 rpm is poorly formed and may slip out of the aluminum alloy under shear tensile stress. For this reason, a minimum speed of 2400 rpm may be recommended for the DC-Al joint. In contrast, the TL-Al coupling has developed a steel bushing with the greatest thickness just at 1900 rpm. At higher speeds, the steel bushing is thinner.

4. Conclusions

The paper presents the results of testing the effect of changing the rotational speed of the tool on the nature of joints formed between dissimilar materials by means of thermal drilling without the use of a screw. Form fit joints are formed based only on the mechanical forming of concentric bushings and their mutual interference. It is found that the joint can only be formed between steel and aluminum alloy. However, the aluminum alloy must be placed in the bottom position. Then the load capacity of the joint will depend on the internal (steel) bushing - its thickness and mechanical properties. The outer bushing made of aluminum alloy will only have a supporting function when the joint is loaded. The best parameters of the formed bushing were achieved with the combination of DC-Al or TL-Al materials, at tool speeds of at least 2400 rpm.

5. References

1. European Aluminium Association: Hybrid joining techniques. Available online: https://www.aec.org/page/extrusion-aluminum-joining-manual (accessed on 07-02-2022).
2. W.S. Messler, Joining of advanced materials, 1st ed.; Butterworth-Heinemann: Oxford, United Kingdom, 1993; 560 p.
3. K. Mori, N. Bay, L. Frantini, F. Micari, A.E. Tekkaya, CIRP Annals – Manuf. Technol. 2013, 62, 673-694. https://doi.org/10.1016/j.cirp.2013.05.004.
4. K. Martinsen, S.J. Hu, B.E. Carlson, CIRP Annals – Manuf. Technol. 2015, 64, 679-699. https://doi.org/10.1016/j.cirp.2015.05.006.
5. M. Kleiner, M. Geiger, A. Klaus, CIRP Annals – Manuf. Technol. 2003, 52, 521-542. https://doi.org/10.1016/S0007-8506(07)60202-9.
6. M. Graf, S.P. Sikora, C.S. Roider, Thin-Walled Struct. 2018, 130, 286-296. https://doi.org/10.1016/j.tws.2018.02.023.
7. F. Aslan, L. Langlois, T. Balan, Int. J. Adv. Manuf. Technol. 2019, 104, 2377 – 2388. https://doi.org/10.1007/s00170-019-04097-z.
8. P. Krasauskas, Mechanika (Kaunas) 2011, 17, 681-686. https://doi.org/10.5755/j01.mech.17.6.1014.
9. C. Özek, Z. Demir, TEM-Journal 2013, 2, 93 – 101.
10. R. Kumar, N.R.J. Hynes, Int. J. Light. Mat. Manuf. 2019, 2, 193 – 205. https://doi.org/ 10.1016/j.ijlmm.2019.08.003.
11. R. Kumar, N.R.J. Hynes, C.I. Pruncu, J.A.J. Sujana, J. Clean. Prod. 2019, 236, 117711. https://doi.org/10.1016/j.jclepro.2019.117711.
12. P. Shalamov, M. Pivtsaeva, A. Chvanova, Shamgunov, A., Mater. Today 2021, 38, 1931-1935. https://doi.org/10.1016/j.matpr.2020.09.071.
13. R. Schmerler, F. Rothe, M. Grunert, Hybrid joining using the flow drill technology. Available on the internet: https://www.researchgate.net/publication/341616091_Hybridfugen_durch_Fliesslochformen_Hybrid_joining_using_the_flow_drill_technology (accessed on 17-01-2022).
14. A. Guzanová, E. Janoško, D. Draganovská, M. Vrabeľ, M. Tomáš, P. Horňak, M. Vojtko, N. Veligotskyi, Metals, 2022, 12, 540. https://doi.org/10.3390/met12040540.

Monitoring the change of corrosion resistance of HCT600X+Z galvanized steel after plastic strain

Erik Janoško[1],*, Anna Guzanová[1], Miroslav Tomáš[2]
Technical University of Košice, Faculty of Mechanical Engineering,
[1]Department of Technology, Materials and Computer Supported Production
[2]Department of Automotive Production
erik.janosko@tuke.sk

Abstract: *This work deals with corrosion measurements of galvanized steel HCT600X+Z subjected to progressively increasing plastic strain. The corrosion resistance measurements were carried out by non-destructive EIS (electrochemical impedance spectroscopy) test and destructive LP (linear polarization) test. As a result of the work, the measured data were analyzed and the results were processed using Nyquist diagram and Tafel analysis.*
Keywords: *CORROSION RATE, STRAIN, ZINC PLATED STEEL, ELECTROCHEMICAL IMPEDANCE SPECTROSCOPY, LINEAR POLARIZATION*

1. Introduction

Galvanized steel sheets are used in many industries due to their good corrosion resistance. This is particularly the case in the automotive industry where the base steel sheet is protected by a Zn coating. As many parts are processed by forming and plastic strain occur in various forming processes, it is important for the automotive industry that the Zn coating exhibits good formability and adhesion. Zn coating during the forming process can be disrupted, the base material revealed and exposed to the aggressive surrounding environment [1]. The Zn coating in the forming process adapts to compressive stresses without peeling away from the base material, which is an advantage of such a coating [2].

The corrosion resistance of deformed galvanized steel was investigated by Sacco et al. [3] who studied the linear polarization of deformed galvanized steel. They found an increased corrosion rate at different strain levels [3]. Other studies [4-6] have been carried out to find out the behaviour of Zn coating on steel sheets in the forming process, but these investigations were focused on the limiting plastic strain during forming, changes in coefficient of friction, lubrication characteristics, etc. and not on the corrosion resistance after the forming process.

This work deals with the corrosion behaviour of galvanized steel sheet that has been deformed by uniaxial tension at four different strain rates. The aim was to investigate the corrosion resistance of the Zn coating and to determine the dependence of the corrosion rate on the level of plastic strain. Accelerated corrosion laboratory measurements such as electrochemical impedance spectroscopy (EIS) and linear polarization (LP) were used to obtain the specified characteristics.

2. Materials and Methods

Materials

High strength low alloy steel HX340LAD+Z with a thickness of 0.8 mm and a Zn layer of 100 g/m^2 was used for the experiment. The chemical composition and mechanical properties of the material are shown in Tables 1 and 2.

Table 1: *Chemical composition of the material wt. %*

C	Mn	Si	P	S	Al min	Nb	Ti	Fe
0.070	0.600	0.007	0.016	0.007	0.034	0.025	0.001	Bal.

Table2: *Mechanical properties of the material*

Rp 0.2 [MPa]	Rm [MPa]	A80 [%]
351±1.3	427±1.7	26±0.1

Plastic strain of samples

The specimens for static tensile testing, of appropriate shape and dimensions, manufactured in accordance with EN 10002-1, were deformed by uniaxial tension on a TiraTest 2300 tensile test machine. The strain rate was 10 mm/min. Before the test, the complete stress-strain curve was recorded, and then, four strain rates (5%, 10%, 15% and 20%) were selected on the curve for observing the corrosion behaviour of the materials, Fig. 1.
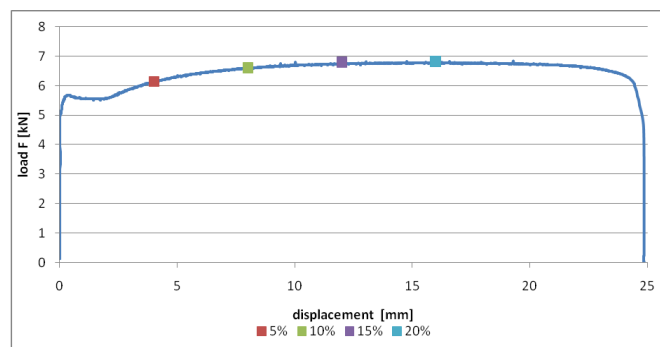
Fig. 1 *Stress-strain diagram of the material with four strain levels marked*

Corrosion studies

The BioLogic SP-150 potentiostat was used for experimental determination of corrosion resistance. The tested area of the samples was 0.636 mm^2. The ambient temperature during the tests was 23±1°C. The preparation of the samples consisted of degreasing with nitrocellulose solvent C 6000 and subsequent rinsing with demineralised water. The electrolyte chosen was a 3.5% NaCl solution to simulate an aggressive environment. The samples were placed in this solution for 24h (i.e., the stabilization period). A three-electrode setup was used for the measurements. As counter electrode was used platinum, reference electrode was supersaturated calomel electrode (SCE), as working electrode was the measured material. The beginning of each test was stabilization of the working electrode, i.e., stabilization of the open circuit potential (OCP).

For electrochemical impedance spectroscopy, the following parameters were used: frequency range from 10mHz to 100kHz, sinusoidal amplitude ±10mV. The number of frequencies per decade was 10 (51 different frequencies in total).

The settings for linear polarization were ±0.2 V from Ecorr and the scan rate was 0.5 mV/s.

Each measurement was repeated until a minimum of three stable results were obtained. Measurements were processed using the EC-Lab v11.27 software.

3. Results

EIS

An equivalent circuit, shown in Fig. 2, was used to process the measured results. In this circuit, R1 represents the resistance of the electrolyte, R2 represents the resistance of the zinc layer, and R3 represents the resistance of the base material. The variable capacitance Q1 is located at the interface between the electrolyte and the zinc layer, the variable capacitance Q2 is located at the interface between the zinc layer and the base material.
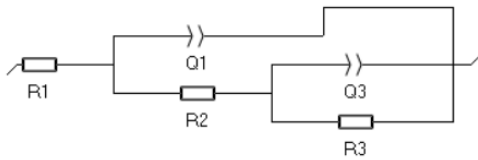
Fig. 2 *Equivalent circuit for analysis of measured PEIS results*

The measured results were processed in the Nyquist coordinate system. Fig. 3 shows the analysis of the measured data with an iterative curve (Z-fit).
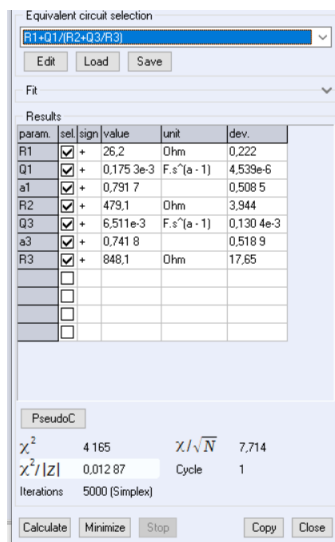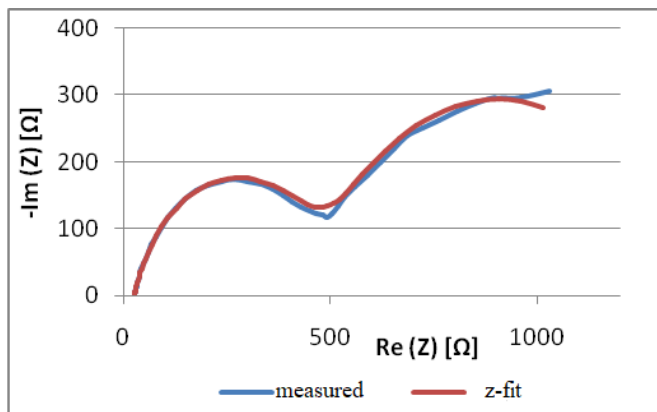
Fig. 3 *Principle of analysis of PEIS results*

The course of the PEIS measurement is shown in Figure 4. The main parameter that indicates the resistance of the deformed samples in our case is the value of R2 (Tab. 3), which represents the polarization resistance of the zinc layer. It was found that the R2 value for all the strain levels varied in the minimum range. In Fig. 3,4 it is this value represented by the first impedance loop, and it can be concluded that, the zinc layer protects the base material at strain levels up to 20%.
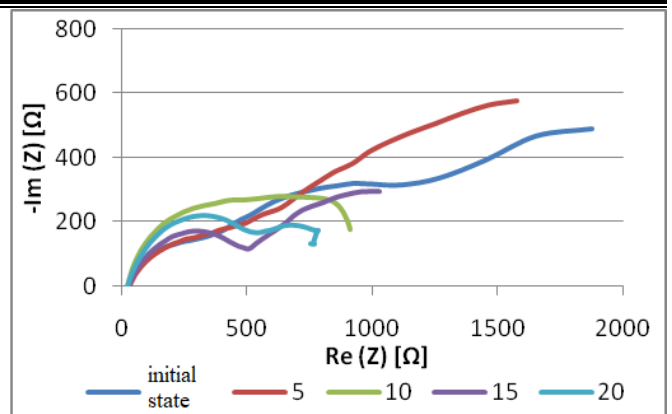
Fig. 4 *PEIS measurements at different strain levels*

Table 3: *Measured values by the PEIS method*

Strain level [%]	R1 [Ω]	R2 [Ω]	R3 [Ω]	Q1 [F.s]	Q3 [F.s]
Initial state	28±1	492±198	1827±207	0.221±0.018	2.284±0.253
5	28±1	460±14	1675±95	0.135±0.120	1.494±0.968
10	27±2	437±63	886±142	0.151±0.010	1.270±0.300
15	26±1	415±95	639±182	0.186±0.014	5.059±2.231
20	25±1	423±21	230±85	0.191±0.044	5.416±3.071

Linear polarization

The analysis of the measured LP data is presented in Fig. 5 using Tafel fit. In processing the measured data, emphasis was placed on ensuring that the tangents βa and βc were superimposed over the measured data in strongly linear regions.
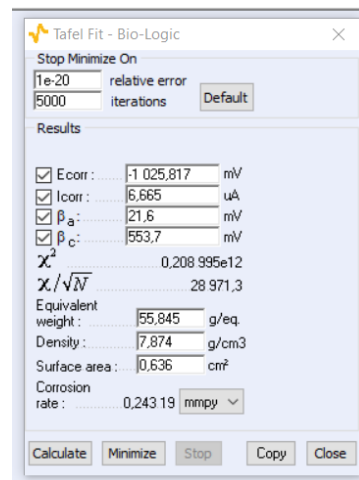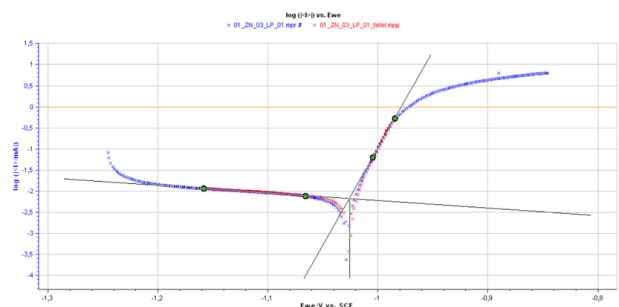
Fig. 5 *Principle of analysis of LP results using Tafel curves*

The measured curves are shown in Fig. 6. The decisive parameters in this case are the potential Ecorr, Icorr and corrosion rate. As the strain level increases, the Ecorr potential becomes more and more negative. Also, Icorr increases with increasing strain

level. So we can say that, with increasing strain rate, the corrosion process accelerates while a thin layer of Zn corrosion products is formed on the surface.
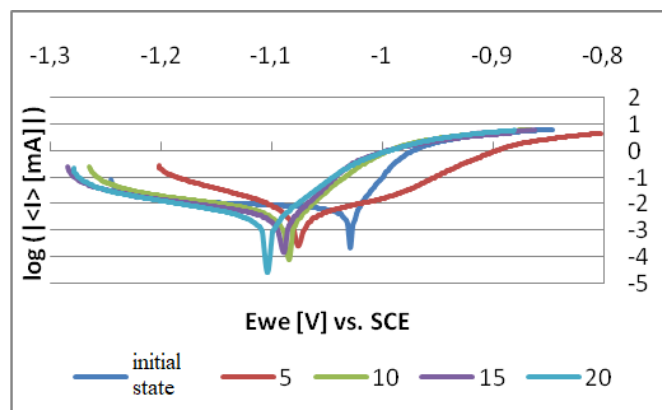
Fig. 6 Curves obtained by the linear polarization method after different strain levels

In Table 4, the measured data are analyzed using the Tafel method. As the strain level increases, Icorr increases thereby the evolution of H_2 is accelerated ($H^+ + e \rightarrow (1/2) H_2$).

Table 4: Results obtained by linear polarization

Strain level [%]	Ecorr [mV]	Icorr [uA]	βc [mV]	βa [mV]	corr. Rate [mmpy]
Initial state	-1042.5±23.3	4.6±0.6	307±65	22±3	0.168±0.024
5	-1073.9±9.3	9.1±0.2	125±21	316±20	0.257±0.027
10	-1078.1±9.6	7.2±0.4	176±70	70 ±1	0.262±0.150
15	-1088.8±6.2	11.3±0.1	252±15	30±1	0.413±0.003
20	-1126.5±22.4	10.6±0.5	109±20	100±3	0.484±0.017

Fig. 7 shows the dependence of the corrosion rate on the strain level. After including the measurement deviations, it can be said that this is a linear dependence. The conclusion is that an increase in the strain level leads to the revealing of the steel base material and its reaction with the electrolyte.
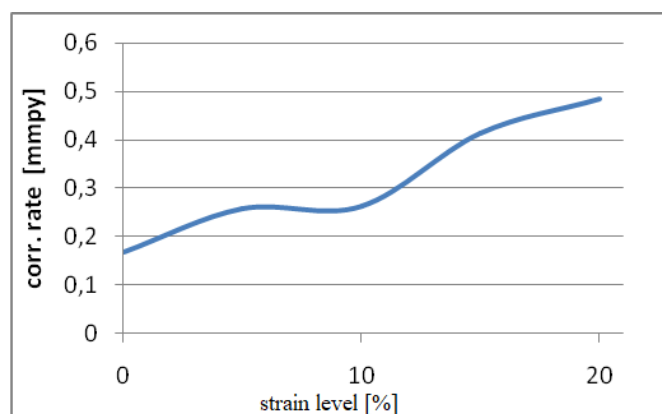
Fig. 7 Dependence of the corrosion rate on the strain level

4. Conclusion

Analysis of the results of corrosion measurements proved following facts:

• EIS measurements showed high durability of the Zn layer after all strain levels. This can no longer be said for the base material, where the polarization resistance of the base material decreased significantly with increasing strain level.

• A linear dependence between the strain level and the corrosion rate was found by linear polarization analysis. It was also found by measurement that Icorr and corrosion rate increased with increasing strain level.

5. References

1. J. Gronostajski, W. J. Ali, M. S. Ghattas, J. Mater. Process. Technol, **23**, 21-28, (1990)
2. J.M Matainge, SEA Trans., volume 5, 29, (2001)
3. E.A. Sacco, N.B. Alvarez, J.D. Culcasi, C.I. Elsner, A.R. DiSarli, Surf. Coat. Technol, **168**, p. 115-122,)2003)
4. M.R. Lovell, Z. Deng, Tribol. Int, **35**, 85-95, (2002)
5. H.M. Jiang, X.P. Chen, H. Wu, C.H. Li, J. Mater. Process. Technol., **151**, 248-254, (2004)
6. K.L. Lin, C.H. Chue, B.C. Kou, Mater. Chem. Phys., **50**, 82-87, (1997)

Roll leveler for straightening sheet blanks

Tamila V.[1], Klubovich V.[2], Liaukovich V.[3]
Belarusian National Technical University [1,2], The Physical-Technical Institute of the NAS of Belarus [3], Belarus
levkovich@phti.by[3]

Abstract: *The report presents the design of a 13-roll leveler for straightening sheet blanks of complex configuration. The roll leveler is equipped with a mechanism for controlling the roll gap, which during the levelling process compensates for the elastic deformation of the housing and maintains the specified levelling conditions. The levelling process was analyzed using the finite element method (FEM) with the determination of forces acting on the rollers during levelling of sheet blanks up to 50 mm thick.*
***KEYWORDS**: LEVELLING PROCESS, LEVELLING FORCE, MOTOR POWER*

1. Introduction

Sheet blanks are widely used in industrial production. For their cutting, laser and plasma cutting is often used. After that, sheet blanks often have insufficient geometric accuracy (flatness). To improve the geometric accuracy of sheet blanks various methods can be used, including roller levelling.

Roller levelling is a technological process of metal forming, used to minimize the flatness of sheet blanks and reduce the level of residual stresses. When levelling, the workpiece is subjected to cyclic alternating bending with decreasing amplitude. In this case, the penetration depth of deformation should be at least 0.7 of the thickness of the workpiece [1].

The existing experience of the world's leading manufacturers of process equipment (ARKU, KOHLER, etc.) shows the feasibility of using multi-roll levelers both for straightening piece sheet parts and for integrating levelers into existing and planned automated lines for the production of piece sheet blanks of a wide range for machine-building, petrochemical, aerospace and other branches of industrial production.

Multi-roll levelers are used for cold straightening of steel sheet blanks and blanks of non-ferrous alloys up to 50 mm thick and up to 5000 mm wide. Hot straightening of steel sheet blanks is carried out at temperatures of 500-700 °C, mainly immediately after leaving the working stand of the rolling mill. Hot straightening cannot provide a sufficiently even surface of the blanks, since they undergo buckling during the cooling process. Sheets with a thickness of over 40 - 50 mm are usually straightened in a cold state under presses.

At present, there is a demand for versatile and productive equipment for levelling sheet blanks with complex contours. These requirements are met by multi-roll levelers.

2. Components of the roll leveler

Roll leveler mainly composed of 6 parts (fig. 1):
- Upper and lower roll frames. They include upper and lower leveling rolls, which are used for cyclic alternating bending of sheet blanks. The roll frames also contain back up rolls which are designed to prevent excessive bending of the leveling rolls under operating loads.
- Upper and lower frames.
- Mechanisms for adjusting the inlet and outlet inter-roll gap. Used for the initial setting of the roll leveler for straightening blanks of a certain thickness.
- Drive unit. The leveling rolls are driven by a drive unit. It consists of electric motors and reducers.
- Compensation mechanisms. Serve to compensate for the elastic deformation of the elements of the roll leveler under the working load.
- Mechanical means for moving blanks.

The roll leveler is designed for straightening blanks with a thickness of 6 to 50 mm with a maximum width of up to 2000 mm. It is equipped with 13 leveling rolls with a diameter of 200 mm and 15 back up rolls. The distance between rolls is 205 mm (Fig. 2). In the roll leveler, a roll arrangement is used, in which the upper frame of rolls is located at an angle to the lower one, which ensures cyclic

bending with decreasing amplitude of the billet. The levelling speed is in the range from 3 to 12 m/min.
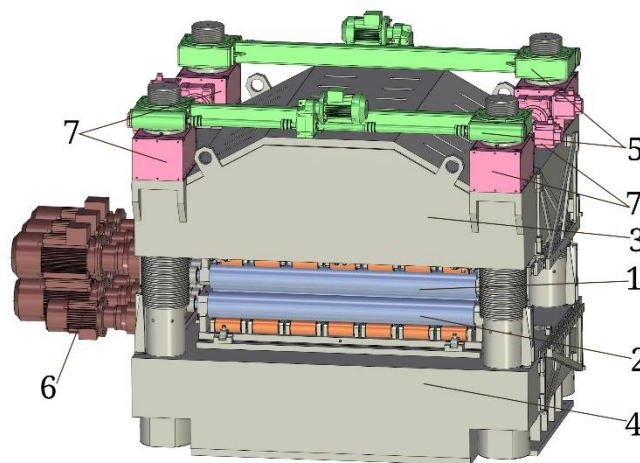
Fig. 1. Components of the roll leveler
1 – upper roll frame; 2 – lower roll frame; 3 – upper frame; 4 – lower frame; 5 – mechanisms for adjusting inlet and outlet inter-roll gap; 6 – drive unit; 7 – compensation mechanisms
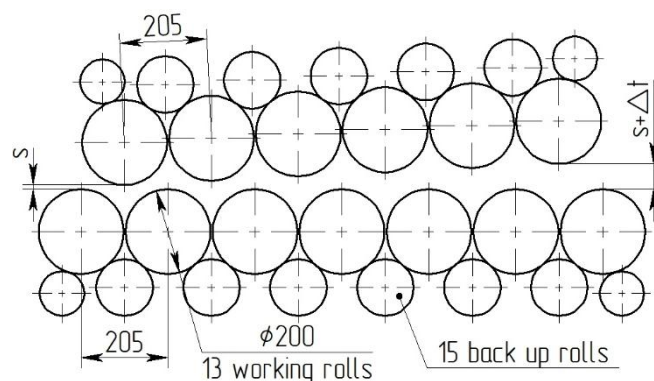
Fig. 2. Roll arrangement
s – inlet inter-roll gap; s+Δt – outlet inter-roll gap

Using the finite element method, the straightening force of a sheet blank 50 mm thick and 650 mm wide was determined. The following characteristics of the material were used: Young's modulus 210000 MPa, Poisson's ratio 0.3, density 7850 kg/m³, yield strength σ_t=390 MPa, tensile strength 530 MPa, relative elongation δ=19 %. With these parameters, the force on the most loaded leveling roll reaches 5 MN, the total force during leveling is 30 MN.

The total power of the drive unit is 115 kW. Electric motors with a total capacity of 15 kW are also installed to adjust the roll leveler (moving the upper frame and operation of the compensation mechanisms).

When leveling under the influence of the working load, elastic deformation of the roll leveler structure occurs. Back up rolls are used to prevent leveling rolls from bending. Upper and lower frames have a cellular structure. Stretching and bending of the pillars of the roll leveler (leveler has 4 pillars with a diameter of 300 mm) connecting the upper and lower frames are controlled using four inductive sensors. During the straightening process, the deformation of the pillars is constantly monitored and, based on these data, the roll gap is corrected using a compensation mechanism. The maximum elastic deformation of the pillars is 4 mm.

3. Conclusion

When developing sheet-straightening mills, it is necessary to take into account many phenomena occurring in metal subjected to alternating loading with decreasing amplitude (interaction of elastic and plastic deformation, the Bauschinger effect, etc.). In this process, there are conditions that make straightening difficult (hardening) and facilitating (Bauschinger effect). All this can give rather large differences in the results of calculations performed by different methods. For various materials over the entire range of thicknesses, setting up the leveling rolls can vary significantly. Therefore, for any leveler, it is required to create a correct computer model, taking into account as many necessary parameters as possible.

References

1. Korolev A.A. Konstrukciya i raschet mashin i mekhanizmov prokatnyh stanov [Design and calculation of machines and mechanisms of rolling mills]. Moscow, Metallurgiya Publ., 1985. 376 p. [in Russian]

Development and implementation of closed loop position control concepts on electromechanical linear system using Beckhoff controller

Vito Tič[1,*], Darko Lovrec[1]

University of Maribor, Faculty of Mechanical Engineering[1]

vito.tic@um.si

Abstract: *Electromechanical linear axes are used as actuators in many areas of industrial automation. Such axes are a fundamental building block of any machine tool, manipulator or similar device, whether they implement only one- or multi-axis positioning. Usually, servomotors or stepper motors are used to drive the axes, and the control is performed by a variety of PLC controllers and controller concepts.*

The paper presents the implementation of a multi-purpose electromechanical linear axis, which enables the study, research and comparison of various linear drive concepts and types of closed loop controllers. The linear axis incorporates two different motor types: a BLDC servomotor as well as a stepper electric motor, and thus also enables comparison of these two motor types and corresponding control concepts. A multi-core Beckhoff soft PLC is used as a controller, which can implement either built-in closed loop controllers or can also implement controllers designed in the Matlab/Simulink environment.

PID closed loop position controller built-in Beckhoff TwinCAT 3 is presented in the paper. Further on, it is compared by PID closed loop controller developed in Matlab/Simulink which was exported and imported into Beckhoff TwinCAT 3 environment in order to confirm the adequacy of importing and using Matlab/Simulink controllers on Beckhoff soft PLCs.

Keywords: ELECTROMECHANICAL LINEAR AXIS, SERVOMOTOR, STEPPER MOTOR, CLOSED-LOOP CONTROL, SOFT-PLC

1. Introduction

The paper presents the planning and implementation of linear axis control with the aim of using our own developed position controller. This allows us to use any position controller to control the system. The system does not allow this by using the standard controllers, which are part of the Beckhoff TwinCAT 3 software environment, as it uses a specific program block for absolute axis travel, which performs motor rotation according to the specified parameters.

The main advantage of standard TwinCAT 3 controllers (program blocks) is that they are as easy as possible to use in industry, as the user does not need to design its own controller, but only select one of the controllers available in the TwinCAT 3 software and set individual parameters. For simple operations, the PID controller is the most commonly used, which is usually sufficient to control industrial applications. The aim of the research was to replace the standard TwinCAT 3 PID controller with custom closed-loop controller develepod in Matlab/Simulink and confirm the adequacy of importing and using Matlab/Simulink controllers on Beckhoff soft PLCs.

For the development and implementation of our own closed loop controllers, we first had to build a demonstration system and get familiar with the soft PLC environment. Once we had the system built and developed industry standard closed-loop control of the axis using TwinCAT 3 program blocks, we were able to start creating our own closed-loop controllers using the Matlab/Simulink environment. In order to confirm the consistency of the purposed method, we had compared the functionality of the standard PID closed loop controller in TwinCAT 3 and the functionality of the same controller developed in Matlab/Simulink that was imported into TwinCAT 3 system. As presented in this paper, we have achieved almost identical results, which confirmed the possibility to develop new types of different non-linear controllers in Matlab/Simulink and incorporate them in industrial applications using Beckhoff soft PLCs.

2. System overview

For the purpose of research, it was first necessary to design a linear positioning unit with a linear axis. The design is based on Festo DGE-25 linear axis, which converts rotational motion into linear motion with the help of a toothed belt and is designed for medium loads. Such linear systems are commonly used for transporting, lifting, manipulating and performing feeding movements.

To drive the linear axis, two different Beckhoff motors are mounted on the drive. One is Beckhoff AS1050-0120 stepper motor and the other is Beckhoff AM8113-0F20 BLDC servo motor, which has an integrated 18-bit absolute incremental encoder. The motors are connected via the shafts to the pulleys of the linear module that drive the linear axis by means of a toothed belt, which allows fast and dynamic movement of the linear axis. A track guide with a ball-bearing carriage is also attached to the linear axis. The carriage is used for mounting weights, which allows the use of ten smaller weights of 500 g each. Weights can be removed or added as needed, and depending on the weight of the load, the dynamics of the system also changes. It should be noted that both motors never drive the linear axis at the same time, but they can be connected and disconnected via the shaft coupling. The appearance of the linear positioning unit with installed motors and weights is shown in Figure 1.
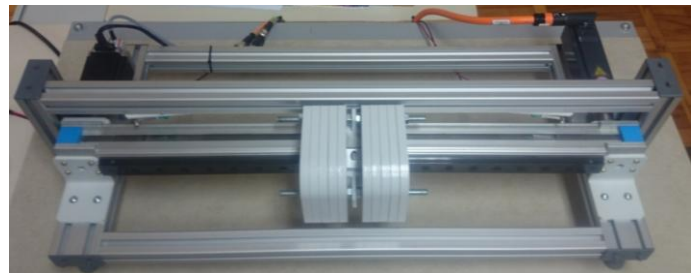
Fig. 1 *Electro-mechanical linear axis with servo- and stepper-motor.*

The advantage of the toothed belt is the cushioning of sudden shocks and changes to the system, so the dynamics of the system remain without major changes, as the rotational motion is transmitted directly to the belt. Thus, the system is more demanding to control, as we can achieve great external influences on the system.

The axis control system is designed using the TwinCAT 3 software environment, which enables the development and implementation of control programs for Beckhoff soft PLC controllers. In the TwinCAT 3 software environment, we can add various modules for motor and axis control, such as servo motor control and numerically controlled axis modules (*NC axis* module). *NC axis* module allows us to change the type of closed loop controller (PID and their combinations) and its parameters, scaling factors for the incremental encoder and other axis parameters.

In order to monitor the response of the system, the *Scope* function was used in TwinCAT 3, which allows us to monitor and record system data in very short sample times (e.g. 1 ms or 0,1 ms).

3. User interface

In order to create a more complex and sophisticated user interface, the user interface between the user and the TwinCAT 3 software environment (HMI) was created in Visual Studio C # Windows Forms Application, which is designed to build graphical applications. As shown in Figure 2, the user interface (on the left) allows us to select different types of controllers (P, PI, PD and PID), set the controller parameters and define the new set-point for our system. After enabling the motion, the response can be monitored and recorded on the right side of the screen by using *Scope* function that was implemented in the WinForms application.

Fig. 2 *User interface developed in Visual Studio C# as Windows Forms Application.*

In order to access the real-time PLC variables (the program created in TwinCAT 3) from the WinForms user interface created Visual Studio C#, the Beckhoff ADS (Automation Device communication protocol is used, which defines an interface of an independent device on an independent network. The TwinCAT 3 architecture allows individual software modules to be considered as stand-alone devices. For each task, the software uses a module that acts as a server or as a client. Messages between objects are exchanged through the ADS interface, more precisely in the message center, through which information is distributed across the system via a TCP/IP connection. In this way, all data and commands necessary for the operation of the program are transmitted. The ADS protocol is therefore a communication protocol in Beckhoff TwinCAT 3, developed for data exchange between different software modules, for example for communication between PLC and *NC axis*.

This protocol allows the use of other communication tools in the TwinCAT programming environment. If you need to communicate with another computer or device, the ADS protocol is used on top of TCP/IP. This means that all data in the network is accessible from any desired point and the user can connect to almost any connection method and connect to a device that changes the parameters [1].

To analyze the responses obtained from the real system, the TwinCAT 3 built-in function for plotting diagrams *Scope* is used. The *Scope* is used to plot the set-point motion line, the actual motion line and the deviation between these two values. The use of *Scope* also proves to be excellent for monitoring and observing responses at various controller parameters, as we can monitor the operation of the linear by using different controllers and controller settings in real time.

Scope settings were generated in the TwinCAT 3 programming environment and imported to the WinForms in Visual Studio C# with program code. In addition to *Scope* itself, we also added the possibility of creating X and Y cursors that measure the value of the difference between responses. We have also added a save function, which saves our response to a CSV file format that we can access at any time.

4. TwinCAT 3 PID controller

The system allows closed loop control of either the servo-motor or the stepper motor using different control concepts. Hereafter, the closed loop position control of the servomotor will be presented more in detail.

Servo motor control is performed by two control systems. One is implemented by a virtual controller and the other is implemented in the servo motor control module (Beckhoff EL7211). For the control system that is operated by a virtual controller, we can also select the controller type in the *Motion* (*Axis – Ctrl* tab) and set the control parameters in the same way as for a stepper motor.

The control system in the "EL7211" motor control module, which drives and controls the servomotor, is implemented in a cascade procedure. Figure 3 shows the control diagram, which represents the cascade control for the control of the AM8113 servo motor used. Cascade control in this case consists of three controllers. These are the position controller, the speed controller and the current controller.
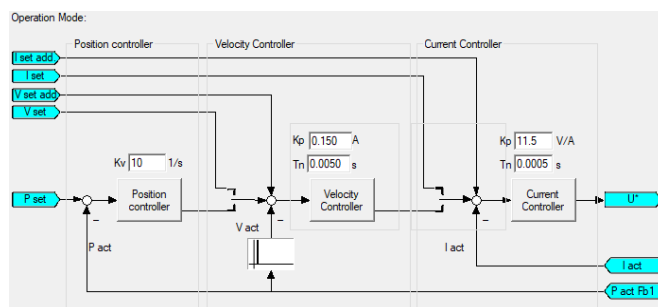
Fig. 3 *TwinCAT 3 cascade closed-loop controller for servo-motor.*

Complex system control often cannot be achieved with a single feedback loop. The reason for this is that complex systems are managed on the basis of only one information about the system and that is its output size. The controller reacts to changes that occur within the system only when their effect is expressed on the output of the output quantity. This usually results in a slow response to the control error [2]. Therefore, cascade control is often used in automation, where it is necessary to have fast and exact response of the system.

Commonly, the cascade control system consists of two control loops where the internal loop is slave or auxiliary. The outer loop is the superior or the main one. In such a cascade structure, the main controller does not act directly on the actuator, but forms a reference value for the slave controller. The effect of a fault in the auxiliary control loop is practically compensated in this loop [2].

The output of one controller therefore changes the set-point of the auxiliary controller. Cascade control loops can consist of two or more controllers. Each controller has its own variable that is measured in the process. Cascade control is typically used to isolate the primary system from interference, nonlinearity, and drive-related problems.

Cascade control brings improvement only when the dynamics of the internal control loop is fast enough compared to the external control loop. It does not make sense to use cascade control if the inner loop is not at least three times faster than the outer control loop. If the inner loop is not much faster than the outer one, there is a great chance of interaction between the two loops that can cause instability [3].

In the scope of this research we have concentrated only on the external loop of our cascade controller, that is the PID closed loop position controller of the servo-motor.

5. *Matlab/Simulink PID controller*

In the scope of this research a Matlab/Simulink PID controller was developed in order to in order to confirm the adequacy of importing and using Matlab/Simulink controllers on Beckhoff soft PLCs, which will further allow us to design and implement other types of controllers, such as nonlinear closed loop controllers. The Matlab/Simulink software environment enables us to generate program code for the TwinCAT 3 software environment, in which we design the system control program. Thus, we can directly convert the designed controller model into the TwinCAT 3 program code. Thus, at first step, we have only implemented the PID controller in the Matlab/Simulink software environment and compared the response of the implemented controller with the response of the TwinCAT 3 *NC Axis* system controller.

The implemented PID controller was designed in the Matlab/Simulink software environment with sampling time of 1 ms, as the execution on the controller is discrete and not continuous. The sampling time had to be the same as set in the TwinCAT 3 software environment project. The PID controller was designed using a transfer function consisting of different blocks such as add, multiply, divide, delay and input and output block. Figure 4 shows a diagram of the implemented PID controller in Matlab/Simulink.

Fig. 4 *PID controller developed in Matlab/Simulink.*

The created diagram in Matlab/Simulink is then used to create *Subsystem* and prepare it to generate code suitable for import into TwinCAT 3 software environment. The generated code is then imported into the TwinCAT 3 program as *POU* using the import function (*PLCopenXML* format). This generates a program block including the created controller with corresponding input and output variables.

6. *Results*

The aim of the research was not only to control the linear system using Matlab/Simulink designed and implemented PID closed loop position controller, but also to evaluate its proper operation and response, which was achieved by comparing the responses of the TwinCAT 3 PID controller and the controller developed in the Matlab/Simulink environment. In this way, we were able to verify that the axis control system and the closed loop controller were properly designed and implemented. In case we have implemented everything correctly, the behavior of both systems should be the same. Figure 5 shows the response of the system using both PID controllers (above TwinCAT 3 PID controller, below Matlab/Simulink controller) with the same PID settings and trajectory of set-point change with speed of 1000 mm/s and acceleration/deacceleration of 500 mm/s^2.

The green line represents the start of the set-point chage, while the orange line shows the generated position trajectory representing the set-point value and the red shows the actual axis position when moving relative to the generated trajectory. The difference between the set-point and actual position in represented by blue line. The

Figure clearly shows that the response of the both PID position controller are more or less identical, confirming that the design and the implementation of PID controller in Matlab/Simulink and import into TwinCAT 3 control software was successful.

Fig. 5 *TwinCAT 3 PID controller response (above) in comparison to Matlab/Simulink PID controller response (below). Green: start point; Yellow: position set-point value; Red: actual position value; Blue: difference between set-point and actual value.*

7. *Conclusion*

The main aim of the research was to build a linear-axis research system consisting of industrial type of servo motor and stepper motor and to test the design and implementation of Matlab/Simulink closed-loop controllers in Beckhoff TwinCAT 3 system. Thus, a positioning axis with a linear guide driven by an industrial servo motor or stepper motor was designed and manufactured. Further on, the TwinCAT 3 PLC program and corresponding user interface for controlling the system was developed in Visual Studio C# WinForms application. This further allowed us to implement and test PID position controller from TwinCAT 3 system and the one built in Matlab/Simulink, which was imported into TwinCAT 3.

The final aim of the research at this point was to confirm the suitability of the PID controller designed in the Matlab/Simulink software environment, which was then imported into TwinCAT 3 software environment. The results of both controller responses fully confirms the adequacy of importing and using Matlab/Simulink controllers on Beckhoff soft PLCs. By confirming the results and obtaining an identical response, we confirmed the adequacy of the process of development and implementation of closed loop controllers from Matlab/Simulink environment.

The design and implementation of PID position controller from Matlab/Simulink software environment into TwinCAT 3 system allows us to use more advanced, more complex, more responsive

and faster controllers. We are able to compare different controllers for each system, so we can choose the most optimal controller for application needs. By adding even more different controllers, we gain the ability to test and compare new high-end controller concepts and are no longer limited to TwinCAT 3 controller types. This further enables us to develop and test different nonlinear controllers, such as a soft logic controllers. Soft logic controllers use experiential rules such as natural language words. In addition to non-linear controllers, linear controllers can also be used by changing the parameters during operation, which has the advantage that the parameters are set to the optimal ones.

8. References

1. Beckhoff, *BX9000 Bus Terminal Controller for Ethernet 2.0.0*, 2017
2. V. Ambrožič, P Zajec, *Električni servo pogoni*. Ljubljana: Slovensko združenje elektroenergetikov, 2016.
3. N. Bolf, Kaskadna regulacija, *Kem. Ind. 65* (11-12) (2016) 665–66

Comparison of different position controllers implemented with a Beckhoff controller and TwinCAT 3 software

Darko Lovrec[1*], Vito Tič[1]

University of Maribor, Faculty of Technical Engineering[1]

darko.lovrec@um.si

Abstract: *Achieving the required dynamics and accuracy of movement of electromechanical linear axes is one of the basic tasks in the field of modern production machines and devices. In addition to a sufficiently powerful electric motor, e.g. electric servomotor, the appropriate controller and control concept also play a key role. As the top performance of the electromechanical axle controller is still a key feature of efficient and quality production, this topic is discussed in this paper.*

At the forefront of the paper are the development and implementation of various position controllers developed in the Beckhoff TwinCAT 3 environment. In addition to the classic PID controller already available in the Beckhoff software, a special PID controller has been developed in the Matlab / Simulink environment, as well as a Fuzzy controller and a Feedforward control strategy. For all mentioned types of controllers, the basic characteristics, design approach and parameterization of the controllers are presented. The efficiency of individual position controllers on an industrial-type electromechanical linear axis, driven by an electric servomotor, was tested experimentally and the results are compared.

The efficiency of these closed loop controllers was also tested in terms of robustness and ability to adapt to changes in the control loop, where a different load of moving mass was used as a characteristic change in the control loop.

Keywords: ELECTROMECHANICAL LINEAR AXIS, POSITION CONTROL, BECKHOFF TWINCAT 3, CONTROLLERS

1. Introduction and test device structure

Different approaches and concepts, as well as different hardware and software, are used to control the linear servo axis, which are often used within industrial and other manipulators. In the present case, a powerful Beckhoff industrial controller and the Visual Studio software environment with the TwinCAT 3 software add-on or software extension were used. In the TwinCAT 3 environment, different types of controllers were first designed and then implemented and compared.

The designed system allows to implement different types of controllers suitable for position control. Among them was also self-developed customized PID type controller, which was designed in the MATLAB-Simulink software environment. This was designed and used due to the limited possibilities of using the existing PID controller. Except the classic and customized PID controller, a non-linear controller based on Fuzzy logic was also designed and tested, as well as Feedforward control strategy. All types of controllers were tested, and their effectiveness was compared based on the step response to a constant change of position at a constant load. [1], [2]

For the linear axis control, it was used a servomotor that allows precise control of speed, acceleration, and position. The servomotor is controlled by a closed loop via the position sensor, as shown in principle in Figure 1.
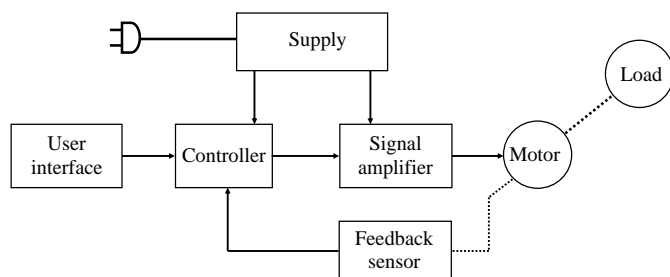
Fig. 1 *Basic structure of the servosystem.*

The control system consists of a trajectory generator and a linear axis as a controlled object - Figure 2. From the trajectory generator, the position reference r and the rate of change of the position reference (trajectory tangent) dr are led to the input of the tracking system. The controlled system is implemented according to the cascade principle. Speed and current loops are already available and set inside the Beckhoff controller.

The considered system for practical testing of different types of controllers consists of electrical, mechanical, constructional and control elements. The Festo linear axis of the FESTO-DGE-25-500- ZR-LV-RV-KF type converts the rotational movement of the servomotor into a linear displacement by means of a toothed belt and is designed for medium loads. The Beckhoff servomotor type AM8113-0F20-0000, which has an integrated 18-bit absolute incremental encoder, is used as a linear axis drive. The linear axis is connected to the servomotor motor via a toothed belt, which allows us to move the trolley with the load quickly and dynamically.
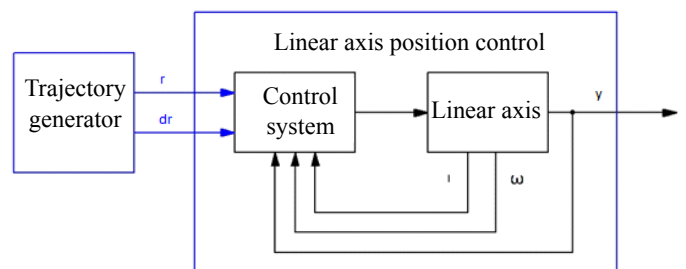
Fig. 2 *Block diagram of the considered system.*

Up to 5 kg of weights can be attached for variable weight regulator testing purposes. Shock absorbers are installed at the end positions of the linear axis to physically restrict the end position of the trolley. The additionally installed pneumatic cylinder supplied with a pressure of 2 bar and actuated via a controller, represents an additional switching load to generate additional movement disturbance.

The entire linear axis, together with the supporting frame, is mounted on a table under which the controller and power supply and the corresponding electronics are installed. The actual appearance of the entire system is shown in Figure 3.
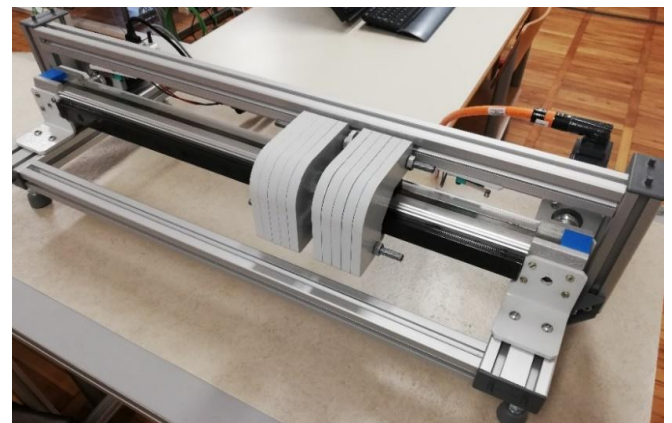
Fig. 3 *The actual appearance of the test facility.*

2. User interface – graphical form

To create a more complex and sophisticated user interface, the user interface between the user and the TwinCAT 3 software environment (HMI) was created in Visual Studio C# Windows Forms Application, which is designed to build graphical applications. As shown in Figure 4, the user interface allows us to select different types of controllers: P, PI, PD and PID as well as the Fuzzy controllers and customized controller type. It also allows setting all the necessary parameters of different types of controllers as well as control devices and selecting/entering a new setting value for the system. After enabling the motion, the response can be monitored and recorded on the right side of the screen by using *Scope* function that was implemented in the WinForms application.
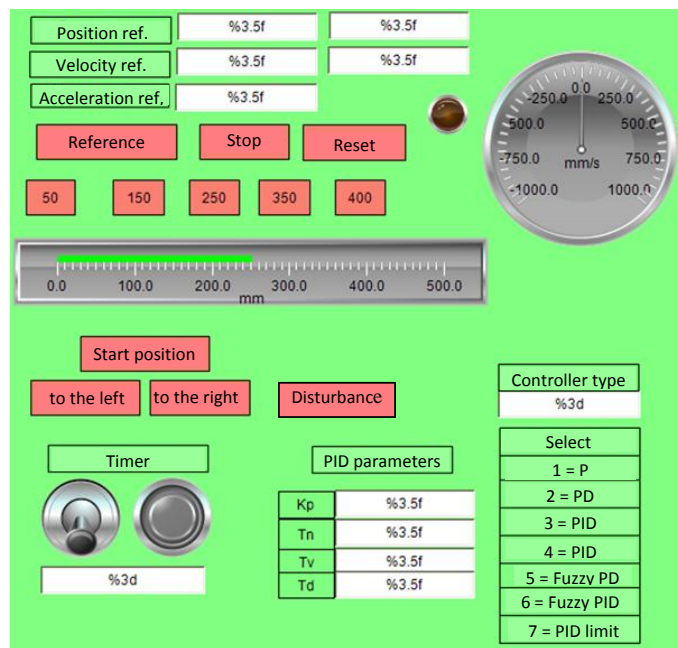
Fig. 4 *Graphical form of the user interface developed in Visual Studio C# as Windows Forms Application.*

The graphical form of the interface is divided into individual sections. The first part is intended to specify the parameters required for system operation. It consists of the desired position, the desired speed (maximum speed) and the desired acceleration (maximum acceleration). The desired values of each quantity are entered in the corresponding empty boxes marked with %, where the actual values are shown next to them.

To make it easier to test individual controllers, hotkeys have been added, as each time entering a value for the desired position is a time-consuming system bottleneck. Clicking on an individual hotkey triggers the transcript of the selected value to the desired position and moves the linear axis to the desired value. Speed keys are defined according to the distance of the linear axis; values 50, 150, 250, 350 and 400 mm (see Figure 4).

Since the main purpose is to test and compare different types of controllers, the possibility of quick selection of the type of controller is added. In this way, when changing the type of controller, it is not necessary to interfere with the program code and reload it on the control unit. For the selected controller, it is only necessary to enter the controller number, which is listed in the table below the controller selection. For optimal setting of the response on the controller, the possibility of changing individual parameters for the selected controller is added (on the left side of the controller selection table).

In case the system loses power, it also loses information about the location of the axis - so the "Start position" button was added, which moved the linear axis to the limit switch and set the starting position to "0". With the buttons "to the left" or "to the right", the linear axis moves in the selected direction, at a certain speed,

regardless of the setting of other parameters. The "Disturbance" button is used to trigger the disturbance function – triggering the pneumatic additional load (if necessary – disturbance response).

In addition to the mentioned parameters, a timer is also available. With the timer we were able to set the time of movement of the linear axis in the desired direction.

The graphical interface also displays values for the current speed and current axis position in graphical form. The "speed indicator" is used to display the speed (in mm/s), which shows the current speed value with the help of a pointer and a circular scale, and a linear position scale with a green slider (in mm) is used to display the position (Figure 4).

3. Controller design in TwinCAT 3 environment

The system allows closed loop control of either the servomotor or the stepper motor (optional) using different control concepts. In our case, the use of a servomotor was at the forefront.

Servomotor control is performed by two control systems. One is implemented by a virtual controller and the other is implemented in the servo motor control module (Beckhoff EL7211). For the control system that is operated by a virtual controller, we can also select the controller type in the *Motion* (*Axis – Ctrl* tab) and set the control parameters.

The control system in the "EL7211" servomotor control module, which drives and controls the servomotor, is implemented in a cascade procedure. Figure 5 shows the control diagram, which represents the already mentioned cascade control for the control of the AM8113 servomotor (Beckhoff) used. Cascade control in this case consists of three controllers. These are the position controller, the speed controller, and the current controller.
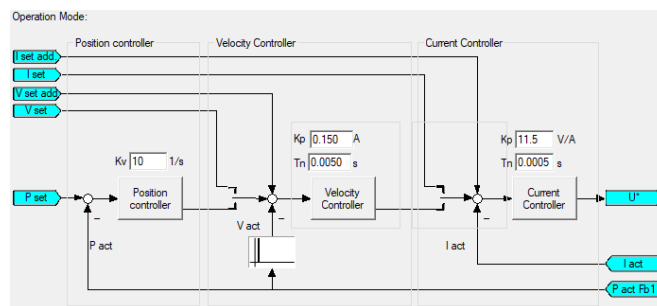
Fig. 5 *TwinCAT 3 cascade closed-loop controller for servomotor.*

Complex system control often cannot be achieved with a single feedback loop. The reason for this is that complex systems are managed based on only one information about the system and that is its output size. The controller reacts to changes that occur within the system only when their effect is expressed on the output of the output quantity. This usually results in a slow response to the control error. Therefore, cascade control is often used in automation, where it is necessary to have fast and exact response of the system. [3]

In the considered case, the cascade control system consists of two control loops, with an inner and an outer loop, with the outer loop being the superior or main loop. In such a cascade structure, the main controller does not act directly on the actuator but forms a reference value for the internal loop, slave controller. The effect of a fault in the auxiliary control loop is practically compensated in this loop. The output of one controller changes the set-point of the auxiliary controller. Each controller has its own variable that is measured in the process.

Cascade control is only effective when the dynamics of the internal control loop is much faster compared to the dynamics of the external loop; for example three times faster. If the inner loop is not much faster than the outer one, there is a great chance of interaction between the two loops that can cause instability [3].

3.1 Matlab/Simulink PID controller

In the scope of this research a Matlab/Simulink PID controller was developed to confirm the adequacy of importing and using Matlab/Simulink controllers on Beckhoff soft PLCs, which will further allow us to design and implement other types of controllers, such as nonlinear closed loop controllers. The Matlab/Simulink software environment enables us to generate program code for the TwinCAT 3 software environment, in which we design the system control program. Thus, we can directly convert the designed controller model into the TwinCAT 3 program code. Thus, at first step, we have only implemented the PID controller in the Matlab/Simulink software environment and compared the response of the implemented controller with the response of the TwinCAT 3 *NC Axis* system controller.

The implemented PID controller was designed in the Matlab/Simulink software environment with sampling time of 1 ms, as the execution on the controller is discrete and not continuous. The sampling time had to be the same as set in the TwinCAT 3 software environment project.

The transfer function of the PID controller is already available on the Beckhoff website - Equation 1 [4]. The equation had to be converted from the continuous form to the discrete form shown by Equation 2.

$$[G_{PID}(S) = K_p * (1 + \frac{1}{T_n*S} + \frac{T_V*S}{1+T_d*S})12]. \tag{1}$$

$$G_{PID}(Z) = K_p * (1 + \frac{1}{T_n} * T_S * \frac{1}{z-1} + \frac{T_V * \frac{1}{T_d}}{1 + \frac{1}{T_d} * T_S * \frac{1}{z-1}}) \tag{2}$$

The transfer function is built from individual blocks, which need to be named and connected into a whole - Figure 6.
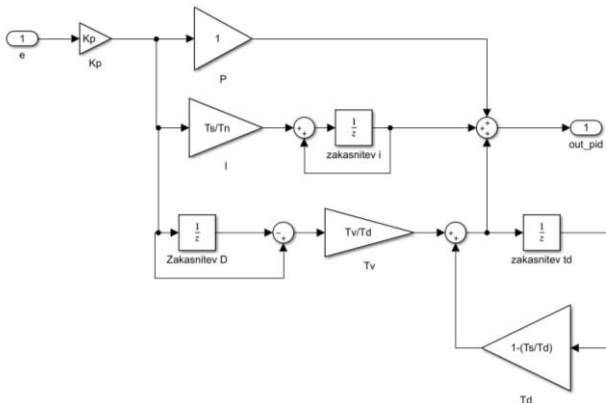
Fig. 6 PID controller developed in Matlab/Simulink.

The created diagram in Matlab/Simulink is then used to create *Subsystem* and prepare it to generate code suitable for import into TwinCAT 3 software environment. The generated code is then imported into the TwinCAT 3 program as *POU* using the import function (*PLCopenXML* format). This generates a program block including the created controller with corresponding input and output variables.

3.2 Fuzzy PID controller

The Fuzzy PID controller was also designed using the MATLAB-Simulink software environment. The process of designing a Fuzzy PID controller is basically the same as the described process of designing a classic PID controller, so only key differences will be mentioned.
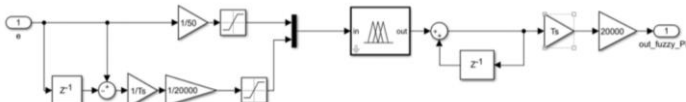
Fig. 7 Fuzzy PID controller.

The differences are in the scheme, the equation which is used to make the controller and the subsystem block. For the Fuzzy PID controller, the transfer function shown in Figure 7 was created using blocks.

3.3 Feedforward controller

In principle, we use the Feedforward control system to perform fast movements that do not have enough time to obtain feedback or if we want to speed up the operation of the system. The response is thus faster than the time required to receive, process, and control the signal. With such control, the disturbance is detected and considered before it affects the system. Figure 8 shows, for comparison, a scheme of a system without a controller - open loop (a) and a system with a feedforward controller, which compensates for the influence of disturbance (b) [5].
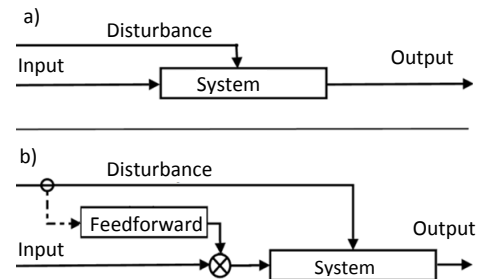
Fig. 8 Non-controlled system (a) and Feedforward system [5]

Since we do not usually know the exact transfer function of the control object, and because the real system is not linear, it makes sense to use a combined system with a feedback loop of the controller. The block diagram of the combined system is shown in Figure 9.
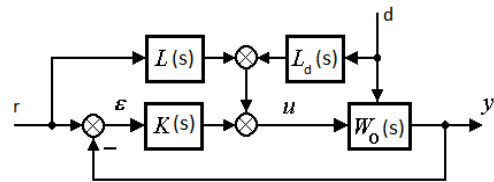
Fig. 9 Structure of combined system [5].

The block diagram of the combined control system in the variant with PID controller is shown in Figure 10 and in the variant with Fuzzy controller in Figure 11.
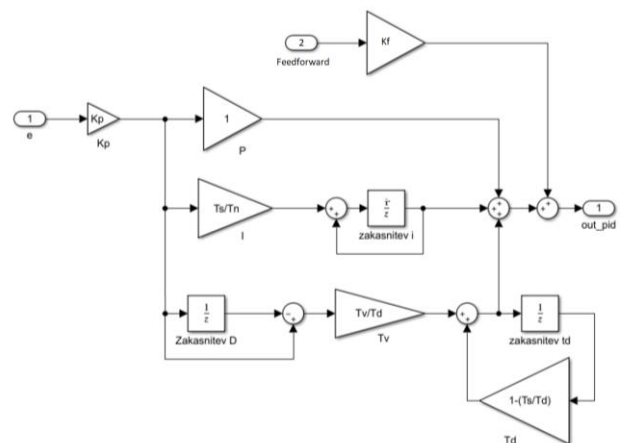
Fig. 10 Block diagram of Feedforward with PID controller.
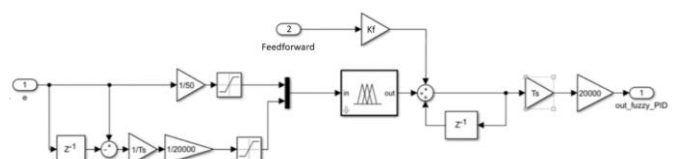
Fig. 11 Block diagram of Feedforward with Fuzzy controller.

4. Results and comparison

The aim of the research was not only to control the linear axis using Matlab/Simulink designed and implemented PID closed loop position controller, but also to evaluate its proper operation and response, which was achieved by comparing the responses of the TwinCAT 3 PID controller and other controller types. In this way, we were able to verify that the axis control system and the closed loop controller were properly designed and implemented. In case we have implemented everything correctly, the behavior of both systems should be the same. Figures 12 to 15 show the responses of the system using presented controller types for the case of minimal load (0,5 kg). The green line represents the set-point change, while the orange line shows the generated position trajectory representing the set-point value and the red shows the actual axis position when moving relative to the generated trajectory. The figures clearly show that the responses different position controller is more or less identical.
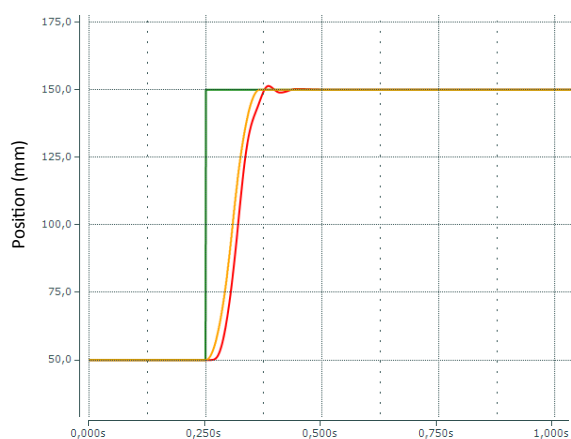
Fig. 12 Step response - PID controller optimized by Ziegler-Nichols method.
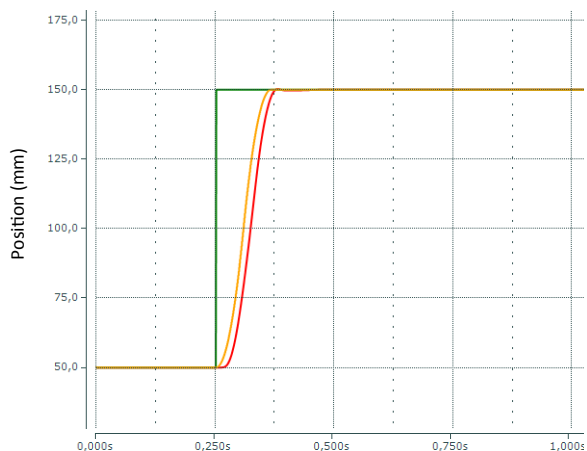
Fig. 13 Step response - Fuzzy controller
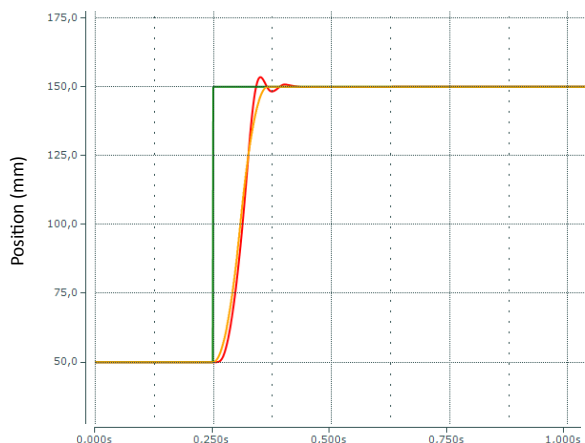
Fig. 14 Step response - Feedforward and PID controller.
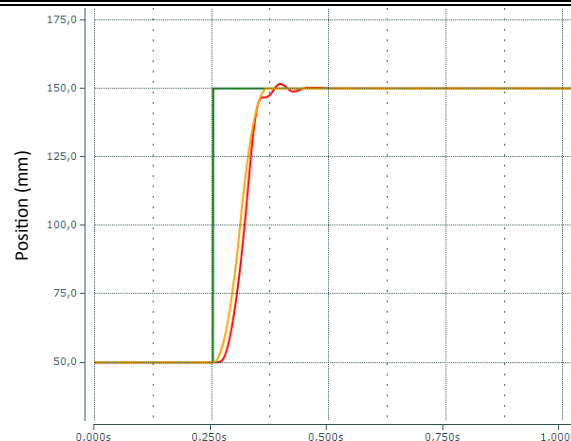
Fig. 15 Step response - Feedforward and Fuzzy controller.

5. Conclusion

The main goal of the research was to build a linear feed system consisting of an industrial type of servomotor to test the design and implementation of different types of controllers suitable for use in the Beckhoff TwinCAT 3 system. On this purpose the TwinCAT 3 PLC program and corresponding user interface for controlling the system was developed in Visual Studio C# WinForms application. This enabled the implementation and testing of various types of position controllers. In addition to research related to different types of controllers, the system allows research into the dynamic behavior of the system in the case of a step input change of position, the dynamic behavior in the case of a disturbance e.g. when changing the load as well as the combined step-disturbance behavior, all for different loads.

The design and implementation of PID position controller from Matlab/Simulink software environment into TwinCAT 3 system allows us to use more advanced, more complex, more responsive, and faster controllers - from the classic PID type, nonlinear Fuzzy controller, and Feedforward control strategy. We can compare different controllers for each system, so we can choose the most optimal controller for application needs. By adding even more different controllers, we gain the ability to test and compare new high-end controller concepts and are no longer limited to TwinCAT 3 controller types.

By confirming the results - approximately the same dynamic responses of different types of regulators, the adequacy of the process of development and implementation of closed loop controllers from the Matlab / Simulink environment is confirmed.

6. References

1. Araki, M. PID CONTROL, Kyoto University, Japan [www], Access: http://www.eolss.net/ebooks/Sample%20Chapters/C18/E6-43-03-03.pdf, [Date of access: 20.4.2022]
2. PID Control System Analysis, Design, and Technology, University of Glasgow [www], Access: http://eprints.gla.ac.uk/3817/1/IEEE3.pdf [Date of access: 20.4.2022].
3. R. Iserman, *Digital Control Systems: Volume 1: Fundamentals, Deterministic Control*, 2nd ed. 1989. Softcover reprint of the original 2nd ed., (1989).
4. Beckhoff Information System for FB_CTRL_PID [www], Access: https://infosys.beckhoff.com/english.php?content=../content/1033/tf4100_tc3_controller_toolbox/9007199500176779.html&id [Date of access: 5.4.2022].
5. K. Graichen, Feedforward Control Design for Finite-Time Transition Problems of Nonlinear Systems with Input and Output Constraints Paperback – Import, December 19, (2006).

Investigation of Heat-Treated Steels Using the Magnetic Noise Method

Yonka Ivanova

Sofia University "St.Kliment Ohridski", Faculty of Physics, Sofia, Bulgaria[1]

Institute of Mechanics at Bulgarian Academy of Sciences, Sofia, Bulgaria[2]

yonivan@phys.uni-sofia.bg,yonka@imbm.bas.bg

Abstract: *This paper presents the results of an investigation conducted on samples of high-quality heat-treated carbon steel using the magnetic noise method. The objective of the work was to find the proper informative parameters for identifying the obtained structures with different hardness. To this end, samples were prepared using quenching and tempering heat treatment at different temperatures, from 150°C to 500°C. After microstructural analysis and hardness measurements, the samples were investigated using the magnetic noise method. The signals were visualized and analyzed using a digital oscilloscope and the Multi Instrument 3.8 software program. The RMS informative parameters and the registration time of the magnetic noise signals were used to identify the obtained microstructures with different characteristics and hardness.*

Keywords: MAGNETIC NOISE METHOD, HEAT-TREATED STEELS, HARDNESS, INFORMATIVE PARAMETERS, RMS, REGISTRATION TIME OF MAGNETIC NOISE SIGNALS

1. Introduction

The magnetic noise method is widely used for the investigation of the microstructure of ferromagnetic materials. It is based on the phenomenon that occurs when a ferromagnetic material is magnetized [1]. The structure of a ferromagnetic material consists of magnetic domains separated by domain walls [1, 2, 3]. In the absence of a magnetic field, the domains are randomly oriented [2]. When a magnetic field is applied, the magnetic domains align in the direction of the applied field by moving their domain walls. This movement is strongly affected by the microstructural features of the ferromagnetic material such as grain boundaries, other phases, inclusions, dislocations, residual stresses, etc. [2]. As a result, abrupt magnetization and induction of voltage in the magnetic test coil occur. The resulting magnetic noise was first recorded and explained by Prof. Heinrich Barkhausen in 1919, though it took until the early 1980s to attract the attention of researchers and the industry. The advantages of this method include good sensitivity, straightforward experimental procedure and no requirements for surface preparation [1-3]. The magnetic noise signal depends on the measurement parameters, the magnetizing current and frequency, and the frequency response characteristic in the analysis of the registered magnetic noise [1]. This method also has some disadvantages related to the need to calibrate the magnetic test coil and the non-standardized approach to the measurement and selection of proper magnetic noise parameters for identifying relationships with the microstructural features of the studied material.

The analysis of the literature shows that the magnetic noise method is sensitive to the carbon content [4], the size of the crystallites [5, 6] and the different microstructures such as: ferrite [5, 7], pearlite [10, 11] and martensite [12, 13].

One or more parameters such as root mean square (RMS) voltage, energy, pulse height, position of the maximum signal as well as the parameters of the magnetic noise envelope were used for qualitative and quantitative assessment of the changes in the microhardness and the structure of the materials [2, 3, 11, 12, 13]. Thus, the Barkhausen noise analysis technique can be used to assess the surface integrity of a manufactured part. In recent years, the researchers have focused their efforts on developing scanning techniques such as the Barkhausen continuous noise method [14] or the use of a rotating coil [15], which makes it possible to expand the application of this method in industrial settings.

The objective of this paper is to search for and find the proper informative parameters of the magnetic noise signals for identifying the obtained microstructures of high-quality carbon steel after quenching and tempering heat treatment.

2. Experiments

2.1. Preparation of samples for conducting experiments

Cylindrical samples of high-quality carbon steel with a diameter of 5.5 mm and a length of 100 mm were prepared. The chemical composition of the steel type used was: C 0.42-0.5%, Si- 0.17-0.37%, Mn - 0.5-0.8%, P < 0.035%, Ni < 0.25%, Cr- < 0.25%, S < 0.04%, Cu < 0.25%. Five groups of samples were prepared, four of which were subjected to heat treatment, which consisted of quenching and subsequent tempering at the following temperatures: 150°C /group 2/, 250°C /group 3/, 350°C /group 4/ and 450°C /group 5/. The heat treatment modes are presented in column 2 of Table 1. By the means of metallographic analysis, the type of the obtained microstructure was determined. The microstructure of the non-heat-treated samples was ferrite and pearlite /Fig. 1a/.

The hardness was measured with a Zwick/Roell ZHV 10 hardness test machine under a load of 9.807 N.

Table 1: *Heat treatment of investigated samples*

	Heat treatment	Microstructure	Vickers hardness HV
Group 1	Non-heat-treated	Ferrite and pearlite	320
Group 2	Quenching T = 850ºC Tempering T = 150ºC	Tempered martensite	750
Group 3	Quenching T = 850ºC Tempering T = 250ºC -	Tempered martensite	620
Group 4	Quenching T = 850ºC Tempering T = 350ºC	Tempered troostite	400
Group 5	Quenching T = 850ºC Tempering T = 500ºC	Tempered sorbite	340

2.2. Experimental installation for conducting investigations using the magnetic noise method

MULTITEST-MC 04 device [16], which consists of a magnetizing unit, a converter for recording magnetic noise signals and measuring magnetic noise voltage, and a signal amplifier with several bandpass filters was used for preliminary investigations. Sinusoidal magnetization with a frequency of 76 Hz was applied. A cyclic sinusoidal field was induced in the sample using a magnetic-noise converter. The Barkhausen signals were visualized and recorded by the means of a digital oscilloscope VT DSO 2810 at a sampling rate of 100 MSPS and the data acquisition software Multi-Instruments Pro 3.8.

3. Results and Discussion

3.1. Results from the performed heat treatment

The results from the performed heat treatment and metallographic analysis are presented in Table 1. Columns 3 and 4 show the type of the obtained microstructure and the mean values of the measured hardness (HV), respectively.

After quenching and tempering at T = 150°C, the obtained microstructure was tempered martensite with a hardness HV = 750 /Fig. 1b/; after quenching and tempering at a temperature of 250°C, the result was tempered martensite with a hardness HV = 600 /Fig. 1c/; after quenching and tempering at temperatures of 350°C и 500°C, the result was tempered troostite /Fig. 1d/ and tempered sorbite /Fig. 1e/, respectively.

The changes in the structure after a low-temperature tempering are related to the decomposition of martensite, the reduction of the carbon content in the main volume of the martensite and the beginning of the formation of iron carbides [17]. The processes that take place during tempering at temperatures of 200-250°C can be explained by the decomposition of residual austenite, which results in the reduction of the internal stresses in the structure and lower hardness. When tempering is performed at temperatures higher than 250°C, the existing martensite decomposes to ferrite and cementite. The troostite formed by tempering at intermediate temperatures /T = 350°C/ is a finely dispersed mixture of ferrite and cementite. With tempering at temperatures of 500°C and above, the formed carbides coagulate and the result is a dispersed mixture of ferrite and cementite called tempered sorbite. The hardness decreases, but the impact strength and ductility increase.
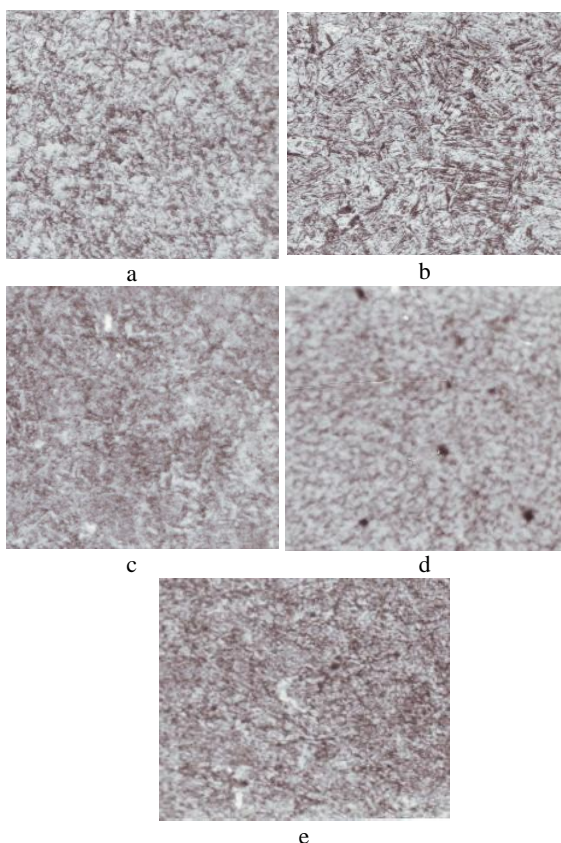
Fig. 1 The microstructure of the tested samples; initial ferritic and pearlitic structure before heat treatment (a), martensitic structure after quenching and low-temperature tempering at T = 150°C (b), martensitic structure after quenching rend tempering at T = 250°C (c), tempered troostite - structure after quenching and tempering at T = 350°C (d), tempered sorbite - structure after quenching and tempering at T = 500°C (e).

3.2. Results of a study using the magnetic noise method

Tests were conducted using the magnetic noise method. The samples described in paragraph 2.1 were analyzed. The frequency of the magnetizing field did not change during the tests. In order to select the optimal magnetization level, the samples were magnetized using magnetizing currents ranging from 100 to 250 mA. A series of magnetic noises was recorded during each magnetization. The magnetization parameters had an effect on the count of the pulses as well as on their size and shape.

To analyze the magnetic noise (MN) parameters, 6 signal bursts were used for each sample, each of them corresponding to half a cycle of magnetization. A bandpass filter of up to 100 kHz was used. The following parameters were used for the preliminary assessment of the magnetic noise signals:

- the RMS value - calculated by the following formula:

$$RMS = \sqrt{\frac{1}{n}\sum_{i=0}^{n-1} x_i^2}$$

as x_i is the amplitude of the magnetic noise signal that passes through the bandpass filter.
- Magnetic noise counts
- Mean width of the magnetic noise signal bursts.

Figure 2 shows part of the recording performed during the magnetization of the tested samples and the magnetic noises that occur at a magnetization current of 200 mA.
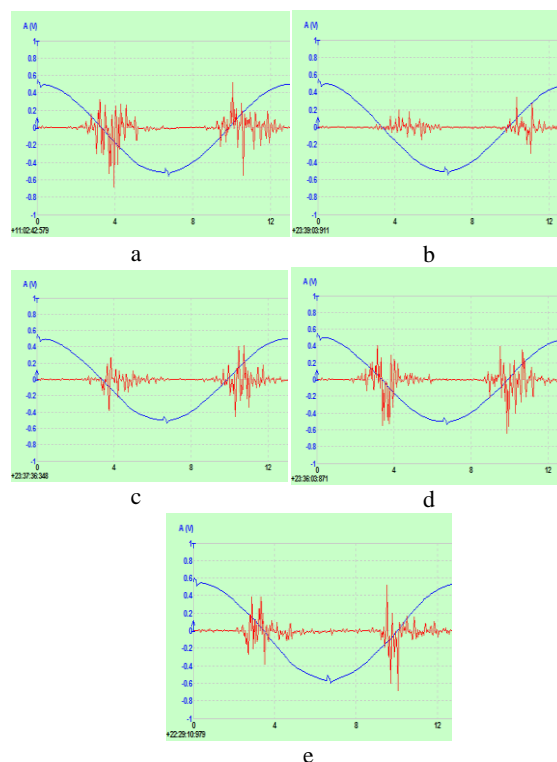
Fig. 2 Recordings of magnetic noises over time obtained from the tested groups of samples at a magnetizing current of 200 mA: specimens group 1 (a), group 2 (b), group 3(c), group 4 (d), group 5 (e).

The results of the analysis of the magnetic noise parameters for the first group of samples for three magnetization cycles are presented in Table 2. As the magnetizing current increases, the RMS value and the bandwidth of the magnetic noise also increase, but the magnetic noise count decreases /Table 2, Fig. 3/.

In the case of half a cycle of magnetization, the sample is demagnetized and then magnetized in the opposite direction. This activates the movement of the domain walls, which overcome the obstacles posed by the different microstructural phases. Under the alternating magnetic field, the generation and the proliferation of magnetic domains are affected by the magnetic polarity reversal. This process depends on the microstructural features, the different phases, the boundaries between the crystallites, the dislocations, the presence, shape and size of the carbide inclusions, the carbide grains, etc. The maximum amplitude and the RMS values of the magnetic noises depend on the magnitude of the magnetic domain jumps with the corresponding magnetizing current.

Table 2: *The results of the analysis of the magnetic noise parameters for the first group of samples*

In,mA	RMS	MN Count	Pulse width,mks
100	79.84	1425	21
150	129.5	1031	25
200	166.3	930	33
250	191.8	900	29
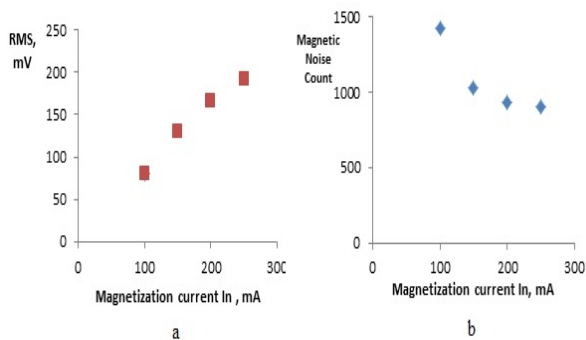
Fig.3 *Change in the RMS /a/ and the magnetic noise counts /b/ with the increase of the magnetizing current for one magnetization cycle in samples before heat treatment.*

Figure 4 shows the change in the RMS of the magnetic noise depending on the magnetizing current in the tempered samples. A high degree of distinctness is observed at a magnetizing current of 150 mA. The samples subjected to quenching and low-temperature tempering which have tempered martensite structure feature the lowest RMS values. In the other groups of samples /3, 4, 5/, an increase in the RMS value is observed, which can be explained by the type of the obtained microstructures of the tempered martensite, troostite and sorbite.
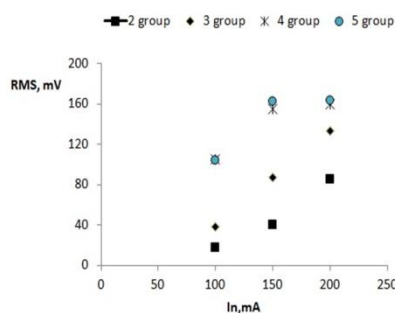
Fig.4 *Change in the RMS of the magnetic noises depending on the magnetizing current in samples subjected to heat treatment*

The recorded magnetic noise signals feature a different time of noise occurrence depending on the magnetization current sine wave.

Therefore, signal processing should be performed. The signals were smoothed and normalized. After the signal processing, the noise envelopes and the peak values were determined.

The time of magnetic noise occurrence, determined from the maximum value of the signal envelope relative to the zero value of the magnetization field, is defined as the parameter (Δt), which is used to identify the microstructure type. Figure 5 shows the envelopes of the magnetic noises of the samples from the tested groups. There is a shift of the peak values at the field value of zero as well as differences in the shape of the envelope. In the tempered martensite structures, the peak value is small and the magnetic noise envelope is wide. In the transition from tempered martensite with high hardness to troostite and sorbite with hardness close to the initial hardness, there is an increase in the peak values and sharpening of magnetic noise envelope at magnetic field values around zero.

The differences in the shift over time as well as in the shape of the magnetic noise can be explained by the irreversible movement of the domain walls when overcoming obstacles due to the different microstructures, i.e. the microstructure of the material directly affects the dynamic behavior of the domains during magnetization.
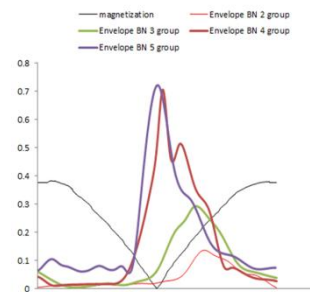
Fig.5 *Magnetic noise envelopes determined during magnetic polarity reversal with In = 150 mA in the tested groups of samples with a different structure*

Figure 6a shows the changes in the time of magnetic noise occurrence parameter (Δt) for group 1 which has ferrite and pearlite structure in an equilibrium state, and Figure 6b shows the results for the shift over time in the other groups.
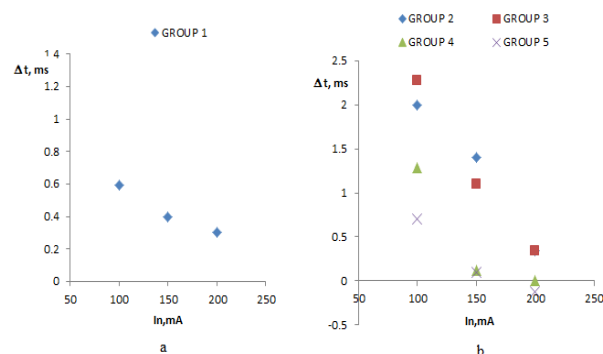
Fig. 6 *The changes in the time of magnetic noise occurrence parameter (Δt) for investigated group samples*

The greatest shifts over time occur at low magnetizing currents with the martensite structure obtained by low-temperature tempering. According to [12, 13, 14, 18], the magnetization of martensite results in many small domains due to the characteristics of martensite and the presence of multiple martensite needles.

Martensite features a high density of dislocations and high internal stresses. That is why a greater value of the magnetizing field is needed in order to move the domains and create new ones.

The obtained peak value of the magnetic noise is small and it occurs at relatively higher values of the magnetizing current. This also explains the different shapes of the magnetic noise in the martensitic structure shown in Figure 5.

Magnetic polarity reversal requires a higher value of the magnetic field and the displacements of the domain walls are small due to the characteristics of martensite. The morphological change from martensitic needles to ferritic and pearlitic structures in the form of troostite and sorbite makes the magnetic structure larger and the average size of the domain walls increases [18]. Magnetic polarity reversal becomes easier. At a magnetizing current of 200 mA, the amplitude of the magnetic noise signal increases significantly and the values of the parameter (Δt) get close to zero.
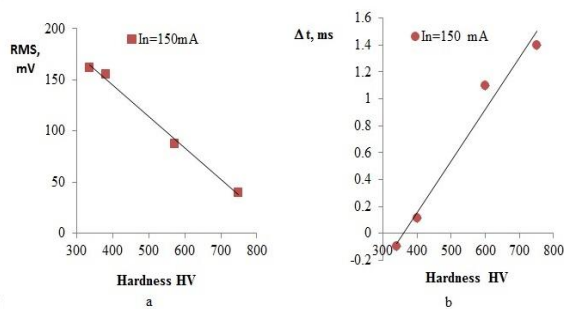
Fig. 7. Change in the RMS parameters /a/ and the shift over time of the occurrence of the magnetic noises (Δt) /b/ depending on the hardness of the obtained structures at a magnetizing current of 150 mA.

Figure 7 shows how the RMS informative parameters and the time of occurrence of magnetic noises, determined relative to the zero value of the magnetic field, change depending on the hardness of the tempered samples. These dependencies can be represented by a linear relationship. The proposed informative parameters characterize the changes in the structure and can be used to assess the hardness as well as for qualitative assessment of the type of the microstructure of structural medium-carbon steels after tempering.

4. Conclusions

By studying tempered samples using the magnetic noise method, data for a series of voltage pulses as a function of time and the related values of the magnetizing field were obtained. Various parameters such as the RMS of the noise, magnetic noise counts per magnetization cycle, etc., were used to characterize the noise signals. It was found that the time of noise registration, as determined from the zero point of the magnetization sine wave to the maximum value of the magnetic noise envelope, is a suitable informative parameter for the analysis of microstructures. After signal processing, the values of this parameter were determined and a relationship in their behaviour was found to exist due to the magnetic polarity reversal processes in the microstructures obtained after tempering. The study found linear relationships between the RMS, the time of magnetic noise occurrence and the hardness of the structures obtained after tempering.

Acknowledgements

References

1. Barkhausen Noise for Non-destructive Testing and Materials Characterization in low carbon steels, ed.by Tu Le Manh, Duxford Woodhead Publishing, Elsevier Ltd (2020)
2. B. Nahak, Material Characterization using Barkhausen Noise Analysis Technique - A Review, Indian J Sci Technol. 10, 14 (2017)
3. E. S. Gorkunov, Yu. N. Dragoshanskii, M. Mikhovski, Barkhausen Noise and its Utilization in Structural Analysis of Ferromagnetic Materials, Review Article V, Russ. J. Nondestruct. Test. 36, 6 (2000)
4. A. Sorsa, Prediction of material properties based on nondestructive Barkhausen noise measurement, Acad. dissertation, University of Oulu, OULU 2013.
5. J. Capo-sanchez, J.A. Perez-Benitez, L.A. Padovese, C. Serna-Giraldo, Dependence of the magnetic Barkhausen emission with carbon content in commercial steels, J. Mater. Sci. 39 (2004)
6. C. Gatelier-Rothea, J. Chicois, R. Fougeres, P. Fleischmann, Characterization of pure iron and (130 ppm) carbon–iron binary alloy by Barkhausen noise measurements: study of the influence of stress and microstructure, Acta Mater. 46 (1998)
7. V. Moorthy, S. Vaidyanathan, T. Jayakumar, B. Raj, On the influence of tempered microstructure on the magnetic Barkhausen emission in ferritic steels, Philos. Mag. A 77 (1998)
8. O. Saquet, J. Chicois, A. Vincent, Barkhausen Noise from plain carbon steels: Analysis of the influence of microstructure, Mater. Sci. Eng. A 269 (1991)
9. P!erez-Beniteza J.A., L.R. Padovese, Investigation of the magnetic Barkhausen noise using elementary signals parameters in 1000 commercial steel, J. Magn. Magn. Mater 263, 1–2 (2003)
10. L. Clapham, C. Jagadish, D.L. Atherton, The influence of pearlite on Barkhausen noise generation in plain carbon steels, Acta Metall. Mater. 39 (1991)
11. F. A. Franco , M.F.R. González, M.F. de Campos, L.R. Padovese, Relation between magnetic Barkhausen noise and hardness for jominy quench tests in SAE 4140 and 6150 steels, J Nondestruct. Eval 32 (2013)
12. K. Davut, C.H. Gur, Monitoring the microstructural evolution in spheroidised steel by magnetic Barkhausen noise measurements, Proceedings of the 7th International Conference on Barkhausen Noise and Micromagnetic Testing, ICBM-7, July 15–16, 2009, Aachen, Germany.
13. Zerovnik P.l., D. Fefer, J. Grum, Surface integrity characterization based on time-Delay of the magnetic Barkhauseн noise voltage signal, Journai of Mechanicai Engineering 60, 1 (2014)
14. C.C.H. Lo, C.B. Scruby, G.D. Smith, Dependences of magnetic Barkhausen emission and magnetoacoustic emission on the microstructure of pearlitic steel, Philos. Mag. 84 (18) (2004)
15. F. Noris Leosdan et al., Continuous Scanning Technique with Barkhausen Magnetic Noise for Carbon Steel Sheets, Mat. Res. 22, 1 (2019)
16. G. Velev, A. Markovski, Investigation of the structure of ferro-magnetic materials using methodology based on Barkhausen effect, 7 Int. Conference on Barkhausen noise and Micromagnetic testing, July 15-16, 2009.
17. G. Totten, *Steel heat treatment handbook*, *Metallurgy and technologies* (Taylor and Fransis Group LLC, NW, 2006)
18. C. Gür, Çam İbrahim, Comparison of magnetic Barkhausen noise and ultrasonic velocity measurements for microstructure evaluation of SAE 1040 and SAE 4140 steels, Mater. Charact. 58 (2007)

Experimental and statistical models for determining the critical values of external action parameters on optical elements in extreme conditions of their operation

Iryna Yatsenko[1], Victor Antonyuk[2], Vyacheslav Vashchenko[1], Tatiana Butenko[1], Sergey Kolinko[1], Kateryna Semenchuk[1]

Cherkasy State Technological University[1], Ukraine; National Technical University of Ukraine " Kiev Polytechnic Institute name of Igor Sikorsky"[2], Ukraine

E-mail: irina.yatsenko.79@ukr.net

Abstract: *The study has been carried out and experimental and statistical models have been developed to determine the critical values of external extreme action parameters (intense heat flows, times of their action, increased external pressures) on optical elements made of glass and ceramics, the excess of which leads to their surface destruction (the appearance of cracks, chips and other defects) and, ultimately, to the failure of optoelectronic devices.*

KEYWORDS: *OPTOELECTRONIC DEVICES, ELECTRON BEAM, OPTICAL GLASS AND CERAMICS*

1. Introduction

Modern optoelectronic devices (pulsed laser rangefinders of sight complexes, laser medical devices, IR devices, etc.) with optical elements made of glass (optical glass K6, K108, K208, etc.) and ceramics (optical ceramics KO1, KO2, KO3, etc.) (Fig. 1) during their storage, transportation and use are subjected to extreme external actions (intense heating flows and external pressures, shock thermal actions in the conditions of shot and flight, etc.) [1 – 7]. At the same time, under these conditions, the surface destruction of the above mentioned elements occurs (cracks, chips, depressions and other defects appear), which ultimately leads to a significant deterioration in the technical and operational characteristics of the devices and their failure.

Therefore, the preliminary determination of the critical values in the main parameters of external actions (external heat flows, times of their action, external pressures, etc.) on the surface of optical elements is of significant importance. Determination of these critical parameters at the stage of design and bench testing will allow to prevent their possible failures in the extreme operating conditions (Fig. 2).

Nowadays, external actions on the surface of optic elements haven't been investigated sufficiently: there are only separate calculation results of the maximum permissible values of thermoelastic stresses in optical elements leading to their destruction [8 – 11]; experimental studies on determining the considered parameters of external actions on elements for different conditions of their operation are absent.

Therefore, the **objective** of this paper is to conduct experimental studies and develop experimental and statistical models to determine the dependences of critical values of the external heat flow $q_n{}^*$ from the critical values of its impact t^* at normal and increased external pressures.

2. Research results and their analysis

Plates with thickness of $H = 2\ldots6\cdot10^{-2}$ m were used to study parametrical impact of external thermal actions (heat flow q_n and time of its action t)) on the working surfaces of optical glass elements (К8, К108, К208, БК10, ТФ110) and ceramics КО1, КО2, КО3, КО5, КО12), the main physical and mechanical characteristics can be found in the studies [12 – 15].

For modeling exterior thermal actions on optical elements at normal conditions ($P = 10^5$ Pa, $T = 273$ K), controlled IR heating with quartz lamps of КГМ-220-1000-1 type was used with РИФ-101 thermal sensors to control temperature on the surface of elements in the range of 300... 1900 K and external heat flows in the range of $1{,}5\cdot10^5\ldots2{,}3\cdot10^6$ W/m^2 [1, 3].

Modeling of the increased heating temperature effects (up to 1500 K) and external pressures (up to 10^7 Pa), as well as supersonic speeds of air flow (up to $2\cdot10^3$ m/s) and angular rotation speeds (up to $4\cdot10^3$ rad/s) at semispherical optical elements (operating conditions of supersonic equipment) were carried out on standard testing facilities [1, 3]. Installations are made of a unit with three test chambers, which house optical elements, volumetric electric heaters and modules for controlling the heating process; multiplier to increase pressure in the chambers; chambers with heated air; replaceable nozzle; states with fixed element; rotation node; control panel.

Flat and curvilinear plates

Rectangular elements of different sizes

Cylindrical elements

Hemisphere streamliners of different thicknesses
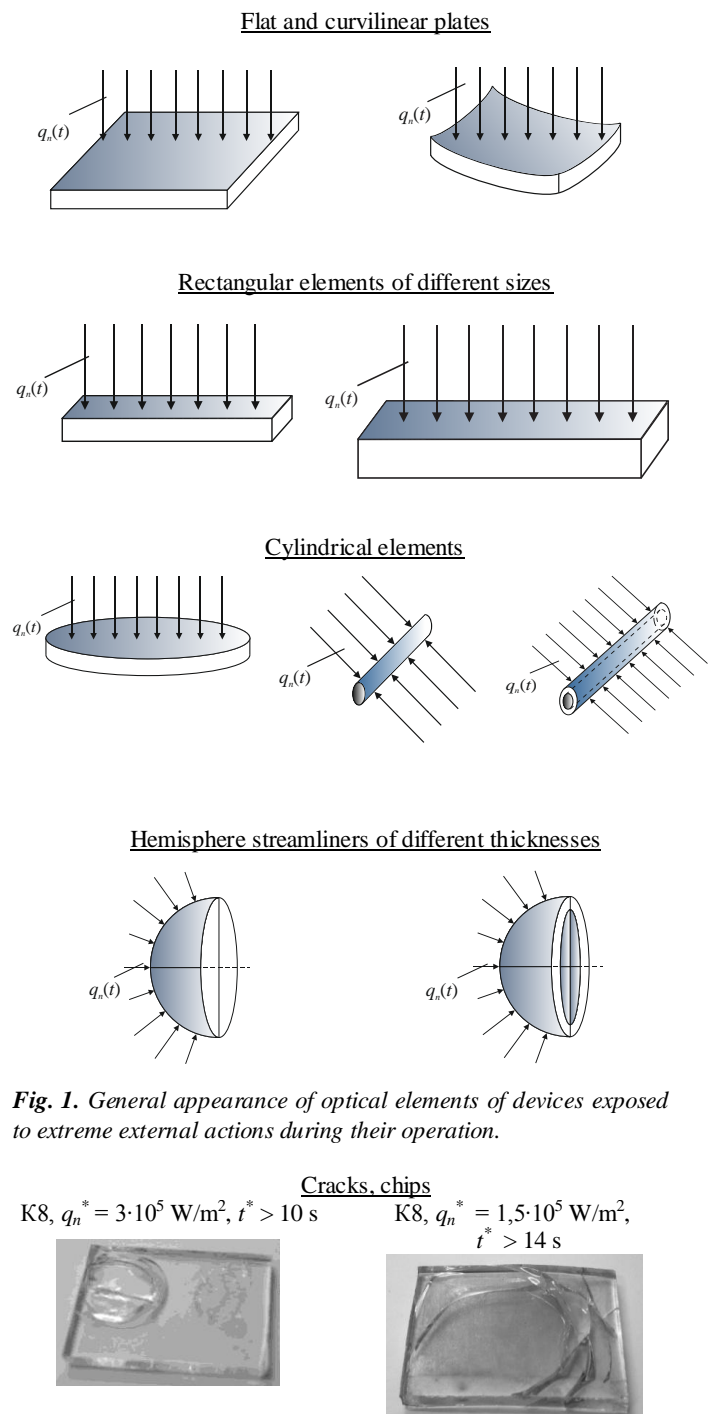
Fig. 1. *General appearance of optical elements of devices exposed to extreme external actions during their operation.*

Cracks, chips

K8, $q_n{}^* = 3\cdot10^5$ W/m^2, $t^* > 10$ s   K8, $q_n{}^* = 1{,}5\cdot10^5$ W/m^2, $t^* > 14$ s

KO2, $q_n^* = 1{,}2 \cdot 10^6$ W/m², $t^* > 25$ s
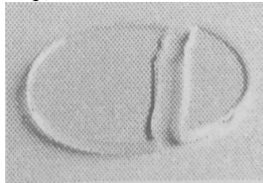
Influxes, undulating surfaces	Areas of rapid boiling
K108, $q_n^* = 6 \cdot 10^5$ W/m², $t^* > 6$ s	K8, $q_n^* = 10^6$ W/m², $t^* > 4$ s

Fig. 2. *Observed destructions of the elements from optical glass (K8, K108) and ceramics KO2 by exceeding the parameters of external actions of their critical values (q_n^*, t^*).*

The influence of external heat flows and the time of their action on the surface of optical plates during their uneven heating. The dependences of the critical values of the external heat flow q_n^* on the critical values of the impact t^* at normal and increased external pressures (fig. 3 - 6), when the surface layers of optical elements are destroyed, has been established as a result of experimental studies (relative error did not exceed 5... 7 %).

Elements made of optical glass. From the data presented in fig. 4, 5, it can be seen that when t^* is increased from 4 s to 24 s, the value q_n^* decreases by 5... 6 times; at the same time, an increase in external pressure from $P = 10^5$ Pa to $P = 10^7$ Pa leads at the given t^* to the decrease in q_n^* by 1,2…1,7 times, and at the given q_n^* – to the decrease of t^* by 1,3…1,5 times.

To increase the efficiency of practical use of these data when designing and manufacturing various devices based on optical elements using well-known methods of mathematical statistics [16] the following experimental and statistical models have been obtained (relative error of 3... 5 %):

$$q_n^*(t^*, P) = (a_0 + a_1 \cdot P + a_2 \cdot P^2) \cdot (t^*)^{b_0 + b_1 \cdot P + b_2 \cdot P^2} \qquad (1)$$

where q_n^* – in W/m²; t^* – in s; P– in Pa; a_0, a_1, a_2, b_0, b_1, b_2 - empirical constants, the values of which depend on the nature of optical glass (Table 1).
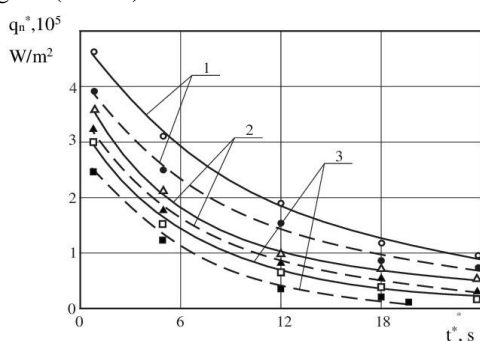
Fig.3 *Dependences $q_n^*(t^*)$ for elements from optical glass K8 (1), K208 (2) and K108 (3), untreated by the electron beam (the width of the sample is $H = 4 \cdot 10^{-3}$ m):* ——— $– P = 10^5$ Pa; $– – – – P = 10^7$ Pa; •, ○, Δ, ▲, □, ■ – experimental data.
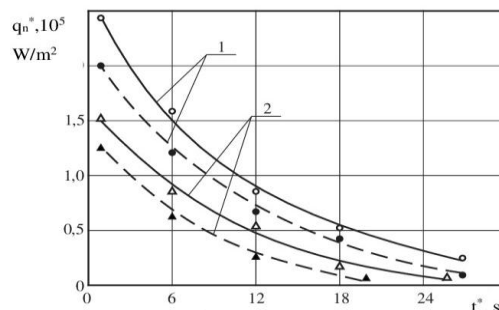
Fig.4. *Dependences $q_n^*(t^*)$ from the elements of optical glass ТФ110 (1) and БК10 (2), untreated by electron beam (the width of the sample $H = 4 \cdot 10^{-3}$ m):* ——— $– P = 10^5$ Pa; $– – – P = 10^7$ Pa; •, ○, Δ, ▲ – experimental data.*
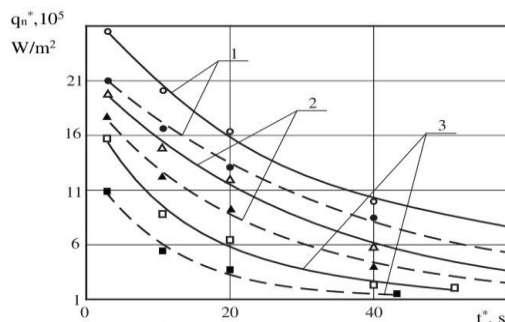
Fig.5. *Dependences $q_n^*(t^*)$ for elements from optical ceramics KO5 (1), KO1 (2) and KO12 (3), untreated by electron beam (the width of the sample is $H = 6 \cdot 10^{-3}$ m):* ——— $– P = 10^5$ Pa; $– – – – P = 10^7$ Pa; •, ○, Δ, ▲, □, ■ – experimental data.*
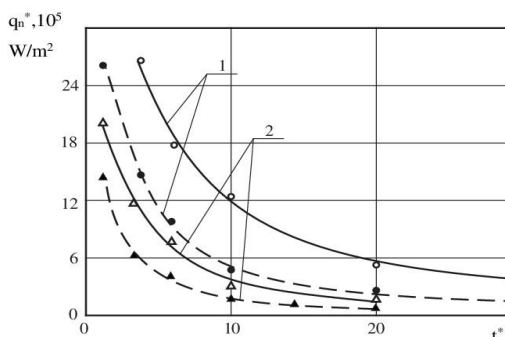
Fig. 6. *Dependences $q_n^*(t^*)$ for the elements from optical ceramics KO2 (1) and KO3 (2), untreated by electron beam (the width of the sample is $H = 6 \cdot 10^{-3}$ m):* ——— $– P = 10^5$ Pa; $– – – – P = 10^7$ Pa; •, ○, Δ, ▲ – experimental data.*

Elements made of optical ceramics. The data presented in fig. 5, 6, demonstrate that both for the optical elements processed by the electronic beam and for the untreated ones, with a decrease of q_n^* from $2{,}5 \cdot 10^6$ W/m² to $1{,}5 \cdot 10^5$ W/m², the value of t^* increases by 6... 8 times. At the same time, the decrease in external pressure from $P = 10^7$ Pa to $P = 10^5$ Pa leads at the given q_n^* to an increase of t^* by 2…2,5 times, and with the given t^* – to an increase of q_n^* by 3... 4 times.

Table 1: *Empirical constant values in experimental and statistical models (1) for optical glass elements*

Brand of glass / Constant	K8	K108	K208	БК10	ТФ110
a_0	$1{,}76 \cdot 10^6$	$1{,}53 \cdot 10^6$	$1{,}67 \cdot 10^6$	$9{,}02 \cdot 10^5$	$1{,}28 \cdot 10^6$
a_1	-10^{-2}	$0{,}31$	$0{,}16$	$0{,}13$	$3{,}6 \cdot 10^{-2}$
a_2	$4{,}7 \cdot 10^{-10}$	$-2{,}5 \cdot 10^{-13}$	$-2{,}4 \cdot 10^{-9}$	-10^{-13}	$-6{,}2 \cdot 10^{-14}$
b_0	$-0{,}94$	$-1{,}07$	$-1{,}24$	$-1{,}21$	$-1{,}11$

b_1	$-7,9\cdot$ $\cdot 10^{-9}$	$-9\cdot 10^{-8}$	$5,8\cdot 10^{-8}$	$-8,3\cdot$ $\cdot 10^{-8}$	$-3,7\cdot$ $\cdot 10^{-8}$
b_2	$9,5\cdot$ $\cdot 10^{-17}$	$6,7\cdot$ $\cdot 10^{-15}$	$-1,4\cdot$ $\cdot 10^{-15}$	$5,1\cdot$ $\cdot 10^{-15}$	$3,8\cdot 10^{-15}$

To increase the efficiency of practical use of the obtained results, as well as for elements from optical ceramics, the following experimental and statistical models have been developed (relative error of 5...7 %):

$$q_n^*(t^*, P) = (c_0 + c_1 \cdot P + c_2 \cdot P^2) \cdot (t^*)^{d_0 + d_1 \cdot P + d_2 \cdot P^2} \qquad (2)$$

where q_n^*– in W/m²; t^* – in s; P– in Pa; c_0, c_1, c_2, d_0, d_1, d_2 - empirical constants, the values of which depend on the nature of optical ceramics (Table 2).

Table 2: Empirical constant values in experimental and statistical models (2) for optical ceramic elements

Ceramic \ Constant	KO1	KO2	KO3	KO5	KO12
c_0	$7,84\cdot 10^6$	$5,91\cdot 10^6$	$5,17\cdot 10^6$	$5,68\cdot 10^6$	$5,47\cdot 10^6$
c_1	$0,32$	$-8,3\cdot$ $\cdot 10^{-2}$	$-0,12$	$-4,21\cdot$ $\cdot 10^{-2}$	$0,242$
c_2	$-3,8\cdot$ $\cdot 10^{-8}$	$6,6\cdot$ $\cdot 10^{-10}$	$3,2\cdot$ $\cdot 10^{-11}$	$-1,3\cdot$ $\cdot 10^{-14}$	$9,1\cdot$ $\cdot 10^{-9}$
d_0	$-0,72$	$-0,79$	$-1,13$	$0,48$	$-0,76$
d_1	$-3,2\cdot$ $\cdot 10^{-8}$	$-1,6\cdot$ $\cdot 10^{-8}$	$-7,9\cdot$ $\cdot 10^{-9}$	$2,5\cdot$ $\cdot 10^{-8}$	$-0,24$
d_2	$1,2\cdot$ $\cdot 10^{-15}$	$1,3\cdot$ $\cdot 10^{-16}$	$-2,3\cdot$ $\cdot 10^{-16}$	$1,5\cdot$ $\cdot 10^{-15}$	$-1,6\cdot$ $\cdot 10^{-17}$

Determination of dangerous areas on the surface of hemispherical fairings in IR devices exposed to maximum heating and destruction in the conditions of supersonic blowing by air flow and axisymmetric rotation. The tests have revealed that at a blowing speed of up $8\cdot10^2\ldots1,2\cdot10^3$ m/s 30...40 % the tested fairings are destroyed, while at blowing speeds of $1,5\cdot10^3\ldots2\cdot10^3$ m/s more than 90% of the tested fairings are subjected to destructions. The increase in the angular speed of the axisymmetric rotation of the fairings (up to $4\cdot10^3$ rad/s) practically does not affect the formation of thermo effects of the gas flow on the surface of the fairings and their destruction. In addition, according to the results of schlieren-photographic studies of gas flow structure and directly according to the final results of the tests, it has been established that the main contribution to the destruction of the fairings is provided by turbulent supersonic blowing of the air flow, which leads to significantly uneven heating of their surface and the formation of zones of elevated thermal actions, where local overheating of streamliners occurs, that leads to their destruction.

At the same time, the locations of these zones for laminar wrapping mode are located in the vicinity of the front critical points for all the studied airflow speed ranges V, and in the case of turbulent mode – significantly shifted along the surface of the fairings. As a result of the conducted studies for the turbulent wrapping mode of the hemispheric fairing the following dependence was obtained $\theta(V)$ (θ – the angular coordinate along the surface of the fairing from the front critical point ($\theta = \theta_{max}^* = 0$) to the place, where both the maximum heating of the fairing and its destruction occur ($\theta = \theta_{max}^*$) (Fig. 7). From the results presented in Fig. 7 it follows that with an increase in the speed of blowing of the air flow, the locations of the fairing surface destruction zones practically do not change: with an increase of V from $7\cdot10^2$ m/s to $2\cdot10^3$ m/s, the values θ_{max}^* lie within $21...23^0$.
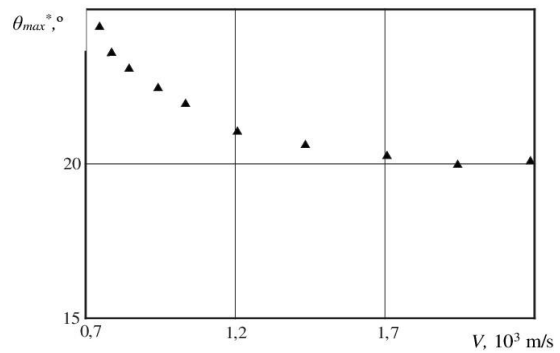
Fig. 7. *Dependence $\theta_{max}^*(V)$ for turbulent blowing of the fairing with supersonic air flow:* ▲ *– results of experimental studies.*
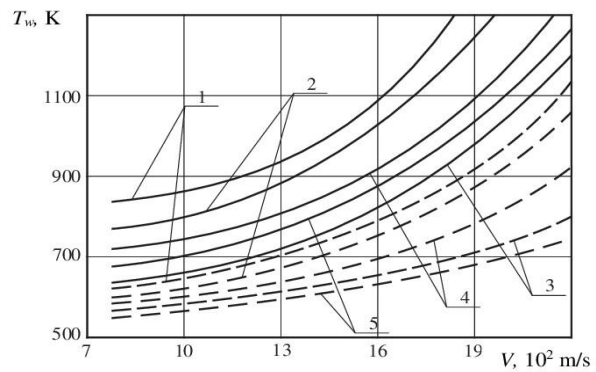
Fig. 8. *Dependence of the temperature T_w in different surface points of fairings from optical ceramics KO1 (1), KO2 (2), KO12 (3), KO3 (4) and KO5 (5) on the speed of the external supersonic gas flow: ——————— temperature in maximum thermal impact zones, which are located along the surface of the fairing from its front critical point ($\theta \neq 0^0$); – – – – – temperature at the front critical point of the fairing ($\theta = 0^0$).*
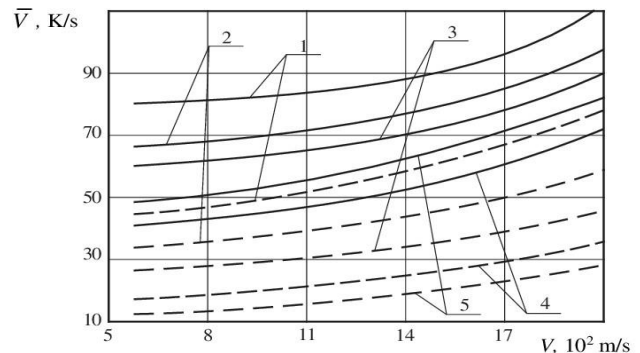
Fig. 9. *Dependence of the average heating speed $\overline{V}$ of the fairing from optical ceramics KO1 (1), KO2 (2), KO12 (3), KO3 (4) and KO5 (5) in different zones, exposed to external supersonic airflow: ——————— – zones with maximum thermal effects, that are located along the surface of the fairing from its frontcritical point ($\theta \neq 0^0$); – – – – – zone with elevated temperature, that corresponds to the front critical point of the fairing ($\theta = 0^0$).*

The obtained test results of fairings made of optical ceramics in conditions of supersonic blowing of air flow are due, as shown by numerical calculations of kinetic heating of the fairing surface [1, 3], by very high temperatures in the areas of the surface of the fairing, that are exposed to destructions during operation: an increase of V to $V = 2\cdot10^3$ m/s leads to an increase in the temperature in stated zones to 1400...1500 K, and at the front critical point – up to 1000...1100 K (Fig. 8). In addition, the estimate of the average heating speed $\overline{V}$ ($\overline{V}$ has been estimated as the average integral characteristic during the action of IR devices with fairings) of the fairing surface in these zones shows its significant values and significant dependence from V (Fig. 9): raising V to $V = 2\cdot10^3$ м/с m/s leads to an increase in the average

heating speed of the product surface in these zones up to 100...120 K/s, and at the front critical point – up to 70...80 K/s.

Increased temperature values and heating speeds of fairing surfaces in the above-mentioned hazardous zones lead to the emergence of significant thermal strains in these zones, which exceed their critical values, that for the considered optical ceramics are the reason of the destruction in the surface layers ofthe fairings.

3. Conclusions

1. For the first time, the following influence patterns of external thermal effects on optical elements have been established:

– <u>with the steady heating of the elements</u>, the increased heating temperatures (up to 1500 K) and external pressures (up to 10^7 Pa), observed when using devices with these elements, do not lead to noticeable violations in the integrity of the surface layers of elements (the appearance of cracks, chips, etc.);

– <u>with uneven heating of the elements</u> the increase in the external heat flow q_n (from $5\cdot10^5$ W/m^{2}до $2\cdot10^6$ W/m^2) and the time of its action t (from 24 s to 60 s) leads to the destruction of elements made of optical glass and ceramics; at the same time, an increase in external pressure from 10^5 Pa до 10^7 Pa reduces their critical values by 1,2…2,5 times;

– for the specified ranges of changes in parameters q_n and t with external influence on optical elements, experimental and statistical models have been developed to determine the dependencies of their critical values $q_n^*(t^*, P)$ (relative error 3...7%), that allows at the stage of design and manufacture of devices to determine possible critical modes of their heating at high external pressures, the excess of which leads to the destruction of optical elements and failure of devices.

2. For the first time, IR device testing with hemispherical fairings made of optical ceramics in the conditions of their blowing with supersonic air flow allowed to establish:

– at a blowing speed of up to $5\cdot10^2…10^3$ m/s 30…40 % of the tested fairings are subjected to destruction, and at blowing speeds of $1,5\cdot10^3…2\cdot10^3$ m/s more than 70% of the fairings are subjected to destructions;

– for laminar mode of wrapping the destruction of fairings is observed next to their critical points $\theta = 0^0$ (θ – spherical coordinate), and in the case of turbulent wrapping mode, the area of destruction shifts along the surface of the fairings from the front critical point at a distance corresponding to $\theta = 21…23^0$, that allows by adjusting the speed and direction of launching products with the considered IR devices by 1,5…2 times to reduce the number of destructions of their fairings in stated hazardous areas and increase their reliability when operating in the conditions of shot and flight.

4. References

1. Vashchenko V. A., Yatsenko I. V., Lega Y. G., Kirichenko O. V. Osnovy elektronnoi pbrobky vyrobiv z optychnych materialiv (The basics of electronic processing of optical materials) Kiev: Naukova Dumka, 2011, 562 p.

2. A.R. Glushchenko, V.I. Gordienko, A.A. Burkovsky et al., Lazernyye sistemy tankovykh pritselov (Laser systems for tank sights), Cherkassy: Maklaut: 2009.

3. Yatsenko I. V., Antoniuk V. S., Vashchenko V. A., Tsybulin V. V. Prevention of possible destruction of optical elements of precision instrumentation in conditions of external thermo-influences, Journal of Nano- and Electronic Physics, 2016, Vol. 8, 1, P. 01027 – 01032.

4. Yatsenko I.V., V.A. Vashchenko, Yu.I. Kovalenko1 , V.P. Kladko , O.Yo. Gudymenko, P.M. Lytvyn , A.A. Korchovyi, S.V. Mamykin, O.S. Kondratenko, V.P. Maslov, H.V. Dorozinska, G.V. Dorozinsk. Effect of electron-beam treatment of sensor glass substrates for SPR devices on their metrological characteristics. SPQEO, 2019. V. 22, N 4. P. 444-451.

5. Yatsenko I.V., Antonyuk V.S., Vashchenko V.A.,Kyrychenko O.V., Tishchenko O.M.Regularities of influence of electron-beam technology modes on the performance characteristics of optical elements. Journal of Nano- and Electronic Physics. 2019. 11 (2). C. 02014 (7cc).

6. V. Maslov, G. Dorozinsky, I. Yatsenko, V. Kladko, H. Dorozinska, O. Gudymenko. Improvement of sensor glass substrates for surface plasmon resonance devices. 40th International Conference on Electronics and Nanotechnology (ELNANO), 2020 IEEE, p. 81-84.

7. Yatsenko I.V., Antonyuk V.S., Gordienko V.I., Vaschenko V.A., Kiritchenko O.V. Determining the critical parameters of the electron beam with surface melting of the optical elements of precision instrumentation. Journal of Nano- and Electronic Physics. 2017. № 9 (1). C. 01010 (5cc).

8. I.V. Yatsenko, V.S. Antonyuk, V.A. Vashchenko, V.V. Tsybulin, Nanoengineering, 10(52), 38 (2015).

9. I.V. Yatsenko, V.S. Antonyuk, V.A. Vashchenko, V.V. Tsybulin, Nanoengineering, 12(54), 20 (2015).

10. Yatsenko I.V., Antonyuk V.S., Gordienko V.I., Kiritchenko O.V., Vaschenko V.A.The Increase in the Probability of Failure-Free Operation of the IR-Devices Homing and Tracking by the of Electron Beam Processing of Optical Fairings on the Areas.Journal of Nano- and Electronic Physics. 2018. №10 (4). C. 04028 (7cc).

11. I. V. Yatsenko, V. Antoniuk, O. Kiritchenko, V. Gordienko and V. Vashchenko, "Increase of reliability of optic-electronic devices by means of finishing electron-beam processing of their optical elements", Int. Sci. J. "Machines. Technologies. Materials". 4, 160 – 164, (2018).

12. V.A. Panov, M.Ya. Kruger, V.V. Kulagin et al., Handbook of the designer of optical-mechanical devices (Leningrad: Mashinostroenie: 1980).

13. Glass and ceramics - XXI. Prospects for Development, ed. Zhabreva V. A., Konakova V. G., Schultz M. M. (St. Petersburg: Janus, 2001).

14. M.A. Okatov, E.A. Antonov, A.B. Baigozhin, Handbook of an optician-technologist (St. Petersburg: Politekhnika: 2004).

15. V.A. Zverev, E.V. Krivopustova, T.V. Tochilin, Optical materials. Textbook for designers of optical systems and devices (St. Petersburg: SP NIUITMO Publishing House: 2009).

16. S.Ya. Vilenkin, Statistical processing of the results of the study of random variables (Moscow: Energy: 1979).

Application of submodeling in strength analysis of horizontal tank for storage of petroleum products

Prof. Dr. Pejo Konjatić[1], Sara Radojičić[2] Dorian Turk[3], Matej Pudić[4]
University of Slavonski Brod, Croatia[1]
pkonjatic@unisb.hr
University of Slavonski Brod, Croatia[2]
dturk@unisb.hr
University of Slavonski Brod, Croatia[3]
sradojicic@unisb.hr
TD Komunalac d.o.o., Croatia[4]
matejpudic.sfsb@gmail.com

Abstract: This paper shows the approach of submodeling in finite element analysis in process of designing the horizontal tank for storing petroleum products. Those kinds of tanks are made at exact standards or slightly altered by customers' demands. Before the numerical analysis of the tank, the tank standards are described as well as numerical analysis. In the paper, the methods which will be used in obtaining solutions by finite element method were described. 3D finite elements have been used for numerical analysis. After getting the results of full tank model meshed with 3D tetrahedral final elements, the technique of submodeling has been used to achieve more accurate results in critical locations of the tank. In the final aspect, result analysis was conducted, where the results were confirmed so that the tank complies with the standard and meets all the criteria given to the designer.

Keywords: FINITE ELEMENT METHOD, SUBMODELING, HORIZONTAL FUEL TANK, LIFTING LUG

1. Introduction

Fuel tanks are used for the storage of various types of liquid fuels, fuel oils and similar liquids with a maximum density of up to 1,9 kg/l, which assigns fuel tanks to Class A according to the relevant standard which is used in this analysis EN 12285-1:2018. [1]. They are manufactured as single-wall and double-wall tanks. Single-wall tanks are used when the tank is located in a location that protects the environment from possible fuel leaks. With double-wall tanks, there are no restrictions on the location of the tanks. Double-walled tanks allow continuous leakage control (negative or positive pressure) and provide long-term safety in use [2].

Fuel tanks are considered pressure vessels subjected to tensile forces within the walls of the container. The normal stress in the walls of the container is proportional to the pressure and radius of the vessel and inversely proportional to the thickness of the walls. [3]. Pressure vessels and tanks are different in both design and construction: tanks, unlike pressure vessels, are limited to atmospheric pressure; and pressure vessels often have internals pressure while most tanks do not have that [4].

It is imperative for an engineer to design and analyze the pressure vessel that will provide safety, durability and serviceability to the end user. Accomplishing this task will require a very good knowledge of design parameters, the most important being, geometry of pressure vessel that must be analyzed to comply design standards [5]. For this reason, many studies have been carried out to explain the design and finite element analysis of horizontal tanks on saddle supports [6-9].

The standards also include lifting lugs for transporting and lifting tanks. Each tank must be equipped with lugs for lifting the tank. The number of these lifting lugs shall be at least one for a tank up to 20 m^3 and not less than two above 20 m^3. They shall be placed so that the tank can be lifted in a horizontal position. The lugs welded to the tank shall be of such size and number that the empty tank can be lifted. The minimum diameter of the hole on the tank lifting lug must be 60 mm [1].

This paper presents the results of the numerical analysis of the strength of the horizontal tank used for storage of petroleum products. The ANSYS 18.0 [10] software package was used to obtain the results of the stresses and strain in the tank. Before using the ANSYS software package, it was necessary to create a 3D model of the tank to be used in the software. The tank 3D model was created in SOLIDWORKS 2021 [11].

2. Problem description

This paper aims to verify the structure of the horizontal tank for storing oil derivates and determine whether design changes are needed. The verification will be performed by determining the equivalent von Mises stresses and the maximum total displacement of the fuel tank. The results are acquired by comparing the stresses obtained by FEM analysis from global model and for each submodel.

Fuel tanks are normally mounted on two stands. The stand can be welded to the tank or can be movable in relation to the tank. The baseplate has holes for fixing the plinth to the base plate and the ribs have holes for the floor connection. The plinths are primed and given a final coat of paint, i.e. bitumen board or Recitol if the plinth is used for the installation of tanks in the excavation pit [12]. An overview of the tank model developed in the SOLIDWORKS 2021 software can be found in Figure 1.
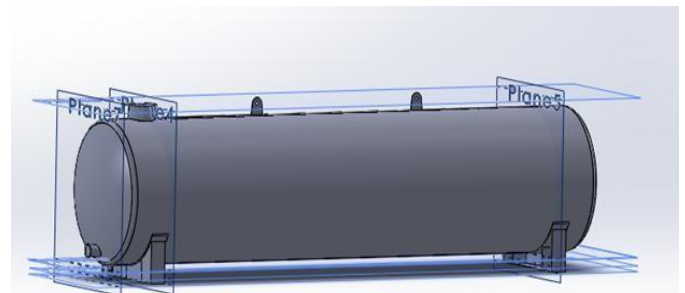
Fig. 1 *3D model of horizontal tank for storage of petroleum products*

The tank is used for the storage of petroleum products (liquid fuels up to 1,1 kg/l) with wall thickness of 7 mm and is supported by two saddles, which are also made according to the standards for the tank manufacturing. Investigated tank is manufactured according to standard mentioned earlier in the paper. Its dimensions and other data can be seen in Figure 2. As this is a 50 m^3 tank, a lot of computational power is needed to create a high-quality mesh for the meshing of a geometric model from appropriately selected finite elements.
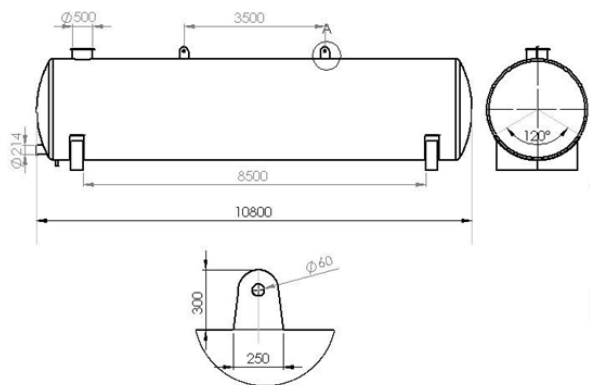
Fig. 2 Dimensions of the 50 m^3 horizontal tank

3. Finite element analysis of the global model

In order to obtain the required results, material properties of steel S235JR are assigned to the model. The Young's modulus of elasticity $E = 210$ GPa, yield strength $R_{p0,2} = 235$ MPa and the value of Poisson's ratio $v = 0,3$ [13, 14].
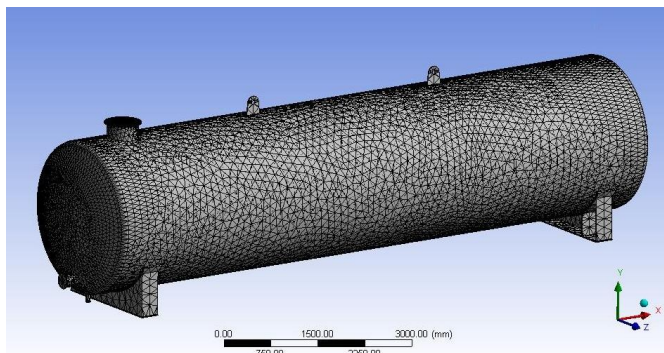
Fig. 3 Display of a 3D finite elements mesh

Global model with a coarse mesh is made with tetrahedral finite element mesh size of 100 mm and boundary conditions are applied (Figure 3 and Figure 4). Total number of finite elements in global model is 54271 with 106702 nodes. As a boundary condition, fixed support is used as well as displacement support with restrained y-direction and a test pressure of 0,2 MPa is set.
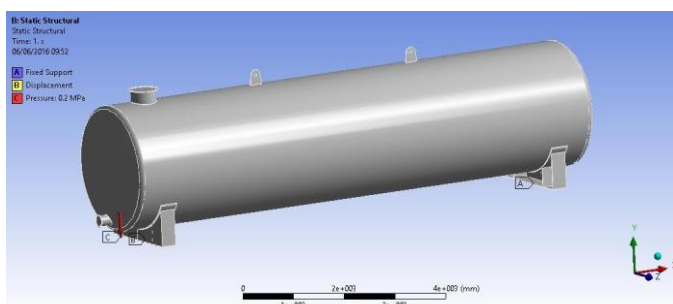
Fig. 4 Boundary conditions of the 3D model

The representation of the equivalent von Mises stresses in the 3D model is shown in Figure 5. With the 3D model, the highest stresses are at the junction between the cylindrical and the bottom part of the tank. The magnitude of the maximum equivalent stresses is 191,76 MPa.
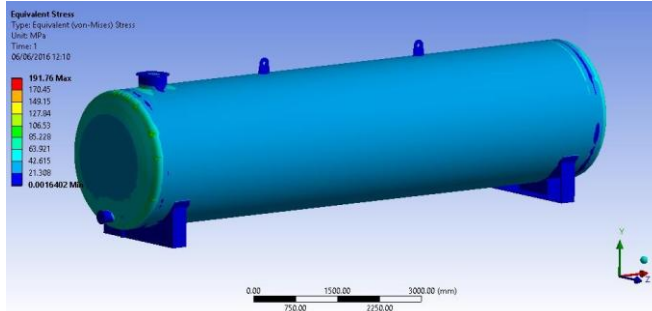
Fig. 5 Distribution of the equivalent von Mises stress

It can be seen that for largest part of the tank, the stress intensity does not exceed 50 MPa. The distribution of the total displacements can be seen in Figure 6. The top opening is analyzed in more detail as submodel in order to obtain more precise stress distribution. The displacements in the largest part of the tank are very small and the maximum displacement is 2,2057 mm at the opening of the tank.
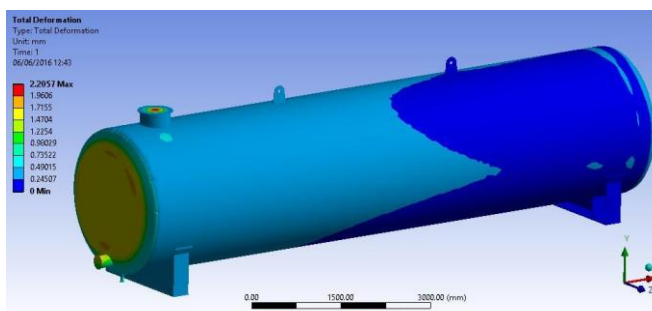
Fig. 6 Global model distribution of the displacement

4. Finite element analysis of submodels

All material and test pressure data given previously were used to obtain results for the tank opening submodel. Displacement results obtained from the global model with coarse finite element mesh are imported into the submodel of the opening, and mesh refinement of submodel is done to obtain more accurate results.

The finite element mesh convergence of the 3D submodel is performed to determine adequate mesh size. Table 1 shows the data of the number of elements, nodes and equivalent von Mises stress in the submodel of the top opening.

Table 1 Number of elements, nodes and equivalent von Mises stress in the top opening submodel

Element size, mm	25	15	13	11
Submodel node numbers	51912	127338	129423	177553
Submodel element numbers	25780	64423	65320	89918
Maximum equivalent von Mises stress, MPa	194,34	184,74	183,17	185,31

The convergence of the von Mises stress solutions is shown in Diagram 1. It can be seen that the deviations are within 5% between the 15, 13 and the 11 mm finite elements, which means that the finite element mesh size of 11 mm is sufficient enough for acquiring accurate results.

Diagram 1 The convergence of the von Mises stress solutions
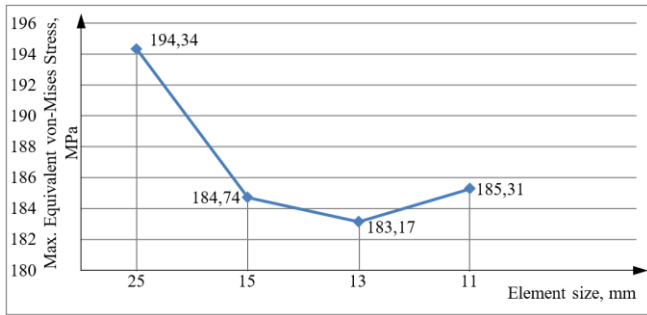
Figure 7 shows a finite element submodel obtained using 11 mm 3D finite elements thus the mesh consists of 177553 nodes and 89912 elements. The mesh in the submodel is significantly denser, showing more accurate results around the tank opening. The submodel of the top opening was created due to the increased displacement and stresses around this area of the tank.
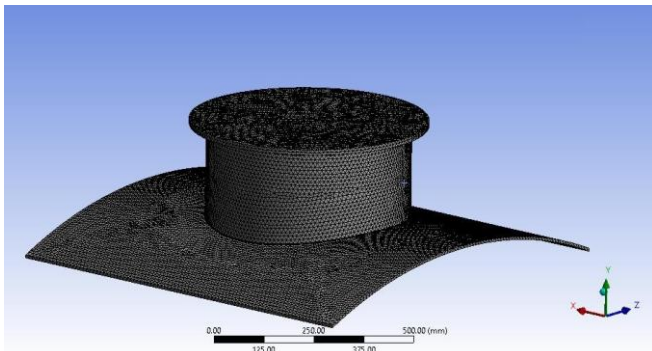
Fig. 7 Submodel with fine mesh of the top opening

An overview of the total displacements at the tank opening can be seen in Figure 8. The maximum displacement of 2,8447 mm has appeared in the area of the top of the opening.
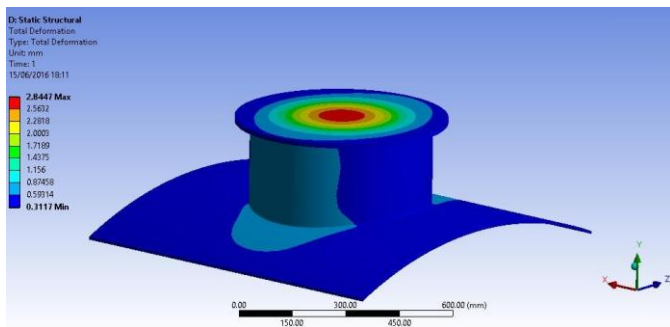
Fig. 8 Distribution of the displacement of top opening submodel

An overview of the equivalent stresses in the top opening model can be seen in Figure 9. The submodel of the top opening shows increased stresses. By increasing the number of elements in the area of the tank opening, the stresses are approaching more accurate values. The largest stresses occur in the inner part where the top opening and the cylindrical part of the tank connect. These stresses do not affect the safety of the structure and they occur at the edge between the cylindrical part of the tank and the tank opening with maximum value of 185,31 MPa.
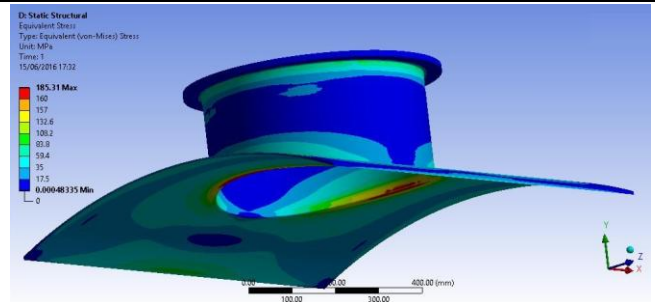
Fig. 9 Distribution of the equivalent von Mises stress of top opening submodel

For the calculation of the submodel for lifting the tank as well as for the submodel for opening the tank, it is necessary to use the results of displacement of the global 3D tank model. As a boundary condition for lifting lug submodel, a calculated force of 28318,23 N needed for lifting horizontal tank is applied. Figure 10 shows the distribution of the displacement of the entire model when lifting the tank, and Figure 11 shows the distribution of the equivalent stress according to von Mises. The lifting lug submodel is made in order to get more accurate displacement and stress distribution. During the lifting of the horizontal tank, maximum displacement is 2,6935 mm on the lifting lug.
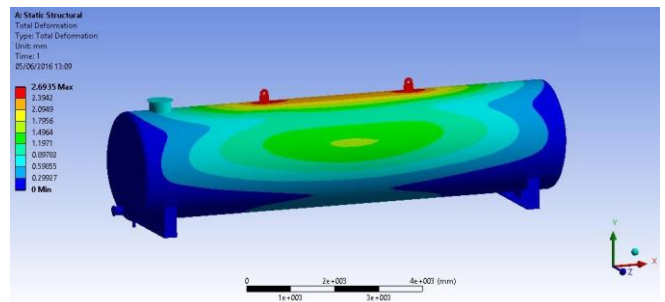
Fig. 10 Distribution of the displacement of global model during lifting of horizontal tank
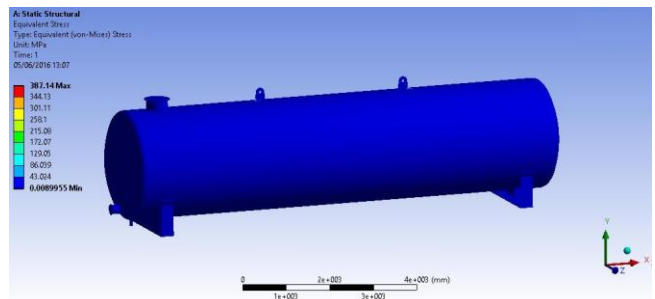
Fig. 11 Distribution of the equivalent von Mises stress of global model during lifting of horizontal tank

A detail of the equivalent von Mises stress distribution around the lifting lug is shown in Figure 12. The maximum stress according to von Mises is 387,14 MPa.
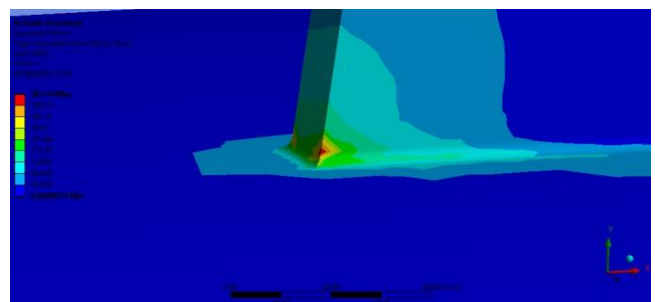
Fig. 12 Distribution of the equivalent von Mises stress of lifting lug submodel

Figure 13 shows a mesh of a lifting lug submodel consisting of 696362 nodes and 423237 finite elements.
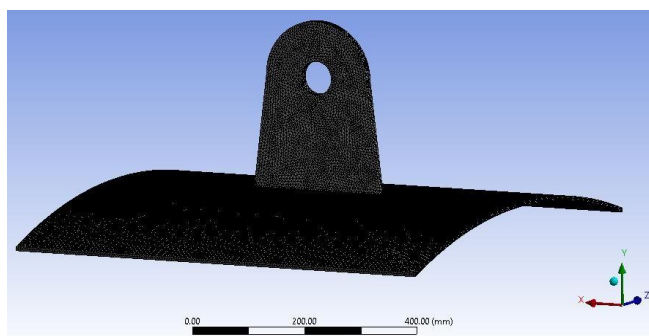
Fig. 13 *Finite element mesh of lifting lug submodel*

After meshing, lifting force was applied as a boundary condition in the tank lifting lug submodel. An overview of the total displacement distribution of the tank lifting lug submodel is shown on Figure 14. The maximum total displacement is 2,9195 mm. The equivalent von Mises stresses in the lug model are presented in Figure 15.
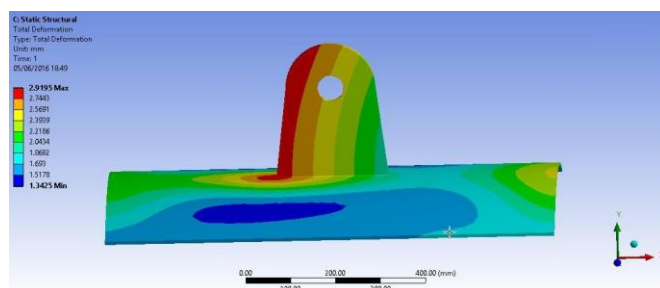
Fig. 14 *Distribution of the displacement of lifting lug submodel*
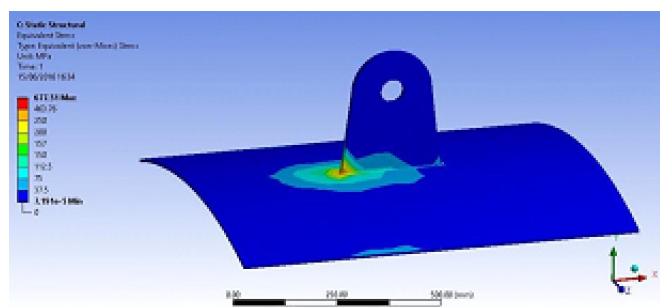
Fig. 15 *Distribution of the equivalent von Mises stress of lifting lug submodel*

Figures 14 and 15 show a high stress of 677,51 MPa at the joint between the tank and the lifting lug in the area where the lifting lug is not fully welded, due to stress concentration caused by geometry. Significant displacements are not visible in this part. The maximum total displacement is at the very top of the lifting lug and along the edge of the lug. The displacement for this part is 2,9195 mm.

4. Conclusions

Tanks for the storage of petroleum products, like all other tanks, whether pressurized or not, are manufactured according to precisely defined standards. The standards determine everything about the tank, from the materials, dimensions, welds, wall thickness, tank supports, etc. Once the tank volume has been determined and selected, it is necessary to follow the procedure specified by the standards to manufacture the tank. The standard used in this paper is EN 12285-1:2018. Since only some dimensions are defined in the standard, all dimensions must be harmonized to obtain a tank with the desired volume.

In this paper, the CAD / FEM has contributed a lot to confirm the required stresses and strains of the tank. In the paper, the tank is tested as specified in the standard. The test is carried out at a precisely specified pressure, which depends on the application of the tank. To achieve greater accuracy of the results, it is necessary to make the mesh as dense as possible at the location of the stress concentration. Increasing the number of elements and nodes would give more accurate results. Since the design is large and lacks computational power, it was useful to create submodels to describe the displacements and stresses at the tanks locations that are of interest.

At the very end, it can be stated that the tank fulfils all the conditions set out in the paper. The tank complies with the standard and meets all the criteria given to the designer in the manufacture of such tanks.

5. References

1. EN 12285-1:2018, *Workshop fabricated steel tanks - Part 1: Horizontal cylindrical single skin and double skin tanks for the underground storage of flammable and nonflammable water polluting liquids other than for heating and cooling of buildings,* 122, (2018.)
2. Pireko d.o.o., Oroslavje, Hrvatska, Technical Catalogue. Fuel tanks.
3. Ibrahim, A., Ryu, Y. and Saidpour, M. *Stress Analysis of Thin-Walled Pressure Vessels.* Modern Mechanical Engineering, 5, 1-9., (2015)
4. Anandhu, P. D., Avis, A. *Design and Analysis of Horizontal Pressure Vessel and Thickness optimization*. International Journal of Innovative Research in Science, Engineering and Technology (IJIRSET), 7, 8171-8177., (2017)
5. Zore, A. Y., Qaimi, M. G. *Design and Optimization of Saddle for Horizontal Pressure Vessel*, International Engineering Research Journal (IERJ) Special Issue 2, 4, 4201-4204., (2015)
6. Birhane, A.H., Hari, Y. *Finite Element Analysis and Design of a Horizontal Tank on Saddle Supports.* Proceedings of the ASME 2002 Pressure Vessels and Piping Conference. Vancouver, BC, Canada. August 5–9, 7, 275-281. (2002)
7. Agale, C.M., Awachat, P.N. *Finite Element Analysis of Horizontal Pressure Vessels Saddle*, International Journal of Innovations in Engineering and Science, Vol. 2, No.2, 7, 7-13. (2017)
8. Patil, Jaydip & Kumbhar, Samir & More, Nilesh & Patil, Ranjit. *Finite Element Analysis of Saddle Support for Stack Heat Exchanger.* International Journal of Engineering Applied Sciences and Technology. 5, 78-85. (2020)
9. Patil R. B., Kulkarni V. V. *Finite Element Analysis of Support Designs for Road Tankers,* International Research Journal of Engineering and Technology (IRJET), Vol. 5, No.2, 8, 836-843. (2018)
10. Ansys, ANSYS 18.0, Ansys Inc., 2017.
11. SolidWorks Premium 2021, Dassault Systems, 2021.
12. W. B. Greyer, *Handbook of storage tank systems: Codes, Regulations, and Designs*, 360, (2000.)
13. EN 10028-2:2017, *Flat products made of steels for pressure purposes – Part 2: Non-alloy and alloy steels with specified elevated temperature properties,* 31, (2008.
14. EN 1993-1-7:2008/NA, *Eurocode 3: Design of steel structures - - Part 1-7: Plated structures subject to out of plane loading*, 5, (2008.)

Design of a press mold for chips compaction and extrusion of aluminum alloys compacts

Конструкция на пресформа за компактиране на стружки и екструдиране на компакти от алуминиеви сплави

Assoc. Prof. PhD. Angel Velikov,
Senior assistant PhD. Tsvetan Tochev, Senior assistant PhD Veselin Petkov
Institute Metal Science, Equipment and Technologies with Hydroaerodynamics Centre "Acad. A. Balevski"- Bulgarian Academy of Sciences

Резюме: Конструирана е специализирана пресформа за компактиране на стружки. Пресформата е изработена и чрез нея са получени компакти от четири вида алуминиеви сплави. Изследвани са и възможностите за екструдиране на получените компакти.
Ключови думи: пресформа, стружки, компактиране, алуминиеви сплави.

Abstract: It has been designed a specialized press mold for chips compaction. The press mold has been made and through it compacts of four types of aluminum alloys have obtained. The possibilities for extrusion of the obtained compacts have also been studied.
Key words: press mold, chips, compaction, aluminum alloys

1. Въведение

Процесът на директното рециклиране на алуминиеви стружки и скрап е екологично решение, което свежда до минимум проблема с разходите за обработка. За да се получат най-високи качества на продукта от директния метод за рециклиране трябва да се обмислят няколко фактора по време на обработката [1,2]. Стружките се получават най-често от процесите стругуване или фрезоване. Стругуването е процес, при който детайла се върти, а режещият инструмент отстранява слой по слой от материала [3]. При процеса фрезоване рязането се осъществява чрез въртеливо движение, извършвано от инструмента, а подавателното движение се предава на заготовката, като най-често то е праволинейно [4]. Компактирането на алуминиеви стружки е процес, при който с прилагане на натиск върху матрица се получава определена форма на заготовката, с плътност, порьозност и уплътняване . Съществуват два начина за компактиране – студено и горещо

2. Конструктивна разработка на пресформа

За осъществяване на гореказания процес е конструирана специализирана пресформа (фиг.1).

Компактирането на стружките до брикети се извърши в контейнер (фиг.1-поз.4) с вътрешен диаметър ⌀40mm на конструирана за целта пресформа. Основните й елементи са: бандажиращ пръстен (фиг.1-поз.6), горен поансон (фиг.1-поз.3) , долен поансон (фиг.1-поз.8) и контейнер (фиг.1-поз.4) . Нагряването на пресформата се осъществява с помощта на нагревател (фиг.1-поз.7). Температурата се контролира с термодвойка желязоконстантан. Поддържането й се осъществява с електронен терморегулатор тип ЕСПА с точност ±5 C°. Избиването на брикета от контейнера се осъществява с долния поансон, който се задвижва от специален хидравличен цилиндър, свързан с поансона посредством присъединителна плоча (фиг.1-поз.9).
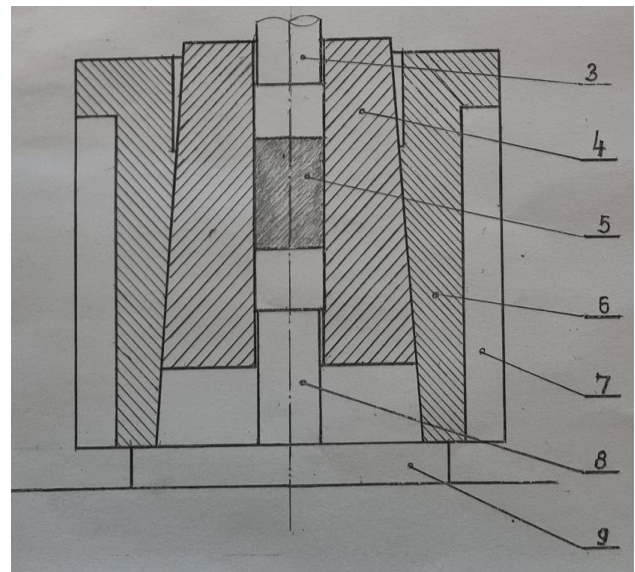
Фиг.1

Операциите за компактиране са в следния порядък:

- Контейнерът се изпълва с определеното количество материал, след което стружките се пресоват.

- Пресформата позволява да се получи брикет с височина 50мм.

- Температурата се контролира с две термодвойки – желязо константан, разположени в идеалния център на обработвания материал и на границата нас вътрешната повърхнина на контейнера, и се поддържа с точност +/- 5°C.

- Пресоването се осъществява на хидравлична преса PYE 250 ss.

- За установяване влиянието на параметрите, които оказват съществено влияние върху свойствата на крайния продукт се извърши вариране в следните диапазони:

1) Сили на пресоване - 50 и 60 tf

2) Времена за осъществяване на пресоването - 30 и 60s

3) Температури на обекта на пресоване и инструменталната екипировка - 20,350,400°C

4) За намаляване на триенето в зоната на контакт между инструмент и пресован материал се извършва нанасяне върху формообразуващите повърхнини на инструменталната екипировка, последователно и в комбинации на слоеве от следните материали:

- COPPER SPRAY – MOTIP

- METALSTAR PA111 – KLUBER LUBRICATION

На фиг.2 е показана пресформа за екструдиране на получените компакти. Екструдирането се извършва в описаната по горе инструментална екипировка, след подмяната на долен поансон (фиг.1-поз.8), с матрица с вътрешен диаметър 12мм (фиг.2-поз.8).
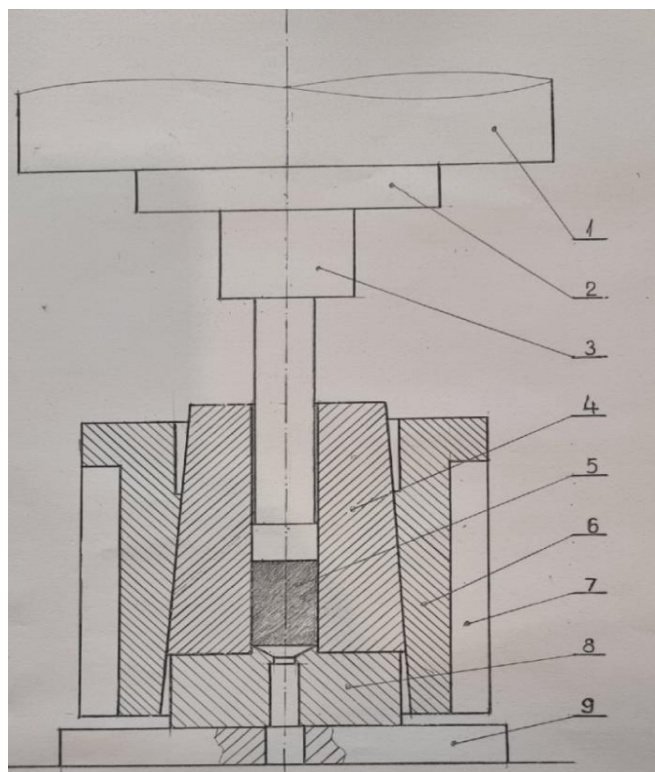
Фиг.2

При екструдиране се преминава през следните операции:

- Полученият компакт при определените за неговото създаване условия, престоява в контейнера до достигане на необходимата температура.

- Температурата се контролира с термодвойка – желязоконстантан, осъществявано от директен контакт между компакт и термодвойка.

- Екструзията се извършва след темпериране на системата компакт – инструментална екипировка със сила на пресоване в диапазона 60-100 tf .

Пресоването се извършва на хидравлична преса РУЕ-250сс, показана на фиг. 3

Фиг.3

3. Заключение

Конструирана е специализирана пресформа за компактиране на стружки и екструдиране на компаакти от алуминиеви сплави. Експериментирани са технологии за получаване на компакти и екструдирани образци, които са съобразена с различни фактори (вид на материала, използвани обмазки, вид и сила на пресоване, температурни вариации на пресформата и обработвания образец), влияещи върху крайния резултат. Изледват се качествата на изработените образци.

4. Благодарности

5. Литература:

[1] M. Hasse, N. Ben Khalifa, A.E. Tekkaya. Improving mechanical properties of chip-based aluminium extrudetes by integrated extrusion and equal channel angular pressing (iECAP), Jurnal Material Sciece and Engineering; 2012: A539 , 194-204.

[2] V. GÜLEY, N. BEN KHALIFA AND A. E. TEKKAYA, Direct recycling of 1050 aluminum alloy scrap material mixed with 6060 aluminum alloy chips by hot extrusion, International Journal of Material Forming (2010) 3 853–856, Supplement 1.

[3] Kalpakjian, S. and S. Schmid.,2006," Manufacturing, Engineering and Technology"5th Eds. Pearson, 1295p.

[4] Matjaz Torkar. Recycling of Steel Chips, Journal Materials and technology 44; 2010: 5, 289-292.

Structural and optical properties of nanostructured ZrO2 films obtained by an electrochemical process deposited on different temperatures.

Hristo Nichev
Academician Emil Djakov Institute Of Electronics
Bulgarian Academy Of Sciences
Sofia, Bulgaria
nitchev@ie.bas.bg

Abstract: The influence of the deposition temperature (in the range from 50 to 80°C) of the aqueous solution containing ZrOCl2 and KCl on the properties of ZrO2 films obtained by electrochemical deposition on SnO2 covered glass substrates is studied. Through the implementation of X-ray Diffraction (XRD), Scanning Electron Microscopy (SEM), optical profilometry, UV-VIS-NIR and photoluminescence spectroscopy, the temperature dependence of ZnO films properties is revealed. The polycrystalline status of the films is confirmed at all deposition temperatures through the obtained characteristic x-ray reflexes of the ZrO2 films. The SEM pictures show that the ZrO2 films deposited at lower temperature comprise nano-grains that transform in nano-walls with increasing the deposition temperature. With a further increase in temperature to 80°C the deposited layers consist mainly of nano-rods. It is demonstrated that the deposition temperature impacts the reflectance and transmittance spectra and haze ratio of the ZrO2 layers. The high values of the diffuse reflectance and transmittance in the spectral range from 380 to 800 nm could be beneficial for application of similar films as rear contacts of thin films solar cells.